Neutron scattering from some light: heavy rare earth alloys

R. G. Curry

NEUTRON SCATTERING FROM SOME LIGHT-HEAVY RARE EARTH ALLOYS.

by

R. G. Curry, B.Sc.

A thesis presented in candidature for the degree of Doctor of Philosophy in the University of Durham.

May 1976.

ACKNOWLEDGMENTS

I am indebted to my supervisor, Professor. K.N.R. Taylor, for his continued assistance throughout the course of this work.

I must also express my thanks to Dr. M. Stringfellow of the U.K.A.E.A., for providing some of the material of Appendix 2, and Dr. R. Day, for allowing me to use the vibrating sample magnetometer at the C.S.I.R.O., Sydney.

Further, my appreciation goes to the entire magnetism group at Durham University and at the University of New South Wales for 'ad hoc' assistance and advice, and to the Heads of each Physics Department, Professor. G.D. Rochester, F.R.S. and Professor. E.P. George respectively, for making research facilities available.

The neutron scattering results presented in this thesis would not have been obtained had it not been for the co-operation of the reactor staff of the U.K. and Australian Atomic Energy Commissions.

The work was performed during the tenure of a maintenance grant from the Science Research Council and the University of New South Wales.

Last, but by no means least, I should like to thank my wife for typing the manuscript so carefully.

ABSTRACT

Neutron scattering and susceptibility measurements as a function of temperature are reported on alloys between the light rare earths Pr and Nd and the heavy rare earths Tb, Dy and Ho over the entire composition range. It is clear from the results that the alloys form three distinct crystallographic and magnetic phases dependent upon composition.

The heavy rare earth rich alloys remain in the h.c.p. phase like the parent heavy rare earth metal and the magnetic properties are essentially those of a magnetic dilution system. The ordering temperatures are shown to follow a $^{2}/_{3}$ power law with reduced de Gennes function in common with many other rare earth alloy systems.

Alloys containing approximately equal proportions of light and heavy rare earth metals adopt the complicated Sm. structure and, as a result, display a complex magnetic structure.

The light rare earth rich alloys display the d.h.c.p. crystallographic structure like Pr and Nd. The magnetic properties of the ferrimagnetic d.h.c.p. alloys are accounted for in terms of a two sublattice model of magnetism.

CONTENTS

Acknowledgments (i)

Abstract (ii)

Contents (iii)

List of Figures (vii)

List of Tables (xi)

Preface (xiii)

CHAPTER 1. INTRODUCTION

1.1 Electronic structure of the rare earths 1

1.2 Crystal structure and alloying 2

1.3 Magnetic properties and magnetic structure of the rare earth elements 6

1.4 Magnetic interactions in the rare earth metals 22

1.5 Rare earth alloys 25

(i) Dilution alloys in the h.c.p. structure 26

(ii) Intra-heavy rare earth alloys 27

(iii) Light-heavy rare earth alloys 28

CHAPTER 2. THEORETICAL BASIS

2.1 Molecular field theory 32

(i) Ferrimagnetism 34

(ii) Heisenberg exchange interaction in the molecular field model 39

2.2 High temperature ordering in the Rare Earths - Helimagnetism 41

2.3 Effect of a magnetic field on a helical spin system 43

2.4 The Exchange Interaction 46

CONTENTS (Continued)

2.5	Theory of the turn angle	49
	(i) Temperature dependence of the turn angle	51
2.6	Low temperature ordering - ferromagnetism	52
2.7	The Crystal Field	54
2.8	Ordering in the light rare earths	60
2.9	Spin Waves	64
	(i) Application to the rare earths	64

CHAPTER 3 NEUTRON SCATTERING

3.1	Elastic neutron scattering	70
3.2	Geometric structure factor, G, and the reciprocal lattice	71
3.3	Debye-Waller Temperature Factor	76
3.4	Preferred Orientation and Absorption	77
3.5	Neutron-magnetic scattering	79
3.6	Magnetic form factor	80
3.7	Neutron scattering from magnetically ordered systems	81
3.8	Observed magnetic neutron scattering powder patterns	85
3.9	Inelastic neutron magnetic scattering	89

CHAPTER 4 EXPERIMENTAL DETAILS

4.1	Specimen preparation and characterisation	91
4.2	A.C. Susceptibility Bridge	
	(i) Experimental apparatus	92
	(ii) Relationship between output voltage and susceptibility	98

CONTENTS (Continued)

4.3	Critical field measurements		99
4.4	Neutron scattering		
	(i)	Elastic neutron scattering	102
	(ii)	Cryostat and temperature control	107
	(iii)	Inelastic neutron scattering	111
4.5	Magnetic structure determinations		115
4.6	Evaluation of the ordered moment at 4.2K		121

CHAPTER 5 EXPERIMENTAL RESULTS

5.1	Structural data		127
5.2	Magnetic data		134
	(i)	H.C.P. Phase	141
	(ii)	Sm. Phase	159
	(iii)	D.H.C.P. Phase	170

CHAPTER 6 DISCUSSION OF RESULTS

6.1	H.C.P. Phase		
	(i)	Variation of the Néel temperature on alloying	185
	(ii)	Variation of the Initial turn angle on alloying	187
	(iii)	Variation of the helical turn angle with temperature	193
	(iv)	Variation of the critical field with temperature	196
	(v)	Low temperature ordering	199
6.2	Sm. Phase		201
6.3	D.H.C.P. Phase		209
6.4	Summary of Results		215

CONTENTS (Continued)

CHAPTER 7	CONCLUSIONS AND SUGGESTIONS FOR FURTHER WORK	218
APPENDIX 1	Derivation of the theoretical scattered intensity for some magnetic structures	224
APPENDIX 2	Evaluation of magnetic structure factors	
	A2.1 Uniform basal plane spiral in the h.c.p. phase	234
	A2.2 Uniform basal plane spiral in the Sm. phase	237
	A2.3 Basal plane ferromagnet in Sm. phase with c-axis modulation	239
APPENDIX 3	Band Structure and $\chi(q)$ calculations for the rare earth metals	246
APPENDIX 4	Derivation of the susceptibility χ, and ordering temperature T_{FN}, for a ferrimagnetic alloy.	252
REFERENCES		257

LIST OF FIGURES

CHAPTER 1

1.1	Schematic representation of f.c.c., h.c.p., d.h.c.p. and Sm. structures	4
1.2	La-Gd phase diagram (after Spedding, 1962)	7
1.3	Low field susceptibility vs. temperature for Dy (after Behrendt, 1958)	11
1.4	Schematic representation of helical spin structure and C.A.M. structure	12
1.5	Schematic representation of the heavy rare earth spin structures	14
1.6	Néel temperatures and initial turn angles for the rare earth elements and alloys vs. de Gennes factor	24

CHAPTER 2

2.1	Effect of an applied field on a spiral spin structure	45
2.2	Crystal field level splitting diagram for cubic and hexagonal sites in Pr^{3+}	63
2.3	Exciton dispersion curves for Pr^{3+} on cubic and hexagonal sites (after Rainford, 1971)	68

CHAPTER 3

3.1	Construction defining scattering vector $\underline{k}$ (after Brown & Forsyth 1973)	72
3.2	Reciprocal lattice for the h.c.p. structure	75
3.3	Construction showing unit vectors $\hat{K}$ and $\hat{J}$ used in the discussion of magnetic scattering (after Bacon 1962).	72

CHAPTER 4

4.1	Electronic layout of A.C. susceptibility bridge	94

LIST OF FIGURES (Continued)

4.2	A.C. Susceptibility apparatus	95
4.3	The neutron diffractometer	103
4.4	B.O.C. closed top cryostat used in conjunction with the neutron diffractometer	108
4.5	Inelastic scattering neutron spectrometer	113
4.6	Diffraction pattern of a uniform basal plane spiral spin structure	116
4.7	Variation of peak intensity with temperature for a ferromagnetic diffraction peak	119
4.8	Diffraction pattern due to a basal plane ferromagnet at 4.2K compared with the scattering from the same sample at room temperature	120
4.9	Comparison of the observed and theoretical diffraction patterns for the basal plane ferromagnet $Pr_{10}Tb_{90}$ at 4.2K	126
CHAPTER 5		
5.1	Lattice parameters for the Pr-Tb and Nd-Tb alloy systems vs. composition	130
5.2	Axial ratio c/a, vs. effective atomic number, Z*	132
5.3	Magnetic transition temperatures vs. composition for Pr-Tb alloy system	135
5.4	Magnetic transition temperatures vs. composition for Nd-Tb alloy system	136
5.5	Magnetic transition temperatures vs. composition for Pr-Dy alloy system	137

LIST OF FIGURES (Continued)

5.6	Magnetic transition temperatures vs. composition for Nd-Dy alloy system	138
5.7	Magnetic transition temperatures vs. composition for Pr-Ho alloy system	139
5.8	Magnetic transition temperatures vs. composition for Nd-Ho alloy system	140
5.9a	Susceptibility vs. temperature for some h.c.p. Pr-Tb alloys	142
5.9b	Susceptibility vs. temperature for some h.c.p. Nd-Tb alloys	143
5.10a	Critical field vs. temperature for Dy and some Dy alloys	149
5.10b	Critical field vs. temperature for $Pr_{30}Dy_{70}$ and $Nd_{30}Dy_{70}$	150
5.11	Exchange integrals vs. temperature for $Pr_{30}Dy_{70}$ and $Nd_{30}Dy_{70}$	152
5.12	Néel temperatures of the h.c.p. light-heavy rare earth alloys vs. reduced de Gennes function	157
5.13	Initial turn angle of the h.c.p. light-heavy rare earth alloys, rare earth elements and rare earth -Y alloys vs. axial ratio.	158
5.14	Diffraction pattern of $Pr_{45}Tb_{55}$ at 4.2K	165
5.15	Magnetic structure in the Sm phase	167
5.16	Temperature dependence of the broad peak and (009) satellite intensities in $Pr_{45}Tb_{55}$	168
5.17	Crystal field level splitting between ground state and first excited states on both the cubic and hexagonal sites in some Pr-Tb alloys vs. Tb. concentration	173

LIST OF FIGURES (Continued)

5.18	Susceptibility vs. temperature for Nd and some Nd-Dy alloys.	176
5.19	Inverse susceptibility vs. temperature for Pr and some Pr-Tb alloys	178
5.20	Inverse susceptibility vs. temperature for Nd and some Nd-Dy alloys	179
5.21	Inverse susceptibility vs. temperature for the alloy $Pr_{80}Dy_{20}$.	180
CHAPTER 6		
6.1	Ordering temperatures and axial ratios for some Tb rich Nd-Tb and Pr-Tb alloys.	191
6.2	Section through the Fermi surface of Dy and $Nd_{30}Dy_{70}$	195
6.3	Spin structures on the two domains in Sm and the resultant	203
6.4a	Antiferromagnetically ordered structure on a cubic site layer	207
6.4b	Ferromagnetic coupling of cubic layers along a (101) direction	207
6.5	Crystal field level splitting of lowest energy levels in $Nd_{90}Dy_{10}$ due to a magnetic field applied in various directions	214
APPENDIX 1		
A1.1	Construction defining cartesian co-ordinates of the magnetic scattering vector	226
APPENDIX 3		
A3.1	Fermi surface for Tm in the double zone scheme	248

LIST OF TABLES

CHAPTER 1

1.1 S, L and J for tripositive rare earth ions with observed and calculated ionic moments and neutron capture cross sections. 9

CHAPTER 2

2.1 Operator equivalents pertinent to the rare earth crystal field terms. 56

2.2 Factor $\bar{V}_{\ell}^{m}$ for the rare earth metals 58

2.3 Contribution of each crystal field term to the anisotropy 61

CHAPTER 3

3.1 Observed magnetic neutron scattering patterns 88

CHAPTER 5

5.1a Lattice parameters, axial ratio and effective atomic numbers for the Pr-heavy rare earth alloys 128

5.1b Lattice parameters, axial ratio and effective atomic numbers for the Nd-heavy rare earth alloys 129

5.2 Magnetic data for the h.c.p. Pr-Tb and Nd-Tb alloys 145

5.3 Magnetic data for the h.c.p. Pr-Dy and Nd-Dy alloys 147

5.4 Data used in evaluating I(1) and I(2) for $Pr_{30}Dy_{70}$ and $Nd_{30}Dy_{70}$ 151

5.5 Magnetic data for the h.c.p. Pr-Ho and Nd-Ho alloys 155

5.6 Magnetic data for the Sm. and d.h.c.p. Pr-Tb and Nd-Tb alloys 161

5.7 Magnetic data for the Sm. and d.h.c.p. Pr-Dy and Nd-Dy alloys 162

LIST OF TABLES (Continued)

5.7a	Further magnetic data for some Nd rich Nd-Dy alloys	163
5.8	Magnetic data for the Sm. and d.h.c.p. Pr-Ho and Nd-Ho alloys	164
5.9	Observed and calculated para-magnetic moments and temperature axis intercepts for some d.h.c.p. light-heavy rare earth alloys	181
5.10	Observed and calculated exchange parameters for the rare earth metals	183

APPENDIX 2

A2.1	Comparison of magnetic structure factors for 60^{o} spiral and modulated Ox ferromagnet in Sm. phase	243

PREFACE

In the two decades since relatively pure rare earth metals became available, the magnetic properties of the metals, their compounds and some of their alloys have been studied in detail. However, the complicated magnetic structures of the rare earth metals would doubtless have remained unsolved until much more recently had it not been for the advent of nuclear scattering techniques, made possible by the construction of high flux nuclear reactors at about the same time. Neutron scattering experiments on pure single crystals have now resulted in the unique determination of the magnetic structures of all the rare earth metals.

The fourteen chemically similar rare earth elements display a diversity of magnetic properties. Gd and at low temperatures, Tb, Dy and Ho are ferromagnetic, whereas Pr and Nd are only weakly magnetic even at 4.2K. The present study was undertaken in an effort to promote magnetic ordering in the light rare earth metals Pr and Nd by alloying each of them in turn with the strongly magnetic heavy rare earth elements Tb, Dy and Ho. Gd was omitted from the study since the naturally occurring, and thus readily obtainable isotope is an almost perfect absorber for thermal neutrons and it would not be possible to study the magnetic structure of this alloy by neutron scattering. The investigation was extended to cover the

complete composition range of the six alloy systems in 10% composition steps across the series. In doing this it was not possible to make neutron scattering measurements on every sample, but only on representative samples, due to the size and thus cost of the neutron scattering samples and the relatively short time allotted to each investigator on the neutron scattering apparatus.

The results from the neutron scattering and susceptibility vs. temperature measurements on the light-heavy rare earth alloys obtained in the course of this investigation are presented in this thesis.

In the first chapter the magnetic and structural properties of the rare earth metals and their alloys are described. The theoretical basis for their understanding is presented in Chapter 2, extended to provide a foundation for the discussion of the magnetic properties of the light-heavy rare earth alloys. The basic equations necessary for the interpretation of the neutron diffraction data are derived in Chapter 3, and the experimental techniques and the experimental results are the subject of Chapters 4 and 5, respectively. The results are discussed in Chapter 6, in the context of the theory presented in Chapter 2, and the conclusions and suggestions for further work form the contents of Chapter 7.

ERRATA

p.46 Last sentence to read "Assuming that the electrons are a free gas, ... etc.

p.84 Line 3 for"crystallographic" read "cartesian"

p.118 Line 19 for "nuclear peaks" read "magnetic contribution at the nuclear peak positions"

p.204 Line 7 for "total angular momentum" read "total angular momentum quantum number"

CHAPTER 1

INTRODUCTION

1.1 ELECTRONIC STRUCTURE OF THE RARE EARTHS

The 15 elements of the lanthanide group (Z = 57 to Z = 71) are so chemically alike that after Lanthanum itself, the other 14 occupy only one entry in the periodic table. Their similarity is due to their electronic structures. Lanthanum has a Xenon core ($1s^2$ $2s^2$ $2p^6$ $3s^2$ $3p^6$ $3d^{10}$ $4s^2$ $4p^6$ $4d^{10}$ $5s^2$ $5p^6$) plus $4f^o$ $5d^1$ $6s^2$ electrons. Proceeding to the next element, Cerium, on increasing the nuclear charge the additional extra-nuclear electron finds it energetically more favourable to occupy the 4f level rather than the 5d level. The other rare earth metals are then created by the sequential filling of the 14 vacancies in the 4f shell.

The 4f shell is both energetically, as well as spatially, buried below the 5s, 5p, 5d and 6s levels, (Taylor & Darby 1972). There are two main consequences of the size of the 4f shell. Firstly, the increased nuclear charge across the lanthanide series is not fully screened and all the electrons are increasingly tightly bound. The subsequent decrease in ionic radius with increasing atomic number is known as the lanthanide contraction. Secondly, the 4f electrons are screened from the local environment by the $5s^2$ and $5p^6$ electrons and, as a result, the magnetic properties of the ion in

a host lattice are almost the same as the free ion and a localised magnetic moment arises (see Section 1.3).

The more stable half-full and full 4f shell ionic configurations are reached by natural progression at Gadolinium and Lutecium, respectively. The elements preceding these two, Europium, $4f^6$, and Ytterbium, $4f^{13}$, also achieve a $4f^7$ and $4f^{14}$ configuration by demoting their 5d electron to the 4f shell. On entering the metallic state the rare earths lose their outer electrons to the valence band to become tripositive ions. In the case of Eu and Yb, though, the elements become divalent ions in the metallic state.

The elements Scandium (Z = 21) and Yttrium (Z = 39) are sometimes considered as rare earths because they have similar electronic and crystal structures.

1.2 CRYSTAL STRUCTURE AND ALLOYING

The rare earths exhibit all the normal metallic crystal structures b.c.c., f.c.c., and h.c.p. as well as d.h.c.p. and Sm structures. The seven elements La to Eu are known as the light rare earths whilst the rest are called the heavy rare earths. Amongst the light rare earths La, Pr and Nd exhibit the d.h.c.p. phase at room temperature, while Ce has a f.c.c. structure and Eu a b.c.c. structure. The room temperature structure of Pm was reported recently by Palmer and Chikalle (1971) to be d.h.c.p. Ce shows the formation of a d.h.c.p. phase at 260K which transforms to a more complex mixed f.c.c. and d.h.c.p.

phase below 100K (Gschneidner 1961). Sm has a complicated nine layer structure which is unique to this element, (Daane et al 1954). The heavy rare earths, together with Y and Sc,exhibit the hcp structure at room temperature. A schematic representation of the f.c.c., h.c.p., d.h.c.p. and Sm structures is shown in Fig. 1.1. As indicated in the figure these structures may be viewed in terms of the stacking of three basic layers, A, B and C. The stacking sequences are then,

h.c.p. : ABAB....; Sm : ABABCBCAC....;

d.h.c.p. : ABAC....; f.c.c. : ABCABC....

Denoting ions which have a cubic nearest neighbour environment by c and those which have hexagonal site symmetry by h, the stacking sequences become:

h.c.p. : hhhh....; Sm : hhchhchhc....;

d.h.c.p. : hchc....; f.c.c. : cccc....

From La to Lu then, the room temperature crystal structures of the metals show an increasing proportion of the hexagonal phase. Eu and Yb do not follow this general trend as they are divalent ions in the metallic state. The b.c.c. crystal structure is the high temperature phase for all the rare earths except Er, Th and Lu.

The room temperature crystal structures of the rare earth metals are retained to 4.2K with the exception of Dy. At 85K,at the onset of ferromagnetic ordering,the crystal structure spontaneously distorts

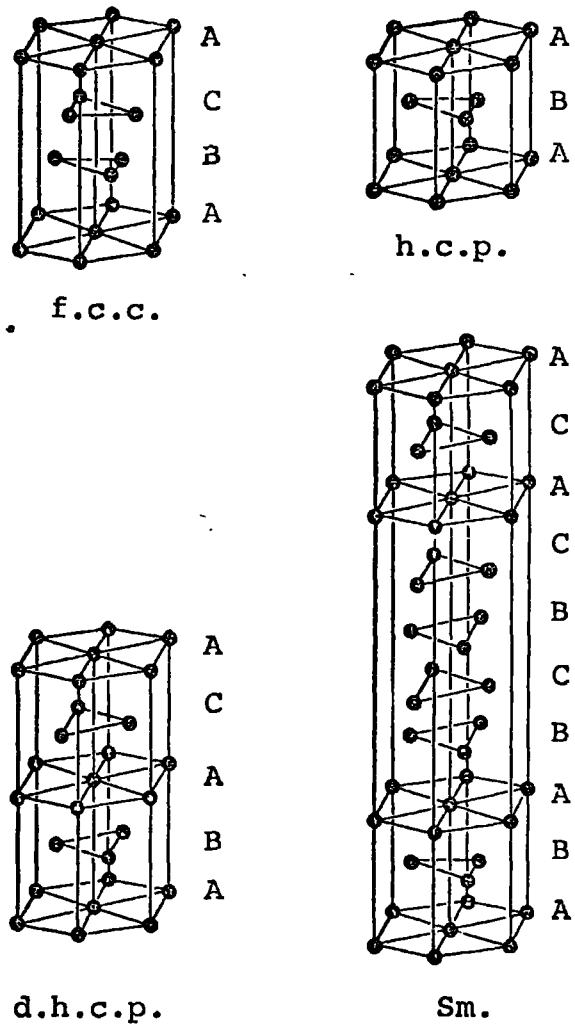

FIG. 1.1 Schematic representation of f.c.c., h.c.p., d.h.c.p., and Sm. structures showing stacking sequence of layers.

from hcp to orthorhombic relieving the stresses resulting from the magnetic transition (Darnell et al 1963) (see Section 2.6).

Recently Johansson et al (1975) have constructed a generalised phase diagram for the rare earth elements which accounts qualitatively for the trend in crystal structure. They also point out that the same structure sequence, h.c.p. → Sm → d.h.c.p. → f.c.c. is followed by all the individual elements under the influence of large applied pressures and they successfully explain this trend too.

The ratio of the axial and basal plane lattice parameters of the rare earths, 'c' and 'a' respectively, also varies uniformly across the series. In the heavy rare earths the c/a ratio varies between 1.59 and 1.57 from Gd to Lu. For comparison purposes the axial ratio of the Sm structure is divided by 4.5 and the axial ratio of the dhcp structure by 2 to reduce them both to an effective two layer structure. The axial ratios of the light rare earths from La to Pm are approximately 1.61, which is close to the theoretical value of 1.63 for the closest packing of spheres. The axial ratio of Sm is 1.602 (Taylor 1970).

The rare earths with the exception of Eu and Yb are extensively soluble in one another and in Sc and Y according to the Hume-Rothery criteria (Hume-Rothery 1939, Gschneidner 1961). By alloying light rare earths with

heavy rare earths, structures are obtained which are intermediate between those of the component elements. The crystal structure of an alloy can be identified with its effective atomic number (Harris et al 1969). The effective atomic number Z* is defined as

$$Z^* = x\ Z_A + (1 - x)\ Z_B$$

where x is the fractional concentration of the component with atomic number Z_A and Z_B is the atomic number of the other alloy constituent. A systematic study of intra-rare earth alloys was made by Spedding (1962). His phase diagram for the alloying of La with Gd (Fig 1.2) is typical for alloys formed between dhcp and hcp rare earth metals (Nachman et al 1963). From the figure it is clear that on the addition of Gd (increasing hcp content) the dhcp structure becomes unstable, transforming to the Sm structure at approximately 60 atomic % Gd. The Sm phase is only stable over a narrow concentration range and in turn transforms to the hcp phase. The high temperature f.c.c. phase becomes increasingly less stable with respect to the dhcp phase and finally disappears for concentrations greater than approximately 20 at % Gd.

1.3 MAGNETIC PROPERTIES AND MAGNETIC STRUCTURE OF THE RARE EARTH ELEMENTS.

The magnetic moment of a rare earth ion resides in its unfilled 4f shell. The ionic spin angular momentum,

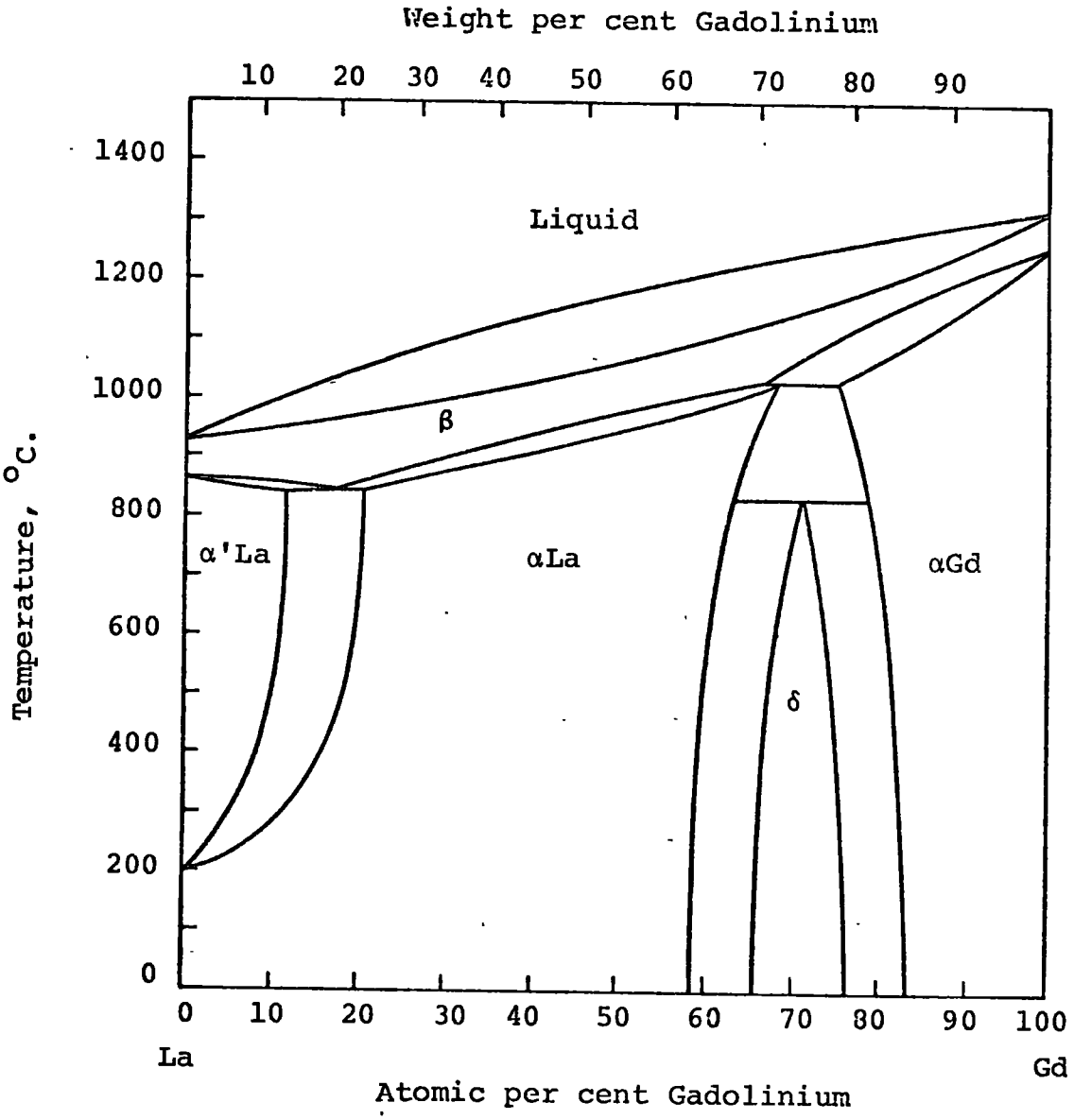

FIG. 1.2 Phase Diagram for La-Gd system (after Spedding 1962).

$\underline{S}$, and the orbital angular momentum $\underline{L}$ may be calculated using Hund's Rule and Pauli's principle and then the total angular momentum $\underline{J}$ may be calculated using Russell-Saunders' coupling. For a less than half full 4f shell the orbital and angular momenta couple anti-parallel i.e. $\underline{J} = \underline{L} - \underline{S}$ and for a more than half full 4f shell they couple parallel i.e. $\underline{J} = \underline{L} + \underline{S}$. The observed paramagnetic moments in the rare earth salts and indeed in the rare earth metals, agree well with the theoretical value of $g_J \mu_B \sqrt{J (J + 1)}$ for the magnetic moment of the ground state of a system of non-interacting ions, (see Table 1.1), where g_J is the Landé splitting factor and μ_B is the Bohr magneton. The discrepancy between the observed and predicted moment values for Sm and Eu can be understood in terms of Van Vleck's postulate of the admixture of higher electronic levels into the groundstate, (Van Vleck 1932). Yb enters the metallic state as a divalent ion (see Section 1.1) and was reported in the literature to have a very small temperature independent susceptibility. More recently Bucher et al (1970) have reported that Yb is diamagnetic.

In spite of the localised nature of the 4f shell, eleven of the fifteen lanthanide elements exhibit some form of spontaneous magnetic ordering below 300K. The exceptions are La, Pr, Yb and Lu. La and Lu have zero and 14 electrons respectively in their 4f shells, and consequently have temperature independent susceptibilities.

TABLE 1.1

SOME MAGNETIC PROPERTIES AND NEUTRON CAPTURE CROSS SECTION OF THE RARE EARTH METALS

					Paramagnetic Moment		Saturation Moment				
					$g_J\sqrt{J(J+1)}\,\mu_B$		$g_J\,\mu_B$				
Ion	L	S	J	gJ	calc.	obs. ie μ_{eff}	calc.	obs.	σ cap barns	T_N† ^oK	T_c† ^oK
La^{3+}	0	0	0	0	0.00	0			8.9		
Ce^{3+}	3	1/2	5/2	6/7	2.56	2.51			0.7		
Pr^{3+}	5	1	4	4/5	3.58	3.56			11.2		
Nd^{3+}	6	3/2	9/2	8/11	3.62	3.30			46.0		
Pm^{3+}	6	2	4	3/5	2.68	-			-		
Sm^{3+}	5	5/2	5/2	2/7	0.84	1.74			5500		
Eu^{3+}	3	3	0	-	0.00	7.12			4600		
Gd^{3+}	0	7/2	7/2	2	7.94	7.95	7.0	7.55	46000	-	293
Tb^{3+}	3	3	6	3/2	9.70	9.70	9.0	9.34	44.0	229	221
Dy^{3+}	5	5/2	15/2	4/3	10.60	10.64	10.0	10.33	11.00	179	85
Ho^{3+}	6	2	8	5/4	10.60	10.89	10.0	10.34	64	132	20
Er^{3+}	6	3/2	15/2	6/5	9.60	9.50	9.0		166	85	20
Tm^{3+}	5	1	6	7/6	7.60	7.62	7.0	7.14	118	58	25
Yb^{3+}	3	1/2	7/2	8/7	4.50	4.50			36		
Lu^{3+}	0	0	0	0	0.00	0			108		

† The saturation moments and ordering temperatures for the light rare earths are discussed in the text.

(Finemore et al 1968). Yb has been discussed above. The absence of ordering in Pr will be discussed in detail later (see Section 2.8).

The first magnetic data on the rare earths, particularly the heavy rare earths, were from susceptibility and magnetisation measurements. The temperature dependence of the low field susceptibility of Dy is shown in Fig. 1.3 (after Behrendt et al 1958). Two magnetic transitions are evident. The cusp at 179K denotes the onset of antiferromagnetic ordering and is referred to as a Néel point. The sharp increase in susceptibility followed by saturation evidences a change to ferromagnetic ordering. The point of inflection of the susceptibility vs. temperature curve in this region is taken as the Curie point as indicated in the figure.

Classical magnetisation measurements could not determine the precise orientation of the spins in the antiferromagnetic state and it was not until good single crystals were available that the structures were elucidated by neutron diffraction. The most commonly found antiferromagnetic structure in the heavy rare earths which occurs for example between 179K and 85K in Dy is the helical spin structure shown in Fig. 1.4. In this structure the moments on the ions in the basal plane of the hcp structure are aligned ferromagnetically, but the moment direction on successive layers is displaced by a constant angle, ω, the turn angle. The turn angle

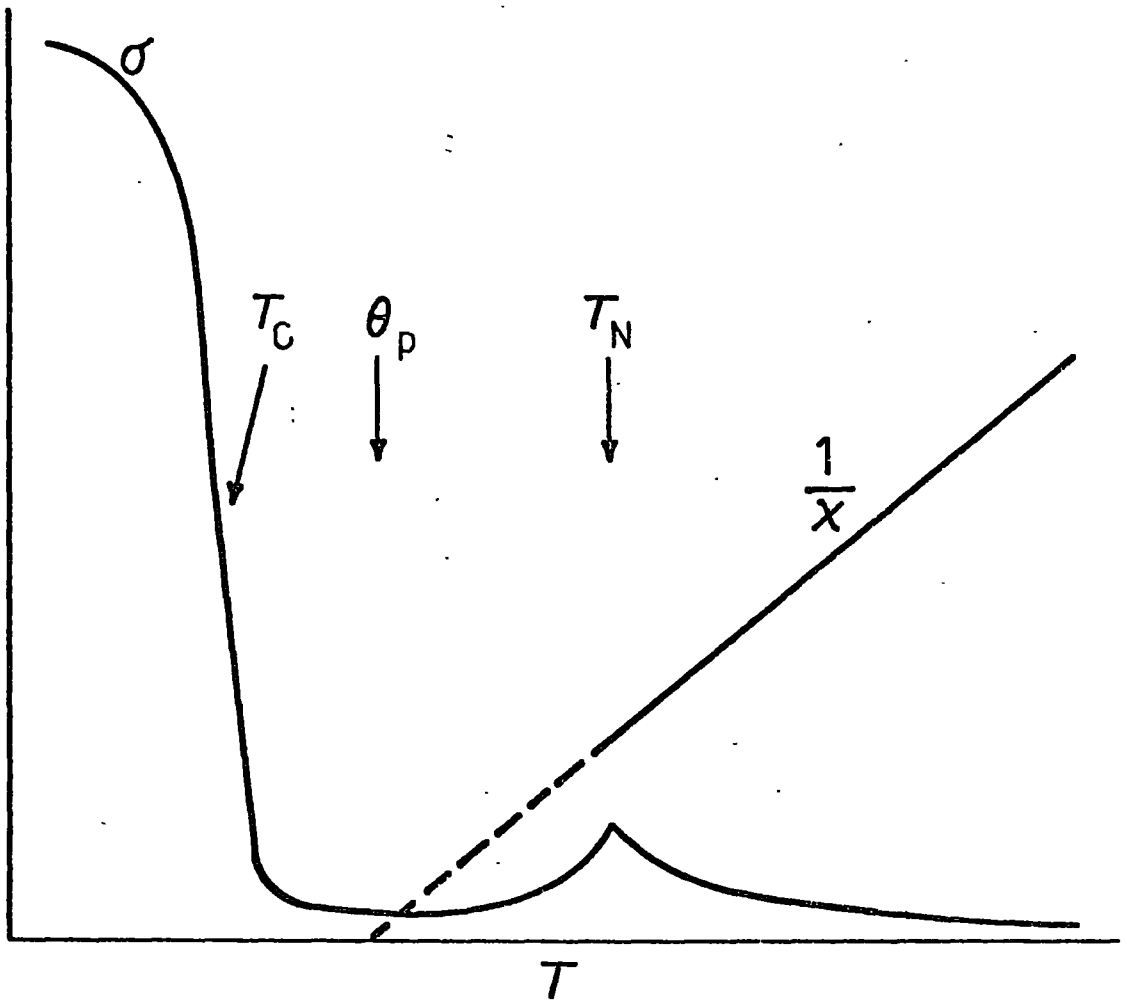

FIG. 1.3 Low field susceptibility of Dy (after Behrendt et al 1958).

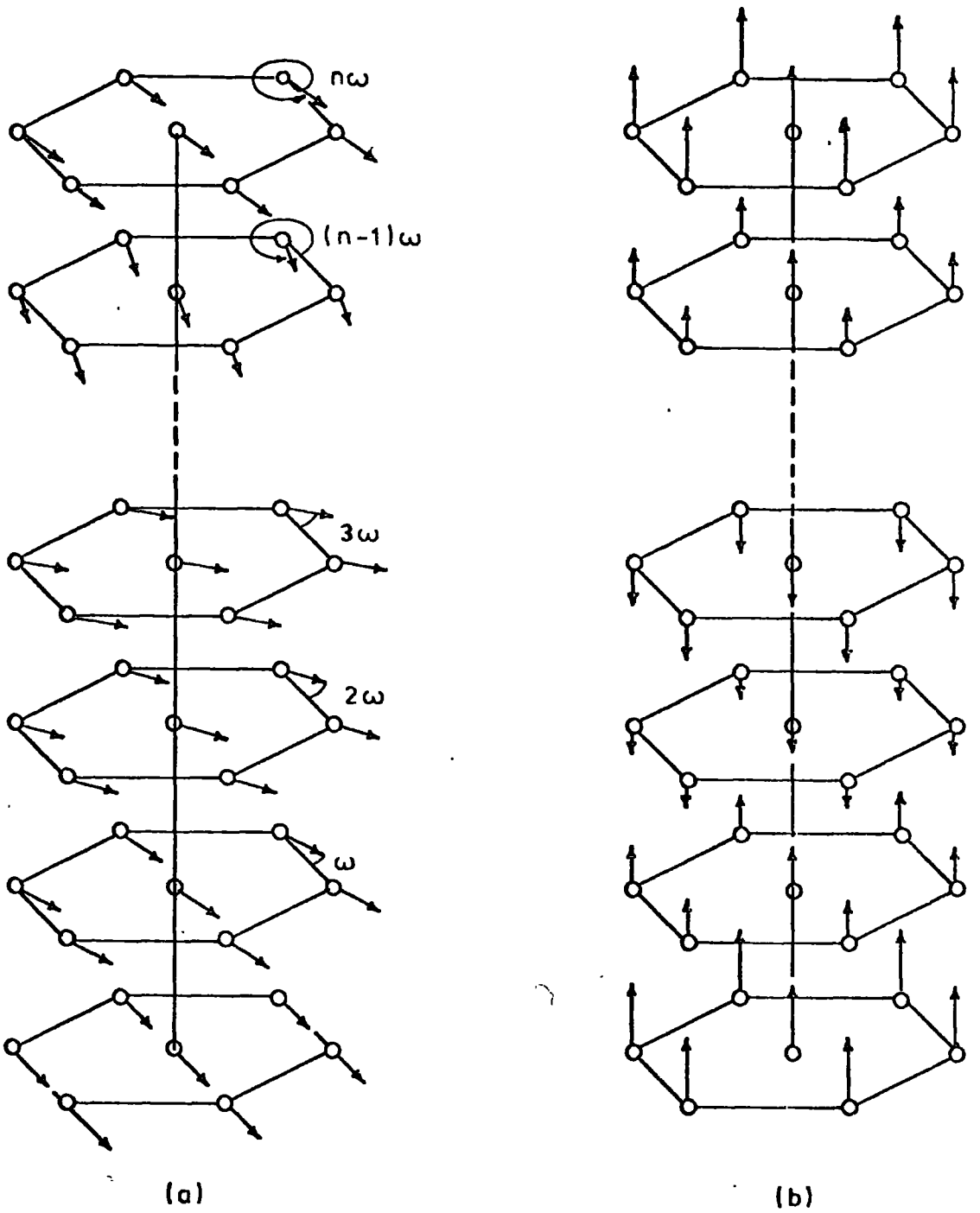

FIG. 1.4 Schematic representation of (a) uniform basal plane spiral structure and (b) c-axis modulated structure on a hexagonal lattice.

of the magnetic structure is temperature dependent and decreases from its initial value ω_i at T_N with decreasing temperature to fall abruptly to zero at the Curie temperature T_c from a finite value ω_f just above the Curie temperature. In general the periodicity of the magnetic structure is not related to the crystal structure periodicity.

The spin structures of all the heavy rare earths have now been deduced. A schematic representation of all the spin structures is given in Fig. 1.5.

Will et al (1964) have reported that Gd is ferromagnetic below 293K. Their work has been repeated by Kuchin et al (1969) on a single crystal of Gd enriched in the low capture cross section isotope ^{160}Gd with the same result. Whilst it appears that Gd is spontaneously ferromagnetic throughout the entire ordered region, the torque measurements of Graham (1962) and Corner et al (1962) show that the easy direction of magnetisation in Gd is temperature dependent. The moment direction is parallel to the c-axis from the Curie temperature to 232K, and then moves away to a maximum deviation of 65° at 180K and then back to about 32° from the c-axis at low temperature.

An antiferromagnetic spiral phase exists in Tb only over the small temperature range from 229K to 221K (Koehler et al 1963). At lower temperatures it spontaneously transforms to the ferromagnetic state.

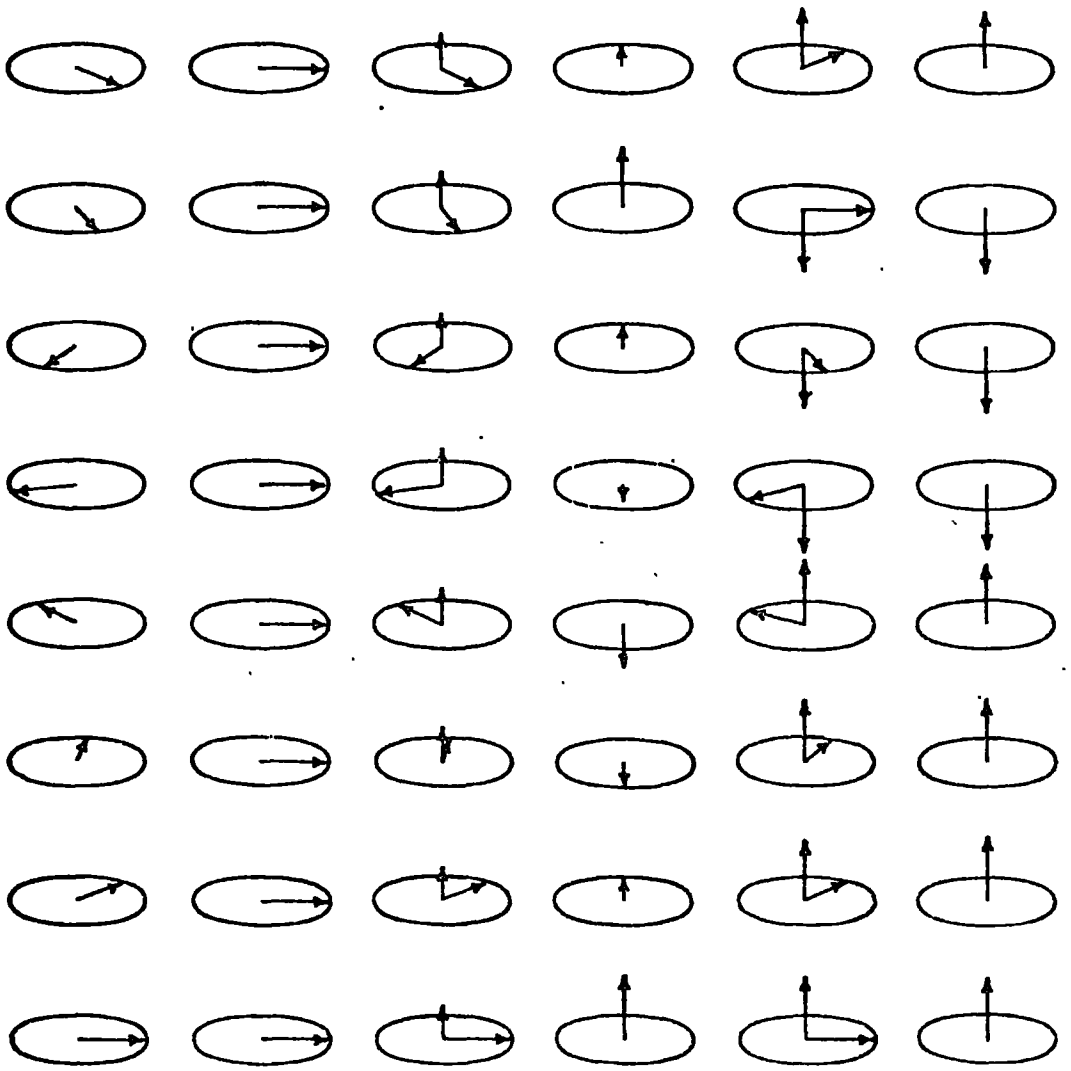

Tb	$228° \geq T \geq 218°$	$T < 218°$				
Dy	$179° \geq T \geq 87°$	$T < 87°$				
Ho	$133° \geq T \geq 20°$		$T < 20°$			
Er			$T < 20°$	$80° \geq T \geq 53°$	$53° \geq T \geq 20°$	
Tm				$T \leq 56°$		$T \sim 4°$

FIG. 1.5 Schematic representation of heavy rare earth spin structures.

The ionic moment at 4.2K measured from the neutron diffraction data was $9.0\mu_B$ which is in good agreement with the theoretical saturation magnetic moment of $gJ\mu_B$. Dietrich and Als-Nielsen (1967) reported the existence of the spiral phase over a slightly greater temperature range, 216K to 226K, with a turn angle varying from 16.5^o at 216K to 20.7^o at 226K. The magnetisation data of Hegland et al (1963) gives a saturation moment of $9.34\mu_B$ which is slightly greater than the theoretical value and the neutron diffraction value, with an easy direction of magnetisation along the b-axis of the hcp structure. The significance of the excess saturation moment in Tb (and in other heavy rare earths) will be discussed in Section 2.4. Fields of order 1k0e are sufficient to destroy the helimagnetism and align all the spins ferromagnetically.

Dy adopts the helical spin configuration between its Néel temperature, 178K, and 85K when it orders into the ferromagnetic state. The initial and final turn angles of the helical structure are 43.2^o and 26.5^o respectively, (Wilkinson et al 1961 (a)). The ordered moment from the neutron diffraction results was determined to be $9.5\mu_B$ which is slightly less than the theoretical value of $10.0\mu_B$. The magnetisation data of Behrendt et al (1958) for Dy give a saturation moment of $10.2\mu_B$ which is in excess of the theoretical value, $gJ\mu_B$, directed along easy a-directions. The temperature at which Dy spontaneously

becomes ferromagnetic can be raised above 85K by the application of a field in the basal plane. The field required to destroy the helical spin structure and produce ferromagnetic alignment at a given temperature is referred to as the critical field. The magnetisation data show that the critical field varies almost linearly from 0k0e at the Curie temperature to 11k0e at 160K. Above 135K the spiral structure does not collapse simply to a ferromagnetic structure, but rather to a fan structure about the field direction. The observations of Bly et al (1969) that the easy direction changes above approximately 130K are probably connected with the appearance of the fan structure. The critical field will be discussed in more detail in Section 2.3.

Ho displays a helical spin configuration from 132K to 20K (Koehler et al 1962 (a)). At 20K a small ferromagnetic component of $1.7\mu_B$ develops parallel to the crystallographic c-axis whilst a helical spin structure remains in the basal plane, though somewhat distorted. This structure is generally referred to as the ferromagnetic cone structure and in Ho the semi-cone angle is 80°. The turn angles reported in the literature all vary slightly. The samples studied by Koehler showed an initial turn angle of 50° which decreased with decreasing temperature becoming constant at about 20K, but with values ranging from 30.0° to 36.7°. The reason for the variety of final turn angles is thought

to be related to the competition between the ordering mechanism in the rare earths and the interaction with the crystalline environment, (see Section 2.7). The basal plane moment is $9.5\mu_B$ giving a total moment of $9.7\mu_B$. Only when a field is applied along the easy b-axis is the full ionic moment of $10.0\mu_B$ developed. The neutron diffraction results agree with the magnetisation results of Strandberg et al (1962) who found a moment value of $10.3\mu_B$ in a 5kOe field applied along the b direction. Both Strandberg et al (1962) and Koehler et al (1967) have shown that the magnetisation process in Ho above 20K is very complicated. Along both the a and the b axes the transition to ferromagnetism in an applied field proceeds in two distinct steps. These humps in the magnetisation data indicate that the collapse of the spiral is not smooth with applied field and are evidence for the existence of an intermediate spin structure.

Below its Néel point at 85K, the magnetic structure Er is one in which the moments are sinusoidally modulated up the crystallographic c-axis with no basal plane component. This structure is referred to as c-axis modulated or CAM, (Cable et al 1961). (see Fig. 1.4). At 53K the basal plane moments order in a helical configuration with a temperature independent turn angle of 51.4° and simultaneously the c-axis components order into an anti-phase domain configuration with 4 moments pointing along the c-axis and 4 moments anti-parallel

to the c-axis. A third transition occurs at 20K to a ferromagnetic cone structure, like Ho, with a semi cone angle of 29^{o} and a constant turn angle of 44^{o}. At 4.2K, the moment in the basal plane is $4.3\mu_B$ and $7.6\mu_B$ in the c-direction, yielding a total moment of $8.7\mu_B$ in good agreement with the theoretically predicted value of $9.0\mu_B$ for the saturation moment. The spin structure determined from neutron diffraction is in agreement with the magnetisation data of Green et al (1961) and the high field measurements of Flippen (1964). For a field applied along the c-axis a moment of $8.0\mu_B$ develops at 4.2K, whereas for a field applied in the basal plane the magnetisation saturates at $3.8\mu_B$. The basal plane magnetisation shows a sharp increase at 15k0e indicating the transition from a helical structure to a collapsed structure.

Thulium orders in the CAM structure below 56K (Koehler et al 1962 (b)). From 40K, the configuration begins to distort to give an antiphase domain structure at 4.2K in which there are four spins parallel to the c-axis for every three spins anti-parallel. At 4.2K the moment configuration is ferrimagnetic with a net moment of $1.0\mu_B$ parallel to the c-axis.

The magnetisation results of Richards and Legvold (1969) show that the ferrimagnetic structure in Tm at 4.2K can be uncoupled by the application of fields in excess of 28k0e along the c-axis giving a ferromagnetic

moment in that direction of $7.1\mu_B$. The observed saturation moment is slightly in excess of the theoretically predicted value. The basal plane remains a magnetically hard direction even in very high fields.

Interpretation of the neutron diffraction and magnetisation data for the light rare earths has proved much more complicated because of their complex crystal structures.

Using powder neutron diffraction, Wilkinson et al (1961 (b)) have shown that an ordered magnetic state forms in dhcp Ce at 12.5K. The structure consists of ferrimagnetically ordered planes stacked such that the overall ordering is antiferromagnetic along the c-axis with an ordered moment of magnitude $0.6\mu_B$.

Johansson et al (1970) have found no spontaneous order in a single crystal of Pr down to 4.2K although previously an antiferromagnetic transition for a powdered sample of Pr was reported by Cable et al (1964).

The high field of data of McEwen et al (1973)shows that the magnetic moment increases smoothly with a field applied in the basal plane, although at 350k0e it is still some way from the theoretical saturation value of $3.2\mu_B$. The effect of an applied field along the c-axis is more pronounced. The magnetisation rises linearly to about $1\mu_B$ at 300k0e and then rises steeply to $2\mu_B$ within 2k0e at 315k0e. Previous susceptibility measurements by Johansson et al (1971) and Schieber et al (1968) at

lower fields indicated that the total moment is developed on the cubic sites of the dhcp structure, whilst the hexagonal sites are completely non-magnetic. McEwen ascribes the first order transition to be a change from a non-magnetic state to a metamagnetic state on the hexagonal sites (see Section 2.8).

In Nd the moments on the hexagonal sites order at 19K and the moments on the cubic sites order at 7.5K (Moon et al 1964). Between 19K and 7.5K there is a net antiferromagnetic coupling between hexagonal site layers with a sinusoidal modulation of the moment value within each layer. The moments lie in the basal plane parallel to the a-direction. The cubic site moments order in the same fashion as the hexagonal sites, but adopt a moment direction 30° to the a-direction in the basal plane. The high field magnetisation results of McEwen (1973) show that in the c-direction and in the basal plane the moment is far from the theoretical saturation value of $3.27\mu_B$ even at 350k0e.

Koehler et al (1972) have recently elucidated the magnetic structure of Sm using a single crystal enriched in the low capture cross section isotope ^{154}Sm. Below 106K each plane of hexagonal sites forms a ferromagnetic sheet with the moments in the sheet parallel to the crystallographic c-axis. This series of ferromagnetic sheets has the sequence 0++0--0++ along the c-axis. The zeros represent the cubic site planes and the '+' a spin

'up' and the '-' a spin 'down' i.e. parallel and anti parallel to the c-axis respectively. In this structure the influence of a pair of hexagonal layers at a cubic layer is exactly balanced by a corresponding pair of layers with an equal and opposite moment. As a result the moments on the cubic sites are disordered at 106K. At 14K the cubic sites order antiferromagnetically in a basal plane layer with moments pointing along the c-axis. These ordered planes couple along the c-axis in such a way as to give ferromagnetic sheets parallel to the (101) planes. The magnetic easy direction at 4.2K is in the basal plane, but only a small fraction of the theoretically predicted saturation moment is developed at 350k0e. (McEwen et al 1973).

Eu undergoes a transition to a helical magnetic structure below 94K with the moments parallel to a (100) direction in the b.c.c. structure (Nereson et al 1964). The interlayer turn angle of Eu varies only slightly with temperature from 51.4^{o} at T_N to 50^{o} at 4.2K. The behaviour of Eu in an applied magnetic field is different from the rest of the lanthanide elements in that it appears to have no easy direction of magnetisation. Both McEwen et al (1973) and Johansson et al (1971) report that it does not reach its saturation magnetic moment in an applied field.

The ordering temperature along with the observed and predicted saturation magnetic moments of the rare

earths are summarised in Table 1.1

1.4 MAGNETIC INTERACTIONS IN THE RARE EARTH METALS

Using the Weiss molecular field model of magnetism the long range force responsible for magnetic ordering in the rare earths can be represented as a large internal magnetic field. Heisenberg has shown this internal magnetic field to be the result of a quantum mechanical exchange interaction between individual spins on pairs of ions. Leaving aside the origins of such an interaction in a localised moment system and any interactions with the crystalline environment the exchange Hamiltonian between two atoms with total spin S_i and S_j may be written as

$$\mathcal{H}_{ex} = -2 \sum_{ij} I_{ij} S_i . S_j \qquad \ldots.(1.1)$$

where I_{ij} is the exchange integral. The state of a rare earth ion is specified by its total angular momentum, $\underline{J}$, and thus it is necessary to project $\underline{S}$ onto $\underline{J}$. This is done by eliminating L between the expressions $\underline{L} + 2\underline{S} = g_J \underline{J}$ and $\underline{L} + \underline{S} = \underline{J}$ which gives the result

$$\underline{S} = (g_J - 1)\, \underline{J} \qquad \ldots.(1.2)$$

where g_J is the Landé splitting factor. Substituting (1.2) into (1.1) gives

$$\mathcal{H}_{ex} = -2 \sum_{ij} I_{ij} J_i J_j (g_J - 1)^2 \qquad \ldots.(1.3)$$

Restricting the summation to the neighbours of the ith atom (1.3) may be re-written

$$\mathcal{H}_{ex} = -2(g_J - 1)^2 J_i \sum_{ij} I_{ij} J_j \qquad \ldots.(1.4)$$

In the spirit of the Weiss approximation (see for instance Smart 1966), at T = 0 (1.4) becomes

$$\mathcal{H}_{ex} \ (T = 0) = -2(g_J - 1)^2 I_{ij} J^2 \qquad \ldots.(1.5)$$

For all other temperatures (4) becomes

$$\mathcal{H}_{ex} \ (T \neq 0) = -2(g_J - 1)^2 I_{ij} J(J + 1)$$

Assuming I_{ij} is isotropic and of constant value throughout the rare earth series the exchange energy on this simple model is expected to be proportional to the factor

$(g_J - 1)^2 J (J + 1)$ - the de Gennes factor, G.

The Néel temperatures and the initial turn angles of the heavy rare earths are found to vary smoothly with this factor across the series with $T_N \propto G^{2/3}$ (see Fig. 1.6). The 2/3 power law, as it is known, is empirical in origin.

This model of rare earth magnetism does not explain the transitions to different magnetic phases at low temperatures nor does it account for the existence of magnetically hard directions in the metals. A preferred direction of magnetisation is due to the interaction of the ionic spin with the crystalline environment. The

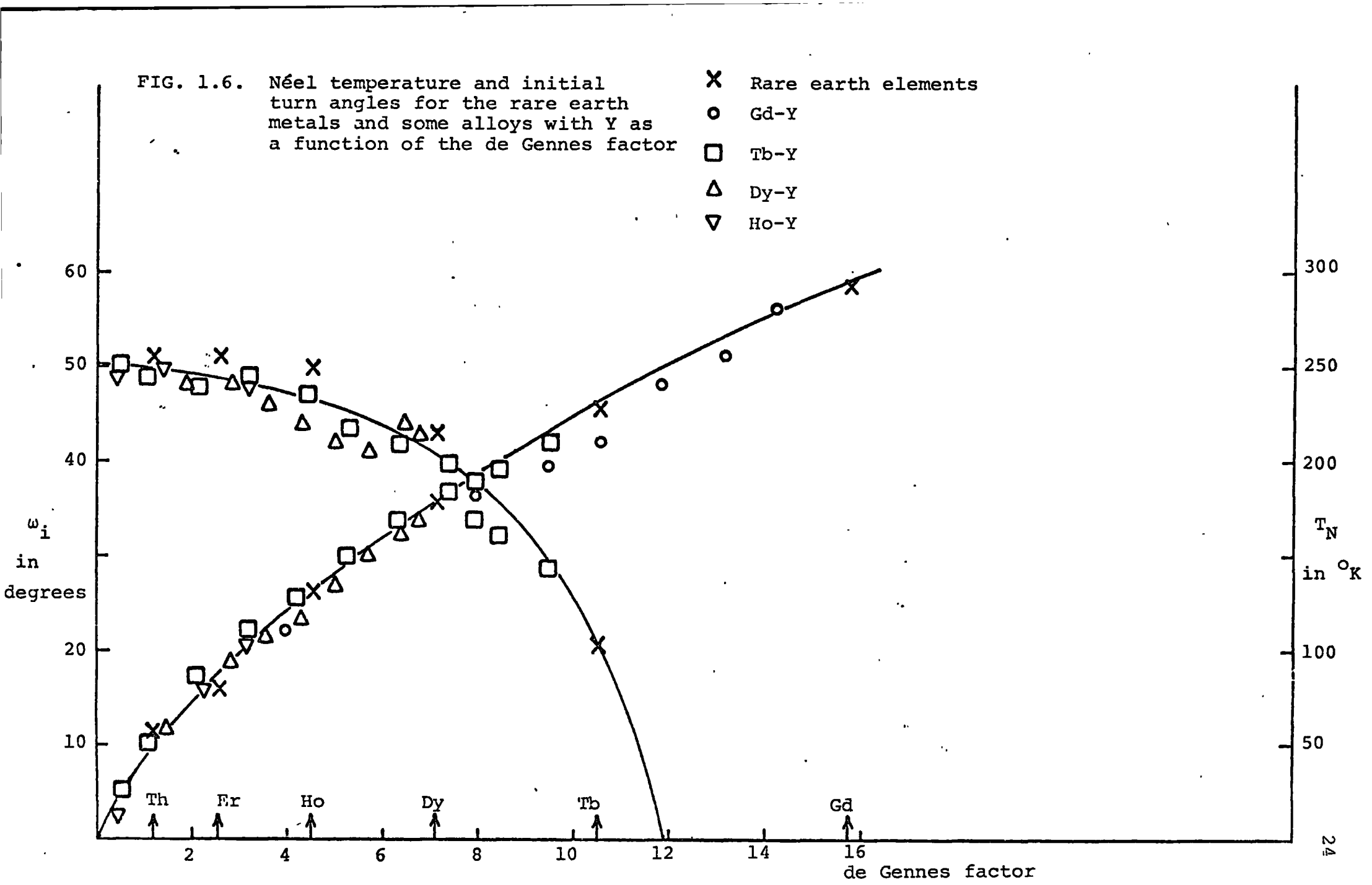

FIG. 1.6. Néel temperature and initial turn angles for the rare earth metals and some alloys with Y as a function of the de Gennes factor

regular arrangement of ions in a crystal produces an intense electric field at another ion site which aligns the aspherical 4f charge cloud. Since S and J are fixed in relation to one another by the strong spin-orbit coupling then the magnetic moment of the ion is also fixed in a particular direction (Bowden 1975). The anisotropy energies of the rare earths, as measured by the field required to pull the magnetic moment out of an easy direction into a hard direction, are very large, (see Section 1.3). The influence of the crystalfield in rare earth magnetism, particularly in the case of the light rare earths, will be dealt with in Section 2.8.

1.5 RARE EARTH ALLOYS

As mentioned previously,the rare earth elements, with the exception of Eu and Yb, form continuous solid solutions with one another and with Y and Sc. Consequently, the magnetic properties of a large number of rare earth alloy systems have now been reported. Since the rare earths from Gd onwards and Y and Sc have the same hcp structure, the alloys formed between the heavy rare earths and Y or Sc and the intra heavy rare earth alloys themselves all have the same structure over the entire composition range. The magnetic properties of the light-heavy rare earth alloys, however, are complicated by the fact that the crystal structure is concentration dependent.

The results for each type of alloy system will be presented in turn.

1.5 (i) DILUTION ALLOYS IN THE H.C.P. STRUCTURE

The heavy rare earth - Y alloys have been studied extensively by Child (1964) by neutron diffraction. His results, and those of Thoburn et al (1958) on Gd - Y, for the Néel temperature and initial turn angle are summarised in Fig. 1.6 where they are plotted against the reduced de Gennes function, $\overline{G}$

$$\overline{G} = c\ (g_J - 1)^2\ J(J + 1) \qquad \ldots(1.6)$$

where c is the concentration of the magnetic constituent. Both T_N and ω_i are universal functions of $\overline{G}$ with $T_N \propto \overline{G}^{2/3}$. For low concentrations of rare earths (i.e. low $\overline{G}$ values) the interlayer turn angle stabilises at about 50^o per layer and for $\overline{G} > 11.5$ the interlayer turn angle falls to zero, implying ferromagnetism. For Er, Ho and Dy only small amounts of Y are required to suppress the ferromagnetic transition whereas in Tb about 20% is required and in Gd only the alloys with less than 60% Gd do not show ferromagnetic ordering. The Curie temperatures for these Gd - Y alloys lie close to the universal curve. With the exception of the Gd - Y alloys with greater than 40% Y the high temperature ordered phases are the same as the pure metals. The moment directions are the same as in the parent heavy rare earth, too, indicating that the anisotropy changes little on dilution.

Both Lu and Sc have been used as non-magnetic diluents for the heavy rare earths. For the two Lu alloy

series studied, Gd - Lu (Bozorth et al 1966) and Tb - Lu (Child et al 1965) the Néel temperatures (T_c's for Gd - Lu) follow the universal curve quite well. The effect of Lu as a diluent is similar to Y although the interlayer turn angle, as measured in the Tb - Lu alloys, appears to saturate at a value slightly lower than the Tb - Y alloys. The situation in the R - Sc alloys, where R is a heavy rare earth, is quite different; (Nigh et al 1964, Child et al 1968). The addition of Sc favours the helical antiferromagnetic phase, but the transition temperatures are generally lower for a given value of $\bar{G}$ than the corresponding Y or Lu alloys. The alloys cease to exhibit any magnetic ordering for concentrations of the rare earth element below about 25%. The atomic volume of Sc is about 10% smaller than that of Y and Wollan (1967) has suggested that alloying with Sc would bring the rare earth ions closer together, in the same way as applying external pressure, and depress the transition temperatures. A qualitative agreement has been obtained for Gd - Sc alloys.

1.5 (ii) INTRA HEAVY RARE EARTH ALLOYS

A large number of binary heavy rare earth alloys have now been investigated, mostly at O.R.N.L. (see for example Koehler 1972). The properties of all the binary alloys just below the ordering temperature were found to be characteristic of the alloy, not of either constituent. However, the ordering at low temperature was found to be

composition dependent. For the alloys the reduced de Gennes function, $\bar{G}$, is defined as

$$\bar{G} = \sum_i c_i G_i \qquad \ldots(1.7)$$

where G_i is the de Gennes factor of the ith magnetic component and c_i is its concentration. When the initial interlayer turn angle, ω_i, and the Néel temperatures, T_N of the alloys were plotted against $\bar{G}$, they exhibited the same universality as the dilution alloys. Since both constituent moments order simultaneously this indicates that the exchange interaction must still be oscillatory and long range and some average of the exchange interactions of each constituent alone. Shabita and Nagamiya (1975) have used this concept and a similar one of average anisotropy to explain the observed changes in the low temperature ordering at certain concentrations in various alloy systems.

1.5 (iii) LIGHT-HEAVY RARE EARTH ALLOYS

The magnetic properties of the light-heavy alloys are dependent upon their crystal structure. Most work has been done on the hcp (heavy rare earth rich) and dhcp (light rare earth rich) phases with little work done specifically on the intermediate Sm phase.

The heavy rare earth metal Gd has been alloyed with La (Thoburn 1958), Pr (Tissot and Blaise 1970) and Nd and Sm (Fujimori et al 1974). The results were all

obtained using conventional magnetometers as direct magnetic structure determinations by neutron diffraction could not be made. In the hcp phase all four sets of workers report a lowering of the initial ordering temperatures and magnetic moments with increasing light rare earth concentration, with La having the greatest effect, then Sm, Nd and Pr. The results indicate that the Sm, Nd and Pr atomic magnetic moments are aligned ferrimagnetically with the Gd atomic magnetic moment. In a more detailed study of La - heavy rare earth alloys, Koehler (1965) showed that in the hcp phase the addition of La stabilises the ferromagnetic structure at the expense of the high temperature anti-ferromagnetic structure. Koehler's study of Ho - La has been extended by Kawano and Achiwa (1975). They observe the same reduction in ordering temperature and moment value for each alloy, but only one alloy, Ho_{90} La_{10}, exhibits a ferromagnetic cone structure like pure Ho. Although the other alloys are antiferromagnetic, the addition of La causes a marked reduction in initial turn angle over the pure Ho value.

The Gd - La and Gd - Pr magnetisation results extended over the entire composition range and showed that in the Sm phase both alloys became antiferromagnetic and that in the dhcp phase there was no magnetic ordering.

Magnetisation data on Tb with Ce and Pr have been reported by Speight et al (1968) and neutron diffraction data on Tb with Pr and Nd in the Sm phase by Achiwa and

Kawano (1973). Speight notes the rapid change in susceptibility in the hcp phase and the low susceptibility in the dhcp phase. Achiwa reports that in the Sm phase the alloys display a magnetic structure which resembles that of Sm metal, (see Section 1.3). The moments on the hexagonal layers are ordered with the sequence ... ++0--0++ ... along the c-axis where '+' denotes the moment direction on a hexagonal plane and '-' denotes that the moment direction is opposite.. The zeros denote that there is no ordered moment on the cubic sites. The net moment on any hexagonal layer is in the basal plane, i.e. perpendicular to the c-axis, unlike Sm itself where the net moment per layer is parallel or antiparallel to the c-axis. In this magnetic structure the exchange at the cubic site planes due to the ordered hexagonal layers is cancelled out because of the crystallographic and magnetic symmetries which is identical to the situation in Sm. The cubic site layers in the Pr-Tb and Nd-Tb alloys do not exhibit any ordering down to 4.2K, though.

The object of this investigation is to study the magnetic properties of alloys between the light rare earth metals Pr and Nd and the heavy rare earth metals Tb, Dy and Ho across the entire composition range. Apart from susceptibility and magnetisation measurements the choice of these particular elements allows neutron diffraction experiments to be performed to determine the spin structures in the alloys. Magnetisation measurements on the system

Dy-Nd have already been reported by Chatterjee and Taylor (1972).

CHAPTER 2

THEORETICAL BASIS

2.1 MOLECULAR FIELD THEORY

The well known Weiss molecular field model of ferromagnetism (see e.g. Kittel 1971) has been used to explain the behaviour of the spontaneous magnetisation below the Curie point, at the Curie point and in the paramagnetic region. The model has been extended to include other types of magnetic ordering. The approach adopted by the model is phenomenological in that it does not provide an explanation of the ordering mechanism, but merely a model to describe the ordering. The central assumption of the Weiss theory is that the magnetic field at an ion site is composed of an applied field, plus an exchange field due to the other ions i.e.,

$$\underline{H} = \underline{H}_{app} + \underline{H}_{ex} \qquad \ldots(2.1)$$

$$\text{and} \quad \underline{H}_{ex} = \lambda \underline{M}$$

where M is the magnetisation per unit volume and λ is the exchange constant. For an ion with its orbital angular momentum $\underline{L}$, and its spin angular momentum $\underline{S}$, strongly coupled to give $\underline{J}$, the magnetisation per unit volume is

$$M = Ng\mu_B \, J \, B_J(x) \qquad \ldots(2.2)$$

where N is the number of atoms each with total angular momentum $\underline{J}$ and Landé splitting factor g, per unit volume.

$B_J(x)$ is the Brillouin function and is written

$$B_J(x) = \frac{2J+1}{2J} \coth \left[\frac{2J+1}{2J}\right]x - \frac{1}{2J}\coth \frac{x}{2J}$$

where $x = \frac{gJ\mu_B H}{kT}$

Below the Curie point and in the absence of an applied field

$$H = \lambda M$$

$$\text{i.e. } M(T) = Ng\mu_B \, J \, B_J\left[\frac{g\mu_B J\lambda M}{T}\right] \qquad \ldots(2.3)$$

As $T \to 0$ $B_J(x) \to 1$ and

$$M(0) = Ng\mu_B J$$

$M(0)$ is referred to as the spontaneous magnetisation at absolute zero and in atomic theory is the maximum magnetisation possible. The critical temperature below which there is a spontaneous magnetisation is the Curie temperature and this can be evaluated from

$$T_c = \frac{Ng^2\mu_B^2 \, J(J+1)\lambda}{3k} \qquad \ldots(2.4)$$

The susceptibility χ $(=\frac{M}{H})$ above the Curie point is given by the expression

$$\chi = \frac{C}{T-\theta} \qquad \ldots(2.5)$$

where C is the Curie-Weiss constant, $\frac{Ng^2\mu_B J(J+1)}{3k}$

and θ is the paramagnetic Curie point, $= C\lambda$.

2.1(i) FERRIMAGNETISM

A ferrimagnetic material may be defined as one which below a certain temperature possesses a spontaneous magnetisation arising from a non-parallel arrangement of strongly coupled atomic moments. This may be caused by unequal moments oppositely aligned or equal (or unequal) moments in some canted structure. Antiferromagnetism is a special case of ferrimagnetism in which there are two anti-parallel sublattices A and B with equal moments on equal numbers of sites. In this arrangement there is no net spontaneous magnetisation below the transition temperature. The molecular field treatment of an antiferromagnet, due originally to Néel (1932), is shown below.

The molecular field H_{ma}, acting on an ion at an A site may be written

$$H_{ma} = -\lambda_{aa}M_a - \lambda_{ab}M_b \qquad \ldots(2.6)$$

where M_a and M_b are the magnetisations on the A and B sublattices respectively and λ_{aa} is the molecular field constant for the A-A interaction and λ_{ab} is the molecular field constant for the A-B interaction. Similarly, the molecular field H_{mb}, acting on an ion in the B sublattices may be written

$$H_{mb} = -\lambda_{bb}M_b - \lambda_{ab}M_a \qquad \ldots(2.7)$$

Since the same type of ions occupy the A and B sublattice sites, at equilibrium

$$\lambda_{aa} = \lambda_{bb} = \lambda_1$$
$$\lambda_{ab} = \lambda_{ba} = \lambda_2 \qquad \ldots(2.8)$$

λ_2 may be identified with the interaction between nearest neighbours and λ_1 with the interaction between next nearest neighbours. For an antiferromagnet $\lambda_2 > 0$ whilst λ_1 may be positive, negative or zero depending upon the material. Then if a field H is also applied, the fields H_a and H_b at an ion site on the A and B sublattices respectively are given by

$$H_a = H - \lambda_1 M_a - \lambda_2 M_b$$
$$H_b = H - \lambda_2 M_a - \lambda_1 M_b \qquad \ldots(2.9)$$

In the paramagnetic region i.e. for high temperatures, the magnetisation on a sublattice may be written (from eqn 2.2)

$$M = \frac{C}{2T} H$$

$$\text{i.e. } M_a = \frac{C}{2T} (H - \lambda_1 M_a - \lambda_2 M_b)$$
$$\text{and } M_b = \frac{C}{2T} (H - \lambda_2 M_a - \lambda_1 M_b) \qquad \ldots(2.10)$$

The total magnetisation $M = M_a + M_b$ and hence the susceptibility is

$$\chi = \frac{M}{H} = \frac{C}{T+\theta} \qquad \ldots(2.11)$$

where $\theta = \frac{C}{2}(\lambda_1 + \lambda_2)$

The Néel temperature, T_N, is defined as the critical temperature below which the two sublattices are ordered antiferromagnetically and may be evaluated from eqn. 2.10 by putting H = 0 and setting the determinant of the coefficients of M_a and M_b to zero. Application of this condition yields

$$T_N = \frac{C}{2}(\lambda_2 - \lambda_1)$$

The preceeding results for an antiferromagnet may easily be extended to describe a ferrimagnetic configuration. For two sublattices the molecular fields for a ferrimagnet are formally the same as those for an antiferromagnet, as in eqns. 2.6 and 2.7. The equilibrium conditions (eqn. 2.8) are not the same for a ferrimagnet since $\lambda_{aa} \neq \lambda_{bb}$ and $M_a \neq M_b$, although $\lambda_{ab} = \lambda_{ba}$ as in the case of an antiferromagnet. Thus, the magnetisation on each sublattice may be written,

$$M_a = \frac{C_a}{T}(H - \lambda_{aa}M_a - \lambda_{ab}M_b)$$
$$M_b = \frac{C_b}{T}(H - \lambda_{bb}M_b - \lambda_{ab}M_a) \qquad \ldots(2.12)$$

where C_a and C_b are the Curie-Weiss constants for the ions on the A and B sublattices respectively. Following Lax and Button (1962) the sublattice magnetisations may be written

$$M_a = \frac{C_a(T+C_b\lambda_{bb}) - C_aC_b\lambda_{ab}}{(T+C_a\lambda_{aa})(T+C_b\lambda_{bb}) - C_aC_b\lambda_{ab}^2} H$$

$$M_b = \frac{C_a(T+C_a\lambda_{aa}) - C_aC_b\lambda_{ab}}{(T+C_a\lambda_{aa})(T+C_b\lambda_{bb}) - C_aC_b\lambda_{ab}^2} H \qquad \ldots(2.13)$$

and the inverse susceptibility $1/\chi$ $(\equiv \frac{M_a+M_b}{H})$ as

$$\frac{1}{\chi} = \frac{T}{C} + \frac{1}{\chi_o} - \frac{K}{T-\theta'} \qquad \ldots(2.14)$$

where $C = C_a + C_b$

and $$\frac{1}{\chi_o} = -\frac{1}{C^2}(C_a^2\lambda_{aa} + C_b^2\lambda_{bb} + 2C_aC_b\lambda_{ab})$$

$$K = \frac{C_aC_b}{C^3}\left[C_a^2(\lambda_{aa}-\lambda_{ab})^2 + C_b^2(\lambda_{bb}-\lambda_{ab})^2 - 2C_aC_b\left[\lambda_{ab}^2 - (\lambda_{aa}+\lambda_{bb})\lambda_{ab} + \lambda_{aa}\lambda_{bb}\right]\right]$$

$$\theta' = -\frac{C_aC_b}{C}(\lambda_{aa} + \lambda_{bb} - 2\lambda_{ab})$$

The ferrimagnetic Néel temperature can be found from eqn. 2.12 by setting the determinant of the coefficients of M_a and M_b to zero. This yields,

$$T_{FN} = -\frac{1}{2}(C_a\lambda_{aa}+C_b\lambda_{bb}) + \frac{1}{2}\left[(C_a\lambda_{aa}-C_b\lambda_{bb})^2 + 4C_aC_b\lambda_{ab}^2\right]^{\frac{1}{2}}$$

To extend the above results to the case of a ferrimagnetic alloy (e.g. the light-heavy rare earth alloys) it is necessary to include a factor which accounts for the

differing populations on the two sublattices. This may be done by re-writing eqn. 2.12 as

$$M_a = \frac{C_a}{T}(H - x\lambda_{aa}M_a - (1-x)\lambda_{ab}M_b)$$

$$M_b = \frac{C_a}{T}(H - (1-x)\lambda_{bb}M_b - x\lambda_{ab}M_a) \qquad \ldots(2.15)$$

where x is the fractional concentration of A ions.

Following an identical procedure to that outlined above the susceptibility and ordering temperature for a ferrimagnetic alloy are derived in Appendix 4. The result is

$$\frac{1}{\chi} = \frac{T}{C} + \frac{1}{\chi_o'} - \frac{K'}{T-\theta'} \qquad \ldots(2.16)$$

The inverse susceptibility of a ferrimagnetic alloy has the same form as eqn. 2.14, and θ' may be identified as the paramagnetic ordering temperature where

$$\theta' = -\frac{C_aC_b}{C}(x\lambda_{aa} + (1-x)\lambda_{bb} - 2\lambda_{ab}) \qquad \ldots(2.17)$$

The other symbols are defined in Appendix 4 in terms of the molecular field constants etc. The ferrimagnetic Néel temperature is given by

$$T_{FN} = -\frac{1}{2}\left[C_a x\lambda_{aa} + C_b(1-x)\lambda_{bb}\right] + \frac{1}{2}\left[\left[C_a x\lambda_{aa} - C_b(1-x)\lambda_{bb}\right]^2 + 4C_aC_bx(1-x)\lambda_{ab}^2\right]^{\frac{1}{2}} \qquad \ldots(2.18)$$

Eqns. 2.17 and 2.18 form the basis of the discussion

of the magnetic ordering in the dhcp phase light-heavy rare earth alloys to be presented in Section 6.3.

2.1(ii) HEISENBERG EXCHANGE INTERACTION IN THE MOLECULAR FIELD MODEL.

In Section 1.4 the long range ordering in the rare earths was attributed to an exchange interaction between the spins on adjacent ions of the form

$$\mathcal{H}_{ex} = - 2I(r_{ij})\ \underline{S}_i.\underline{S}_j \qquad \ldots(2.19)$$

where $\underline{S}_i$ and $\underline{S}_j$ are the total spin angular momenta on each ion site and $I(r_{ij})$ is the exchange integral. This expression treats the ordering on a microscopic level whereas eqn. 2.1 treats it on a macroscopic level. Nevertheless, $I(r_{ij})$ is a phenomenological parameter since it gives no indication of the origin of the exchange interaction. A relationship between $I(r_{ij})$ and λ may now be obtained (see e.g. Morrish 1965). If the exchange integral in eqn. 2.19 is constant and only the nearest neighbour interactions of the atom on the ith site are considered then eqn. 2.19 may be written,

$$\mathcal{H}_{ex} = -2I\Sigma_j\ \underline{S}_i.\underline{S}_j \qquad \ldots(2.20)$$

Further, resolving the vector dot product into its cartesian components and taking the z-axis as the axis of quantisation

$$\mathcal{H}_{ex} = - 2I\Sigma_j\ S_{zi}S_{zj}$$

Since the magnetisation, assumed along the z-direction of the specimen, is given by

$$M = Ng\mu_B S_{zj}$$

and there are z nearest neighbours, the exchange Hamiltonian may be written

$$\mathcal{H}_{ex} = - 2z \frac{S_{zi} IM}{Mg\mu_B}$$

The Hamiltonian in terms of the Weiss field λM is given by

$$\mathcal{H}_{ex} = gS_{zi}\mu_B \lambda M$$

Equating the last two eqns. gives

$$\lambda = \frac{2zI}{Ng^2\mu_B^2} \qquad \ldots(2.21)$$

where the symbols have their usual meaning and N is the number of atoms per unit volume.

This result, and all the other results in this chapter, have been derived assuming that the exchange field and the applied field are the only components of the total Hamiltonian acting at an ion site. So far any interaction with the crystalline environment has been neglected. Clearly a complete description of the magnetic properties of the rare earth metals can only be obtained from a solution of the full Hamiltonian, $\mathcal{H}$, where

$$\mathcal{H} = \mathcal{H}_{ex} + \mathcal{H}_{cf} + \mathcal{H}_{app} \qquad \ldots(2.22)$$

$\mathcal{H}$ is the exchange field Hamiltonian, $\mathcal{H}_{cf}$ is the crystal field Hamiltonian (see Section 2.7) and $\mathcal{H}_{app}$ is any external applied magnetic field. Bowden et al (1971) have examined the modifications necessary to the Weiss molecular field model to include crystal field effects. A ..... solution to eqn. 2.22 was obtained in Section 1.4 by assuming that $\mathcal{H}_{cf}$ could be neglected near the Néel point, yielding

$$T_N \alpha G^{2/3}$$

assuming that I is constant. In the following sections the theory of ordering in the rare earth metals will be described.

2.2 HIGH TEMPERATURE ORDERING IN THE RARE EARTHS - HELIMAGNETISM.

In all of the various moment arrangements in the heavy rare earths the moments of the ions lying on a given hexagonal plane are parallel, but the moment direction varies from plane to plane up the c-axis. The spin structures of the heavy rare earths can be described in terms of a wave vector $\underline{q}$ parallel to the hexagonal or c-axis, giving the periodicity, and a polar angle θ giving the spin orientation with respect to the c-axis. The spin structure may then be written as

$$J_{i\mu} = J_o\cos\theta \ , \ J_{i\nu}=J_o\sin\theta\cos(q_i.R_i) \ , \ J_{i\eta}= J_o\sin\theta\sin(q_i.R_i) \qquad \ldots(2.23)$$

where μ is along the c-axis, ν is directed towards a

nearest neighbour in the basal plane and η is at right angles to ν in the basal plane. R_i is the interplanar spacing and J_o is the thermal average of the total angular momentum at some temperature, T. The general moment direction described by eqn (2.23) is a cone as in Ho and Er at low temperature. (see Section 1.3). For $\theta = \frac{\pi}{2}$ and $\underline{q} \neq 0$ the moment arrangement is a basal plane spiral as in Tb, Dy and Ho, just below their Néel temperatures. For $\underline{q} = 0$ the structure is ferromagnetic with θ giving the spin direction with respect to the c-axis. If $\theta = \frac{\pi}{2}$ and $\underline{q} = 0$ the structure described is that of Tb or Dy below their Curie temperatures. The spin structures of all the heavy rare earth metals are shown schematically in Fig 1.

The value of $\underline{q}$ maximising the exchange and thus minimising the free energy of the structure is the spiral wave vector of the structure. To consider the dependence of $I(r_{ij})$ on $\underline{q}$ it is necessary to define the fourier transform of the exchange,

$$I(q) = \sum_j I(r_{ij}) \exp(iq.r_{ij})$$

The simplest model showing the experimental behaviour of the heavy rare earths is the five plane interaction model first used by Enz (1961). Along the c-axis with $\underline{q}$ parallel to c

$$I(q) = J^2 \left[I(0) + 2I(1)\cos qc + 2I(2)\cos 2qc \right] \quad \ldots(2.24)$$

where $I(0)$ is the in-plane interaction. $I(1)$ is the

interaction between nearest neighbour planes and I(2) is the interaction between next nearest neighbour planes. J_o is again the thermally averaged value of the total angular momentum. For the system described in eqn. 2.24 to be stable the condition

$$\frac{d}{d(qc)} \quad I(q) = 0 \qquad \ldots(2.25)$$

must be satisfied. This leads to the result, with $\underline{q}_o$ being the equilibrium value of $\underline{q}$,

$$\cos(\underline{q}_o c) = - \frac{I(1)}{4I(2)} \qquad \ldots(2.26)$$

Here $q_o c$ is the equilibrium interlayer turn angle of the helical structure, usually written as ω. If only three planes (i.e. nearest neighbours only) had been considered, then the values of ω which gave energy minima would have been 0 and π corresponding to ferromagnetic and antiferromagnetic alignment respectively. From eqn. (2.26) it follows that the helical structure is stable only if I(1) and I(2) are of opposite sign and also if $I(1) < 4I(2)$. Hence $I(r_{ij})$ must be of long range, and oscillatory with distance.

2.3 EFFECT OF A MAGNETIC FIELD ON A HELICAL SPIN SYSTEM.

For the helical spin system described by eqn. (2.24) (which is one in which the hexagonal layers are ferromagnetically aligned with the net moment in the layer) the application of a field in the basal plane will

introduce a further term in the exchange at each ion site such that we get

$$I(q) = J^2\left[I(0) + 2I(1)\cos(qc) + 2I(2)\cos 2(qc)\right] + J.H \sum_n \cos n(qc)$$

For sufficiently large external fields the helical spin structure becomes energetically unfavourable with respect to the ferromagnetic phase. In practice the transition from an antiferromagnetic structure to a ferromagnetic structure is characterised by two distinct changes in magnetisation with increasing field. The first is due to the collapse of the helical structure to a fan structure with the magnetisation vectors pointing in the direction of the applied field. (see Fig. 2.1). Herpin and Meriel (1961) have shown that the value of the external field, H_c, at this transition is given by

$$H_c = -7.76\mu_s\, I(2)\sin^4\frac{\omega}{2} \qquad \ldots(2.30)$$

where μ_s is the spontaneous moment per atom, ω is the turn angle of the undistorted helix at that temperature and I(2) is the antiferromagnetic next nearest neighbour interaction. Further increase in magnetic field strength serves only to decrease the deviation of the fan structure from full ferromagnetic alignment. This process is complete and full ferromagnetic alignment established at

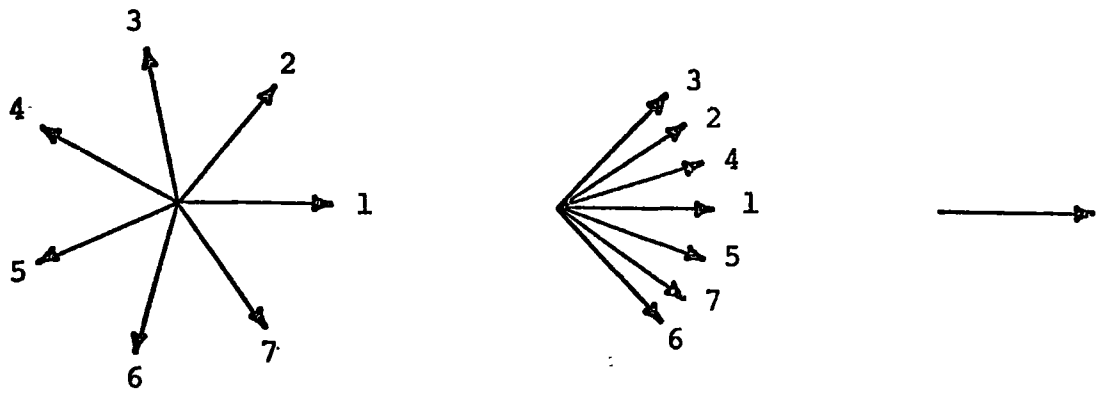

FIG. 2.1 Effect of a magnetic field applied in the basal plane of a uniform basal plane spiral magnetic structure.

a field $H_f = 2.06H_c$. The magnetisation process of a spiral spin system has been dealt with in detail by Kitano and Nagamiya (1964). Eqn. 2.30 in conjunction with eqn. 2.26 provides a means for estimating the exchange parameters I(1) and I(2) for a given temperature. Belov et al (1964) have discussed this in detail for Dy and Ho.

2.4 THE EXCHANGE INTERACTION.

Since the 4f wave functions on the rare earth ions have been shown to be localised (Section 1.3) there can be no appreciable overlap and the exchange interaction between ions must proceed indirectly. Such an indirect exchange interaction which propagates via the polarisation of the conduction electron charge cloud around an ion site was first developed by Rudermann and Kittel (1954) to explain line broadening in n.m.r. experiments. The theory was subsequently extended by Yosida (1957) and applied to rare earths by Kasuya (1956).

In this interaction (known as the RKKY interaction) a localised 4f electron with spin S_i interacts with an electron from the conduction band via the Coulomb interaction and scatters it from a momentum state k' below the Fermi energy into a state k". Assuming that both electron wave functions are Bloch wave functions i.e. the electrons are a free gas, the Hamiltonian for the interaction between a conduction electron of spin s and an ion of spin S may be written

$$\mathcal{H}_{sf} = A(k'' - k')\ \underline{s}.\underline{S}$$

The exchange integral is usually assumed to be isotropic and a function of $(k''-k') = q$ only. In the RKKY theory $A(q)$ is taken to be a constant A_0. The exchange integral may be written in direct r-space

$$A(\underline{r}) = \sum_{q} A(\underline{q})\exp(i\underline{q}.\underline{r})$$

Then the exchange interaction between a conduction electron at r and an ion at position R may be written

$$\mathcal{H}_{sf} = - A(r-R)\underline{s}.\underline{S}$$

In the RKKY approximation $A(r-R) = A_0\delta(r-R)$. Using perturbation theory the effect of an ionic spin on the conduction electron cloud may be calculated. Because $\mathcal{H}_{sf}$ is spin dependent, the energy of one spin state of the electron cloud will be lower than the other and hence the conduction electron cloud will become polarised. In direct r-space and at T = 0 the polarisation may be written

$$P(\underline{r}) = \frac{9\pi S_z Z^2}{2\Omega^2 E_f} \int \phi\left[2k_f(\underline{r}-\underline{r}')\right] A(\underline{r}')\,d\underline{r}'$$

where Z is the number of conduction electrons per atom, Ω is the atomic volume and

$$\phi(x) = \frac{\sin x - x\cos x}{x^4}$$

In the RKKY approximation

$$P(\underline{r}) = \frac{9\pi S_z Z^2 A_0}{2\Omega^2 E_f}\ \phi(2k_f r) \qquad \ldots(2.31)$$

Thus in the RKKY approximation the polarisation has a long range oscillatory behaviour falling off as $\frac{\cos(2k_f r)}{r^3}$ for large r. In the limit $r \to 0$ ϕ diverges, however this divergence does not affect the oscillations at large r which are important in determining the magnetic properties. In q space the polarisation may be written

$$P(\underline{r}) = \sum_{\underline{q}} A(\underline{q})\ \chi(\underline{q}) \exp(i\underline{q}.\underline{r})$$

where $\chi(\underline{q})$ is referred to as the generalised susceptibility function and is just the Fourier transform of $\phi\ (2k_f r)$

$$\sum_{\underline{q}} \chi(\underline{q}) \exp(i\underline{q}.\underline{r}) = \frac{9\pi Z^2}{2\Omega^2 E_f}\ \phi(2k_f r) \qquad \ldots(2.32)$$

Physically the function $\chi(q)$ completely describes the response of a free electron gas to a small perturbation. $\chi(q)$ is the quantity generally determined in band structure calculations (see Appendix 3) and is of central importance in the theory of magnetic ordering in the rare earths (see Section 2.5). The polarisation produced by an ionic spin at r interacts with another 4f electron of spin S_j localised on an ion a distance r_{ij} away from S_i.
In Section 1.4 the exchange interaction $\mathcal{H}_{ij}$ between two ionic spins a distance apart was written

$$\mathcal{H}_{ij} = -2I(r_{ij})\underline{S}_i.\underline{S}_j$$

In the RKKY approximation the exchange integral $I(r_{ij})$ in the Heisenberg exchange interaction may be identified

as (from eqn. 2.31)

$$I(r_{ij}) \equiv \frac{9\pi Z^2}{2\Omega^2 E_f} A_o^2 \phi (2k_f r_{ij})$$

$$\text{i.e. } I(r_{ij}) = \sum_q A^2(\underline{q}) \chi(\underline{q}) \exp(i\underline{q}.r_{ij}) \qquad \ldots(2.33)$$

by eqn. (2.32) and using the fact that in the RKKY approximation $A(\underline{q}) = A_o$. The exchange integral behaves like the polarisation, being simply $A_o P(r_{ij})$. Besides giving rise to exchange coupling between ionic moments, the polarisation of the conduction electrons produces a magnetic moment. (Liu 1961). Thus, the observed saturation moments of the heavy rare earth metals from magnetisation measurements are all in excess of the theoretical value and the value determined from neutron diffraction measurements (see Table 1.1 and Section 1.3). This contribution to the moment from the conduction electron polarisation is not measured during neutron diffraction experiments due to the diffuse nature of the conduction electrons (Cable et al 1968. See also Section 3.3).

2.5 THEORY OF THE TURN ANGLE

Employing the RKKY approximation the exchange integral defined in eqn. 2.33 may be written in q-space as

$$I(\underline{q}) = A_o^2 \chi(\underline{q}) \qquad \ldots(2.34)$$

Since the function $\chi(\underline{q})$ in eqn. 2.34 has a maximum value at $\underline{q} = 0$ so does $I(\underline{q})$ and therefore this model cannot predict the appearance of an oscillatory spin structure.

Relaxing the RKKY approximation to allow A to depend upon $\underline{q}$ produces the same result, as $A(\underline{q})$ may in general be assumed to have a maximum at $\underline{q}=0$. In order to produce a maximum in $I(q)$ for $\underline{q}\neq 0$ it is necessary to consider a more realistic electronic band structure.

Yosida and Watanabe (1962) included the symmetry of the hcp lattice whilst retaining the free electron gas approximation. This yielded a maximum in the exchange integral for q parallel to the c-axis when $qc = 48^{o}$. This value is close to the observed initial turn angles of Tm, Er and Ho where $\omega_i = qc = 51^{o}$ but is not in agreement with the initial turn angles of Tb or Dy, nor did the computation predict the absence of any periodic order in Gd.

Since 1964 more realistic band structure calculations have become available. The essential features of the band structure of all the heavy rare earths (see Appendix 3) are the central trunk composed mainly of the s and f electrons and the flat d bands perpendicular to the c-axis (see Fig. A3.1). The appearance of a webbing feature in the Fermi surface may be associated with a spiral spin structure in the material (Gd has no webbing feature and shows no helical spin region). The vector which calipers the webbing of the whole Fermi surface near L, determines the position of the peak in the generalised susceptibility function $\chi(q)$, and is therefore identified with the turn angle. Keeton and Loucks (1968) first observed that the

thickness of the webbing has the same order of magnitude as the wave vector associated with the spin structure. Further, it shows the correct trend through the heavy rare earth series.

The properties of the paramagnetic Fermi surface clearly play a fundamental role in determining the turn angle at the onset of magnetic ordering. However, the variation of the turn angle with temperature cannot be explained in terms of the paramagnetic Fermi surface and it is necessary to consider the effect of magnetic order upon the bands.

2.5(i) TEMPERATURE DEPENDENCE OF THE TURN ANGLE.

At the onset of magnetic ordering the ionic moments on each lattice site couple with the conduction electrons through the exchange interaction $\mathcal{H}_{sf}$. The periodicity of the helical magnetic ordering is different from that of the lattice and this has the effect of introducing a new periodic potential into the structure. This new periodicity gives rise to an energy discontinuity, referred to as a superzone boundary, and an energy gap in the conduction electron band (Elliot and Wedgewood 1964). The re-distribution of the conduction electrons across these energy gaps affects the coupling between a localised 4f electron and a conduction electron with a consequent variation in the turn angle. The energy gap is temperature dependent through its dependence on the ionic moment and in this way the turn angle varies with temperature. The superzone

boundaries may be visualised as energy gaps cutting the Fermi surface perpendicular to the c-axis.

The concept of the superzone boundaries will be used in the discussion of the anomalously small variation of the turn angle with temperature in the hcp light-heavy rare earth alloys (see Section 6.1).

Whilst the appearance of a helical spin structure and its variation with temperature is determined by the electron properties of the material, the exact form of the ordering is determined by the interaction with the crystal lattice. This latter interaction favours ferromagnetic alignment of the spins and is strongly temperature dependent.

2.6 LOW TEMPERATURE ORDERING - FERROMAGNETISM

In the phenomological approach adopted earlier (see Section 2.1) the Hamiltonian describing rare earth magnetism was written as

$$\mathcal{H} = \mathcal{H}_{ex} + \mathcal{H}_{app} + \mathcal{H}_{cf} \qquad \ldots(2.35)$$

The exchange interaction, $\mathcal{H}_{ex}$, is long range and oscillatory and thus favours a stable helical spin arrangement rather than ferromagnetism. In the absence of an applied field the spontaneous transition to ferromagnetism must be driven by the crystal field interaction, $\mathcal{H}_{cf}$. The crystal field Hamiltonian contains the magneto-crystalline interactions, the magnetostriction and the magneto-crystalline anisotropy.

$$\mathcal{H}_{cf} = \mathcal{H}_{ms} + \mathcal{H}_{a}$$

The anisotropy, $\mathcal{H}_a$, has been discussed earlier (see Section 1.4) and it acts only to align the moments along some preferred direction in the lattice. The magneto-elastic effect has been suggested by many authors to be the driving force which stabilises the ferromagnetic state (see for example Cooper 1968).

The crystal lattice is coupled elastically to the magnetic system such that when the moments are aligned in a certain direction the lattice becomes distorted somewhat in order to minimise the total energy. In the anti-ferromagnetic state the magnetic moments cancel internally and so the lattice does not respond to the magnetic ordering. In this case the antiferromagnetic state has a higher magneto-elastic energy than the ferromagnetic state. Elliot (1961) has shown that the energy difference between these two states is proportional to the sixth power of the magnetisation. He also showed that the anisotropy energy is proportional to the twenty-first power of the magnetisation. Just below the Néel temperature, then, the magnetic properties are almost completely described by the exchange. As the temperature is lowered the contribution to the free energy from the magnetostriction increases and when added to the exchange energy, which favours periodic alignment, the total energy of the crystal may favour a ferromagnetic state at sufficiently low temperature.

The complex magnetic structures of the rare earths are due to the delicate balance existing between the exchange

and the crystal field effects.

2.7 THE CRYSTAL FIELD

Each rare earth ion is tripositively charged when it enters a metal. Thus,between any two ions in the crystal structure there is an intense electric field which reflects the symmetry of the lattice. If the ions are all assumed to be point charges then the crystal field V_c may be written

$$V_c(r) = \sum_i \frac{eZ_i}{(r-R_i)}$$

where eZ_i is the charge on the ith ion.

The crystal field potential may be expanded in spherical harmonics, hence

$$V_c(r) = \sum_{|m|<\ell} \sum_{\ell} A_\ell^m V_\ell^m$$

The series can be terminated after the sixth order spherical harmonic for the 4f electrons due to the symmetry properties of the wave functions. Further reductions in the number of terms can only be made with reference to the specific point group symmetry. For the hcp lattice the only non-zero terms are:-

$$V_c = A_2^0 V_2^0 + A_4^0 V_4^0 + A_6^0 V_6^0 + A_6^6 V_6^6$$

There are no terms with ℓ odd since the structure has a centre of inversion. The term in m = 6 arises due to the sixfold rotation symmetry of the lattice.

In principle, the crystal field may now be calculated by direct integration from a knowledge of the form of the spherical harmonics and the 4f wave functions. Following Stevens (1952) we can make use of the Wigner-Eckart theorem which relates the spherical harmonics in Cartesian co-ordinates to their operator equivalents and removes the need to perform the complex integrations. In the case of the rare earths the operator equivalents are in terms of J and J_z (see Table 2.1). For the first term in the crystal field Hamiltonian, V_2^0,

$$\Sigma(3z^2 - r^2) \equiv \alpha\langle r^2\rangle\left[3J_z^2 - J(J+1)\right] \equiv \alpha\langle r^2\rangle O_2^0$$

where α is a constant and $\langle r^2\rangle$ is the expectation value of the 4f radius squared. The crystal field Hamiltonian is more usually written

$$V_c(r) = B_2^0 O_2^0 + B_4^0 O_4^0 + B_6^0 O_6^0 + B_6^6 O_6^6 \qquad \ldots(2.36)$$

where $B_\ell^m = A_\ell^m \langle r^\ell\rangle \theta_\ell$ (and are usually taken as adjustable parameters to be fitted to experiment) and $\theta_2 \equiv \alpha$, $\theta_4 \equiv \beta$, $\theta_6 \equiv \gamma$. Elliot (1961) has used as a basis for crystal field calculations

$$A_2^0\alpha = -300; \quad A_4^0\beta = -60; \quad A_6^0\gamma = +15; \quad A_6^6\gamma = -90 \quad \text{in cm}^{-1}$$

Kasuya (1966) has adopted the point charge model and derives the crystal field parameters from the equation

$$B_\ell^m = \frac{Ze^2\langle r^\ell\rangle}{a_0^{(\ell+1)}}\ \theta_\ell\ \overline{V_\ell^m} \qquad \ldots(2.37)$$

TABLE 2.1

OPERATOR EQUIVALENTS RELEVANT TO A HEXAGONAL CRYSTAL FIELD.

Term in Electrostatic Potential	Operator Equivalent	Notation
$V_2^0 = \Sigma\,(3z^2 - r^2)$	$\alpha_J \langle r^2 \rangle \left\| 3J_z^2 - J(J+1) \right\|$	$\alpha_J \langle r^2 \rangle O_2^0$
$V_4^0 = \Sigma\,(35z - 30r^2 z^2 + 3r^4)$	$\beta_J \langle r^4 \rangle \left\| 35J_z^4 - 30J(J+1)\,J_z^2 + 25J_z^2 - 6J(J+1) + 3J^2(J+1)^2 \right\|$	$\beta_J \langle r^4 \rangle O_4^0$
$V_6^0 = \Sigma\,(231z^6 - 315z^4 r^2 + 105z^2 r^4 - 5r^6)$	$\gamma_J \langle r^6 \rangle \left\| 231J_z^6 - 315J(J+1)J_z^4 + 735J_z^4 + 105J^2(J+1)^2 J_z^2 - 525J(J+1)J_z^2 + 294J_z^2 - 5J^3(J+1)^3 + 40J^2(J+1)^2 - 60J(J+1) \right\|$	$\gamma_J \langle r^6 \rangle O_6^0$
$V_6^6 = \Sigma\,(x^6 - 15x^4 y^2 + 15x^2 y^4 - y^6)$	$\gamma_J \langle r^6 \rangle \frac{1}{2} \left\| J_+^6 + J_-^6 \right\|$ where $J_+ = (J_x + iJ_y)$ and $J_- = (J_x - iJy)$	$\gamma_J \langle r^6 \rangle O_6^6$

in which $\overline{V_\ell^m}$ are a measure of the departure of the crystal from ideality. These factors are tabulated in Table 2.2. Z is usually taken as 3 for the rare earth metals and a_o is the basal plane lattice parameter.

To evaluate the level splitting it is necessary to calculate matrix elements like

$$< J,m_J \left| V_c \right| J',m_J' >$$

for a given manifold of J. The terms V_ℓ^o in the crystal field Hamiltonian contain only J_Z, or powers of J_Z so they couple only states where $m_J = m'_J$ and lead to diagonal elements. Terms with $\ell \neq 0$ contain step operators and hence couple states ℓ apart, viz

$$J\pm \left| J,m_J> = \left[J(J+1) \pm m_J(m_J+1)\right]^{\frac{1}{2}} \right| J,m_J+1 >$$

Hutchings (1964) has tabulated the matrix elements of all the crystal field operators, O_ℓ^m, between states $\left|J = \text{const. } m_J\right.$ > for the J values appropriate to the rare earths.

Only matrix elements within a constant manifold of J need be considered as the next J multiplet is usually some 300 cm^{-1} away. Thus, an ion with J = 4(Pr^{3+}) i.e. $J_Z = \pm 4....0$,generates a 9 x 9 matrix. The matrix is diagonalised using numerical analysis techniques. The J = 4 matrix can be re-arranged into submatrices containing only diagonal and one-off diagonal elements pivoted around $J_Z = 0$.

TABLE 2.2

FACTOR $\overline{V_\ell^m}$ FOR HEAVY RARE EARTHS REPRESENTING DEPARTURE FROM CRYSTALLINE IDEALITY.

$$\overline{V_2^0} = -1.035\ (1.633 - c/a)$$

$$\overline{V_4^0} = -\left|\ 0.1127 - 0.752\ (1.633 - c/a)\ \right|$$

$$\overline{V_6^0} = 0.260 + 0.369\ (1.633 - c/a)$$

$$V_6^6 = -\left|\ 2.520 - 0.815\ (1.633 - c/a)\ \right|$$

Conversely, the J = 7/2 matrix may be re-arranged into two identical halves. This illustrates an important theorem in group theory - Kramers theorem. For a half-integral J value all the levels in the absence of an applied field must be at least doubly degenerate, whereas for integral J there must be at least one singlet.

If a field, either external or internal, is applied along the axis of quantisation then a term $- m_J \, g\mu_B.H$ must be added to each diagonal element. In the case of the hcp lattice the crystal field Hamiltonian is written with respect to the c-axis as the quantisation axis. If the field is applied in the basal plane this becomes the axis of quantisation and more terms are required in the crystal field Hamiltonian as the site symmetry is lower. The effect of rotations can be treated in a general way and they have been tabulated by Hutchings (1964) for rotation into and around the basal plane. For example

$$O_2^0 \rightarrow -\tfrac{1}{2} \left[O_2^0 + 3 \, O_2^2 \right]$$

For the rare earths assuming Z = 3 and substituting values in eqn. 2.37 for the B_ℓ^m the main variation in value from element to element is due to the magnitude and sign of θ_ℓ. Now the dominant term in the axial anisotropy V_2^0, is given by

$$V_2^0 = \langle r^2 \rangle \, \alpha \left[3J_z^2 - J(J+1) \right]$$

thus if α is negative the moment will lie in the basal

plane and if α is positive along the c-axis. Negative values of β and γ in V_4^0 and V_6^0 respectively align the moment along the c-direction, whereas positive values tend to make the moment lie at an angle to c but not in the basal plane. The V_6^6 term constrains the moments to lie at some direction to the crystal axes in the basal plane. Using these results the predicted moment directions for the heavy rare earths are summarised in Table 2.3 (after Miwa and Yosida 1961). For $V_2^0 > V_4^0 > V_6^0$ the predicted moment directions give a qualitative agreement with experiment, and the V_6^6 terms predict the observed easy directions.

2.8 ORDERING IN THE LIGHT RARE EARTHS

The crystal field are relatively stronger in the light rare earths because the $\langle r^\ell \rangle$ are much bigger (Elliot 1965). The dhcp structure, too, has two separate site symmetries. Ions on half of the sites have a hexagonal symmetry whilst those on the other half have a face centred cubic nearest neighbour environment. The cubic crystal field may be written (Rainford 1971),

$$V_c = B_2^0 + B_4^0\left[O_4^0 + 20\sqrt{2}\, O_4^3\right] + B_6^0\left[O_6^0 + \frac{35}{\sqrt{8}}\, O_6^4\right] + B_6^6\, O_6^6 \quad \ldots(2.38)$$

and the hexagonal crystal field is given by eqn. 2.36. For a truely ideal cubic symmetry B_2^0 would be identically zero. It is included in eqn. 2.38 to account for the non-ideality of the crystal.

In Pr the crystal fields at the cubic and hexagonal

TABLE 2.3

EFFECT OF THE VARIOUS CRYSTAL FIELD TERMS ON THE MOMENT DIRECTION IN THE HEAVY RARE EARTHS

Term	Tb^{3+}	Dy^{3+}	Ho^{3+}	Er^{3+}	Tm^{3+}
V_2^0	Perp.	Perp.	Perp.	Para.	Para.
V_4^0	Para.	∠	∠	Para.	Para.
V_6^0	Para.	∠	Para.	∠	Para.
V_6^6	b	a	b	c	c

Perp. = Perpendicular to the c-axis

Para. = Parallel to the c-axis

sites lift the (2J + 1) degeneracy giving non-magnetic singlets as ground states (Kramers Rule) so there can be no co-operative effect (Bleaney 1963). Using the crystal field parameters derived by Rainford (1971) from neutron inelastic scattering data a crystal field level diagram was constructed for both the hexagonal and cubic sites. (See Fig. 2.2). The first excited state on the hexagonal sites is a doublet 28K above the ground state and on the cubic sites a triplet 88K above the ground state. In the absence of any exchange an applied field induces a moment at low temperatures due to the admixture of the first excited state with the ground state. For a field applied along the c-axis the $|-1>$ level on the hexagonal sites drops in energy relative to the ground state and crosses it for an applied field of 480k0e. Since a moment bearing level is now the ground state level of the system there is a discontinuous jump in the magnetisation of the system. The predicted behaviour of Pr agrees well with the observed magnetisation data of McEwen (1973) (see Section 1.3) except that the observed discontinuous change in magnetisation occurs at 315k0e. The excess internal field of 165k0e may be ascribed to the exchange between Pr ions. The absence of magnetic ordering in monocrystalline Pr and its presence in polycrystalline Pr led Johansson et al (1970) to suggest that the exchange in Pr is sufficiently close to the threshold for ordering that a small modification of the crystal field splittings,

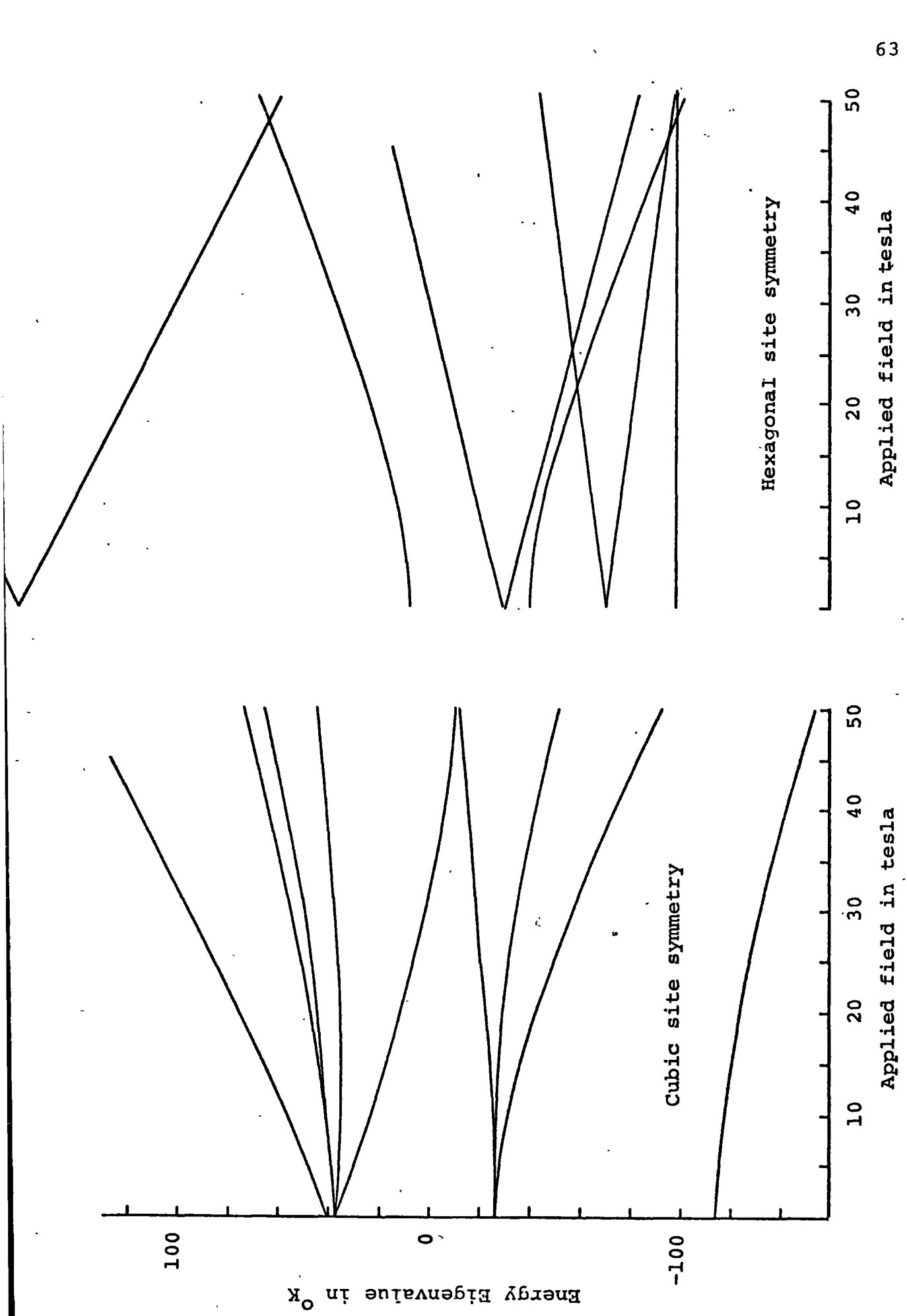

FIG. 2.2 Crystal field level splitting diagram for Pr^{3+} ion.

perhaps due to local strains, could lead to spontaneous ordering. Trammell (1963) has shown that the ratio of the exchange to the crystal field splitting must exceed a certain critical value before spontaneous magnetic ordering can occur.

In the case of Nd, which is a non-Kramers ion and therefore cannot have a singlet state, the exchange is operative and the moments on both the cubic and hexagonal sites order at low temperature (see Section 1.3). The saturation moments in both the basal plane direction and along the c-axis is reduced below the theoretical value of $3.27\mu_B$ even in fields of 350k0e and this is attributed to the crystal field effects.

2.9 SPIN WAVES

The ground state of a magnetically ordered material at T=0 is one in which all the atomic spins are rigidly aligned with respect to one another. If the system is excited, thermally or otherwise, the low lying excited states are those in which the spin deviations travel through the solid as spin waves or, when quantised, magnons. Physically, the spin on each atom is precessing about its mean position with successive spins advanced in phase by a constant angle. Magnons are analogous to lattice vibrations or phonons.

2.9(i) APPLICATION TO THE RARE EARTHS

The total Hamiltonian describing a planar ferromagnet

in the hcp structure (such as Tb and Dy) may be written (following eqns. 2.35 and 2.36)

$$\mathcal{H} = -(g_J-1)^2 \sum_{i=j} I(r_{ij})\, \underline{J}_i.\underline{J}_j - \sum_i \left[B_2^0 O_2^0(i) - \frac{1}{2} B_6^6 O_6^6(i) \right]$$

where the magnetostriction and axial crystal field terms higher than second order have been neglected. Writing out the crystal field terms explicitly (see Table 2.3) gives

$$\mathcal{H} = -(g_J-1)^2 \sum_{i=j} I(r_{ij})\underline{J}_i.\underline{J}_j - \sum_i \left[B_2^0 J_{zi}^2 - \frac{1}{2} B_6^6 \left(\left[J_{xi} + iJ_{yi} \right] + \left[J_{ix} - iJ_{iy} \right] \right) \right]^{\frac{1}{2}}$$

From the Hamiltonian the magnon dispersion relation may be written (Mackintosh and Bjerrum Møller 1971)

$$h\omega(q) = J\left[\left[I(0) - I(q) - 2B_2^0 - 6B_6^5 J^4 \right] \left[I(0) - I(q) + 36B_6^6 J^4 \right] \right]^{\frac{1}{2}} \quad \ldots(2.39)$$

where J is the total angular momentum.

Strictly it is necessary to divide the hcp unit cell into two interpenetrating hexagonal lattices with one atom per unit cell, referred to as the A and B sites. For a given q, then, there are two excitations known as the optical and acoustic magnons respectively. Physically, for q=0 the moment precessions on the A and B sites are in phase for the acoustic mode and in antiphase for the

optical mode. Eqn. 2.39 is the dispersion relation for the acoustic magnon at T=0K. For q=0 i.e. at long wavelengths, the spin wave energy does not go to zero, but exhibits an energy gap of approximately $J^3(72B_2^0B_6^6)^{\frac{1}{2}}$ because of the anisotropy which always tends to oppose deviations of the spins from equilibrium.

The most direct experimental method of obtaining spin wave dispersion curves is to excite the spin system by causing thermal neutrons to be inelastically scattered from it (see Sections 3.9 and 4.4(iii)). In this way spin wave energies may be studied for all values of q except near q=0. A large body of literature now exists on inelastic neutron scattering in the ferromagnetic rare earths fitting expressions like eqn. 2.39 to the dispersion curves and evaluating the crystal field parameters from the observed magnon energy gap. (see for instance Bjerrum Møller 1967, Jensen et al 1975, Lindgard 1975).

Since the crystal field dominates the magnetic properties of the light rare earths the elementary magnetic excitations can be expected to be fundamentally different from the magnons found in the heavy rare earth metals.

In the absence of exchange the excitations of the system correspond to the excitation of a single ion from the ground state to an excited state. Exchange couples the ions together so that the excitations have the form of localised magnetic excitations. The theory of collective

exciton behaviour in materials with a singlet ground state e.g. Pr^{3+}, has been developed by Cooper and Wang (1968 and 1969) (see also Section 3.9).

In the paramagnetic phase at low temperatures the dispersion relation for the excitons has the approximate form

$$h\omega(q) = \Delta \left[1 - \frac{2\alpha^2 I(q)}{\Delta} \right]^{\frac{1}{2}}$$

where Δ is the crystal field splitting between two levels in the absence of exchange and α is the matrix element of an angular momentum operator between them. The condition for spontaneous magnetic ordering then corresponds to the instability of one of these exciton modes. These excitons have recently been studied by Rainford (1971) using inelastic neutron scattering and some of his results are shown in Fig. 2.3. The upper set of excitations in this figure correspond to transitions on the cubic sites whilst the lower excitations correspond to transitions on the hexagonal site between the ground state and an excited doublet. (see Section 2.8 and Fig. 2.2). There are two branches to the lower dispersion curve because of the hcp symmetry of the hexagonal sites. The minimum excitation energy occurs in the optical branch at Γ, which corresponds to a mode in which equal and opposite moments are induced on neighbouring layers in the hcp lattice formed by the hexagonal sites. This mode decreases significantly in energy as the temperature is lowered which is an indication of the incipient antiferromagnetism of Pr, since the instability

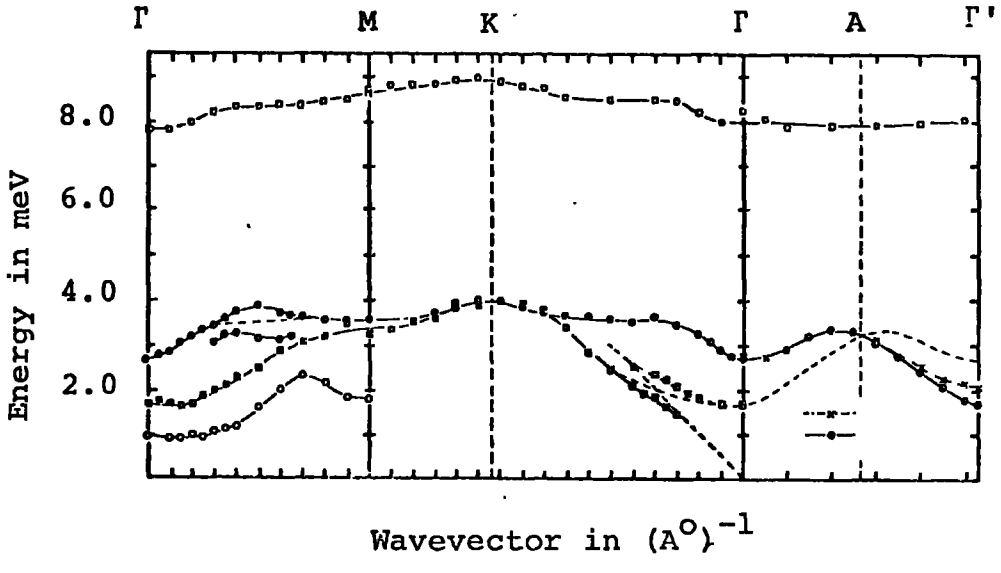

FIG. 2.3 Dispersion relations for magnetic excitons in Pr at 4.2K. (after Rainford 1971).

of this mode would lead to an antiferromagnetic structure.

CHAPTER 3

3.1 ELASTIC NEUTRON SCATTERING

There are two different interactions between a neutron and the atoms of a crystal which give rise to significant scattering; these are the neutron-nuclear interaction and the interaction between the neutron magnetic moment and any magnetic moment which the atoms of the crystal may possess.

The neutron-nuclear scattering gives rise to diffraction peaks at positions related to the periodicity of the atoms in the crystal in the same way as X-ray diffraction, but unlike X-ray diffraction there is no regular increase in scattering cross-section for an increase in atomic number, nor is there any variation in the scattering intensity with angle. Both factors are a consequence of the size of the nucleus. In the first instance, the scattering mechanism is via the Fermi pseudo-potential which is almost constant for increasing atomic number. Secondly, the isotropic nature of the interaction is due to the fact that the dimensions of the nucleus are very much smaller than the wavelength of the thermal neutrons ($1A^{o}$). Hence, the interaction potential for neutron-nuclear scattering is a constant, $\bar{b}$, referred to as the neutron scattering length.

By analogy with X-ray diffraction, then, the intensity of a nuclear line for a sample bathed uniformly in a strictly monochromatic beam is given by:

$$I_{hk\ell} = \frac{A\ m\ G^2_{hk\ell}\ \bar{b}^2\ \exp(-2W)}{L} \qquad \ldots(3.1)$$

A is a geometric factor related to the scattering geometry and the absorption of the sample, (see Section 3.4), m is the number of (hkℓ) planes giving rise to the scattering - the multiplicity, and exp(-2W) is the Debye-Waller temperature factor included to correct for the thermal motions of the nuclei (see Section 3.3). $G_{hk\ell}$ is the geometric structure factor which is a property of the particular crystal structure and L is the Lorentz factor. For a parallel sided lamina sample uniformly bathed in the neutron beam $L = \sin^2 2\theta_{hk\ell}$ and for a cylindrical sample $L = \sin\theta_{hk\ell} \sin 2\theta_{hk\ell}$ where $\theta_{hk\ell}$ is the Bragg angle.

3.2 GEOMETRIC STRUCTURE FACTOR, G, AND THE RECIPROCAL LATTICE.

Consider a plane wave with a wavevector $\bar{k}_o$ $(= \frac{2\pi}{\lambda})$ incident on two nuclei of scattering length $\bar{b}$ in a crystal, separated by a vector distance, r. Let the wave be scattered through an angle θ and leave with a wavevector $\bar{k}'$ (see Fig. 3.1). The phase difference between the two scattered waves at some point B far away from the crystal is

$$\bar{k}_o.r - \bar{k}'.r = (\bar{k}_o - \bar{k}')r = \bar{k}.r \qquad \ldots(3.2)$$

$\bar{k}$ is referred to as the scattering vector and if the scattering is elastic it is of magnitude $\frac{4\pi}{\lambda} \sin\theta/2$.

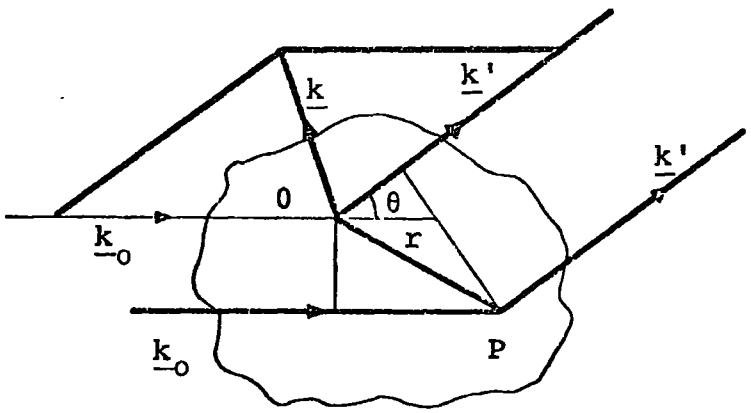

FIG. 3.1 Construction defining scattering vector $\underline{k}$ (after Brown & Forsyth 1973)

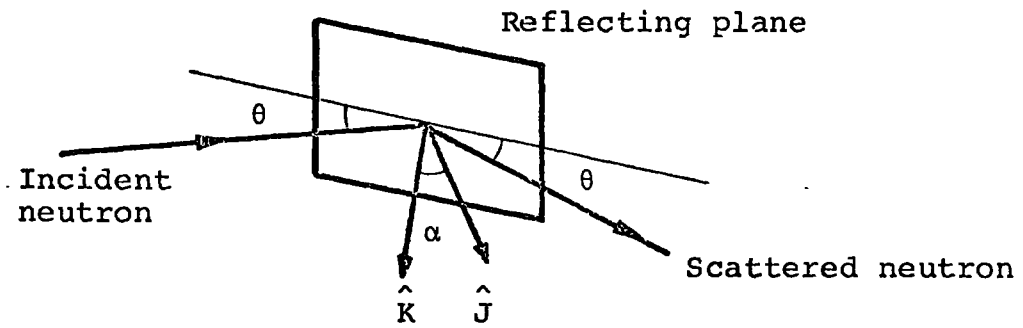

FIG. 3.3 Construction showing unit vectors $\hat{K}$ and $\hat{J}$ used in the discussion of magnetic scattering (after Bacon 1962).

If the incident wave is of amplitude A_0 then the scattered amplitude from a volume element dV at O, arriving at B, a long way from O, is $A_0 \bar{b}\, dV$ where $\bar{b}$ is the nuclear scattering length. Similarly, the amplitude of the scattered wave at B from P, a vector distance r from O, is $A_0 \bar{b} \exp(i\underline{k}.\underline{r})\, dV_r$. The total amplitude at B is obtained by integrating over the volume of the crystal and hence

$$A = A_0 \bar{b} \int \exp(i\underline{k}.\underline{r})\, dV_r \qquad \ldots(3.3)$$

and the total scattering intensity at B is given by

$$I = I_0 \bar{b}^2 \left| \int \exp(i\underline{k}.\underline{r})\, dV_r \right|^2 \qquad \ldots(3.4)$$

If the crystal consists of a discrete lattice of point scatterers then the integral in eqn. (3.4) may be replaced by a summation over all lattice sites and the scattered intensity at B is given by

$$I = I_0 \bar{b}^2 \left| \sum_r \exp(i\underline{k}.\underline{r}) \right|^2 \qquad \ldots(3.5)$$

If the basis vectors of the lattice are $\underline{a}$, $\underline{b}$ and $\underline{c}$ and the Cartesian co-ordinates of the nuclear positions are x, y and z, then

$$r = x.\underline{a} + y.\underline{b} + z.\underline{c} \qquad \ldots(3.6)$$

Substituting eqn. (3.6) into eqn. (3.5) gives

$$I = I_0 \bar{b}^2 \left| \Sigma \exp(i\underline{k}.x.\underline{a}) \exp(i\underline{k}.y.\underline{b}) \exp(i\underline{k}.z.\underline{c}) \right|^2 \qquad \ldots(3.7)$$

Brown and Forsyth (1973) have shown that eqn. (3.7) will have a maximum only if the conditions

$$\underline{k}.\underline{a} = 2\pi h \quad ; \quad \underline{k}.\underline{b} = 2\pi k \quad ; \quad \underline{k}.\underline{c} = 2\pi \ell$$

are fulfilled simultaneously. For all other values it is zero. The factor

$$G_{hk\ell} = \exp(2\pi i \ (\frac{hx}{a_0} + \frac{ky}{b_0} + \frac{\ell z}{c_0})) \qquad ...(3.8)$$

is referred to as the geometric structure factor.

The values of the scattering vector for which scattering occurs are given by

$$\overline{k} = 2\pi \ (ha^* + kb^* + \ell c^*) \qquad ...(3.9)$$

The lattice defined by the basis vectors $\underline{a}^*$, $\underline{b}^*$, $\underline{c}^*$, (often denoted τ_1, τ_2, τ_3) is referred to as the reciprocal lattice. It is constructed of reciprocal lattice points which are the integer values of h, k and ℓ that give non-zero values of the geometric structure factor, arranged in rows and columns. For the hcp structure the reciprocal lattice is shown in Fig. 3.2. Not all integer values of h, k and ℓ give non-zero values of the geometric structure factor, and certain reciprocal lattice points are absent. Physically, this is because the hcp structure contains two atoms per unit cell which destructively interfere. In this case the geometric structure factor contains two terms referring to the position of each atom in the cell. Due to the symmetry of the lattice absences occur

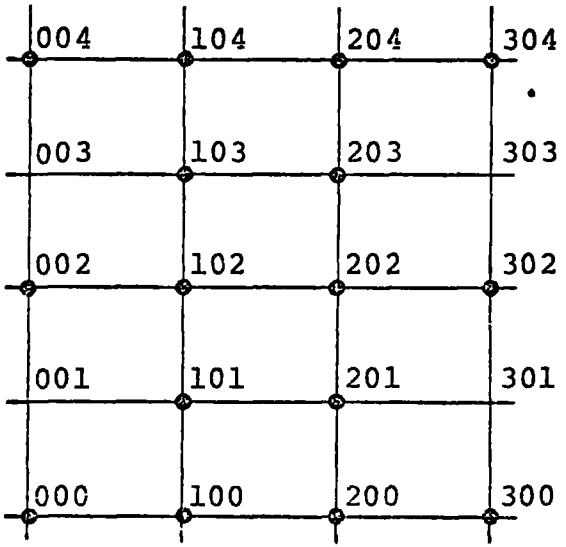

● Denotes allowed nuclear reflection.

Reciprocal lattice for h.c.p. structure

FIG. 3.2

for h - k = 3n and ℓ odd. The intensity of a diffraction line corresponding to a reciprocal lattice point is given by eqn. 3.1.

3.3 DEBYE-WALLER TEMPERATURE FACTOR

The thermal motion of an atom in a solid causes an overall reduction in the observed intensity for a given (hkℓ) reflection over that calculated assuming all the atoms to be at rest. The scattering potential, $\bar{b}$, at all temperatures above zero, then has to be modified to account for the reduction in scattered intensity. The thermal motion of an atom is a result of its intrinsic zero point energy, B_o and its thermal vibration, B_T, which is temperature dependent. In general the temperature parameters are measured together experimentally in the Debye parameter, B, where

$$B = B_o + B_T \qquad \ldots(3.10)$$

although for simple materials like hcp metals B_T may be calculated from the Debye temperature (International Tables for X-ray Crystallography Vol. III). Explicitly the Debye-Waller temperature factor is written

$$\bar{b} \exp\left(- B \frac{\sin^2\theta}{\lambda^2} \right) \qquad \ldots(3.11)$$

where B is the Debye parameter, λ is the wavelength and θ is the scattering angle. The factor $B \frac{\sin^2\theta}{\lambda^2}$ is often written as W. Since it contains a term θ,

the scattering at low angles is largely insensitive to the thermal vibrations.

The tabulated values of the Debye parameter B for La and Gd are almost identical and since the value of the Debye temperature for all the rare earth metals is approximately constant, then throughout this investigation the value of the Debye parameter for each rare earth alloy has been taken as identical to that of Gd.

3.4 PREFERRED ORIENTATION AND ABSORPTION

Besides temperature, the other factors which reduce the intensity of a neutron diffraction line are any preferred orientation of the crystallites in a polycrystalline sample and any absorption of the neutron beam by the sample. The former effect modifies the intensity of one or more peaks in the diffraction spectrum whilst the absorption is a geometric effect depending on the shape of the sample and scattering angle and thus modifies the intensities of all the peaks uniformly.

The consequences of preferred orientation in the samples used in this investigation, in determining the saturation moments of the alloys, are discussed in Section 4.5.

For a cylindrical sample the absorption depends on the dimensionless quantity μR where μ is the linear absorption coefficient and R is the radius of the sample.

(Bacon 1962). For the rare earth alloys used in this investigation with the exception of the Dy alloys, μ is typically 0.7 cm^{-1} and R is 0.4 cm. In this case, where μR is small, the absorption is constant with scattering angle to beyond a scattering angle of 45^{o}.

For the flat plate samples of Pr_{30} Dy_{70} and Nd_{30} Dy_{70} the absorption factor for various scattering angles θ is given by

$$t \exp (-\mu t \sec\theta) \qquad \ldots(3.12)$$

where t is the thickness of the sample in cm. For a uniform sample of thickness 1.0 mm the absorption factor at a scattering angle of 22.5^{o} is 0.01960 which reflects the high capture cross section for Dy. The variation of the absorption factor with scattering angle in the angular range $2\theta = 18^{o}$ to $2\theta = 25^{o}$ is $\pm 1\%$ and the absorption correction may be treated as a constant.

Thus any absorption in the alloys investigated by neutron diffraction manifests itself as an overall reduction in intensity of the observed nuclear peaks. Hence, the ratio of the observed intensity of a diffraction peak to the theoretical intensity in the absence of preferred orientation, should be a constant for each peak, proportional to the absorption and the geometric factor A (see eqn. 3.1). Since the absorption is a constant it can be included in the factor A. A is referred to as the scaling factor.

3.5 NEUTRON-MAGNETIC SCATTERING

Any magnetic moment that the atom possesses resides in the unfilled shells of extra-nuclear electrons. By virtue of the fact that the neutron carries a magnetic moment it interacts with these unpaired electrons. For a spin only paramagnet in which the electronic moments are completely randomly orientated, Halpern and Johnson (1939) have calculated the differential cross-section due to the magnetic interaction to be

$$\frac{d\sigma}{d\Omega} = \frac{2}{3} \; S \; (S + 1) \left[\frac{e^2\gamma}{mc^2}\right]^2 \; f^2 \; (\kappa) \qquad \ldots(3.13)$$

This extra scattering is entirely incoherent and contributes only to the overall background of the crystalline diffraction pattern. The term $\left[\frac{e^2\gamma}{mc^2}\right]$, where γ is the neutron magnetic moment in nuclear magnetons, is the interaction potential for neutron-electron magnetic scattering. The cross-section depends on the scattering angle only through the form factor $f(\kappa)$, where $\kappa = \frac{\sin\theta}{\lambda}$. λ is the neutron wavelength and θ is the scattering angle. A form factor must be included, in contrast to neutron-nuclear scattering, because the electrons which determine the magnetic moment are distributed over a volume of space having linear dimensions comparable with the neutron wavelength. The magnetic form factor falls off more rapidly with the angle than the X-ray form factor since the magnetic

moment of an ion lies in the outer electron shells, whereas X-ray scattering occurs from the inner shells.

3.6 MAGNETIC FORM FACTOR

In the case of the rare earths the magnetic moment resides in the 4f shell and the magnetic form factor is a consequence of the spatial distribution of the 4f electrons. The magnetic form factor can be derived theoretically by integration over the radial part of the 4f wave function, U_{4f} multiplied by the appropriate spherical Bessel function, $j_L(\kappa.r)$ then,

$$< j_L(\kappa) > = \int_0^\infty U_{4f}^2 \; j_L(\kappa.r)\,dr \qquad ...(3.14)$$

In the case of the rare earths it is not necessary to calculate the orbital and spin contributions to the magnetic form factor separately as the spin angular momentum, $\underline{S}$, and the orbital angular momentum, $\underline{L}$, are coupled strongly to give a total angular momentum, $\underline{J}$. The magnetic form factor, then, is just the sum of terms like $< j_0(\kappa) >$, $< j_2(\kappa) >$, $< j_4(\kappa) >$ etc. multiplied by the appropriate coefficients. Physically, the first term in the series $< j_0(\kappa) >$, can be identified with the spin only contribution to the magnetic moment, with succeeding terms a measure of the departure of the 4f charge distribution from sphericity due to coupling with the orbital angular momentum.

Lander and Brun (1970) have shown that for small

values of κ the magnetic form factor for the rare earths may be approximated by the expression

$$f(\kappa) = < j_0(\kappa) > + \frac{c_2}{c_1} < j_2(\kappa) > \qquad ...(3.15)$$

where the $< j_L(\kappa) >$ have been tabulated for the rare earths by Blume et al (1962) and the coefficient $\frac{c_2}{c_1}$ has been tabulated by Lander and Brun (1970.) The coefficient $\frac{c_2}{c_1}$ in eqn. (3.15) is identically zero for Gd^{3+} as it is an S state ion and has no orbital angular momentum. The expression for the form factor is almost identical to the dipole approximation discussed by Lovesey and Rimmer (1969).

In contrast to the tightly bound 4f electrons, the conduction electrons which are responsible for the long range magnetic ordering in the rare earths (see Section 1.4) are distributed over a large volume in the crystal. Consequently, they have a rapidly decreasing form factor and do not contribute to neutron diffraction experiments, although they contribute to an excess moment in the saturation magnetisation (see Section 1.3).

3.7 NEUTRON SCATTERING FROM MAGNETICALLY ORDERED SYSTEMS

Magnetic ordering introduces a new periodicity into the crystal and, as a consequence, extra coherent scattering. If the moments on the ions are all ferromagnetically aligned the magnetic periodicity is the same as the lattice periodicity. Following a

similar argument to that used for neutron-nuclear scattering, the intensity of a magnetic line in a magnetic lattice with the same periodicity as the crystal lattice is:

$$I_{hk\ell} = \frac{A}{L} p^2 m \, G^2_{hk\ell} \exp(-2W) \qquad \ldots(3.16)$$

where the symbols have the same meaning as before except $\bar{p}$ is the magnetic scattering length. Whereas the neutron-nucleus interaction potential is isotropic and can be represented by a scalar quantity, $\bar{b}$, the neutron-electron interaction potential depends on the relative orientation of the neutron spin and the moment direction, a vector quantity. The magnitude of the interaction potential is simply the product of the nuclear and Bohr magnetons multiplied by $\frac{2m}{\hbar^2}$. For an atom in which both spin and orbital moments are operative and are strongly coupled to give an angular momentum operator, $\bar{J}$, Trammell (1953) gives the scattering length as

$$\bar{p} = \frac{e^2\gamma}{2mc^2} \, g \, J \, f(\kappa) \left| \hat{J} - (\hat{K}.\hat{J}) \, \hat{K} \right| \qquad \ldots(3.17)$$

where $f(\kappa)$ is the form factor of the interaction, $\hat{J}$ is a unit vector in the moment direction and $\hat{K}$ is a unit vector in the direction perpendicular to the reflecting plane, i.e. the scattering vector.

Bacon (1962) has shown that $(\hat{J} - \hat{K} \, (\hat{J}.\hat{K})) = \hat{K} \times (\hat{J} \times \hat{K}) = J_{perp}$.

The resultant is the projection of $\bar{J}$ onto the

plane normal to the scattering vector $\overline{K}$ i.e. the reflecting plane. The magnitude of this component is J sinα where α is as shown in Fig. 3.3. The equation for the scattering length then becomes

$$\overline{p} = \frac{e^2\gamma}{2mc^2} g J f(\kappa) \sin\alpha \qquad \ldots(3.18)$$

For an unpolarised neutron beam Halpern and Johnson (1939) have shown that the magnetic and nuclear contributions to the scattered intensity are additive. Thus

$$I_{hk\ell} = \frac{A}{L} m G^2_{hk\ell} \left[b^2 + \frac{e^2\gamma}{2mc^2}(gJ)^2 f^2(\kappa)\sin^2\alpha\right] \qquad \ldots(3.19)$$

This equation applies only to a magnetic structure with the same periodicity as the lattice and to one in which there is a fixed orientation of aligned magnetic moments and the scattering vector.

In cases where the magnetisation points in different directions in different parts of the cell the value of sinα varies from site to site with the periodicity of the magnetic structure.

Hence the term $G^2_{hk\ell}J^2$ in the expression for the scattered magnetic intensity given in eqn. 3.19 must be replaced by a factor which reflects this new periodicity. This factor is referred to as the magnetic structure factor and is written

$$\sum_{ij} \exp\left[i.\kappa\ (r_i - r_j)\right] J_i\ J_j \qquad \ldots(3.20)$$

where i and j run over all spins in the crystal. Although the moments in a domain are aligned, domains will be directed randomly with respect to the crystallographic axes and the magnetic scattering will adopt some average value dependent upon the average direction of the scattering vector. In general, the magnetic structure factor $\left|G^m_{hk\ell}\right|^2$ becomes (Marshall and Lovesey 1971)

$$\left|G^m_{hk\ell}\right|^2 = \sum_{\mu,\nu} \left(\delta_{\mu\nu} - \frac{\kappa_\mu \cdot \kappa_\nu}{\kappa^2}\right) \sum_{i,j} \exp\left[i.\kappa(r_i - r_j)\right] J_i^{\nu} J_j^{\mu} \quad \ldots(3.21)$$

where μ and ν run over x, y and z.

The complete expression for the neutron magnetic scattering is

$$I_{hk\ell} = \frac{A}{L} m \exp(-2W) \left[\frac{e^2\gamma}{2mc^2}\right]^2 (gJ)^2 f^2(\kappa) \left|G^m_{hk\ell}\right|^2 \quad \ldots(3.22)$$

The magnetic intensities predicted by this equation for various magnetic structures are derived in Appendix 1.

Materials which order magnetically in such a way that the periodicity of their magnetic structure is not identical to the periodicity of their chemical structure, are said to display non-commensurate spin structures. The existence of such non-commensurate spin structures was first predicted theoretically by Villain (1959) and Yoshimori (1959) and observed in Mn Au_2 by Herpin, Meriel and Villain (1959). Examples of non-commensurate spin

structures are the spiral and the various antiphase domain magnetic structures which have been found in the rare earth metals (e.g. Koehler 1971 and Section 1.3). In general, the extra periodicity introduced into the crystal structure by the magnetic structure manifests itself as scattered intensity at different Bragg angles to the nuclear scattering, resulting in a complicated diffraction spectrum.

3.8 OBSERVED MAGNETIC NEUTRON SCATTERING POWDER PATTERNS

By virtue of the fact that the neutron senses only the component of the moment which is perpendicular to the scattering vector i.e. lying in the reflecting plane, we may determine in which crystallographic direction the moment lies. For the hcp structure the moments can lie either in the basal plane, giving rise to magnetic scattering at all allowed (hkℓ) positions in reciprocal space, or perpendicular to hexagonal layers i.e. along the c-axis, leading to increased intensity at allowed (hkℓ) positions other than (00ℓ).

Since the periodicity of an antiferromagnetic structure is twice that of a ferromagnetic one, the magnetic structure factor will have finite values for reflections which are normally systematically absent and will be systematically zero for the corresponding even-order reflections.

The magnetic scattering from a non-commensurate

spin structure manifests itself as peaks, referred to as satellites, at positions symmetrically disposed around allowed nuclear reflections. The reciprocal lattice rows on which the satellites are found, determine the direction of the modulation vector of the structure, and the angular separation of a satellite from its associated nuclear peak determines the inter-planar turn angle of the structure, (see Section 4.5). For a uniform spiral there are satellites associated with every allowed nuclear reflection as the structure is not uniaxial, (Koehler 1961 a). Absence of the $(00\ell)^{\pm}$ implies that the spiral has a unique axis - the crystallographic c-axis, and the moments are either parallel or anti-parallel to it, but amplitude modulated from plane to plane. It is assumed that the moments on a hexagonal plane are all ferromagnetically aligned and have the same thermally averaged value, but this value varies sinusoidally and no order is assumed for the perpendicular components. This structure is often referred to as c-axis modulated or C.A.M.

A complex situation arises when a basal plane ferromagnet is also amplitude modulated up the c-axis. The periodicity of the amplitude modulation produces both $(00\ell)^{\pm}$ and $(h0\ell)^{\pm}$ satellites and can only be distinguished from a simple spiral model on the basis of the scattered intensity due to each structure.

The ferromagnetic spiral will exist if the basal

plane anisotropy is sufficiently weak to allow the net moment in a layer to cant at an angle to the c-axis. There is now a component of the moment in the c-direction so there will be magnetic scattering at all reciprocal lattice points other than (00ℓ), as well as $(00\ell)^{\pm}$ and $(h0\ell)^{\pm}$ due to the spiral periodicity which remains.

The final structure to be considered is the antiphase domain configuration, (Koehler 1961 b). In this structure the net moments on n adjacent ferromagnetically aligned hexagonal layers are parallel to one another, either parallel to the c-direction or to some direction in the basal plane, and on the next n layers the moment direction is reversed. This new periodicity introduces new satellites of the allowed nuclear peaks into the structure separated by integer multiples of τ_3/n from the lattice sites. When n is even only odd order satellites occur, and there is no magnetic scattering at (h0ℓ) positions in reciprocal space. When n is odd there is weak magnetic scattering at reciprocal lattice points due to the one uncompensated moment and both odd and even satellites occur. If the moment directions are parallel or antiparallel to the c-axis there will be no satellites of (00ℓ).

The magnetic neutron diffraction patterns are summarised in Table 3.1 and the evaluation of the ordered magnetic moment from the magnetic scattering is discussed in Section 4.6.

TABLE 3.1

MAGNETIC STRUCTURE	OBSERVED MAGNETIC DIFFRACTION PATTERN
1. Ferromagnetic in basal plane	All allowed nuclear peaks.
2. Ferromagnetic along c-axis	All allowed nuclear peaks except (00ℓ).
3. Uniform spiral in basal plane	$(00\ell)^{\pm}$ and $(h0\ell)^{\pm}$ of allowed nuclear peaks.
4. Ferromagnetic along c-axis but modulated from plane to plane	$(h0\ell)^{\pm}$ of allowed nuclear peaks.
5. Ferromagnetic in basal plane but amplitude modulation along c-axis	$(h0\ell)^{\pm}$ and $(00\ell)^{\pm}$ of allowed nuclear peaks but with different intensity than in (3) above.
6. Ferromagnetic spiral along c-axis	$(00\ell)^{\pm}$ and $(h0\ell)^{\pm}$ of allowed nuclear peaks plus magnetic intensity at all allowed nuclear peaks except (00ℓ).
7. Antiphase domain	Satellites of the new periodicity. For n even - odd order harmonics For n odd - odd and even order harmonics, plus scattering at $(h0\ell)$ positions.
8. Antiphase domain along c-axis	As above but no scattering at (00ℓ) nuclear positions.

3.9 INELASTIC NEUTRON MAGNETIC SCATTERING

In any neutron scattering experiment both elastic and inelastic processes are occurring simultaneously. An inelastic scattering event with the correct scattering vector can appear at an angle 2θ in a diffraction experiment as incoherent background. An inelastic scattering experiment is possible if the energies of the scattered neutrons are measured, by timing them over a known distance for instance, and the scattering vector is determined from the system geometry.

The energy of a thermal neutron is 0.025eV which is of the same order as the energy of a phonon in a crystal. In any neutron-phonon interaction, then, the energy change will be quite a significant percentage of the incident neutron's original energy, and will be readily observable. Like the phonon, the quantum of magneto-vibrational energy, a spin wave, is the magnon. At temperatures below the Debye temperature and magnetic ordering temperature, the probability of a phonon-neutron scattering event is low, whereas a magnon-neutron scattering event is highly probable. Many experiments have been performed to observe the spin waves propagating in the heavy rare earths, (See Mackintosh and Bjerrum Møller 1971).

In the light rare earth metals the competition between the crystal field and the exchange severely restricts the formation of an ordered magnetic state

and actually prevents it in Pr. The electronic ground state in Pr is a singlet and excitations progagating in the material are not spin waves but localised modes corresponding to excitations between crystal field states, (see Sections 2.8 and 2.9). Using the theory developed by Van Vleck (1939) for paramagnetic inelastic scattering, it can be shown that the low temperature dispersion relation for these so called magnetic excitons is

$$\hbar\omega(q) = \Delta \left[1 - \frac{2\alpha^2}{\Delta} I(q) \right]^{\frac{1}{2}} \qquad \ldots(3.23)$$

(Mackintosh and Bjerrum Møller 1971), where Δ is the crystal field splitting between the two levels and α is the matrix element of an angular momentum operator between them.

CHAPTER 4

EXPERIMENTAL DETAILS

4.1 SPECIMEN PREPARATION AND CHARACTERISATION

The alloys were prepared by melting together appropriate quantities of 99.9% pure rare earth metals in an argon arc furnace with a non-consumable tungsten electrode. The buttons were inverted and remelted several times to ensure homogeneity. Weight losses due to evaporation on melting were of the order of 0.1%. In view of the low weight losses the nominal alloy compositions were selected on the basis of the atomic percentages and no further analysis of the composition was deemed necessary.

An as-cast button was then polished with fine grade emery paper and annealed in a vacuum for 2 hours at 650^{o}c. The specimens were then X-rayed on a Philips Diffractometer. The diffraction pattern was indexed by hand and lattice parameters assigned using a refinement programme based on Hess' method. The rapid cooling from the melt which occurs during the manufacture of the alloy samples can lead to preferred directions of growth. Evidence of such preferred orientation was sought using neutron diffraction and a standard Laue back reflection technique. Some degree of preferred orientation was observed in all the alloys (see Section 5.1). A full discussion of the consequences of preferred orientation effects in this investigation appears in Section 4.6.

A sample of approximately 2 gm. was made up at intervals of 10% composition change across each alloy system. These samples, and some at intermediate compositions, were used to determine the magnetic transition temperatures of the alloys (see Section 4.2). For the alloys selected to be representative of the three crystal structures of each particular alloy system, (see Section 1.2), five buttons of approximately 5 gm. each were prepared. Neutron diffraction necessitates the use of such large sample volumes because of the low intensity of the reflections from polycrystalline samples. In this investigation typical sample volumes were 3 c.c.s. Because of the high absorption cross section of Dy for thermal neutrons (see Table 1.1), the buttons of Pr-Dy and Nd-Dy were slit into 1 m.m. thick platelets perpendicular to the flat base, with a diamond wheel. The platelets were held between two pieces of thin Tantalum foil and mounted in a "window frame" holder, so as to present as large an area to the beam as possible.

4.2 A.C. SUSCEPTIBILITY BRIDGE

4.2(i) EXPERIMENTAL APPARATUS

The magnetic transition temperatures of the alloys were measured using a low field a.c. susceptibility technique, first developed by Salmans et al (1968). The mutual inductance of two concentric coils, referred to as the primary and secondary coils, is proportional

to the permeability of the core material. As the temperature of the material is varied, its permeability changes in a manner characteristic of the magnetic transitions. The change in induced e.m.f. across the secondary is detected and displayed against the temperature of the core material. For sufficiently low fields the measured permeability is simply the initial permeability of the material and hence the output is a direct measure of the transition temperature.

To increase the sensitivity of the bridge a second secondary coil continuous with the first and of exactly the same number of turns, but wound in the opposite sense, was incorporated in the detection circuit, (see Figs. 4.1 and 4.2. Fig. 4.1 is a block circuit diagram of the A.C. susceptibility bridge and Fig. 4.2 is a diagram of the A.C. susceptibility apparatus.) The output of the detection coil system is identically zero as the induced e.m.f. in one coil is equal and opposite to that in the other coil. The two secondary coils were wound on a "Lexan" former with fine Cu wire. The coils were 1 cm. long and 1 cm. apart. The primary coil was of heavier gauge wire and four times as long as the secondary coil system. The advantage of having the secondary coils close together and inside one primary coil, rather than the original apparatus of Salmans et al, is that changes in temperature affect both coils equally and, as a consequence, the change in mutual inductance with temperature is automatically

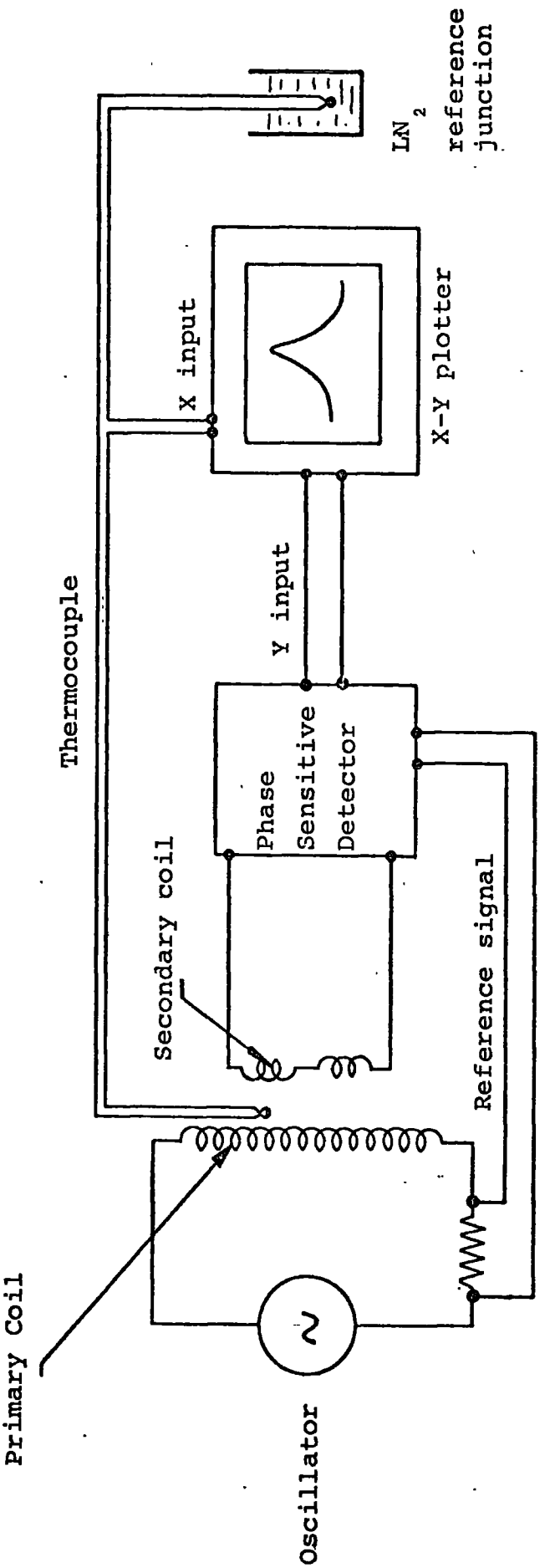

Schematic diagram of the electronics for the A.C. susceptibility apparatus.

FIG. 4.1

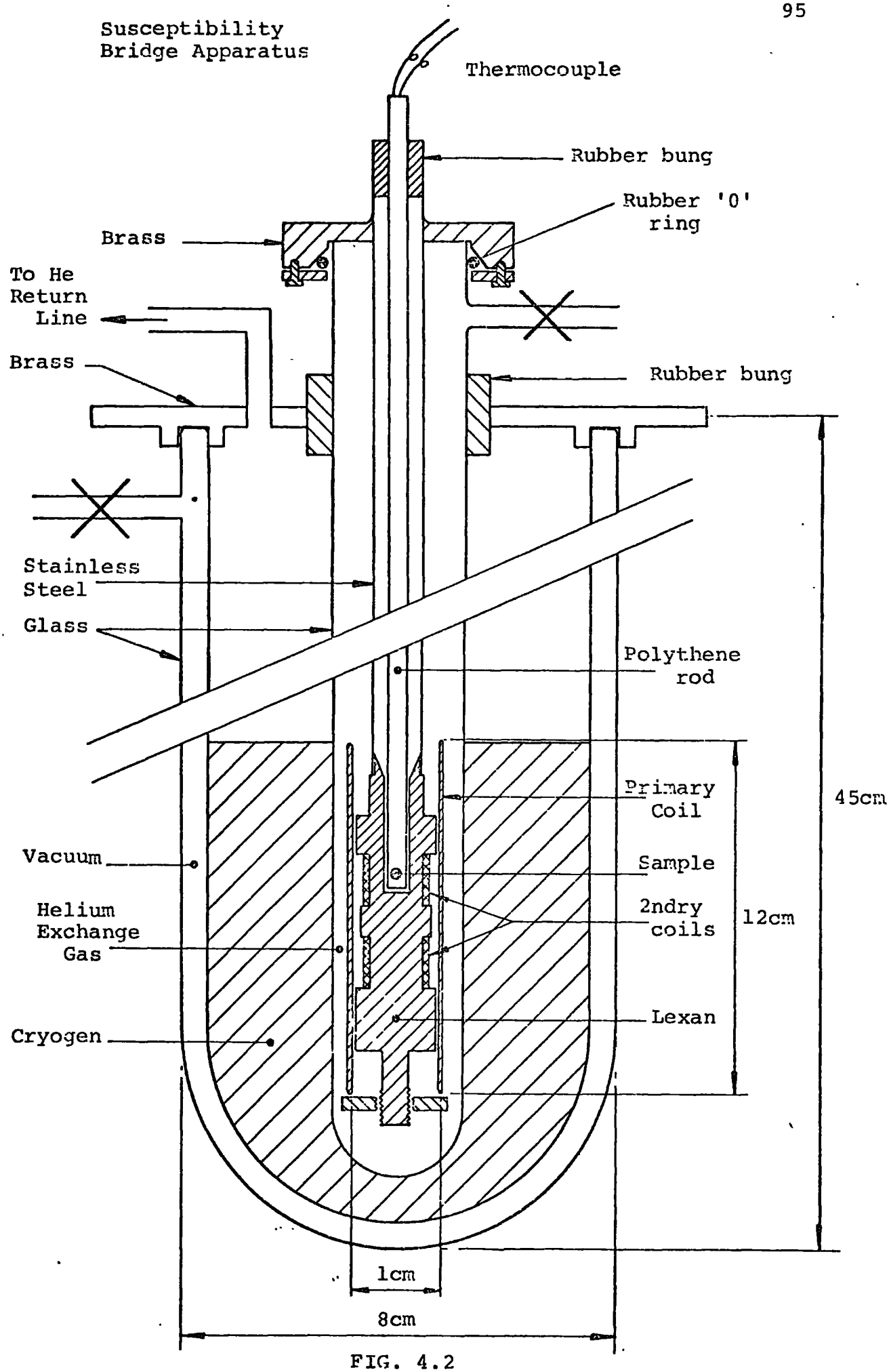
Susceptibility
Bridge Apparatus
Thermocouple
Rubber bung
Rubber '0'
ring
Brass
To He
Return
Line
Brass
Rubber bung
Stainless
Steel
Glass
Polythene
rod
Primary
Coil
45cm
Vacuum
Sample
Helium
Exchange
Gas
2ndry
coils
12cm
Lexan
Cryogen
1cm
8cm

FIG. 4.2

accounted for. Also, by making the primary coil much longer than the detection coil system, both the secondary coils lie in the region of uniform magnetic field strength, away from the ends of the primary coil. Should the primary coil move on cooling, the output from the detection coils remains zero. The primary coil was wound on a glass former which fitted over the Lexan former. This facilitated removal of the primary coil without disturbing the secondary coils.

The driving signal for the primary coil was derived from a high power audio oscillator. The r.m.s. value of the alternating current in the driving coil gave a field of 6.8 Oe at 83 Hz. This frequency was chosen so that the output did not beat with the mains and to be well within the skin depth of the materials studied.

The leads to the driving coils were wound together and the leads from the detection coil system were wound together and then wound in a loose spiral up the stainless steel centre column to prevent 50 Hz pick-up. The leads are not shown in Fig 4.2 for clarity. The stainless steel tube and the coil system were placed in a glass tube which could be evacuated and filled with He gas. The specimen was inserted into the upper of the two secondary coils on the end of a non-magnetic centre stick through a demountable vacuum seal at the top of the stainless steel tube. The centre stick also carried a thermocouple. A Cu v. Constantan thermocouple

with a liquid nitrogen reference junction was used for work above 77K and an Au (0.2% Fe) v. Cu thermocouple with a liquid nitrogen reference junction for determinations below 77K. It was found necessary to measure temperature changes in the regions above and below 77K with different thermocouples because the thermoelectric power of the Cu vs. Constantan thermocouple is very small below 77K and falls to zero at 20K, whilst the thermoelectric power of the Au (0.2% Fe) vs. Cu thermocouple is large below 77K, but falls to zero at higher temperatures. Both thermocouples were calibrated in the laboratory against standard tables.

The sample temperature was varied from liquid nitrogen temperature to room temperature by first immersing the whole apparatus up to the level of the top of the driver coil in liquid nitrogen in a glass cryostat. When the sample had cooled to 77K the whole apparatus was withdrawn from beneath the liquid surface to just above it and the sample allowed to warm up in the stream of cold gas. The height to which the apparatus was raised determined the warming rate. To ensure a slow warming rate the whole apparatus was only withdrawn to a height 1 cm. above the liquid surface at first and then by further increments of 1 cm. until the entire temperature range had been covered. In this way warming rates of 5K/min. and slower were achieved. The presence of the He exchange gas ensured that the two secondary coils were at the same temperature. For experiments

between 4.2K and 77K the whole apparatus was replaced in the cryostat and a small amount of liquid He transferred into the cryostat. The sample was cooled to 4.2K and the remaining He allowed to boil off naturally. When all the liquid He had gone the sample started to warm up slowly.

The output from the detector coil system was fed to a phase sensitive detector and high gain amplifier and then to the X input of an X-Y recorder. The Y input of the recorder was derived from the output of the thermocouple, (see Fig 4.1).

4.2(ii) RELATIONSHIP BETWEEN OUTPUT VOLTAGE AND SUSCEPTIBILITY.

Let a current $i_0\exp(j\omega t)$ flow in a solenoid. The field induced in the coil is

$$H = H_0\exp(j\omega t) \qquad \ldots(4.1)$$

where $H = \dfrac{4\pi n i_0}{10}$ in e.g.s. units and n is the number of turns/cm

The induction, $B = \mu_0 H_0 \exp(j\omega t)$

and the flux in the coil $\phi = \int_A B.n.dA = \mu_0 H_0 A \exp(j\omega t)$

where A is the cross sectional area of the coil.

Thus the voltage, V, induced in a secondary coil is

$$V = -\frac{d\phi}{dt} = -j\omega\mu_0 H_0 A\exp(j\omega t) \qquad \ldots(4.2)$$

For the first secondary coil the output is V_1 and for the second the output is V_2. In the absence of a specimen

$$V_1 - V_2 = 0 \qquad \ldots(4.3)$$

since the coils have equal numbers of turns, but are wound in series opposition.

In the presence of a sample, $B = \mu_o(H + M)$

$$= \mu_o H(1 + \chi)$$

where M is the magnetisation and χ the susceptibility of the sample.

The flux in the coil containing the sample is

$$\phi = \int_A B.n.dA = \mu_o H_o \exp(j\omega t)(1 + \chi)An \qquad ...(4.4)$$

Thus, $V_1 = -\frac{d\phi}{dt} = -j\omega\mu_o H_o \exp(j\omega t)(1 + \chi)An \qquad ...(4.5)$

The output voltage of the two coil system is

$$V_1 - V_2 = -j\omega\mu_o H_o An\chi\exp(j\omega t) \qquad ...(4.6)$$

i.e. $$V_1 - V_2 = -j\omega\mu_o H_o An(\chi' + j\chi'')\exp(j\omega t) \qquad ...(4.7)$$

The imaginary part of the susceptibility, χ'' (the power absorbed) is in phase with the output signal of the bridge and thus with the driving voltage i.e. with the p.s.d. reference signal (see Fig. 4.1) whereas the real part of the susceptibility χ' is 90^o out of phase with the p.s.d. reference signal.

The out of phase component of the detected signal was used as the input to the Y axis of the X-Y recorder, thus the susceptibility versus temperature curves derived in this investigation are proportional to the change in real susceptibility with temperature.

4.3 CRITICAL FIELD MEASUREMENTS

Critical field measurements were performed on three

alloys containing Dy and on elemental Dy. Two of the alloys, Pr_{30} Dy_{70} and Nd_{30} Dy_{70}, had previously been used in neutron diffraction investigations and measurement of the turn angles could be combined with the critical field data to give an estimation of the exchange parameters, (see Section 2.3). The critical field of Pr_{10} Dy_{90} was measured for comparison with the data of Chatterjee and Taylor (1972) on the equivalent Nd alloy, Nd_{10} Dy_{90}, and the data on polycrystalline Dy was compared with the data of Behrendt et al (1958) on single crystal Dy.

The measurements were made on a Foner vibrating specimen magnetometer (see for instance Foner 1956 and 1959) at the C.S.I.R.O., Sydney. The alloy samples were cut so as to be disc-shaped and were mounted in the sample holder with their long axes parallel to the field direction. The sample of Dy was cut from a larger piece and resembled a sphere. The samples were completely demagnetised before each experiment and the magnet was cycled so that there was no remnant magnetic field. This procedure was found to be necessary as earlier investigations had shown that the samples' previous magnetic history affected the results. The position of the sample was adjusted to be in the centre of the magnetic field by maximising the output signal in a given field for each of the x, y and z directions simultaneously. Since all the samples were approximately the same size this procedure was only carried out once and other samples were assumed to be correctly aligned.

The tail section of the cryostat was filled with liquid nitrogen such that the sample was immersed in the liquid and came to 77K. The temperature of the sample was measured with a Au (0.03% Fe) vs. Chromel thermocouple with a liquid nitrogen reference junction, that had been calibrated against standard tables. The magnetisation of the sample was then measured as a function of field strength up to 5 kOe in steps of 200 Oe. To obtain a temperature of 90K the tail section of the cryostat was filled with liquid Oxygen. Intermediate temperatures were obtained by filling the tail section of the cryostat with cryogen such that the level of the cryogenic fluid was below the sample position. Thus the sample vibrated in a stream of cold gas and came to some equilibrium temperature. Once this equilibrium temperature was attained, it remained for long enough to permit a magnetisation run to be performed. Temperatures below 77K were obtained by pumping on liquid Oxygen.

The procedure outlined above was dictated by the construction of the cryostat and the v.s.m. and did not enable specific pre-determined sample temperatures to be obtained, nor could equilibrium temperatures above 120K be attained for long enough to permit measurements to be carried out. However, the results for pure Dy obtained by this method do compare well with those of Behrendt et al 1958 (see Fig. 5.10).

4.4. NEUTRON SCATTERING

The elastic neutron scattering experiments were carried out at the U.K.A.E.A. reactor DIDO and the A.A.E.C. reactor HIFAR and some inelastic scattering experiments at the U.K.A.E.A. reactor PLUTO.

4.4(i) ELASTIC NEUTRON SCATTERING

Since both the diffractometers used in this investigation are constructed on the same principle, it will be sufficient to describe only one, mentioning any differences between them.

Neutrons from the reactor core (and assumed to be in thermal equilibrium with it) are reflected from a monochromating crystal (of Cu, Pb, or squashed Ge) at one end of a collimating tube. (see Fig 4.3). The highly monochromatic beam emerging at the end of the beam tube hits the sample and is diffracted into the Debye-Scherrer cone of semi-angle 2θ. The detector, moving along the circumference of a circle in the plane of the beam and the sample, intersects the cone at the Bragg angle. Powder diffractometers are thus often referred to as two circle diffractometers.

Both diffractometers used in this investigation operated with a neutron wavelength of about $1A^{o}$. In the HIFAR diffractometer a wavelength of $1.08A^{o}$ was produced by reflection from a Cu single crystal and in the DIDO diffractometer a wavelength of $1.15A^{o}$ was produced by reflection from a Pb single crystal. The beam size is

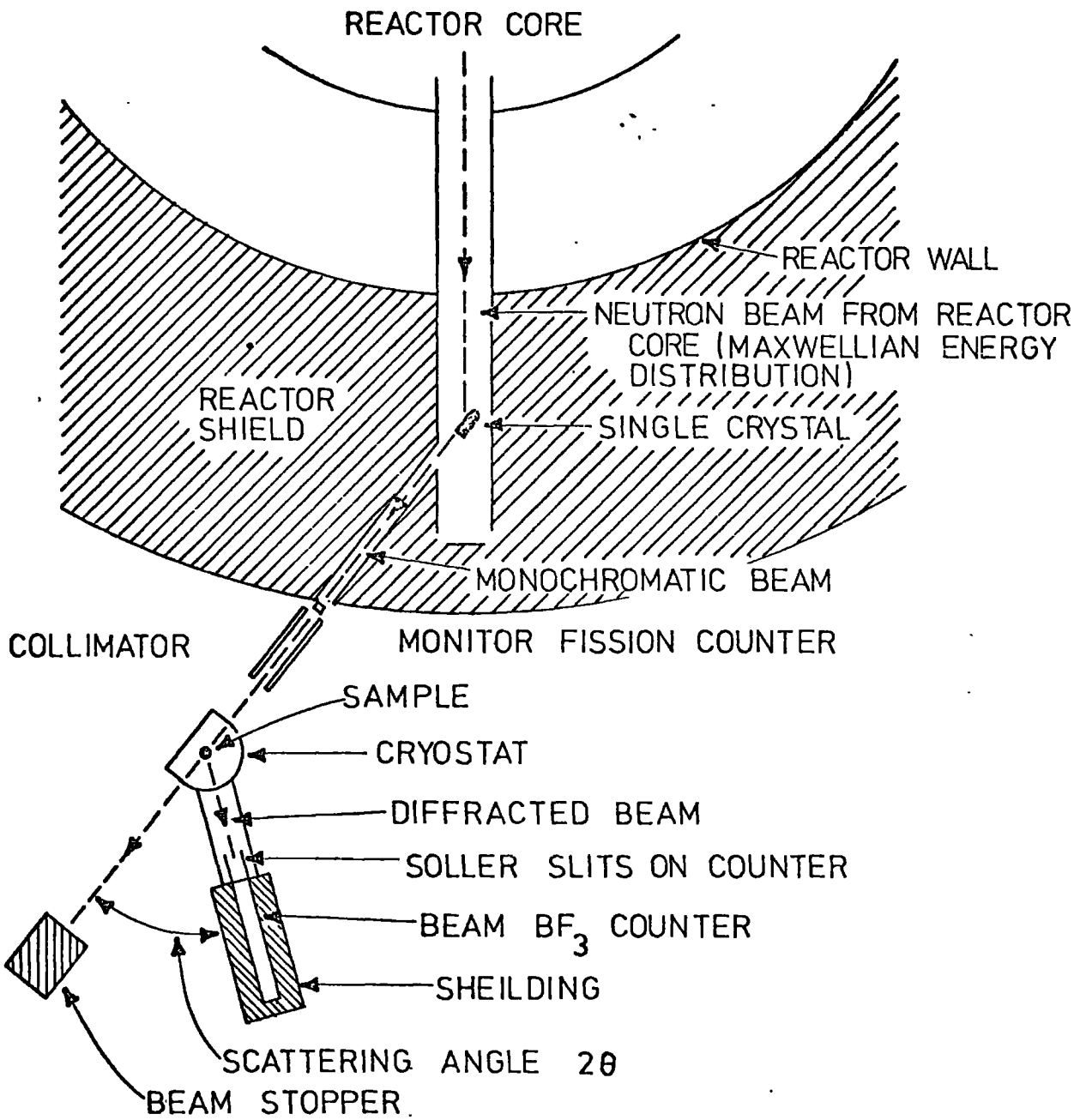

FIG. 4.3 The neutron diffractometer

cut down to the size of the sample by use of a mechanical shutter made of Cd positioned at the end of the beam tube. This ensured that only neutrons passing through the sample or diffracted by it entered the detector. Both diffractometers used conventional BF_3 neutron detectors which were heavily shielded so that only neutrons entering via the end window were counted. The detector is only 1 inch in diameter, so to obtain a high counting efficiency it has to be 2ft in length. As the DIDO diffractometer is primarily for single crystals with their much higher scattering intensities, the detector is only 6 inches long. The angular resolution of the detector is increased either by placing the detector some distance from the sample and inserting a slit system between it and the sample, or by placing a Soller slit system immediately in front of it. In the latter case, it is not necessary to place the detector so far away from the sample. A Soller slit system consists of thin shims of Cd plated mild steel approximately 10 inches long mounted in a holder so that they are strictly parallel to the beam and about ¼ inch apart. They thus absorb any slightly off-axis neutrons. The use of Soller slits enables the detector to have good angular resolutions at a position where the scattered intensity is high, whereas increasing the sample - detector separation gives better resolution at the expense of scattered intensity. Mechanical

considerations, e.g. the amount of space available, and the construction of a platform which will rotate accurately carrying a heavily shielded counter on an arm 4ft long, often make Soller slits a necessity.

A complete neutron diffraction scan consists of recording the scattered intensity per unit time for various settings of the counter angle 2θ. In practice the detector is stepped on automatically after a preset number of neutrons have passed through a fission chamber situated between the end of the beam tube and the sample. The fission chamber is constructed with a very low but known efficiency for the capture of slow neutrons, by impregnating a large area of non-absorbing material with a few milligrams of ^{238}U. One captured neutron from the beam initiates one fission reaction which is detected electronically. When a certain number of neutrons have been absorbed and registered, the counting at that setting of 2θ ceases and the detector moves to the next setting of 2θ, typically 0.1^{o} on. In this way fluctuations in the numbers of neutrons per unit time from the reactor are automatically accounted for. A complete scan from $2\theta = 2^{o}$ to $2\theta = 40^{o}$ stepping 0.1^{o} takes about 24 hours.

Normally room temperature scans are done by placing the powder (in this study in the form of five buttons each of approximately 5 gm) in an Al or V can directly in the specimen position. The can is mounted on a goniometer to facilitate final alignment of the

sample. The alignment was checked by photographing the sample directly with a neutron camera. An Al sample can has a low incoherent background scattering, but two clearly visible peaks which occur at low 2θ values and contribute to the overall diffraction pattern, whereas the V can has no coherent scattering but a higher incoherent scattering. The tail section of the B.O.C. cryostat (see Section 4.4(ii)) was also constructed of Al, but the presence of Al did not affect the interpretation of the diffraction pattern of the sample. To remove the extra coherent scattering from the sample diffraction pattern altogether, the V can was used in conjunction with a V tail section (see Section 4.4(iii)). The Andonian cryostat (see Section 4.4(ii)) was constructed with a tail section of stainless steel, but fortuitously the coherent scattering from stainless steel did not overlap with any of the peaks in the diffraction pattern of the sample.

In this investigation, since the saturation moments of the alloys at 4.2K were being measured as well as the spin structures of the alloys, room temperature scans were done in a cryostat to allow direct subtraction of the nuclear component from the diffraction pattern at 4.2K. (see Section 4.6).

The wavelength of the neutron beam was measured by recording the diffraction pattern of a standard Ni sample. The observed Bragg angles were substituted

into the Bragg equation along with the tabulated interplanar spacings in Ni to give the neutron wavelength.

4.4(ii) CRYOSTAT AND TEMPERATURE CONTROL

During the course of this study, two cryostats and temperature controllers were used. A B.O.C. closed top cryostat in conjunction with a Thor temperature controller, and an Andonian cryostat with an Oxford Instruments temperature controller. With both systems it was possible to maintain sample temperatures to ± 2K for the duration of a scan. The body of both cryostats is made of stainless steel and both are insulated by vacuum jackets which had to be evacuated each time the cryostat was used. The tail section of the Andonian cryostat is also made of stainless steel, whereas the tail section of the B.O.C. cryostat is of Al. Both cryostats have the facility for removing the sample whilst the cryostat still has cryogens in it.

In the B.O.C. cryostat (shown in Fig. 4.4) the centre stick assembly fits into the tail section of the cryostat leaving an annulus of about 0.25 mm. Liquid He fills this annulus and the space directly above it. The drawback with this cryostat is that a small amount of cryogen is in the neutron beam. Hence, liquid Nitrogen, with its high scattering cross section, cannot be used as the main coolant. For scans at and above

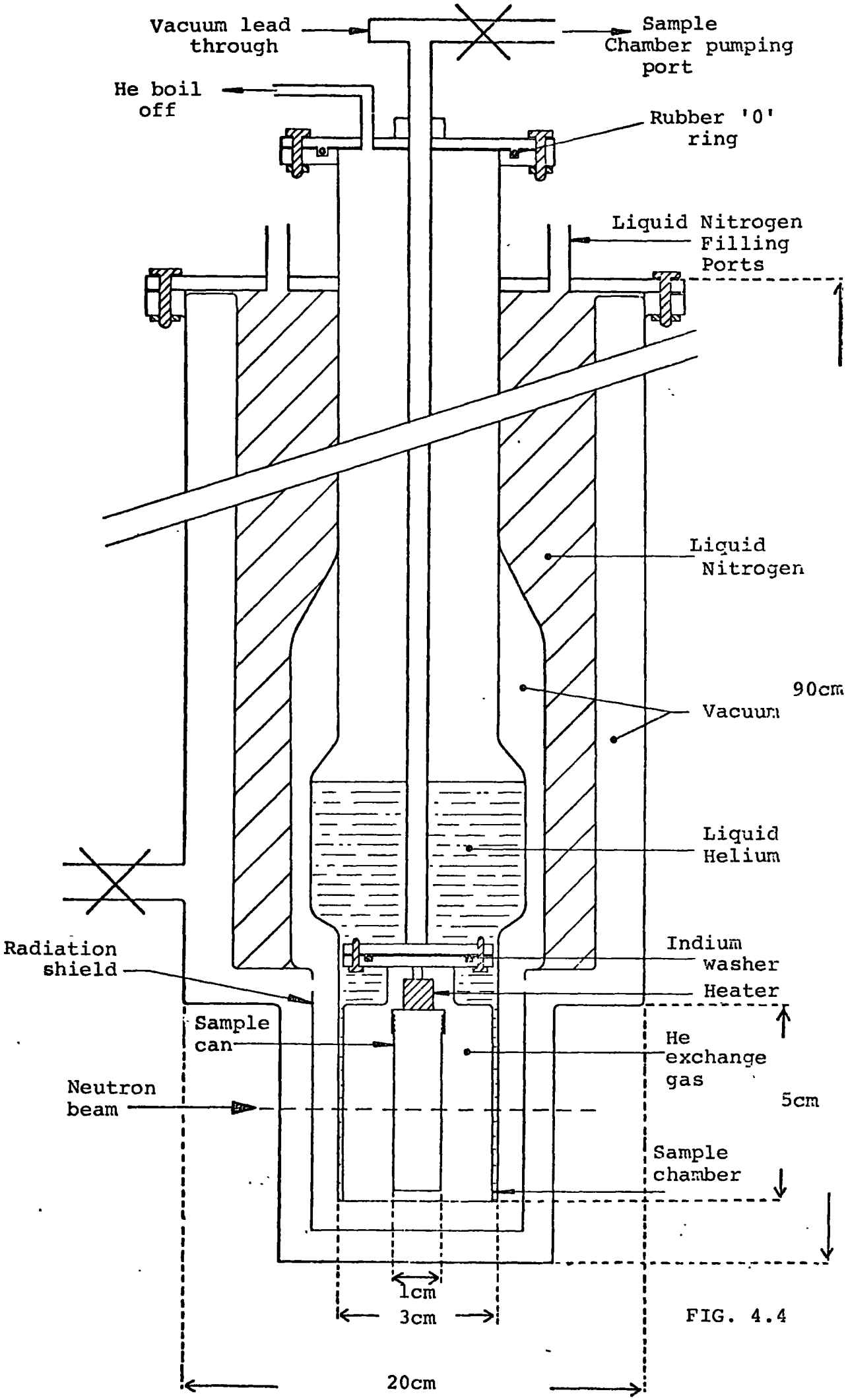
Vacuum lead through
Sample Chamber pumping port
He boil off
Rubber '0' ring
Liquid Nitrogen Filling Ports
Liquid Nitrogen
90cm
Vacuum
Liquid Helium
Radiation shield
Indium washer
Heater
Sample can
He exchange gas
Neutron beam
5cm
Sample chamber
1cm
3cm
20cm

FIG. 4.4

liquid Nitrogen temperature, liquid He must still be used as the main coolant, resulting in high He boil off rates. The Andonian cryostat is like the B.O.C. cryostat, except that it has a liquid He bin between the vacuum jacket and the central section. Thus the sample is cooled by convection down the He gas in the central column. In this cryostat liquid Nitrogen can be used as the main coolant by putting it in the liquid He bin and scans can be done above 77K without rapid boil off of cryogens.

The sample was changed by removing the whole centre stick assembly from the cryostat and, in the case of the B.O.C. cryostat, demounting the outer sample can and indium seal. (See Fig. 4.4). The Andonian cryostat had no outer sample can which made sample changing quicker, but on removing the centre stick assembly, it was necessary to ensure that the He gas in the central column was not replaced by air. This was done by filling the central column with a slight overpressure of He gas, withdrawing the centre stick, and then for all times that the mouth of the cryostat was not sealed either with the centre stick or a bung, blowing He gas across it.

Variable temperatures were achieved by pumping out the He exchange gas from around the sample and heating it with a small 120Ω heater wound on a Cu former just above it. Good thermal contact between the lid of the sample can and the former was achieved

by covering the mating surfaces with a little vacuum grease and then screwing them together tightly. The space above the sample buttons in the sample can was filled with a spring made of Cd which protruded slightly beyond the can. The can was then screwed into the lid against the resistance of the spring until it was tight. Thermocouples were attached to the top and bottom of the sample can with low temperature glue. It was found necessary to pump the system (in the case of the B.O.C. cryostat the sample chamber and in the case of the Andonian cryostat the complete central column) continuously whilst heating the sample, to maintain a stable temperature.

The output of the upper thermocouple attached to the sample can was used as the input to the temperature controller. The lower thermocouple was used to indicate when an equilibrium situation had been reached and a scan could be started. For both cryostats thermal stabilisation took about 2 hours. Using Cu vs. Constantan thermocouples as the temperature sensors, the range 4.2K to 20K had to be monitored with another device because the thermoelectric power of the Cu vs. Constantan thermocouple is almost zero over this range. A carbon resistance thermometer was used to measure temperatures in the range 4.2K to 20K when it was necessary to maintain sample temperatures in this region. The only thermocouple to cover the complete range of interest - 4.2K to 300K - and give a high

thermoelectric e.m.f. is the Au (0.03% Fe) v. Chromel thermocouple. This thermocouple was used in conjunction with the Andonian cryostat and the Oxford Instruments temperature controller with a liquid He reference junction,when maintaining sample temperatures between 4.2K and 77K,and with a liquid Nitrogen reference junction for sample temperatures above 77K.

The Oxford Instruments temperature controller had to be modified to be used with the convection cooled Andonian cryostat, as it delivered far too much power. Several passive networks were installed so by use of a rotary switch different percentages of the power, up to 98%, could be dissipated outside the cryostat. Both the Oxford Instruments and Thor temperature controllers had external switches for varying the time constants of the integral and differential control circuits. In the Thor controller this was commercially available and in the Oxford Instruments controller this was incorporated in the modifications.

4.4(iii) INELASTIC NEUTRON SCATTERING

The following sub-section briefly describes the powder inelastic neutron scattering apparatus at the U.K.A.E.A. PLUTO reactor and the experiments that were performed with it on some Pr-Tb alloys in the d.h.c.p. (light rare earth rich) phase and polycrystalline Pr.

Thermalised neutrons from the core with a Maxwellian distribution of velocities, are incident on

a slotted rotor revolving at very high speed, (see Fig. 4.5.) A burst of neutrons with a velocity spread is allowed through the rotor when the slot is in the "open" position. The second rotor is phased with respect to the first such that only neutrons which traverse the distance between the rotors in a given time reach the second slotted rotor when it is "open". Thus a burst of monoenergetic neutrons is incident on the sample. The resolution of the burst is given by a relationship between the distance between the rotors, the slit size and the slit open time i.e.rotor speed, (for a discussion of rotor design see Turchin, 1965.)

The neutrons scattered from the sample in one of a number of directions in 2θ are timed over a distance of about 1 metre, the flight path in Fig. 4.5 and the number arriving in bin widths of 5μsec are recorded by a BF_3 counter at the end of the flight path. The crystal clock which times the neutrons from the moment they leave the sample, is activated by a fiducial mark on the second rotor. Some neutrons are not scattered, but pass straight through the sample. Before they are absorbed in the beam stop, they pass through three fission chambers spaced at precise distances apart. The time taken to traverse all three fission chambers provides an accurate value of the energy of the burst. For each counter the number of neutrons detected in bins of width 5μsec after the clock has started for each burst are recorded on a PDP 11 computer. The peripheral

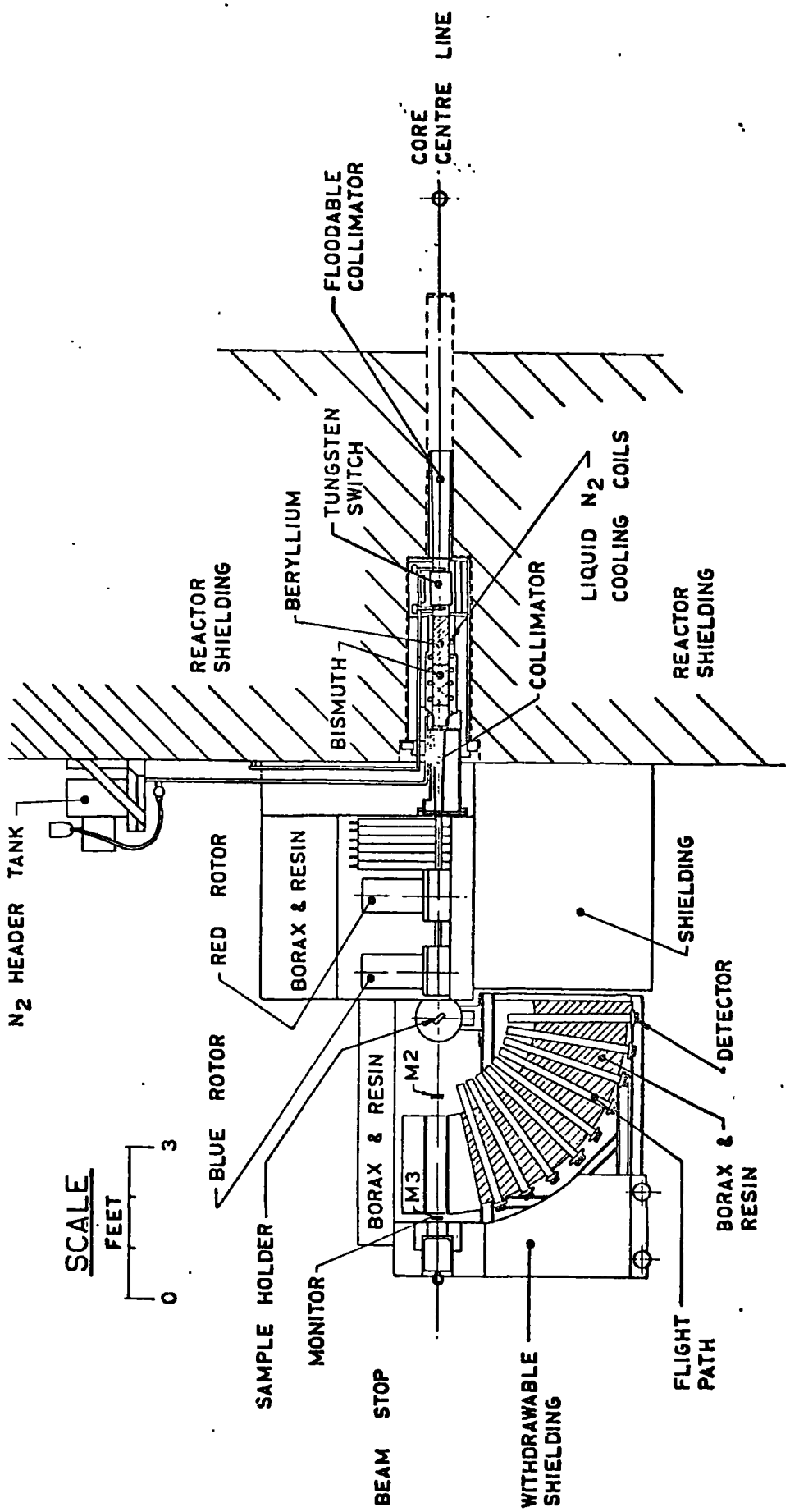

Inelastic neutron scattering spectrometer

FIG. 4.5

computer has been described by Baston (1972). The experiment proceeds until the data in the histogram of each counter is sufficient to give good statistics. The data stored in the buffer memory of the computer is then transferred to magnetic tape for later analysis. This spectrometer has been described more fully by Dyer and Low and multiple rotor spectrometers in general are discussed by Brugger (1965).

After one experiment had been completed the speed of the rotors was changed and the phase adjusted to give a different energy. The incident neutron energies used in this study were 8 meV and 16 meV to investigate the magnetic excitons propagating in Pr^{3+} and assumed to be operative in Pr-Tb alloys with low Tb content. The excitations in Pr^{3+} have energies of 3.2 meV and 8.0 meV above the ground state on the hexagonal and cubic sites respectively and are readily observed in energy loss experiments with incident neutron energies of 8 meV and 16 meV. It was assumed that these energies would be suitable for observing any magnetic excitons in the Pr-Tb alloys.

The buttons of sample were located in the beam in a V sample can kept at 4.2K in a B.O.C. cryostat with a specially manufactured tail section of V rather than Al. V was used wherever possible to remove coherent scattering.

The dispersion relation for a magnetic exciton is given by equation 3.23 in Section 3.9. For a powder

specimen the scattering vector $\bar{q}$ has no meaning as the crystallites are randomly orientated. Thus the inelastic scattering can be viewed from any angle of 2θ and an array of counters is used rather than a single counter. For each counter a histogram is built up of the number of neutrons arriving at a certain time against that time. These times are converted to energy changes and the neutrons which have been inelastically scattered appear as a peak displaced from the elastic peak. Since the resultant in each counter is a spatial average, the contents of each counter are added together to improve the counting statistics. The acquisition of sufficient data in this experiment took approximately 36 hours.

4.5 MAGNETIC STRUCTURE DETERMINATIONS

As mentioned previously (Section 3.7) a spiral spin structure manifests itself as extra scattering at peaks symmetrically displaced about the nuclear peaks, (See Fig. 4.6). Identification of satellites of all allowed nuclear peaks implies that the moment lies in the basal plane with a moment direction that is modulated along the c-axis.

The turn angle of the structure, ω, can be related to the angular displacement of the satellite from the nuclear peak. The satellite of an (00ℓ) reflection may be considered to be due to scattering from a plane with indices $(00\ell \pm \Delta\ell)$. The turn angle may be written

$$\omega = 2\pi\Delta\ell\frac{z}{c_o} \qquad \ldots(4.8)$$

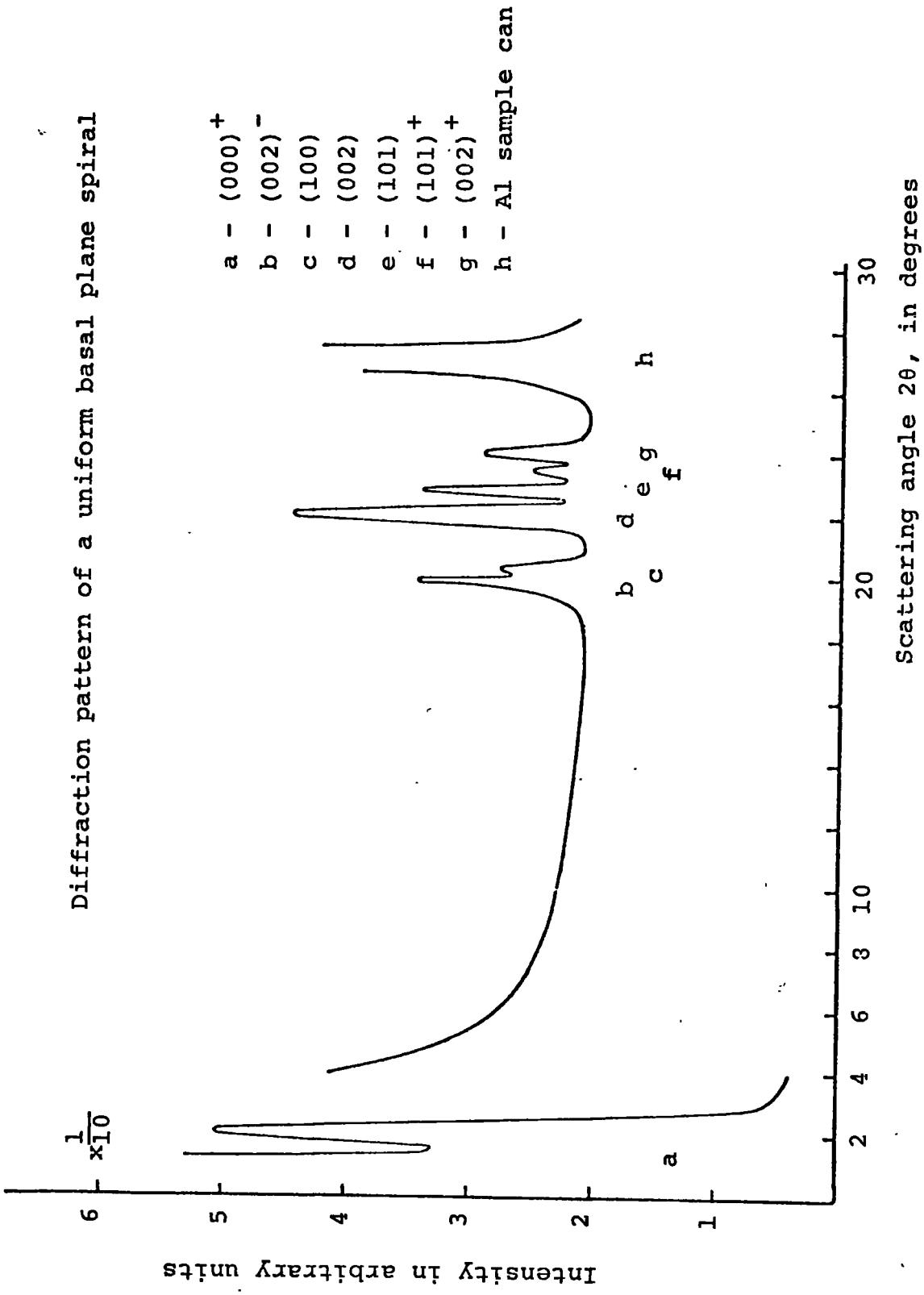
Diffraction pattern of a uniform basal plane spiral
a - (000)+
b - (002)-
c - (100)
d - (002)
e - (101)
f - (101)+
g - (002)+
h - Al sample can
Intensity in arbitrary units
Scattering angle 2θ, in degrees
1/x10
a
b
c
d
e
f
g
h

FIG. 4.6

where c_o is the equilibrium unit cell c-axis parameter and z is the interlayer spacing along the c-axis in units of c_o. Thus for an h.c.p. structure $\frac{z}{c_o} = \frac{1}{2}$, for the Sm structure $\frac{z}{c_o} = \frac{1}{9}$ and for the d.h.c.p. structure $\frac{z}{c_o} = \frac{1}{4}$.

The interplanar spacing d, along the c-axis is given by

$$\frac{1}{d} = \frac{\ell}{c} \qquad \ldots(4.9)$$

The Bragg angle corresponding to diffraction from such an (00ℓ) plane is given by

$$\sin\theta_{hk\ell} = \frac{\lambda\ell}{2c} \qquad \ldots(4.10)$$

and the Bragg angle for an (00ℓ + Δℓ) plane is given

$$\sin\theta_{hk\ell+\Delta\ell} = \frac{\lambda(\ell+\Delta\ell)}{2c} \qquad \ldots(4.11)$$

Subtracting eqn. (4.10) from eqn. (4.11) gives

$$\Delta\ell = \frac{2c}{\lambda}\left(\sin\theta_{hk\ell+\Delta\ell} - \sin\theta_{hk\ell}\right) \qquad \ldots(4.12)$$

Considering only the (000) nuclear peak $\theta_{hk\ell} = 0$ and thus

$$\Delta\ell = \frac{2c}{\lambda}\sin\theta_{hk\ell+\Delta\ell} \qquad \ldots(4.13)$$

The expression for the turn angle becomes

$$\omega = \frac{4\pi c}{\lambda}\,\frac{z}{c_o}\,\sin\theta_m \qquad \ldots(4.14)$$

where θ_m is the angular position of the $(000)^{\pm}$ magnetic peak. Correspondingly more complicated formulae may be derived for the $(00\ell)^{\pm}$ and $(hk\ell)^{\pm}$ satellites.

The magnetisation of the alloys is a long way from saturation in the antiferromagnetic phase and thus the intensity of the satellite peaks is low. The strongest satellite peak is the $(000)^{\pm}$ since both the Debye-Waller temperature factor and the magnetic form factor are almost unity for small scattering angles. The intensity rapidly diminishes with scattering angle and because of this the position of the $(00\ell)^{\pm}$ satellites is much more difficult to assign unambiguously. In a powder pattern some of the $(hk\ell)^{\pm}$ satellites are often hidden under nuclear peaks. The variation of the turn angle with temperature for all the representative alloy samples was evaluated by measuring the angular distance of the $(000)^{\pm}$ from the origin.

The peak intensity of a satellite rises from zero at the Néel temperature to some maximum value then falls abruptly to zero at the Curie temperature and re-appears as scattered intensity at the allowed nuclear positions. The intensity of the nuclear peaks increases with decreasing temperature following a [Brillouin type curve,]^{2} (see Fig. 4.7). The predicted scattering patterns for three types of ferromagnetic ordering (ferromagnetic alignment of spins in the basal plane, along the c-axis and the ferromagnetic spiral) are summarised in Table 3.1. Fig. 4.8 shows the observed diffraction pattern for a basal plane ferromagnet compared with the same structure in the paramagnetic state. In the

Intensity of (101) magnetic peak in a basal plane ferromagnetic structure

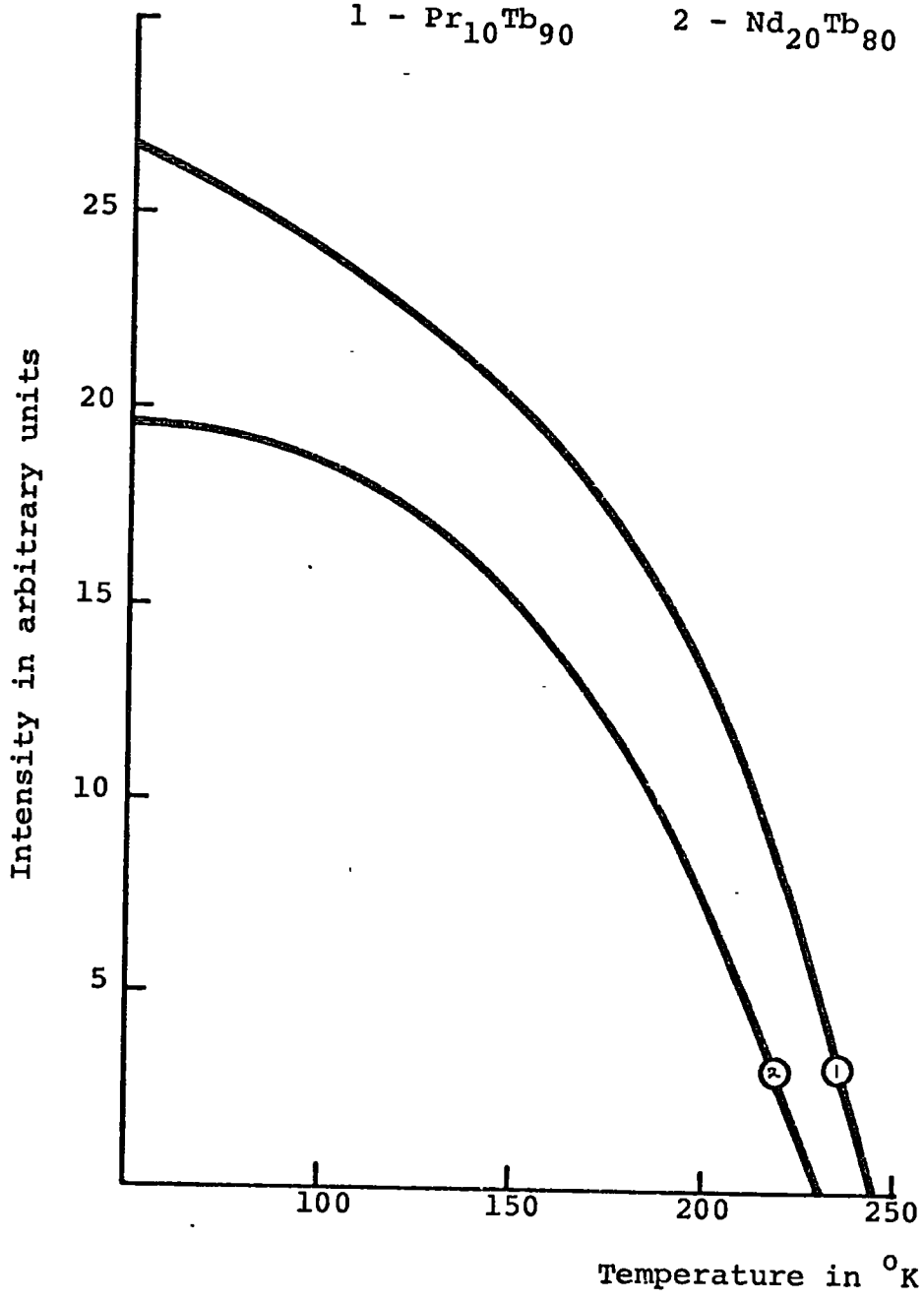

FIG. 4.7

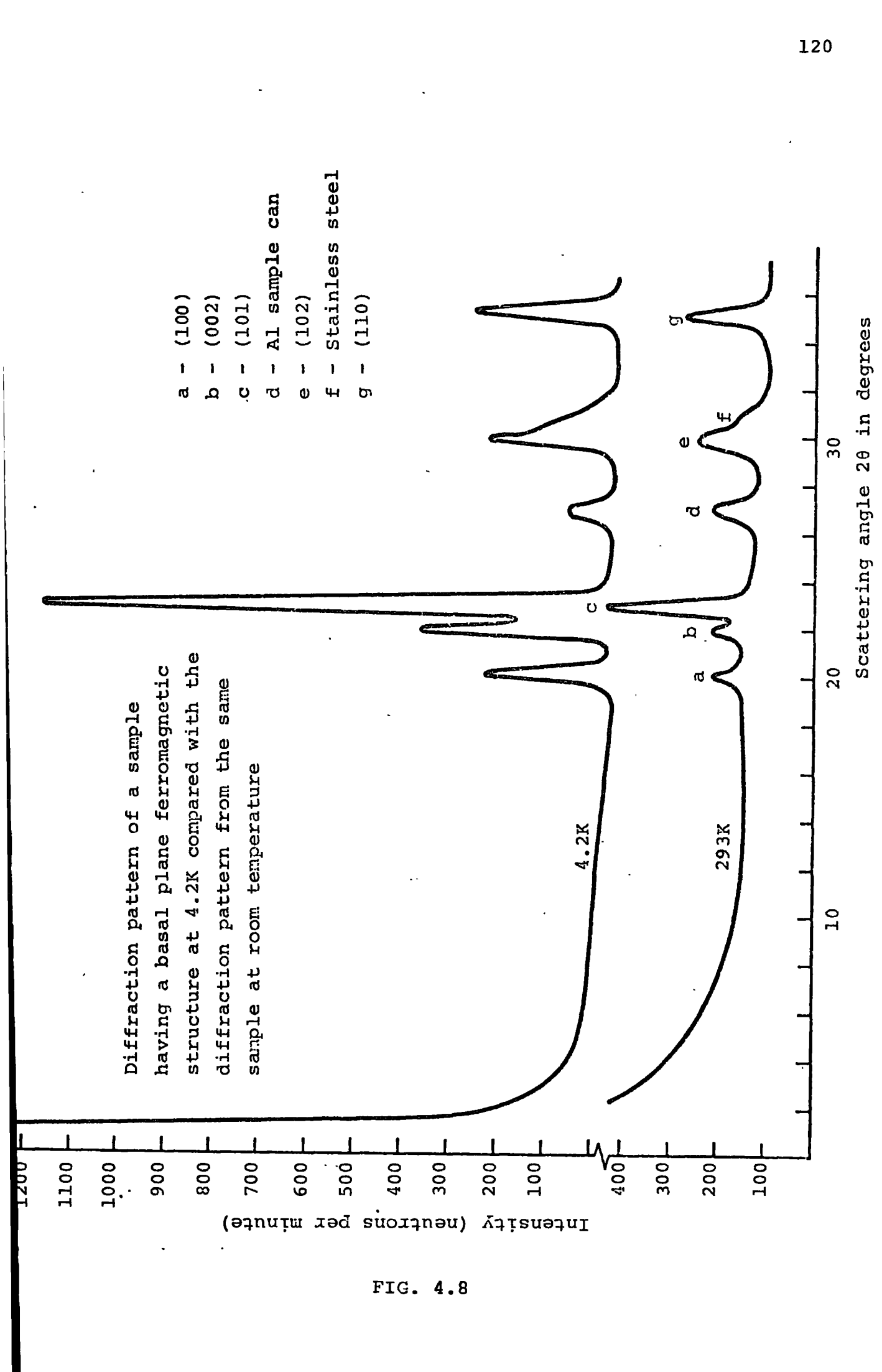
Diffraction pattern of a sample
having a basal plane ferromagnetic
structure at 4.2K compared with the
diffraction pattern from the same
sample at room temperature
a - (100)
b - (002)
c - (101)
d - Al sample can
e - (102)
f - Stainless steel
g - (110)
4.2K
293K
Intensity (neutrons per minute)
Scattering angle 2θ in degrees

FIG. 4.8

ferromagnetic state the incoherent background is lower in accordance with eqn. 3.13.

4.6 EVALUATION OF ORDERED MOMENT AT 4.2K

The magnetic intensity for a general magnetic structure is given by eqn. A1.1. The magnetic contribution to the observed diffraction pattern at 4.2K may be separated from the nuclear contribution by subtracting the paramagnetic intensity from the intensity at 4.2K in accordance with eqn. 3.19.

The integrated intensity of an (hkℓ) peak is determined by counting the number of squares included under the curve after a suitable background level has been established. The units of integrated intensity are count.deg. Since the scans were done at different temperatures account must be taken of the variation in integrated intensity with temperature via the Debye-Waller temperature factor (see Section 3.2). For low scattering angles and low temperatures, the temperature factor may be ignored and only the room temperature integrated intensities corrected before subtraction. The saturation moment is then obtained by comparing the derived magnetic intensity with that calculated theoretically for the appropriate magnetic structure. The theoretical magnetic intensities for a basal plane ferromagnet, a c-axis ferromagnet and a ferromagnetic cone are given by eqns. A1.7, A1.8 and A1,4 and A1.5 respectively.

Consider eqn A1.7

$$I_{hk\ell} = \frac{Am}{L}(\exp -2W)\left[\frac{e^2\gamma}{2mc^2}\right]^2 f^2(\kappa)\left(\frac{gJ}{2}\right)^2 [G_{hk\ell}]^2 \left[1 + \frac{\kappa_z^2}{\kappa^2}\right]$$

The value of A, the scaling factor, should be a constant for every reflection in the diffraction pattern, since it is the ratio of the observed nuclear scattering to the calculated nuclear scattering multiplied by the absorption (see Section 3.4.) For the Tb and Ho alloys A is nearly constant, but in the Dy alloys, there is a marked discrepancy between the values of A calculated for each peak. The results can be ascribed to preferred orientation (see Section 3.4). The existence of preferred orientation and the consequent variation in A, does not affect the calculation of the ordered moment. Assuming the preferred orientation does not change between room temperature and 4.2K, the value of A calculated at room temperature for a specific reflection is appropriate in the calculation of the magnetic intensity of that reflection at 4.2K. Preferred orientation effects are thus automatically accounted for.

The scattering length of the alloys $\bar{b}$ which appears in the calculation of A is derived from the formula

$$\bar{b} = x\bar{b}_1 + (1 - x)\,\bar{b}_2$$

where $\bar{b}_1$ and $\bar{b}_2$ are the scattering lengths of the constituents of the alloys and x is the fraction of constituent with scattering length $\bar{b}_1$, present. The

values of $\bar{b}$ for the rare earths were obtained from Bacon (1962). Evaluation of the other quantities, L, m, $|G_{hk\ell}|^2$, (exp-2W) has been discussed elsewhere, (Sections 3.1, 3.2 and 3.3 respectively.)

The same values of these quantities were used in the evaluation of the magnetic intensity from eqn. A1.7, as were used in the evaluation of A, except that for non-commensurate magnetic structures $|G_{hk\ell}|^2$ has to be re-evaluated. The magnetic form factor for the alloy was derived from a similar formula to that used to derive the alloy scattering length,

$$f^2(\kappa) = xf_1^2(\kappa) + (1 - x) f_2^2(\kappa)$$

where $f_1(\kappa)$ and $f_2(\kappa)$ are the magnetic form factors of each constituent of the alloy and x is the fraction of the constituent with form factor f_1. The evaluation of the form factor for each rare earth is discussed in Section 3.5.

The scattering vector κ, and its component in the c-direction κ_z, are shown in Fig A1.1. In the h.c.p. structure they take the values

$$\kappa_z^2 = \frac{\ell^2}{c^2}$$

$$\kappa^2 = \frac{4}{3a^2}(h^2 + hk + k^2) + \frac{\ell^2}{c^2}$$

and in the orthorhombic structure

$$\kappa^2 = \frac{h^2}{a^2} + \frac{k^2}{b^2} + \frac{\ell^2}{c^2}$$

and κ_z is the same as in the hexagonal structure, a,

b and c are the dimensions of the magnetic cell and (hkℓ) are the Miller indices of the reflection.

For a ferromagnetic structure which is commensurate with the chemical lattice, the value of the magnetic structure factor is identical with the nuclear structure factor. For a non-commensurate structure the simple geometric structure factor is modified to include the effect of the modulation of the spins in either direction or magnitude. The three modulated structures identified as the magnetic structures of the alloys, in particular crystallographic phases and temperature regions, are the ferromagnetic cone structure, the uniform basal plane spiral and the c-axis modulated basal plane ferromagnet. The ferromagnetic cone structure may be visualised as two interpenetrating magnetic structures, one along the c-axis commensurate with the lattice and hence with a magnetic structure factor identical to the nuclear structure factor, and the other a uniform basal plane spiral (See Fig. 1.5).

To assign moments to the alloys, then, it is necessary to evaluate the magnetic structure factors of two non-collinear spin structures, the uniform basal plane spiral A1.2 and the c-axis modulated basal plane ferromagnet A1.3. The structure factors are evaluated in Appendix 2 using the turn angles observed for that structure.

Using the values of the various parameters

calculated on the basis of the discussion in the previous sections, the theoretical diffraction pattern at 4.2K for the basal plane ferromagnet Pr_{10} Tb_{90} is shown in Fig. 4.9 plotted on the same scale as the observed diffraction pattern.

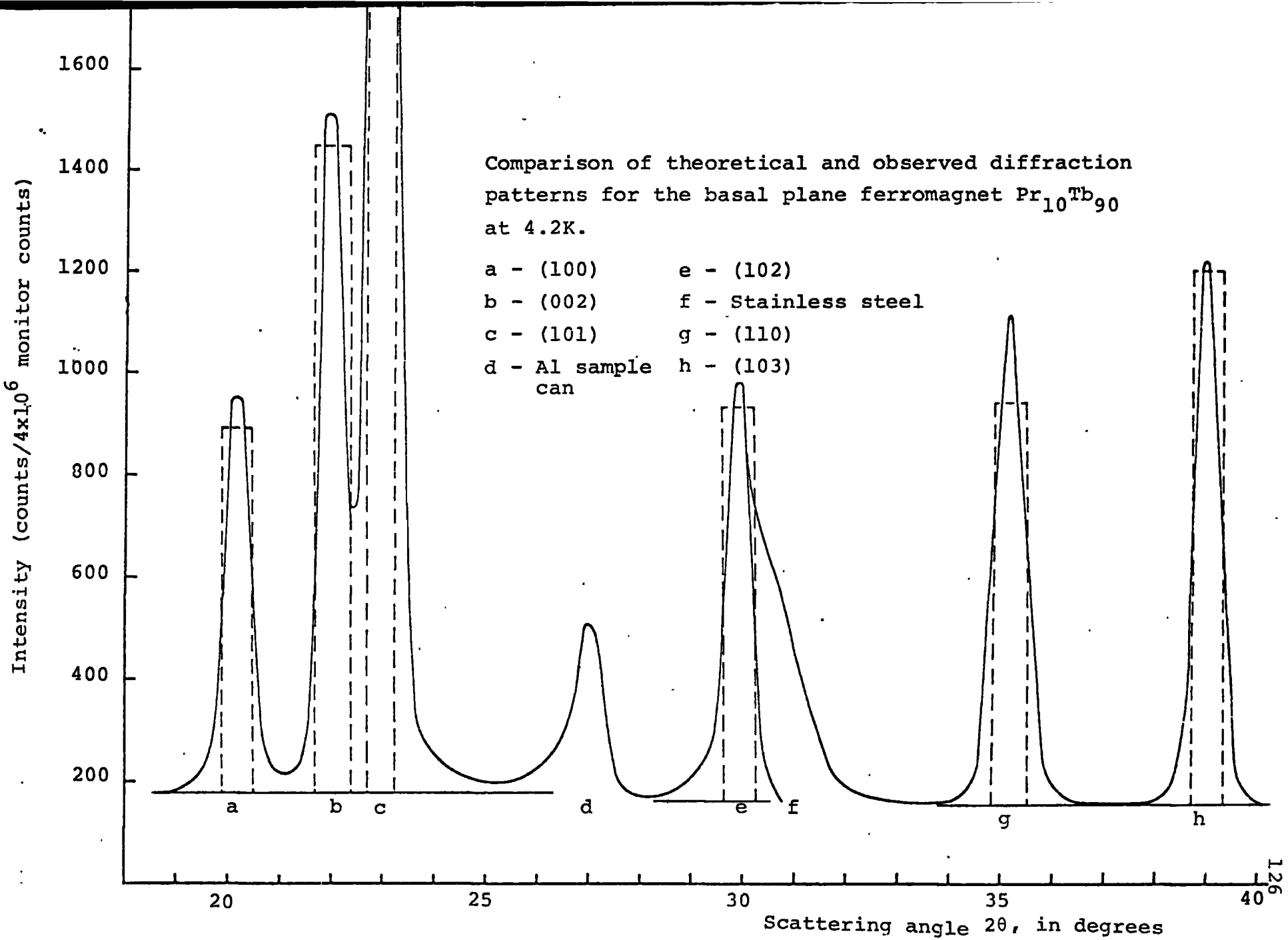
Comparison of theoretical and observed diffraction patterns for the basal plane ferromagnet $Pr_{10}Tb_{90}$ at 4.2K.
a - (100)
b - (002)
c - (101)
d - Al sample can
e - (102)
f - Stainless steel
g - (110)
h - (103)
Intensity (counts/4x10^6 monitor counts)
1600
1400
1200
1000
800
600
400
200
a
b
c
d
e
f
g
h
20
25
30
35
40
Scattering angle 2θ, in degrees

FIG. 4.9

CHAPTER 5

EXPERIMENTAL RESULTS

5.1 STRUCTURAL DATA

The 'a' and 'c' lattice parameters of the light-heavy rare earth alloys selected on the basis of equation 1.1 to be representative of a particular crystallographic phase, are given in Tables 5.1a and 5.1b along with the derived axial ratio c/a. Both the hcp and dhcp structures give sharp X-ray diffraction peaks, whereas the Sm phase gave slightly broader peaks. All three phases were readily indexed and lattice parameters assigned with an error of $\pm$ 0.005A^{o}. Fig. 5.1 shows the a, c, and c/a values of the Pr-Tb and Nd-Tb alloy systems plotted as a function of composition. The data of Speight et al (1968) for Pr-Tb is shown for comparison. The solid line shows the expected variation of each parameter with composition if it obeyed Vegard's law.

For all the alloy systems studied the variation of a, c and c/a with composition was similar to that shown for Pr-Tb and Nd-Tb. In the hcp phase (heavy rare earth rich) the deviation of the lattice parameter from Vegard's law is slight,with the value of the c parameter always closer to the expected value than the a parameter. The deviation increases with increasing light rare earth content across the hcp phase. There appears to be no correlation between the direction of deviation, either positive or negative, and any other parameter of the alloy system, except that the deviations occur in the

TABLE 5.1a

STRUCTURAL DATA FOR PRASEODYMIUM-HEAVY RARE EARTH ALLOYS

Alloy Composition	Crystal Structure	a(A^o) ± 0.005	c(A^o) ± 0.005	† c/a ± 0.01	Z*
Pr_{02} Tb_{98}	hcp	3.613	5.712	1.581	64.9
Pr_{04} Tb_{96}	hcp	3.608	5.707	1.582	64.8
Pr_{10} Tb_{90}	hcp	3.612	5.745	1.591	64.4
Pr_{30} Tb_{70}	Sm type	3.623	26.206	1.600	63.2
Pr_{45} Tb_{55}	Sm type	3.624	26.150	1.604	62.3
Pr_{70} Tb_{30}	dhcp	3.645	11.698	1.605	60.8
Pr_{30} Dy_{70}	hcp	3.625	5.737	1.583	63.9
Pr_{50} Dy_{50}	Sm type	3.622	26.123	1.603	62.5
Pr_{90} Dy_{10}	dhcp	3.663	11.801	1.611	59.7
Pr_{20} Ho_{80}	hcp	3.608	5.693	1.579	65.4
Pr_{60} Ho_{40}	Sm type	3.661	26.303	1.597	62.6
Pr_{90} Ho_{10}	dhcp	3.665	11.806	1.611	59.8

† The axial ratios of the Sm and dhcp structures are shown reduced.

TABLE 5.1b

STRUCTURAL DATA FOR NEODYMIUM-HEAVY RARE EARTH ALLOYS

Alloy Composition	Crystal Structure	$a(A^{o}) \pm 0.005$	$c(A^{o}) \pm 0.005$	† $c/a \pm 0.01$	Z*
Nd_{02} Tb_{98}	hcp	3.607	5.707	1.582	64.9
Nd_{05} Tb_{95}	hcp	3.606	5.706	1.582	64.8
Nd_{10} Tb_{90}	hcp	3.608	5.712	1.583	64.5
Nd_{20} Tb_{80}	hcp	3.621	5.734	1.584	64.0
Nd_{60} Tb_{40}	Sm type	3.626	26.308	1.612	62.0
Nd_{90} Tb_{10}	dhcp	3.653	11.779	1.612	60.5
Nd_{30} Dy_{70}	hcp	3.598	5.744	1.596	64.2
Nd_{50} Dy_{50}	Sm type	3.600	26.010	1.605	63.0
Nd_{90} Dy_{10}	dhcp	3.638	11.750	1.615	60.6
Nd_{20} Ho_{80}	hcp	3.602	5.683	1.578	65.6
Nd_{70} Ho_{30}	Sm type	3.647	26.413	1.609	62.1
Nd_{90} Ho_{10}	dhcp	3.648	11.774	1.614	60.7

† The axial ratios of the Sm and dhcp structures are shown reduced.

Lattice parameters as a function of composition for Pr-Tb and Nd-Tb alloy systems.

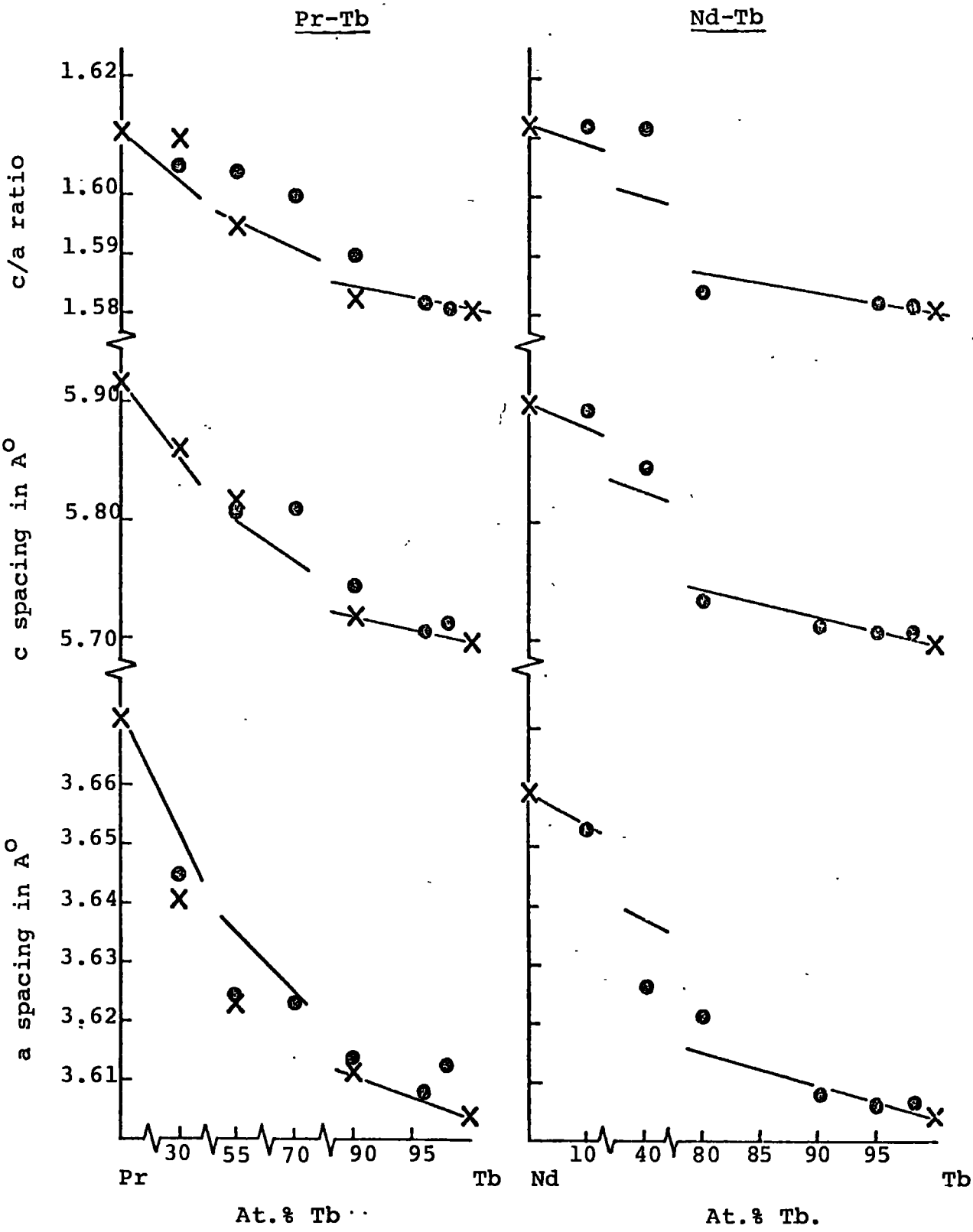

FIG. 5.1

same sense so that the variation of the axial ratio c/a is smooth across the hcp phase. The deviations of the 'a' and 'c' lattice parameters from Vegard's law in the Sm phase are much more pronounced than in the hcp phase. In the Tb-light rare earth alloys and the Dy-light rare earth alloys the deviations of the basal plane lattice parameters from Vegard's law are both negative and the deviations of the axial lattice parameter are both positive, whereas for the Ho-light rare earth alloys both lattice parameters show positive deviations from Vegard's law. In the dhcp phase the deviations of both lattice parameters from ideality are once again small. Fig. 5.2 shows the variation of the axial ratio as a function of the effective atomic number defined by eqn. 1.1. A similar variation for other rare earth alloy systems has been pointed out by Taylor and Darby (1972). The axial ratio of all the alloys and the light rare earths in the dhcp phase is almost constant, although there may be a slight upward trend. In the Sm phase the c/a ratio falls rapidly with increasing atomic number. This is attributable to the large changes observed in both 'a' and 'c' across the Sm phase. The Sm phase exists between effective atomic numbers $Z^* = 61.5$ to $Z^* = 63.5$ (slightly to the right of pure Sm in the figure) although the phase boundaries are not clear. The axial ratio of the structure is centred about 1.602 which is slightly lower than the axial ratio of pure Sm. The variation of c/a with increasing atomic number is more gradual in the

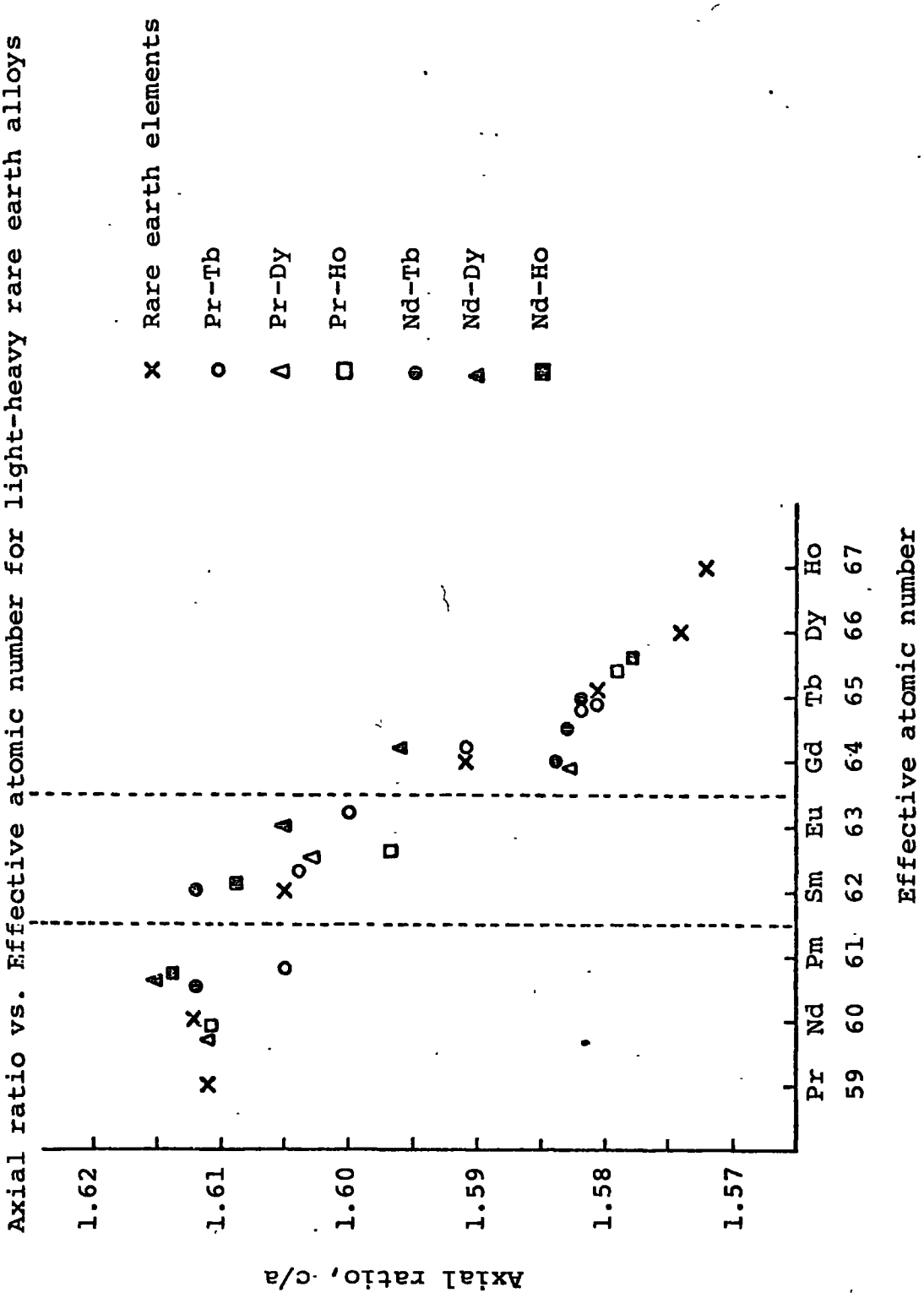
Axial ratio vs. Effective atomic number for light-heavy rare earth alloys
Rare earth elements
Pr-Tb
Pr-Dy
Pr-Ho
Nd-Tb
Nd-Dy
Nd-Ho
Axial ratio, c/a
1.62
1.61
1.60
1.59
1.58
1.57
Pr Nd Pm Sm Eu Gd Tb Dy Ho
59 60 61 62 63 64 65 66 67
Effective atomic number

FIG. 5.2

hcp phase becoming essentially constant for Z* = 66 (Dy) and Z* = 67 (Ho).

The room temperature neutron diffraction patterns were used to assign a space group to the crystallographic structures of the alloys. For the hcp phase the space group was determined to be $P\bar{6}m2$, for the Sm phase $R\bar{3}m$ and the dhcp phase $P\bar{6}mmc$. All the diffraction patterns fitted well except for the hcp dysprosium alloys, Pr_{30} Dy_{70} and Nd_{30} Dy_{70}. A back reflection Laue X-ray investigation clearly showed that there was preferred orientation in the platelets of the Dy alloys. The small differences between the observed and calculated intensities for the nuclear diffraction peaks in the Tb-light rare earth and the Ho-light rare earth alloys and the large discrepancies for the Dy-light rare earth alloy systems were thus ascribed to preferred orientation, since the absorption correction factor is constant with scattering angle for the alloys examined in this investigation and contributes only to the scaling factor,A, (see Section 3.4). The difference in magnitude of the effect between the alloy systems was ascribed to the sample shape. The neutron diffraction samples of the Tb and Ho based alloys were in the form of five or more as-cast buttons piled one on top of the other in the sample can. The random way in which they were stacked served to reduce the preferred orientation effects, whereas the Dy based alloys were in the form of platelets and there was no such randomising. The presence of preferred orientation

in the alloys does not affect the calculation of the saturation moment, as it is calculated from a ratio between the 4.2K and room temperature scattering (see Section 4.6).

The room temperature space groups were also used in fitting the data at low temperature, except for the hcp Dy based alloys where the orthorhombic distortion space group Amm2 gave a better fit. Darnell and Moore (1963) have observed a similar spontaneous lattice distortion to an orthorhombic phase in Dy below the Curie temperature (see Section 1.3).

The phase boundaries between the three crystallographic phases of the light-heavy rare earth alloy systems are not distinct and there appears to be no critical value of either lattice parameter for which there is an abrupt transition. However, the correlation between the axial ratio of an alloy and its effective atomic number serves as a guide.

5.2 MAGNETIC DATA

The low field susceptibility (6.80e) was measured as a function of temperature using the susceptibility bridge described in Section 4.2. Magnetic transition temperatures were assigned and plotted as a function of composition for each alloy system. See Figs. 5.3 to 5.8. The results are given in the following sections presented with reference to the three crystallographic phases of the alloys. The results of the neutron scattering and magnetisation measurements for specific

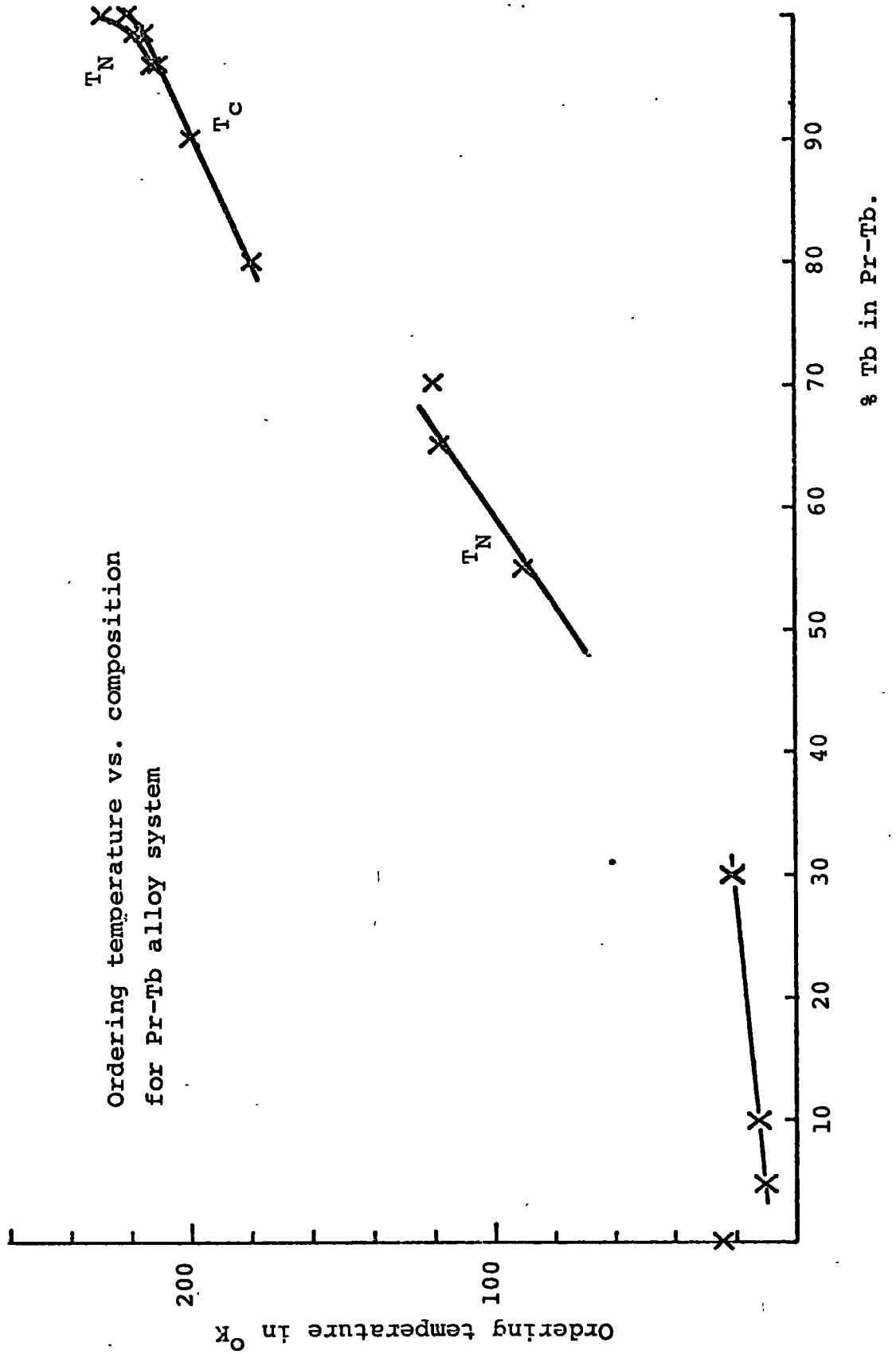
Ordering temperature vs. composition
for Pr-Tb alloy system
Ordering temperature in °K
200
100
10
20
30
40
50
60
70
80
90
% Tb in Pr-Tb.
T_N
T_C
T_N

FIG. 5.3

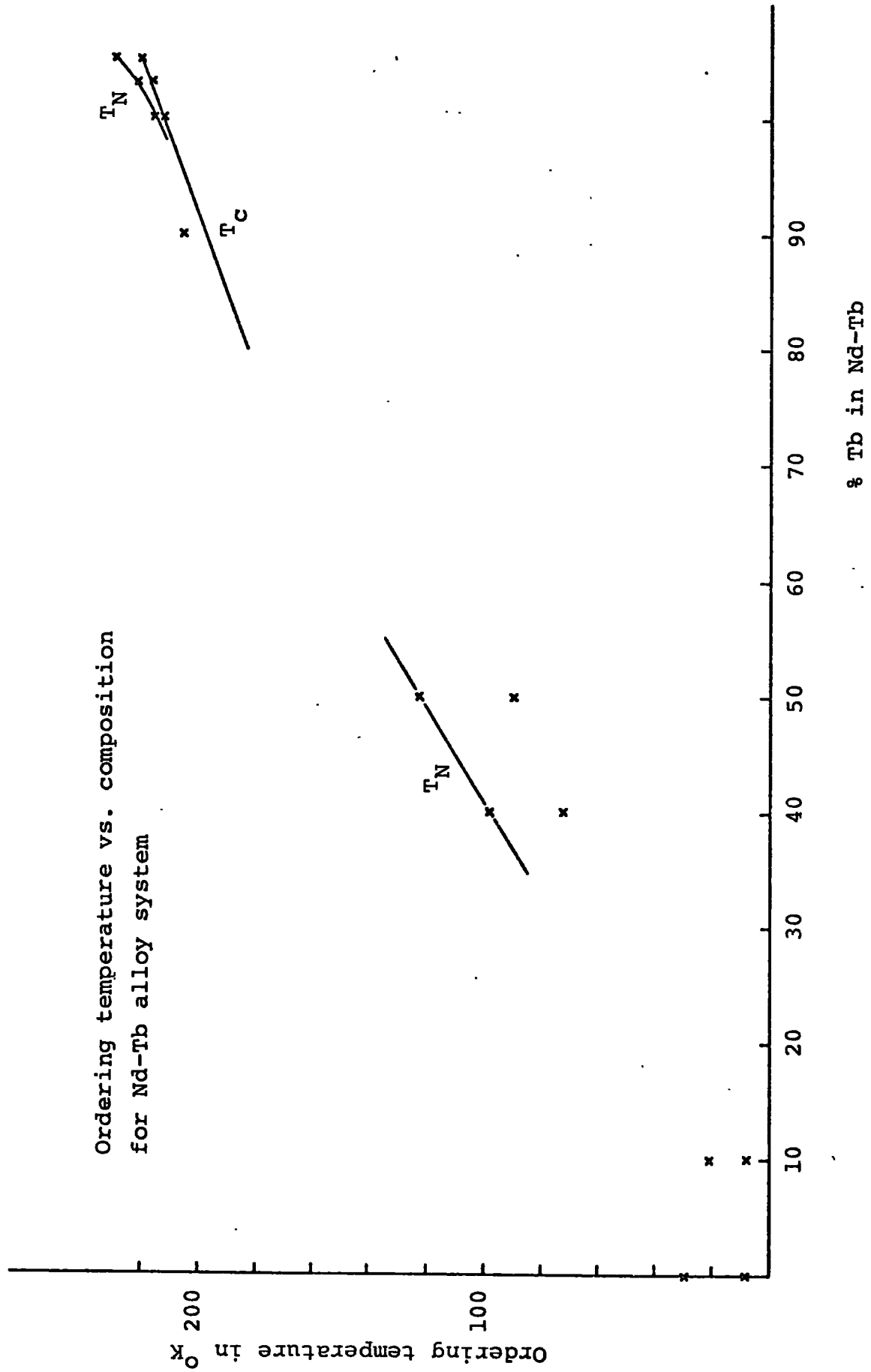
Ordering temperature vs. composition
for Nd-Tb alloy system
Ordering temperature in °K
200
100
10
20
30
40
50
60
70
80
90
% Tb in Nd-Tb
T_N
T_C
T_N

FIG. 5.4

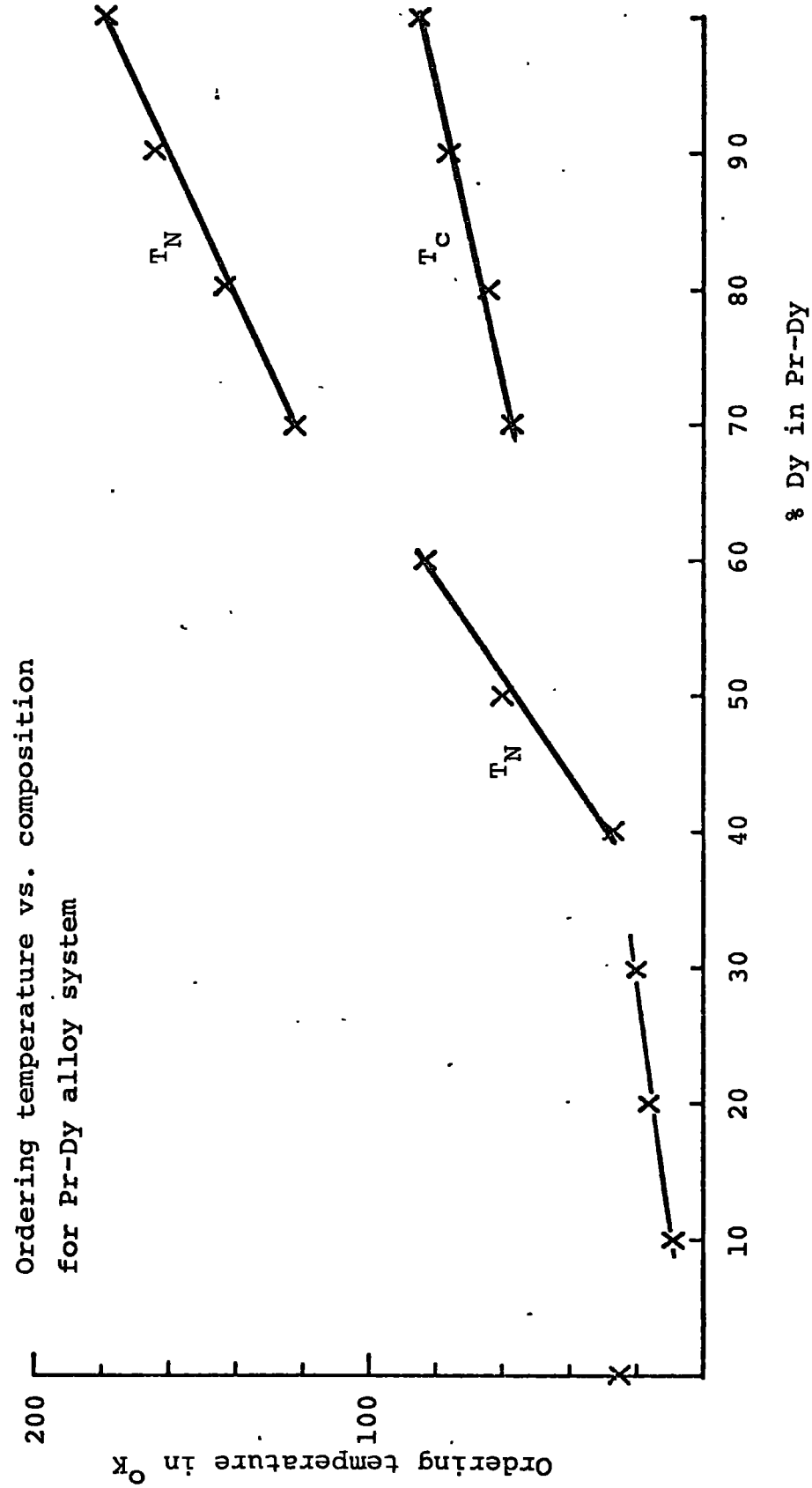
Ordering temperature vs. composition
for Pr-Dy alloy system
Ordering temperature in °K
200
100
10
20
30
40
50
60
70
80
90
% Dy in Pr-Dy
T_N
T_C
T_N

FIG. 5.5

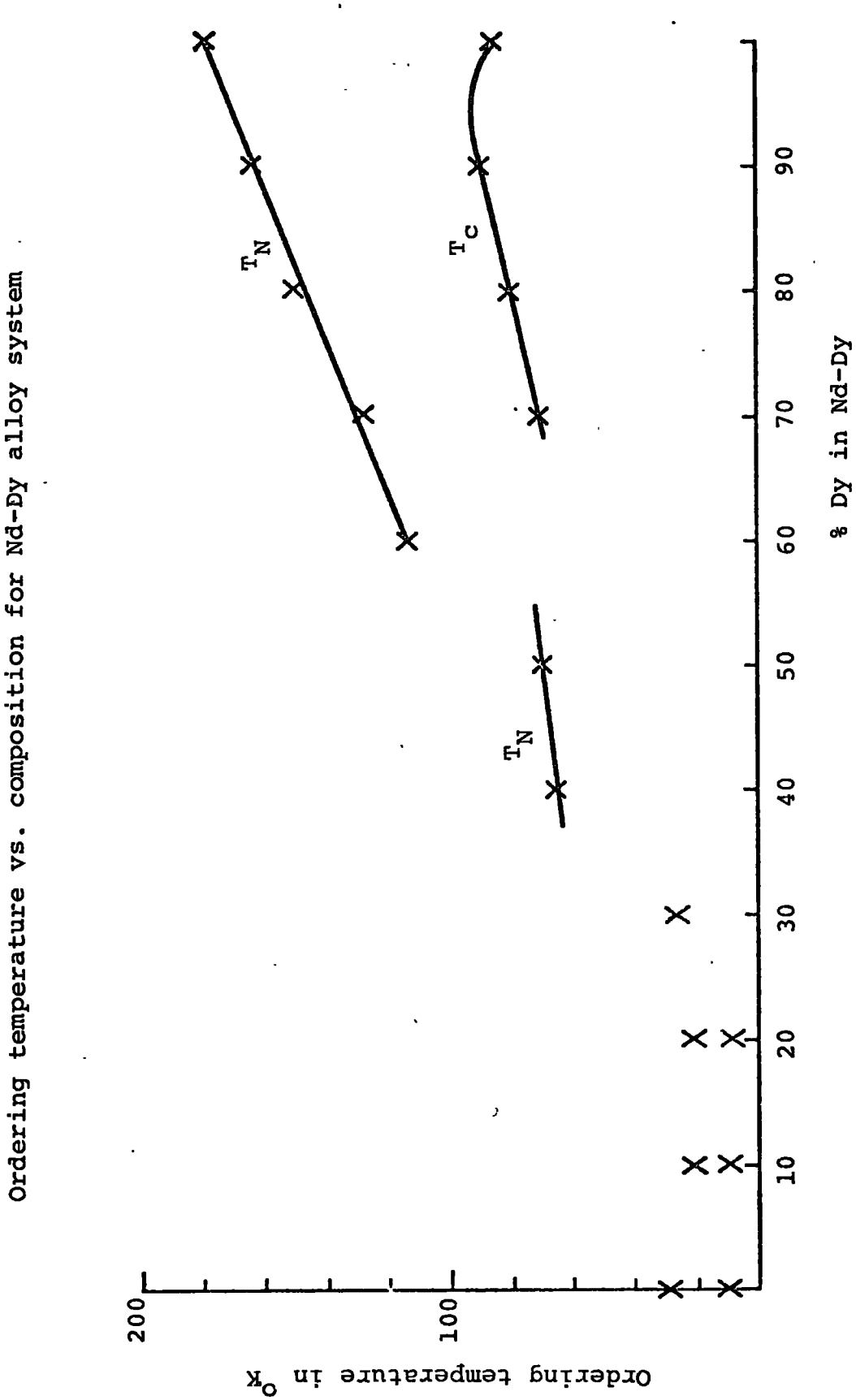
Ordering temperature vs. composition for Nd-Dy alloy system
Ordering temperature in °K
200
100
10
20
30
40
50
60
70
80
90
% Dy in Nd-Dy
T_N
T_C
T_N

FIG. 5.6

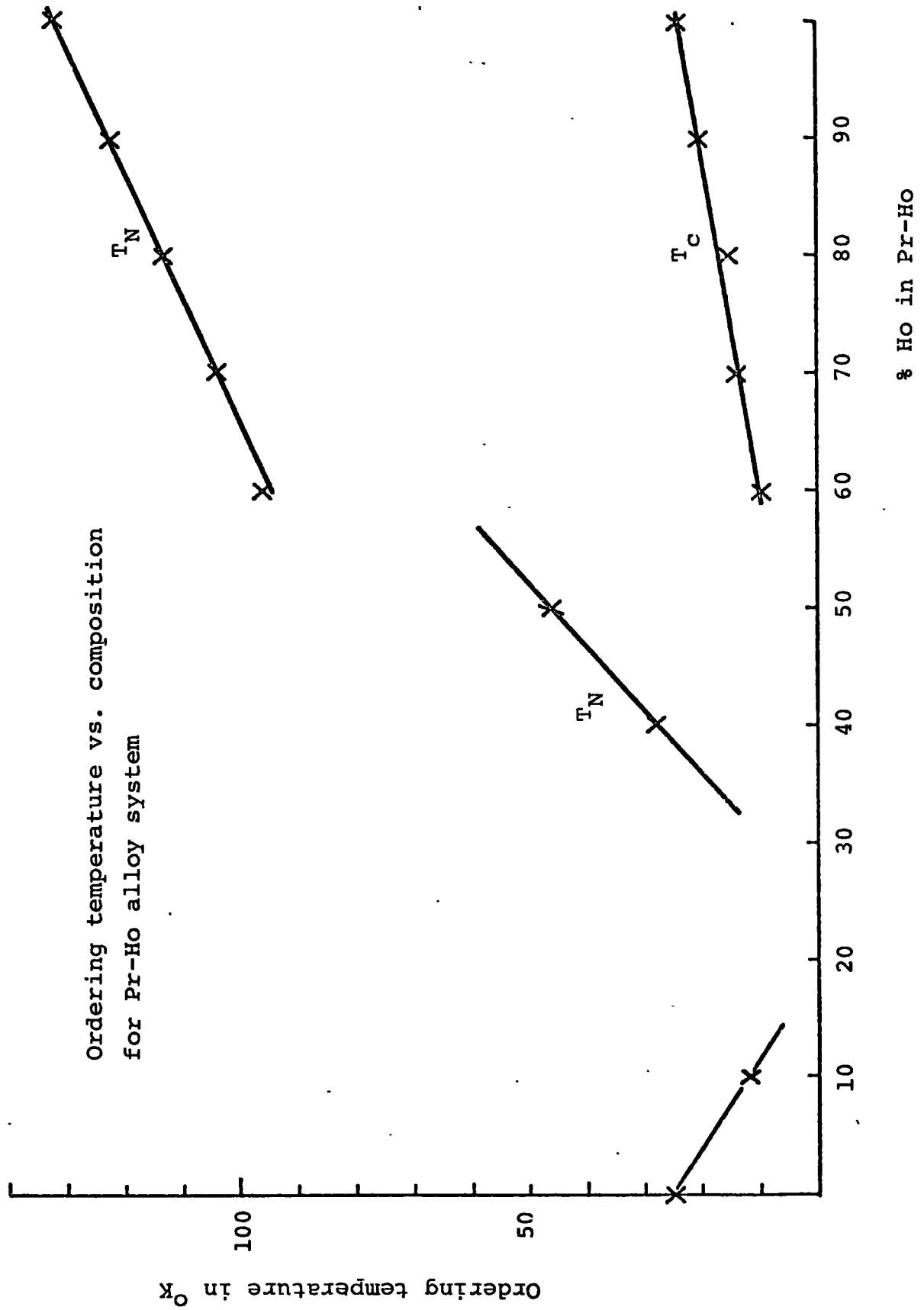
Ordering temperature vs. composition
for Pr-Ho alloy system
Ordering temperature in °K
% Ho in Pr-Ho
T_N
T_C
T_N
100
50
10
20
30
40
50
60
70
80
90

FIG. 5.7

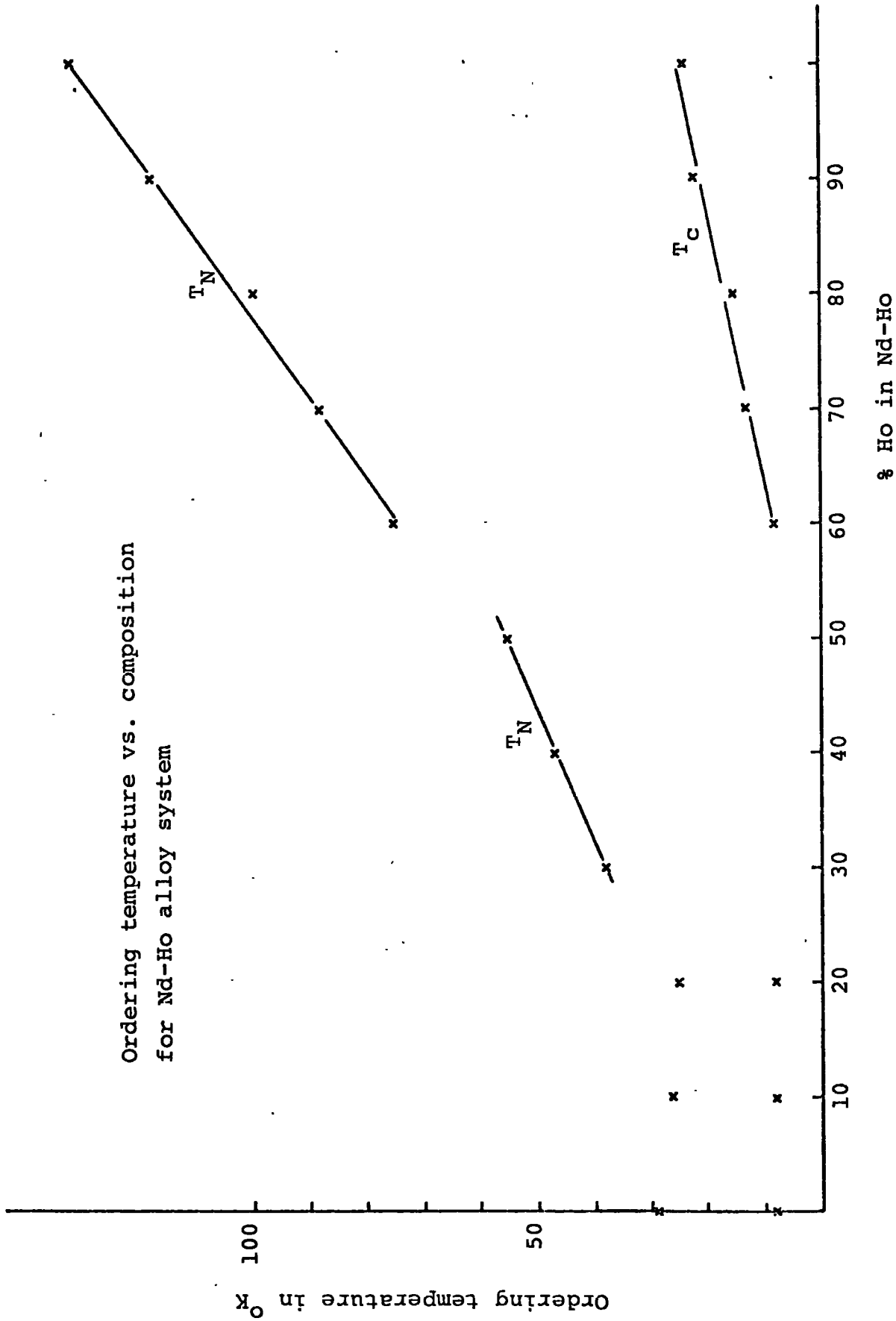
Ordering temperature vs. composition
for Nd-Ho alloy system
Ordering temperature in °K
100
50
T_N
T_N
T_C
10
20
30
40
50
60
70
80
90
% Ho in Nd-Ho

FIG. 5.8

alloys are presented where they occur within these sections.

5.2(i) H.C.P. PHASE

The hcp (heavy rare earth rich) phase is the only one in which there is evidence for two magnetic transitions in each alloy, reminiscent of the magnetic structure of the constituent heavy rare earths.

Figs.5.9a & b show the change in susceptibility as a function of temperature in the region of the transition temperatures for various alloy compositions in the Pr-Tb and Nd-Tb alloy systems, plus the terminal element Tb. The two transitions in Tb are evident. The higher temperature transition has been identified as a Néel temperature and the lower as a Curie point, (see Section 1.3). The addition of the light rare earth element leads to a reduction in the ordering temperature of the host metal Tb. It is clear from these results, Figs. 5.3 and 5.4, that the narrow antiferromagnetic region observed in Tb rapidly disappears on light rare earth addition and for compositions greater than 10% Pr and 20% Nd there is only a single magnetic transition. From the form of the susceptibility data, however, which falls off rapidly with decreasing temperature, it is not possible to determine directly the type of magnetic ordering that occurs at low temperature.

Neutron diffraction measurements were performed as a function of temperature in the ordered state on a single

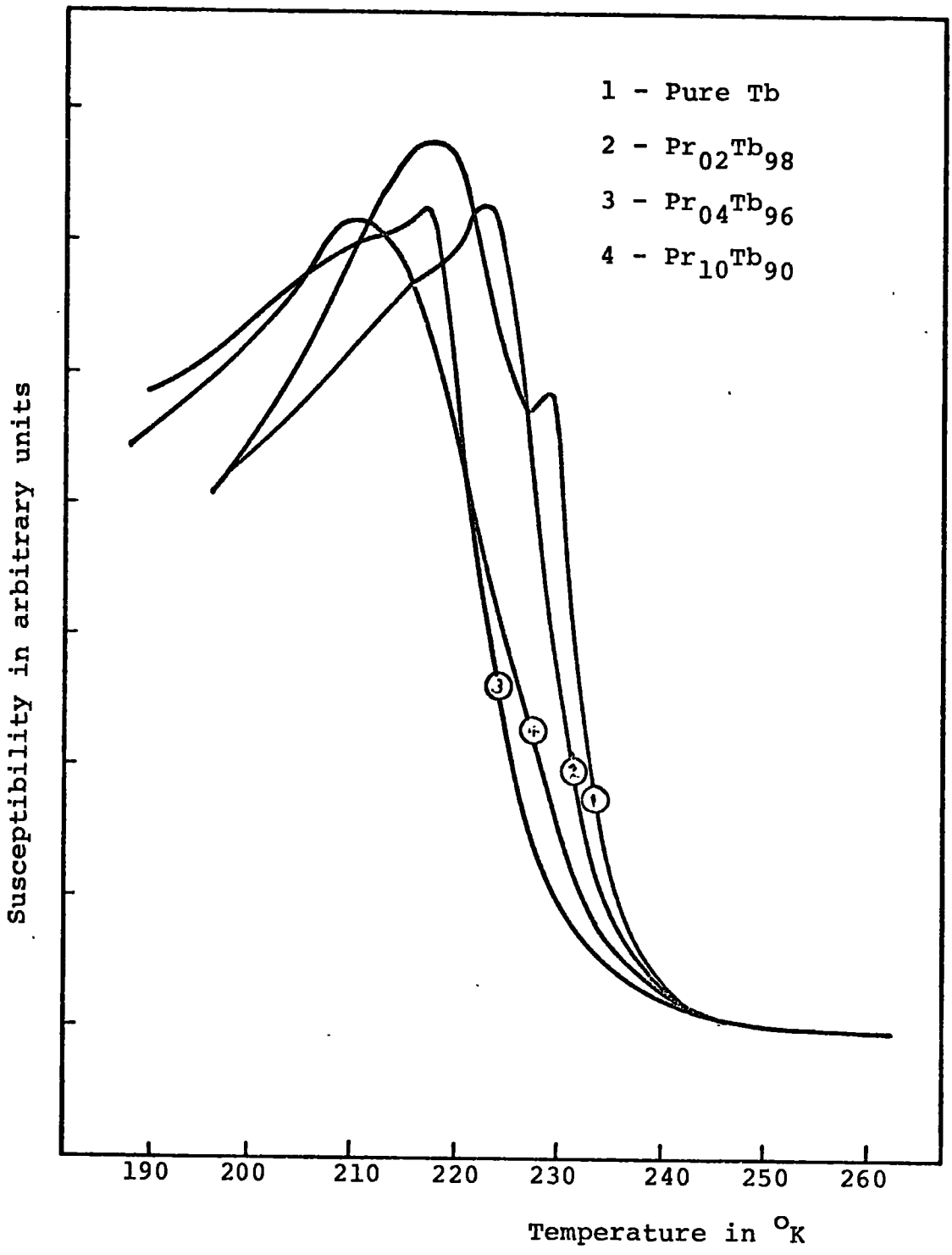

FIG. 5.9a Susceptibility vs. temperature for Tb and some Pr-Tb alloys

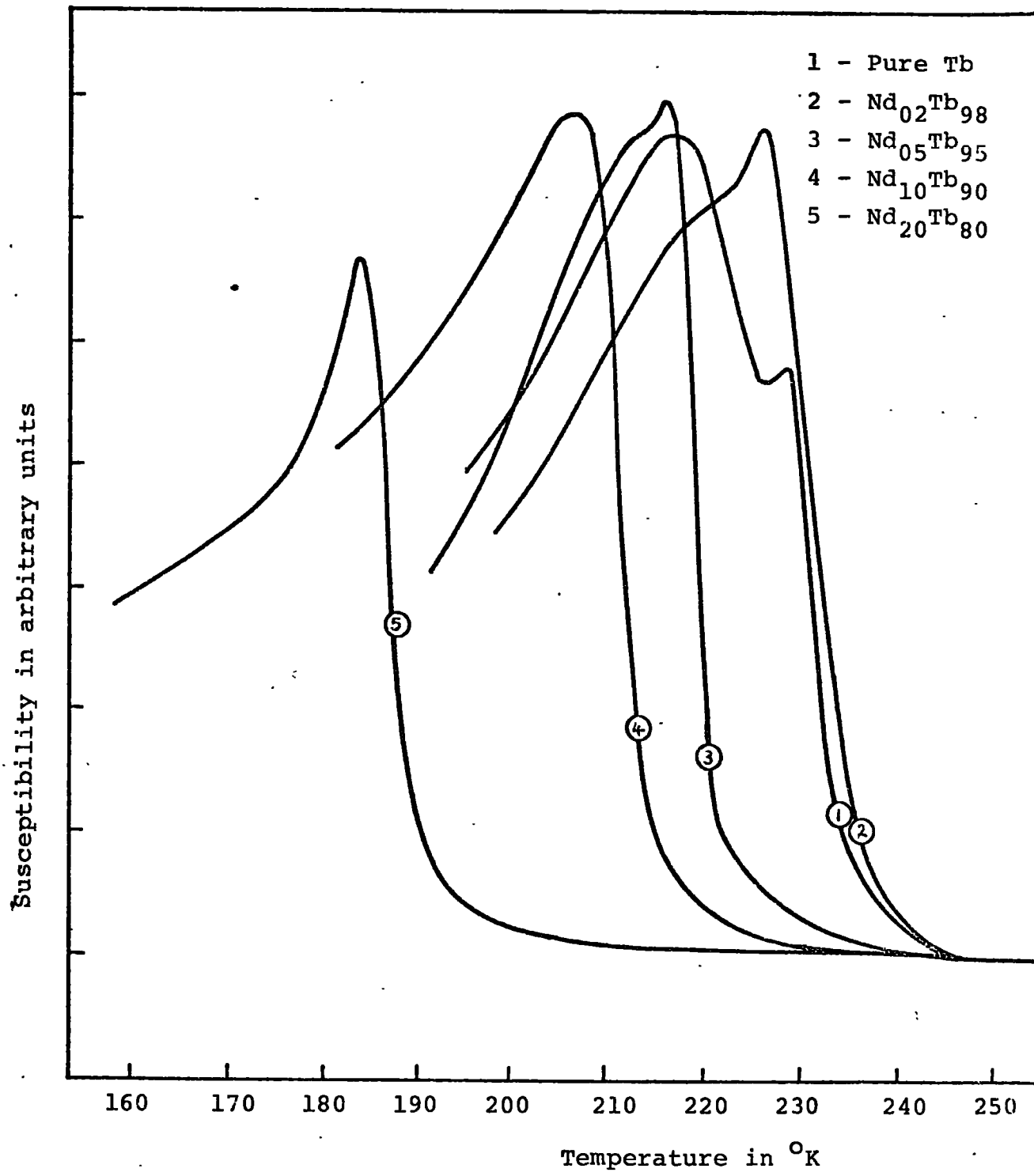

FIG. 5.9b Susceptibility vs. temperature for Tb and some Nd-Tb alloys

representative sample from each alloy system, namely Pr_{10} Tb_{90} and Nd_{20} Tb_{80}. The diffraction patterns of both alloys at all temperatures showed only peaks corresponding in position to the observed high temperature nuclear peaks. No indication of the existence of satellite peaks was found at any temperature. The peak intensity of the nuclear lines increased with decreasing temperature following a Brillouin type curve (see Fig. 4.7). This implies that the alloys transform directly from the paramagnetic state to a ferromagnetic state in which the net moments lie in the basal plane, the antiferromagnetic state being unstable against light rare earth addition.

From an analysis of the intensities of the peaks in the ferromagnetic state at 4.2K (as described in Section 4.6) a magnitude was assigned to the net moments. The values are given in Table 5.2 along with the other magnetic data of the two alloy systems. The calculated moment values are consistent only with an antiparallel alignment of the two moment species in each case. Assuming that the moments on each ion are unchanged from their free ion values,then the calculated moment values are in good agreement with the theoretical values of the saturation moment.

In the Dy alloys, Pr-Dy and Nd-Dy, it was relatively easy to assign the magnetic transition temperatures from the susceptibility data as the magnetic transitions are nearly 100K apart. By comparison with Dy, the

TABLE 5.2

MAGNETIC DATA FOR Pr-Tb AND Nd-Tb ALLOYS IN H.C.P. PHASE

Composition	$T_N \pm 2K$	$T_C \pm 2K$	Ordered Structure at 4.2K	Ordered moment $\pm 0.20\mu_B$
Tb (a)	229	221	Basal plane ferromagnet	$9.00\mu_B$
Pr_{02} Tb_{98}	218	215		
Pr_{04} Tb_{96}	213	211		
Pr_{10} Tb_{90}		200	Net moments ferromagnetically aligned in basal plane	$7.51\mu_B$
Pr_{20} Tb_{80}		180		
Nd_{02} Tb_{98}	222	217		
Nd_{05} Tb_{95}	216	213		
Nd_{10} Tb_{90}		206		
Nd_{20} Tb_{80}		183	Net moments ferromagnetically aligned in basal plane	$6.75\mu_B$

(a) KOEHLER, W.C., et al, 1963, J.A.P. 34 1335-1336

higher temperature transition was identified as a Néel temperature and the lower one as a Curie point. In general, both the Néel and Curie temperatures of the alloys decreased from their values in pure Dy with increasing light rare earth content (see Figs. 5.5 and 5.6) though the Néel temperature falls more rapidly than the Curie temperature for both alloy systems. The behaviour of the Curie point with composition for the Nd-Dy alloys is different from that of Pr-Dy alloys in that it does not fall initially, but rises to a maximum at about 90% Dy and then falls linearly with increasing light rare earth content. The Curie temperature of both alloy systems is still finite at the hcp-Sm phase boundary. From the form of the susceptibility curves no inference could be made about the type of ordering below the Curie point.

An alloy from each system, $Pr_{30}Dy_{70}$ and $Nd_{30}Dy_{70}$ respectively, was selected as representative of the alloys in the hcp phase and neutron diffraction experiments were performed on it as a function of temperature, from just above the Néel temperature to 4.2K. The existence of a helical spin structure, similar to that of pure Dy, was confirmed in each case and the initial and final turn angles of the structure evaluated (see Table 5.3). The measured initial and final turn angles of the magnetic structures of both alloys lie between the corresponding values for elemental Dy. The addition of Nd appears to

TABLE 5.3

MAGNETIC DATA FOR Pr-Dy AND Nd-Dy ALLOYS IN H.C.P. PHASE.

Composition	$T_N \pm 2K$	Spin Structure	$T_c \pm 2K$	Ordered Structure at 4.2K	Ordered moment $\pm 0.20\mu_B$
Dy (b)	178	Helix in basal plane $\omega_i = 43.0^\circ$, $\omega_f = 26.5^\circ$	85	Basal plane ferromagnet.	$10.00\mu_B$
Pr_{10} Dy_{90}	164		76		
Pr_{20} Dy_{80}	143		64		
Pr_{30} Dy_{70}	122	Helix in basal plane $\omega_i = 35.0^\circ$, $\omega_f = 27.7^\circ$	58	Net moments ferromagnetically aligned in basal plane	$5.62\mu_B$
Nd_{10} Dy_{90}	164		90		
Nd_{20} Dy_{80}	150		80		
Nd_{30} Dy_{70}	127	Helix in basal plane $\omega_i = \omega_f = 30.8^\circ$	71	Net moments ferromagnetically aligned in basal plane	$5.44\mu_B$

(b) WILKINSON, M.K., et al 1961, J.A.P. 32S 485-495

remove any temperature dependence in the turn angle altogether,whilst the addition of Pr restricts it.

The magnetisation of these two alloy samples was measured for several temperatures in the antiferromagnetic phase to determine the critical field at that temperature (see Section 4.2). The critical fields for $Pr_{30}Dy_{70}$, $Nd_{30}Dy_{70}$, $Pr_{10}Dy_{90}$, $Nd_{10}Dy_{90}$, and elemental Dy are shown plotted as a function of temperature in Fig. 5.10.a & b. The solid line is the data of Behrendt et al (1958) for single crystal Dy and it can be seen that the experimental data for polycrystalline Dy fits well to this curve. The data of Chatterjee and Taylor (1972) on $Nd_{10}Dy_{90}$ are included for comparison with the data for $Pr_{10}Dy_{90}$. The critical field rises rapidly with increasing temperature for Dy and the 90% Dy alloys. Initially the critical field also rises rapidly from the Curie point in the 70% Dy alloys, but then appears to saturate and become constant over the remaining part of the antiferromagnetic region. The values of the critical field and the interlayer turn angle at a given temperature were used to give an estimate of the exchange parameters, I(1) and I(2) at that temperature, by substituting the values in eqns. 2.26 and 2.30. The data used in the evaluation of the exchange parameters is given in Table 5.4 and the values obtained are plotted as a function of temperature in Figs. 5.11. Initially,the exchange parameters increase with increasing temperature and then saturate for higher temperatures,showing the same

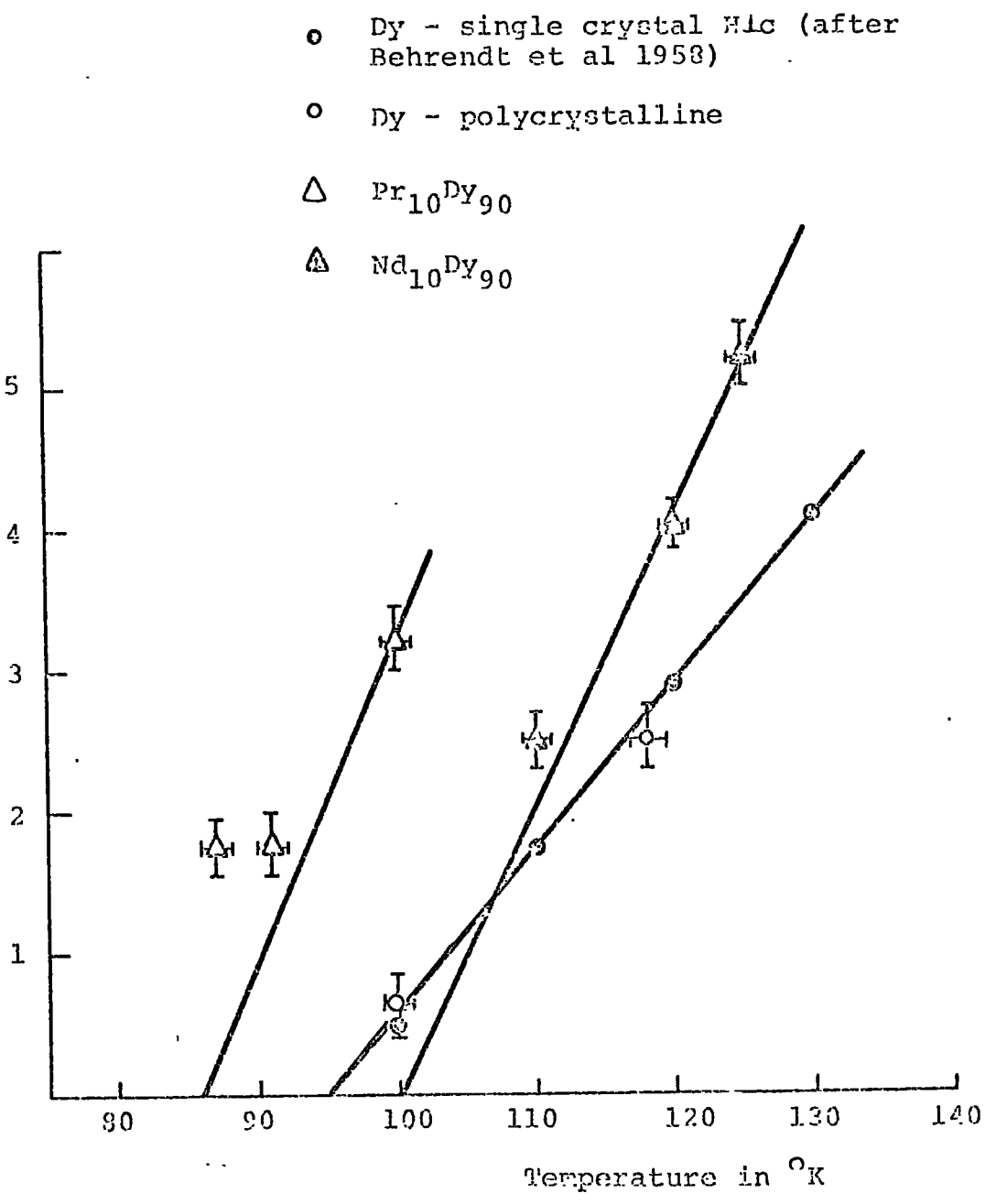
Dy - single crystal H⊥c (after Behrendt et al 1958)
Dy - polycrystalline
$Pr_{10}Dy_{90}$
$Nd_{10}Dy_{90}$
5
4
3
2
1
80
90
100
110
120
130
140
Temperature in °K

FIG. 5.10a

Critical field vs. temperature for $Pr_{30}Dy_{70}$ and $Nd_{30}Dy_{70}$.

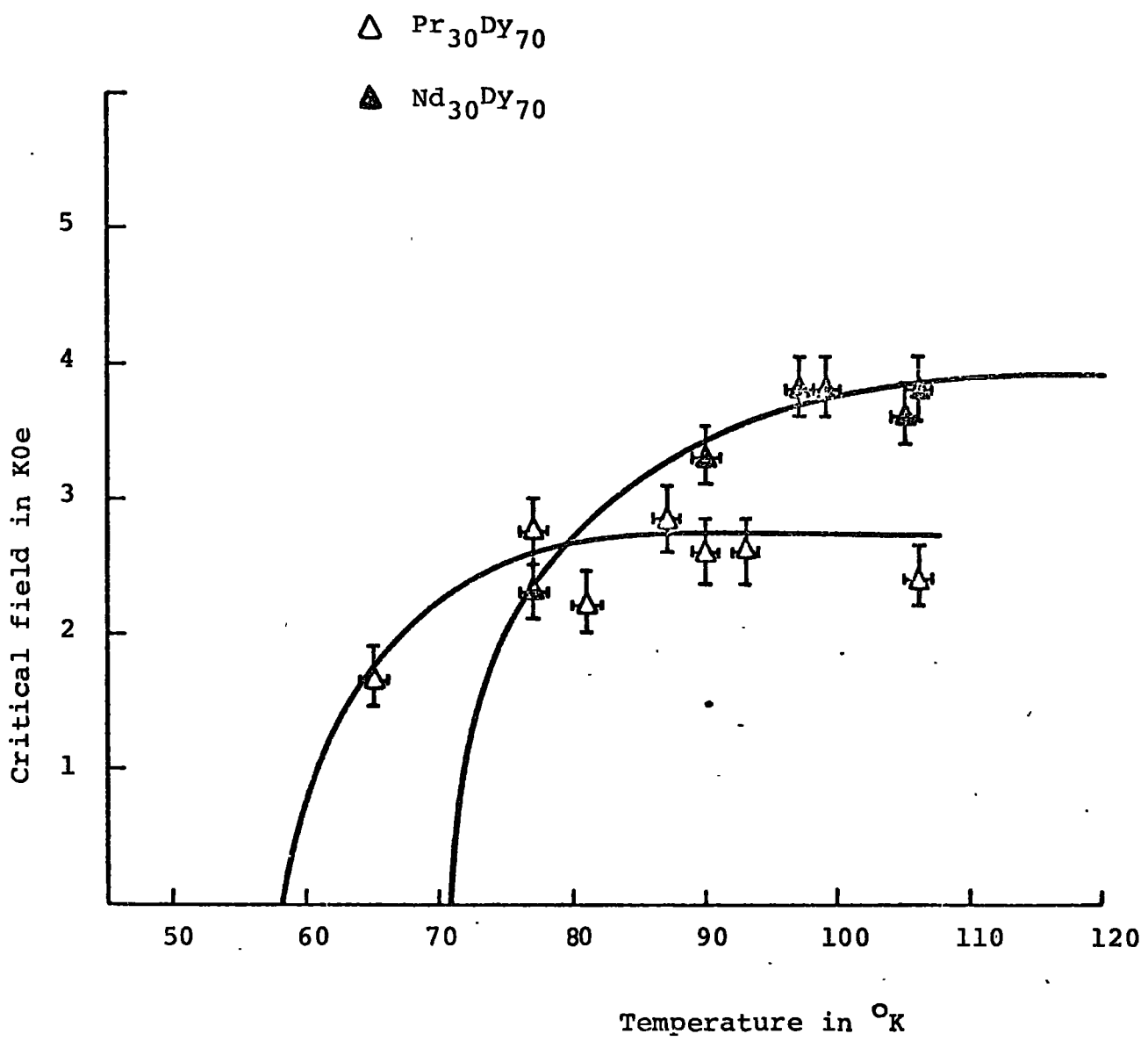

FIG. 5.10b

TABLE 5.4

DATA USED IN THE ESTIMATION OF THE EXCHANGE PARAMETERS I(1) AND I(2) FOR $Pr_{30}Dy_{70}$ and $Nd_{30}Dy_{70}$.

$Pr_{30}Dy_{70}$ T in K ± 2K	H_c in k Oe ± 0.25k Oe	ω in degrees ± 1°	-I(2)	I(1), x 10^{23} (gauss)^2/erg
60	0.65	27.7	3.4 ± 1.8	12.0 ± 6.5
80	2.70	32.5	7.6 ± 1.0	25.6 ± 3.8
100	2.80	35.0	6.0 ± 1.0	19.6 ± 3.7
120	2.80	35.0	6.0 ± 1.0	19.6 ± 3.7

$Nd_{30}Dy_{70}$ T in K ± 2K	H_c in k Oe ± 0.25k Oe	ω in degrees ± 1°	-I(2)	I(1), x 10^{23} (gauss)^2/erg
80	2.60	30.8	9.1 ± 2.0	31.3 ± 7.4
105	3.80	30.8	13.3 ± 2.6	45.8 ± 9.8
115	3.85	30.8	13.5 ± 2.6	46.3 ± 9.8
125	3.85	30.8	13.5 ± 2.6	46.3 ± 9.8

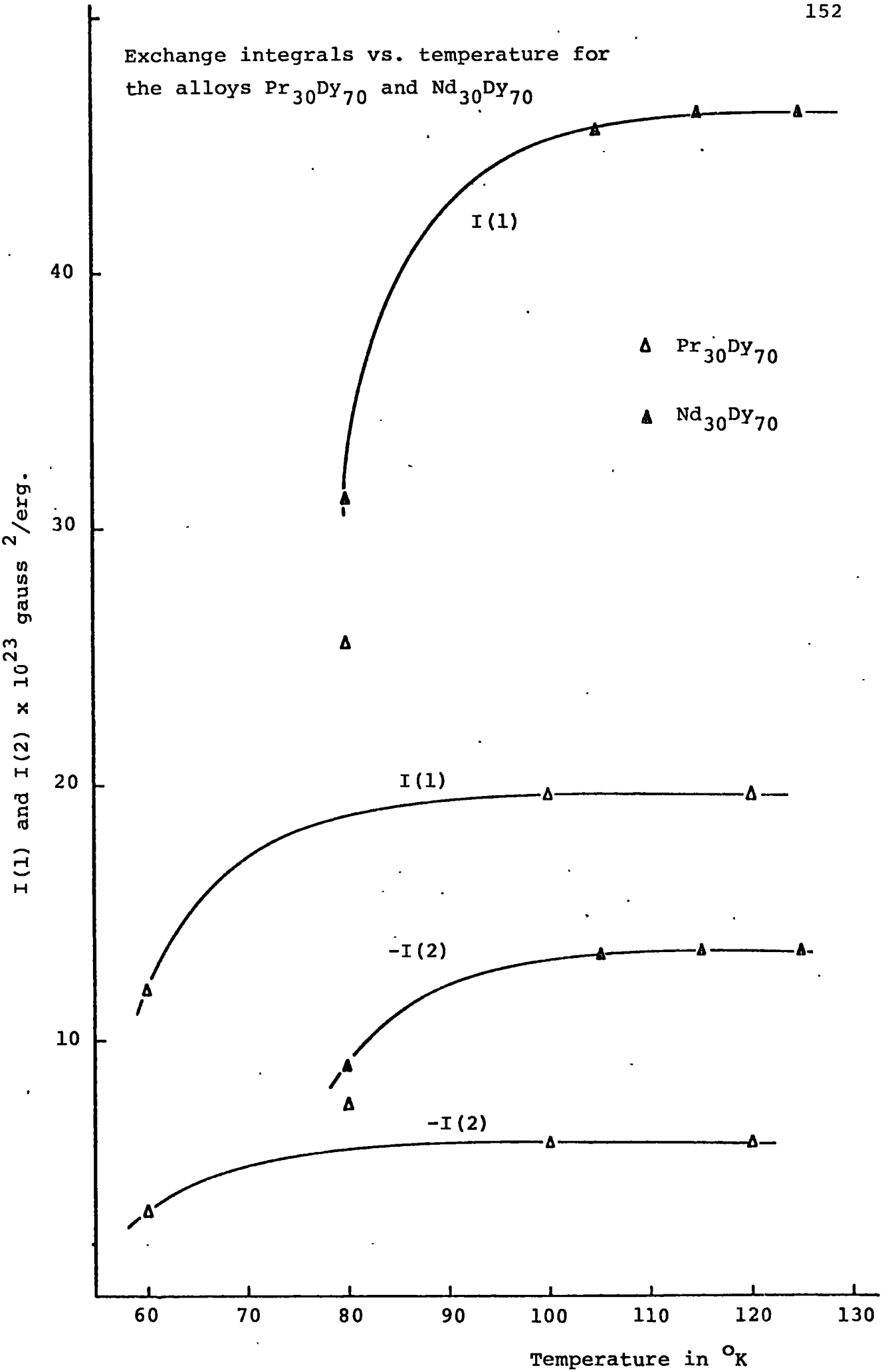
Exchange integrals vs. temperature for
the alloys $Pr_{30}Dy_{70}$ and $Nd_{30}Dy_{70}$
I(1)
$Pr_{30}Dy_{70}$
$Nd_{30}Dy_{70}$
I(1)
-I(2)
-I(2)
40
30
20
10
I(1) and I(2) x 10^{23} gauss ^{2}/erg.
60
70
80
90
100
110
120
130
Temperature in ^oK

FIG. 5.11

behaviour as the critical fields of the alloys as a function of temperature. Because of the large absolute errors on such derived data, it must be emphasised that importance should be placed on the trend rather than the precise values of I(1) and I(2).

At the Curie temperature, the satellite intensity fell abruptly to zero and re-appeared as an increased intensity of all the allowed nuclear peak positions. The intensity at the nuclear peak positions increased with further decreasing temperature and no evidence of extra-nuclear peaks was found in the spectra of either alloy down to 4.2K. The ordered spin structure of the alloys at 4.2K is again ferromagnetic with net moments lying in the basal plane. From the intensities of the peaks at 4.2K values of the saturation moments were assigned to the alloys and these are given in Table 5.3. The moment values are consistent only with an antiparallel alignment of each moment species and are in close agreement with those predicted theoretically, assuming the atomic magnetic moments have their free ion values.

The susceptibility of Ho with decreasing temperature shows a Néel point at 132K and a sharp transition at 24K. This lower temperature transition has been identified as a spin re-orientation transition to a ferromagnetic cone structure (see Section 1.3). The hcp alloys of Ho with Pr and Nd show identical transitions but displaced toward lower temperatures for increasing light rare earth content (see Figs. 5.7 and 5.8). The decrease

in the spin re-orientation temperature with increasing light rare earth content is not so marked as the decrease of the Néel temperature.

Neutron diffraction measurements were made on two representative samples from the Pr-Ho and Nd-Ho alloy systems, $Pr_{20}Ho_{80}$ and $Nd_{20}Ho_{80}$. In the antiferromagnetic region the diffraction patterns of both samples showed satellite peaks of every allowed nuclear reflection, implying that the ordered spin structure in this phase is a uniform basal plane spiral, like antiferromagnetic Ho. The measured initial and final turn angles of the structures are given in Table 5.5 along with the other magnetic data for the alloys. As in the case of the Dy based alloys, the turn angles of the alloys $Nd_{20}Ho_{80}$ and $Pr_{20}Ho_{80}$ show very little temperature dependence and their initial and final values lie well within the range of values spanned by the initial and final turn angles of elemental Ho. A ferromagnetic cone structure was identified as the low temperature magnetic structure in the representative alloys $Pr_{20}Ho_{80}$ and $Nd_{20}Ho_{80}$. At 4.2K the diffraction pattern appropriate to a basal plane spiral spin structure with a turn angle of approximately 36^{o} was observed and also an increase in the scattering at all the allowed nuclear positions except (00ℓ). The net moment per ion calculated from the peak intensities due to this structure is given in Table 5.5.

The Néel temperature of all the hcp light-heavy rare earth alloys, and the Curie temperatures of the

TABLE 5.5

Pr-Ho AND Nd-Ho ALLOYS IN HCP PHASE

Composition	$T_N \pm 2K$	Magnetic Structure	$T_c \pm 2K$	Magnetic Structure	Moment at 4.2K
Ho *	132	Basal plane spiral $\omega_i = 50.0^o$, $\omega_f = 30.0^o$	24	Basal plane spiral $\omega_f' = 30.0^o$ component parallel to c-axis	$\mu_b = 9.50\mu_B$ $\mu_z = 1.70\mu_B$
Pr_{10} Ho_{90}	122		20		
Pr_{20} Ho_{80}	113	Basal plane spiral $\omega_i = 38.3^o$, $\omega_f = 35.6^o$	15	Basal plane spiral $\omega_f' = 36.0^o$, component parallel to c-axis	$\mu_b = 5.03\mu_B$ $\mu_z = 1.37\mu_B$
Pr_{30} Ho_{70}	104		14		
Pr_{40} Ho_{60}	96		10		
Nd_{10} Ho_{90}	118		22		
Nd_{20} Ho_{80}	99	Basal plane spiral $\omega_i = 41.1^o$, $\omega_f = 36.6^o$	15	Basal plane spiral $\omega_f' = 36.3^o$, component parallel to c-axis	$\mu_b = 4.80\mu_B$ $\mu_z = 2.35\mu_B$
Nd_{30} Ho_{70}	88		13		
Nd_{40} Ho_{60}	75		8		

* Ho data due to Koehler, W.C. (1965) J.A.P. 1078-1087

ω_f' turn angle in the distorted spiral structure

μ_z component of the total moment along the z axis

μ_b component of the total moment in the basal plane

Pr-Tb and Nd-Tb alloys are shown in Fig. 5.12 plotted against the reduced de Gennes function for an alloy with two magnetic constituents (see Eqn. 1.7). The Néel temperatures of the heavy rare earth metals are also shown in the figure plotted against the de Gennes factor, G. The transition temperatures are a good fit to a straight line having a slope of 2/3, demonstrating that the empirical relationship $T_N \alpha \bar{G}^{2/3}$ found for the intra-rare earth alloys and the rare earth alloys with Y, also holds for light-heavy rare earth alloys. The Curie temperatures of the alloys show no such universality when plotted against the reduced de Gennes factor (or indeed anything else).

The initial turn angles of the intra-rare earth alloys and the rare earth alloys with Y also exhibit a universality when plotted against the appropriate reduced de Gennes factor (see Section 1.5(i) and Fig 1.6). However, the initial turn angles of the light-heavy rare earth alloys do not lie on this curve. A single plot which does appear to describe the light heavy rare earth alloy systems is obtained when the initial turn angles are plotted against the measured c/a ratios of the alloys (Fig. 5.13). The pure elements and the data for Ho-Ce and Ho-La due to Kawano and Achiwa (1974 and 1975 respectively) are also shown in the figure along with the data for Tb-Y alloys (Child et al 1965). Tb and the Tb rich Tb-Y alloys do not follow the general curve since Tb exhibits very large changes in c/a near

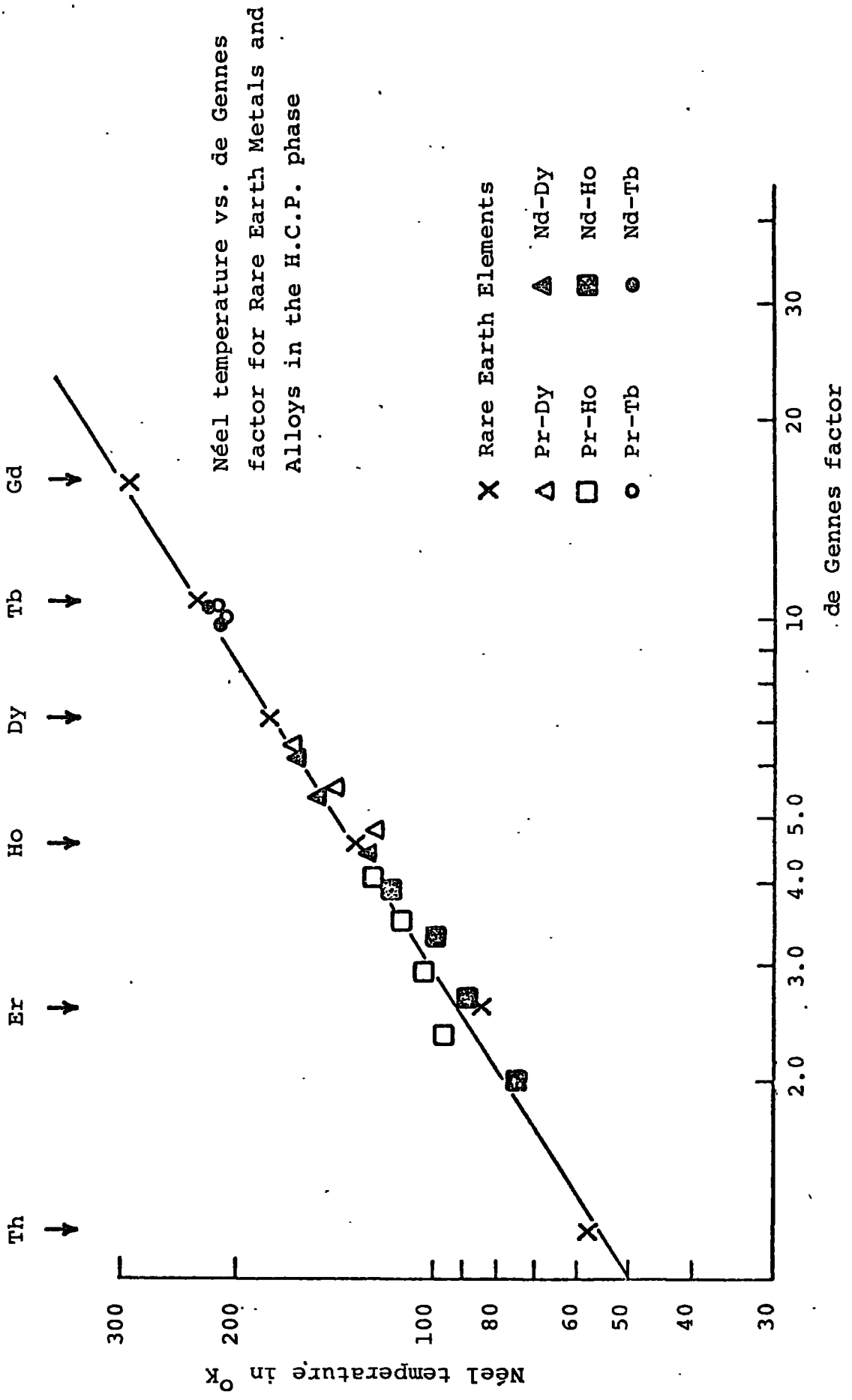
Néel temperature vs. de Gennes factor for Rare Earth Metals and Alloys in the H.C.P. phase
Rare Earth Elements
Pr-Dy
Nd-Dy
Pr-Ho
Nd-Ho
Pr-Tb
Nd-Tb
Th
Er
Ho
Dy
Tb
Gd
Néel temperature in °K
300
200
100
80
60
50
40
30
2.0
3.0
4.0
5.0
10
20
30
de Gennes factor

FIG. 5.12.

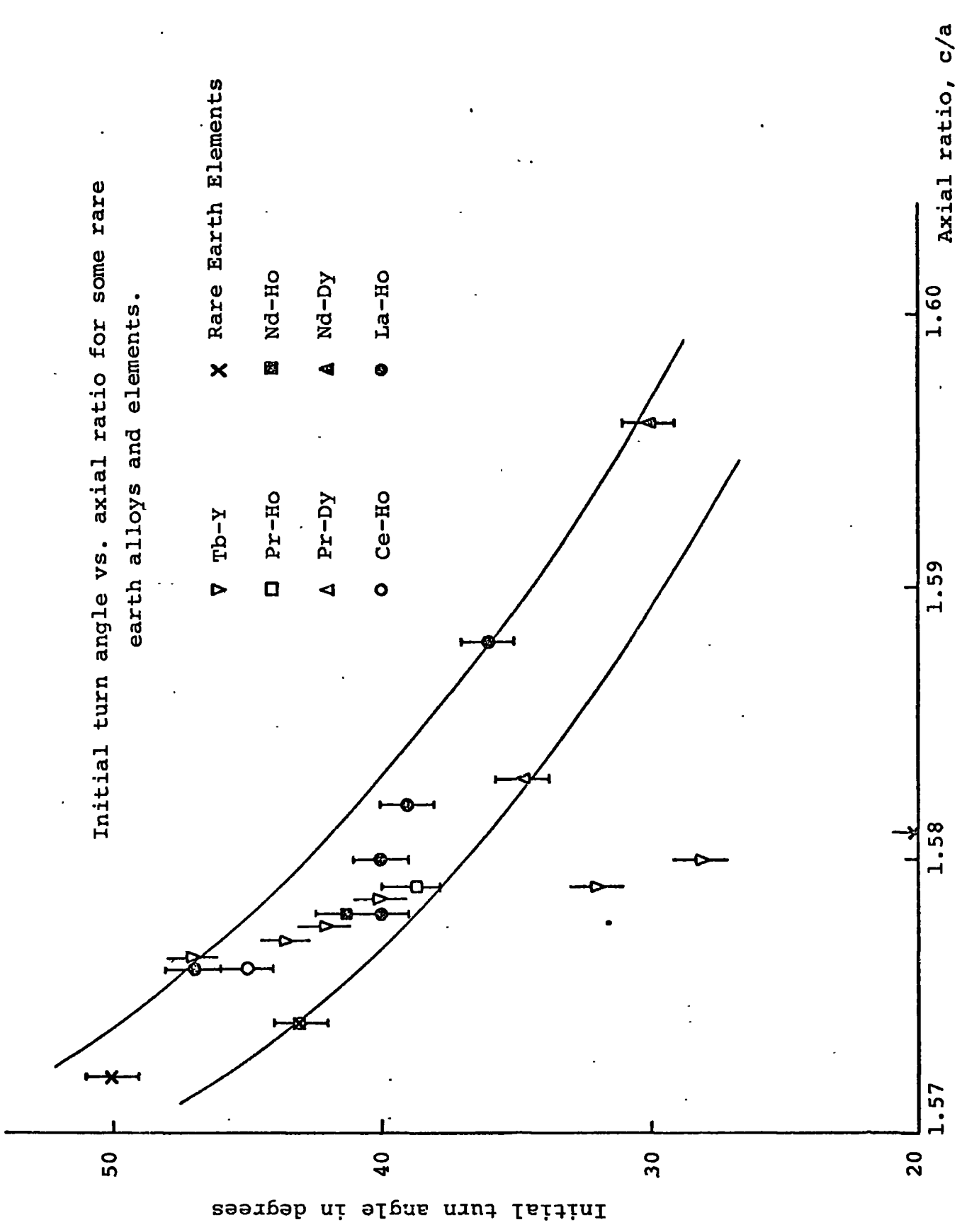
Initial turn angle vs. axial ratio for some rare earth alloys and elements.
Rare Earth Elements
Tb-Y
Pr-Ho
Pr-Dy
Ce-Ho
Nd-Ho
Nd-Dy
La-Ho
Initial turn angle in degrees
50
40
30
20
1.57
1.58
1.59
1.60
Axial ratio, c/a

FIG. 5.13

the ordering temperature due to its large magnetoelastic constants. Alloying with Y serves to dilute the magnetic properties of Tb and for alloys with greater than 30% Y content the initial turn angles follow the general curve. (see also Section 6.1(ii)).

5.2(ii) SM. PHASE

The susceptibility data on the Sm phase alloys (approximately equal proportions of light and heavy rare earth) showed evidence of only one magnetic transition with decreasing temperature, with the exception of the Nd-Tb alloys. From the form of the curve the transition (the higher temperature transition in the Nd-Tb alloys) could be identified as a Néel point. The magnetic transition temperatures were plotted as a function of composition for each alloy system in Figures 5.3 to 5.8. The rate of change of the Néel temperature with light rare earth addition is altered in the Sm phase from its value in the hcp phase. In the Nd-heavy rare earth alloys, the rate of change of the Néel temperature with composition appears to be less than in the hcp phase, whilst in the Pr-heavy rare earth alloys it appears to be increased over its value in the hcp phase.

Neutron diffraction experiments were performed on representative samples from each alloy system. Just below the Néel temperature all alloys gave a diffraction pattern similar to that observed for a uniform basal plane spiral i.e. satellite peaks of observed nuclear reflections. The turn angle of the alloy structure, evaluated from the

angular position of the $(000)^{\pm}$ satellite, was approximately 60^{o} in each case and varied only slightly down to 4.2K. The actual values observed are recorded in Tables 5.6 to 5.8 where the other magnetic data for the alloys are tabulated.

The 4.2K diffraction pattern of $Pr_{45}Tb_{55}$ is shown in Fig. 5.14. The peaks have been indexed on an 18 layer unit cell chosen to be commensurate with both the chemical and magnetic unit cells. The magnetic diffraction pattern at 4.2K was obtained by subtracting the corrected nuclear peak intensities from the 4.2K diffraction pattern revealing extra magnetic peaks hidden under the nuclear peaks,which were also indexed on the 18 layer unit cell. The intensity of the lines in both the magnetic and the nuclear diffraction patterns is much lower than the intensity of the diffraction lines for the samples in the hcp phase. The reduction in intensity of the nuclear lines is a consequence of the low values of the geometrical structure factor, $\left|G_{hk\ell}\right|^2$, for reflections in the $R\bar{3}m$ space group, and the magnetic lines are weak because the magnetisation, even at 4.2K, is small.

The magnetic diffraction pattern of the alloys at 4.2K all have the same form between 18^{o} and 25^{o} in 2θ, with the exception of $Nd_{60}Tb_{40}$. In the $Nd_{60}Tb_{40}$ alloy sample two large peaks grew below 70K at about 20^{o} and 22^{o} in 2θ obscuring all the other magnetic peaks in this angular range. However, the $(000)^{\pm}$ satellite was clearly visible from just below the Néel temperature to 4.2K.

TABLE 5.6

MAGNETIC DATA FOR PR-TB AND ND-TB ALLOYS IN SM AND D.H.C.P. PHASES

Composition	$T_N \pm 2K$	Crystal Structure	Ordered Magnetic Structure at 4.2K	Ordered Moment $\pm 0.2\mu_B$
$Tb_{70}Pr_{30}$	120	Sm. Structure	Net moments in basal plane but amplitude modulated along c-axis $\omega_i = 58.7^o$, $\omega_f = 60.3^o$.	$4.5\mu_B$
$Tb_{65}Pr_{35}$	118			
$Tb_{55}Pr_{45}$	90	Sm. Structure	Net moments in basal plane but amplitude modulated along c-axis $\omega_i = 61.2^o$, $\omega_f = 59.6^o$.	$3.7\mu_B$
$Tb_{30}Pr_{70}$	25	dhcp	Antiferromagnetic structure like polycrystalline Pr.	$0.6\mu_B$ all sites $0.9\mu_B$ hex. sites only
$Tb_{10}Pr_{90}$	13	dhcp	Antiferromagnetic like Pr.	
Tb_5Pr_{95}	11		Antiferromagnetic like Pr.	
Tb_1Pr_{99}			No ordering	
Pr	21	dhcp	Antiferromagnetic in polycrystalline sample.	$0.7\mu_B$ all sites $1.0\mu_B$ hex. sites only
$Tb_{50}Nd_{50}$	123		Cubic sites order at 90K.	
$Tb_{40}Nd_{60}$	99	Sm. Structure	See text Section 6.2 $\omega_i = 62.9^o$ $\omega_f = 60.2^o$ Cubic sites order at 73K.	
$Tb_{10}Nd_{90}$	21	dhcp	Antiferromagnetic structure similar to Nd. Cubic sites order at 8K.	
Nd	29	dhcp	Antiferromagnetic structure on hex. sites with modulation. At 7.5K cubic sites order antiferromagnetically.	$2.3\mu_B$

TABLE 5.7

MAGNETIC DATA FOR Pr-Dy AND Nd-Dy ALLOYS IN SM AND DHCP PHASES

Composition	$T_N \pm 2K$	Crystal Structure	Ordered Magnetic Structure at 4.2K	Ordered Moment
Dy_{60} Pr_{40}	83			
Dy_{50} Pr_{50}	61	Sm Structure	Net moments lie in basal plane but amplitude modulated along c-axis $\omega_f = 62.3^{\circ}$.	$4.0\mu_B$
Dy_{40} Pr_{60}	27			
Dy_{30} Pr_{70}	20			
Dy_{20} Pr_{80}	16			
Dy_{10} Pr_{90}	9	dhcp	Modulated antiferromagnetic structure like polycrystalline Pr.	
Dy_{60} Nd_{40}	114	hcp + Sm Structure		
Dy_{50} Nd_{50}	70	Sm Structure	Net moments lie in basal plane but amplitude modulated along c-axis $\omega_f = 61.2^{\circ}$.	$3.8\mu_B$
Dy_{40} Nd_{60}	63			
Dy_{30} Nd_{70}	26			
Dy_{20} Nd_{80}	21		Cubic sites order at 8K	
Dy_{10} Nd_{90}	21	dhcp	Ferrimagnetically aligned moments at 10° to basal plane. Cubic sites order at 10K.	$2.0\mu_B$ in basal plane $.26\mu_B$ in c direction.

TABLE 5.7a

MAGNETIC DATA FOR SOME LOW CONCENTRATION DY-ND ALLOYS

Alloy	T_N (hexagonal sites) ± 2K	T_N (cubic sites) ± 2K	Remarks
$Nd_{99}Dy_{01}$	30	10	
$Nd_{98}Dy_{02}$	30	9	Hexagonal site peak sharper. Cubic site broader than in Nd.
$Nd_{97}Dy_{03}$	30	11	
$Nd_{96}Dy_{04}$	30	8	Hexagonal site peak almost disappeared. Evidence for new peak at 21K. Cubic site peak very broad.

TABLE 5.8

MAGNETIC DATA FOR Pr-Ho AND Nd-Ho ALLOYS IN THE SM AND DHCP PHASES

Composition	$T_N \pm 2K$	Crystal Structure	Ordered Magnetic Structure at 4.2K	Ordered moment
$Ho_{50}Pr_{50}$	46			
$Ho_{40}Pr_{60}$	28	Sm structure	Net moments lie in basal plane but amplitude modulated along c-axis $\omega_i = 60.4^o$, $\omega_f = 61.4^o$.	$2.8\mu_B$
$Ho_{30}Pr_{70}$	-			
$Ho_{20}Pr_{80}$	-			
$Ho_{10}Pr_{90}$	12	dhcp	No observed magnetic structure from neutron diffraction.	
$Ho_{50}Nd_{50}$	55			
$Ho_{40}Nd_{60}$	47			
$Ho_{30}Nd_{70}$	38	Sm structure	Net moments lie in basal plane but amplitude modultated along c-axis $\omega_i = \omega_f = 61.3^o$.	$1.8\mu_B$
$Ho_{20}Nd_{80}$	25		Cubic sites order at 8K.	
$Ho_{10}Nd_{90}$	26	dhcp	Ferrimagnetic cone structure cubic sites order at 7K.	

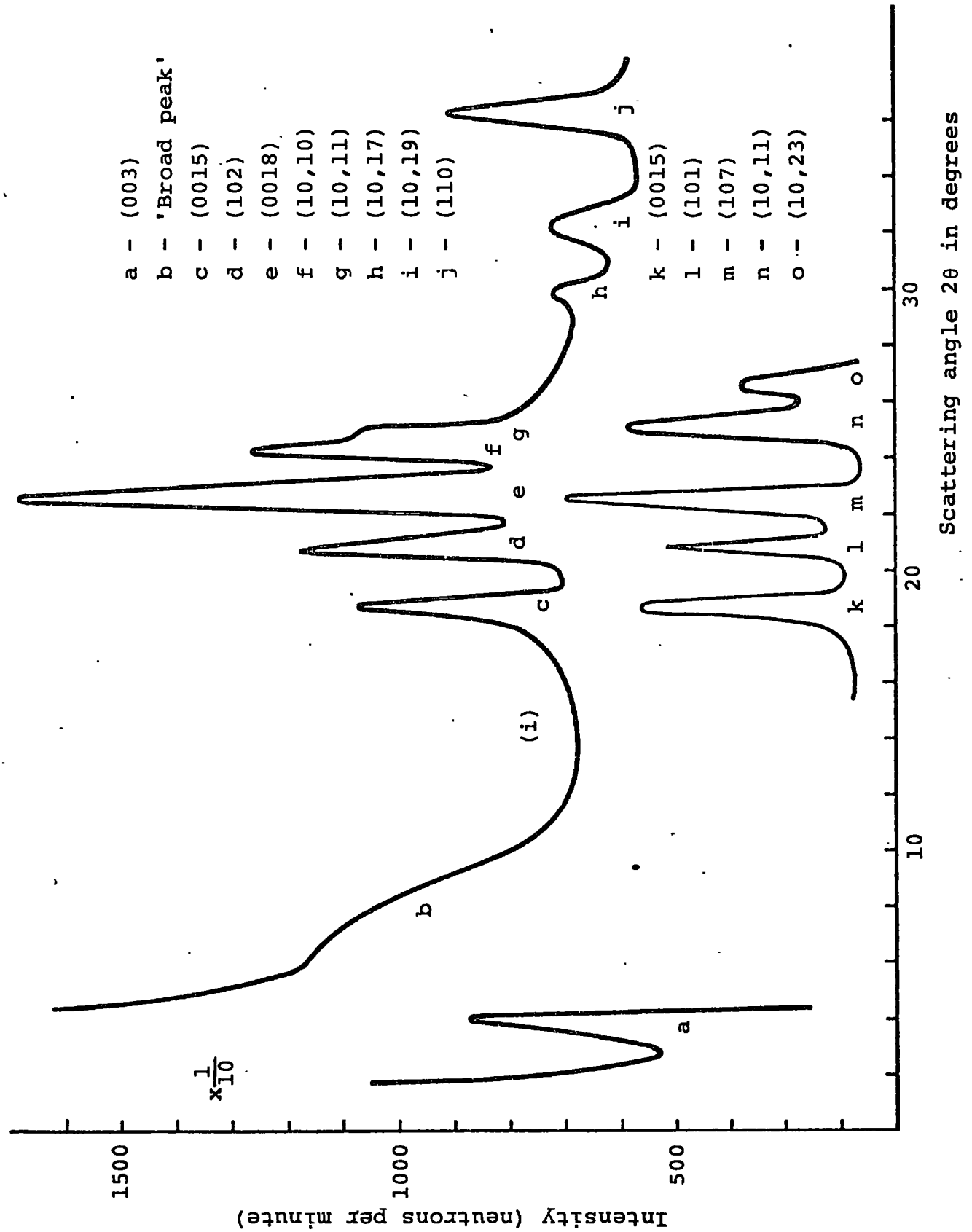

FIG. 5.14 (i) Diffraction pattern of $Pr_{45}Tb_{55}$ at 4.2K and
(ii) magnetic contribution to the diffraction pattern.
Peaks are indexed on an 18 layer unit cell.

From its angular position, the turn angle of the structure was determined to be approximately 60^{o}, varying only slightly throughout the entire ordered region (see Table 5.6). The appearance of the large peaks in the magnetic diffraction pattern of $Nd_{60}Tb_{40}$ below 70K precluded the possibility of determining the ordered structure at 4.2K unambiguously or measuring the ordered moment at 4.2K.

The diffraction pattern of $Pr_{45}Tb_{55}$ at 4.2K shown in Fig. 5.14 also displays a broad peak at low scattering angles which is not shown by the $Nd_{60}Tb_{40}$ sample or the Dy-light rare earth Sm phase alloys or the Ho-light rare earth Sm phase alloys. The broad peak did not interfere with either the magnetic structure determination or the subsequent calculation of the net ordered moment, as it did not obscure the peaks between 18^{o} and 25^{o} in 2θ. The temperature dependence of the broad peak intensity in $Pr_{45}Tb_{55}$ is shown in Fig. 5.16. Also shown in Fig. 5.16 for comparison is the $(009)^{-}$ satellite intensity in $Pr_{45}Tb_{55}$ which is typical of all the Sm phase alloys. It can be seen from the figure that the $(009)^{-}$ intensity falls to zero at the Néel temperature whereas the broad peak is still visible above the background at 150K. The lower ordering temperature in $Nd_{60}Tb_{40}$ determined from the susceptibility vs. temperature scans occurred at the same temperature as the extra coherent scattering appeared in the neutron diffraction patterns at $2\theta = 20^{o}$ and $2\theta = 22^{o}$. However, no evidence of a peak

Magnetic structure of alloys in Sm. phase

Arrows denote moment direction on each hexagonal layer.

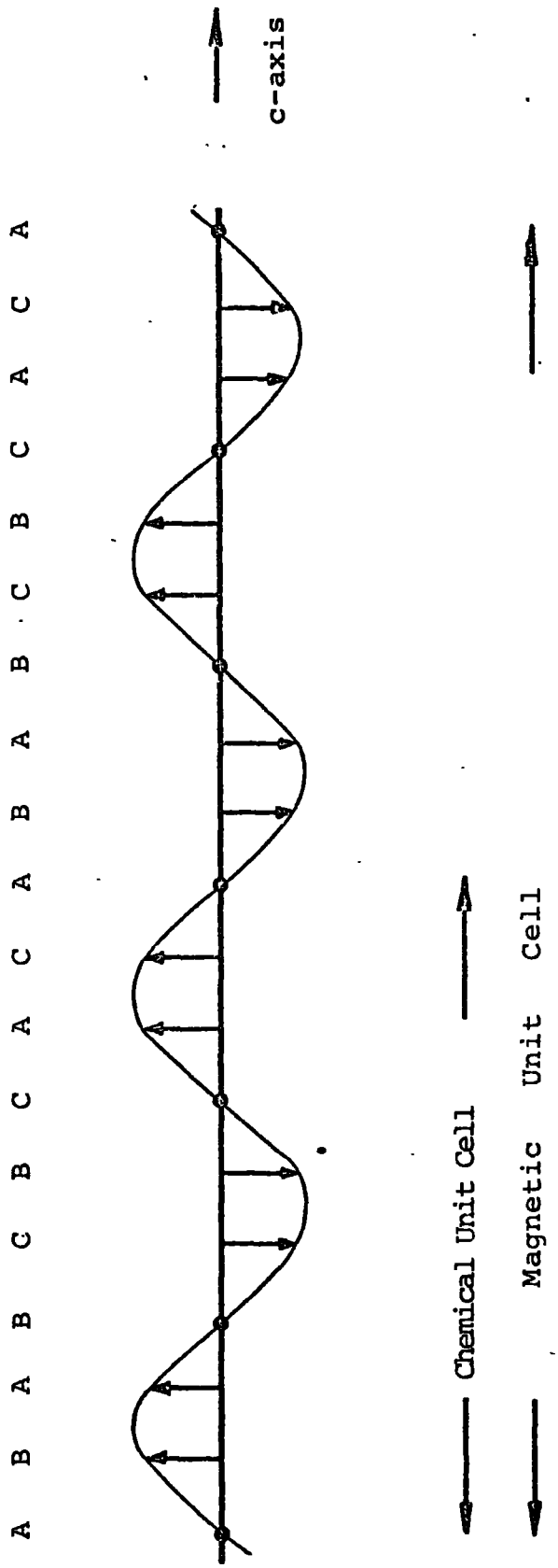

FIG. 5.15.

Intensity of $(009)^-$ satellite and broad peak vs. temperature for $Pr_{45}Tb_{55}$.

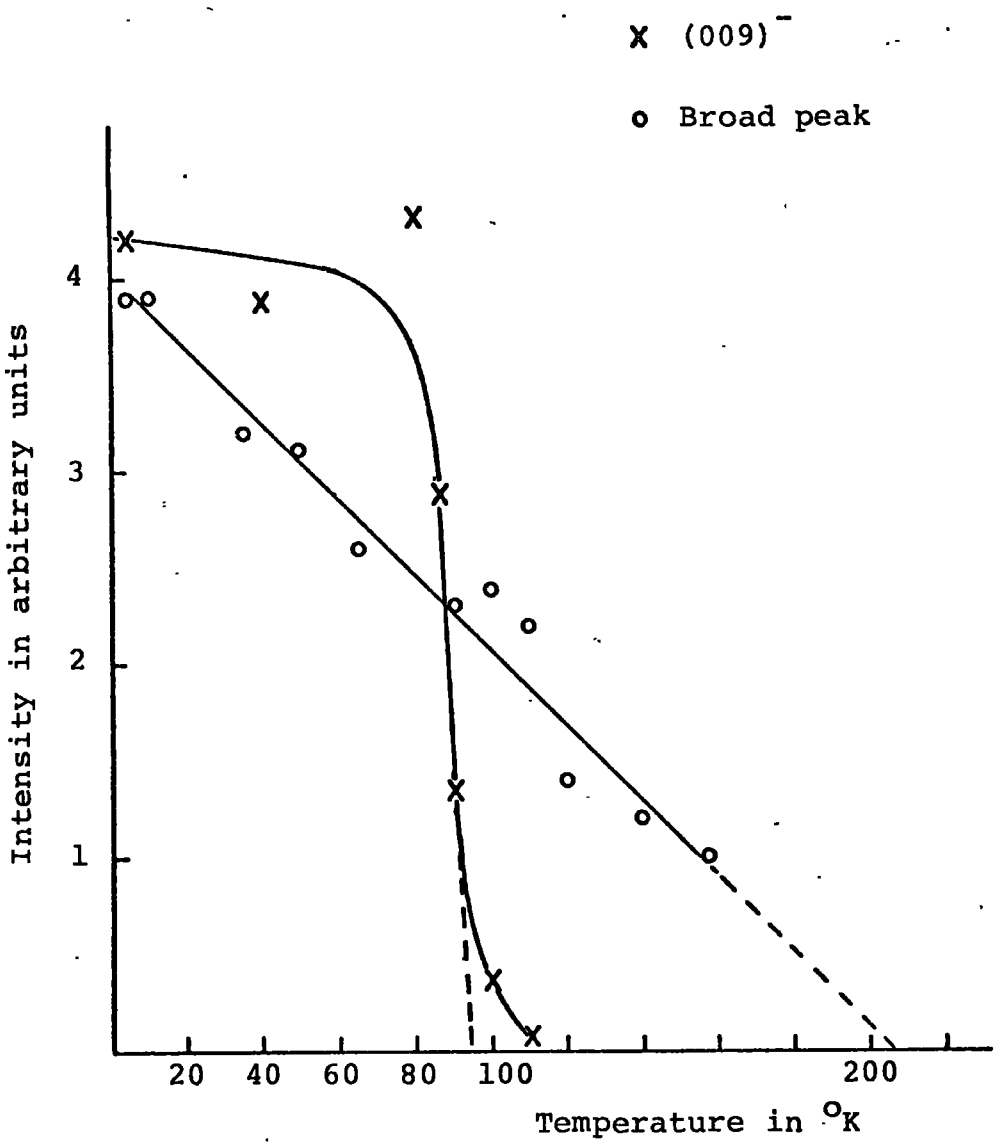

FIG. 5.16

was found in the susceptibility vs. temperature scans of $Pr_{45}Tb_{55}$ which could be associated with the extra scattering observed in the neutron diffraction patterns. A possible origin of the extra scattering in the Tb-light rare earth alloys will be discussed in Section 6.2(ii).

An attempt was made to fit the magnetic peak intensities at 4.2K to a uniform basal plane spiral, but the intensities were found to be consistent only with a structure in which the moments on adjacent layers are ferromagnetically aligned in the basal plane, but with net values which are amplitude modulated along the c-axis of the crystal. (The magnetic structure factor for this configuration is derived in Appendix 1 and evaluated in Appendix 2). The turn angle of the structure, which now no longer has quite the same meaning as in a basal plane spiral structure, is 60^{o} and this implies that at every third layer the amplitude of the net moment of that layer is zero. The plane on which there is no moment can be identified from the intensity of the satellite peaks as the cubic site layers, (see Appendix A2). The structure is shown in Fig. 5.15.

The net moments of the alloys at 4.2K are larger than those predicted theoretically for an antiparallel alignment of the two moment species, assuming that both the constituents of the alloy develop their full ionic moments. If the contribution of the light rare earth to the net moment is reduced to 2/3 of its ionic value then much better agreement is obtained between the

observed and the predicted moment values for the Ho-light rare earth and the Dy-light rare earth alloys. The observed moment on the $Pr_{45}Tb_{55}$ alloy is in good agreement with a predicted value assuming that the Pr ion takes a moment value of $\frac{\sqrt{3}}{2}$ of its full ionic value.

5.2(iii) D.H.C.P. PHASE

The magnetic ordering temperature of the alloys in the dhcp phase and those of the terminal elements Pr and Nd are shown in Tables 5.6, 5.7, 5.7a and 5.8. The ordering temperatures are also plotted as a function of composition in Figs. 5.3 to 5.8.

In the Pr based alloys the observed ordering temperature in pure Pr disappears for small concentrations of heavy rare earth and then reappears as the concentration of heavy rare earth is increased. The neutron diffraction results on the Pr based alloys in the dhcp phase, with the exception of $Pr_{70}Tb_{30}$, showed only very weak magnetic diffraction peaks at 4.2K implying an absence of a well defined long range magnetic ordering in the materials. In $Pr_{70}Tb_{30}$, however, the extra coherent scattering gave rise to strong magnetic peaks at 4.2K, at positions corresponding approximately to (001) and (003) peaks in the dhcp structure. The magnetic scattering is similar to that in pure Pr at 4.2K implying an overall antiferromagnetic structure for the alloy, but with the net moment direction modulated on adjacent hexagonal layers since the (001) and (003) peaks are displaced to slightly

higher $\frac{\sin\theta}{\lambda}$ values. From the limited data available it was not possible to determine whether all the ions contribute to the observed moment or only those ions on sites with either cubic or hexagonal symmetry. From the data, the calculated moment if all the sites contribute is $0.6\mu_B$/ion and $0.9\mu_B$/ion if only half the ions carry moments. The value of $0.6\mu_B$/ion is close to the theoretical value for an alloy of this composition assuming that each ion takes its full ionic moment and that the Tb and Pr moments are antiferromagnetically aligned. The (001) magnetic peak remained visible up to 75K i.e. $3T_N$.

The magnetic reflections observed in the other Pr based dhcp alloys at 4.2K ($Pr_{90}Dy_{10}$, $Pr_{90}Ho_{10}$, $Pr_{95}Tb_5$, $Pr_{90}Tb_{10}$) were all very much weaker than in $Pr_{70}Tb_{30}$. In $Pr_{90}Dy_{10}$ both the (001) and (003) peaks were observed at positions slightly higher in $\frac{\sin\theta}{\lambda}$ than predicted for the dhcp structure, implying a modulated antiferromagnetic structure like Pr. Since the peaks were so weak no reliable estimate could be made of the moment per ion in the alloy. The other three alloys all displayed very weak extra scattering at 4.2K at a single position very close to the theoretical position of the (001).

Assuming that this very weak scattering is due to the incipient antiferromagnetism of Pr, inelastic neutron scattering experiments were carried out on a series of Pr-Tb alloys and on elemental Pr, (see Section 4.4(iii)).

From the experimental data, the crystal field level splitting from the ground state to the first excited state on the cubic and hexagonal sites were evaluated and these are shown plotted as a function of Tb concentration in Fig. 5.17. From the figure it can be seen that the crystal field level splitting decreases rapidly for small Tb concentrations but does not go to zero on either the hexagonal or cubic sites for larger concentrations, implying that there is no crystal field level crossing situation. This may be due to the fact that there are no uniquely determined crystal field levels in these higher percentage composition alloys.

Elastic neutron scattering experiments on representative Nd based alloys in the dhcp phase indicate that they are all ordered. $Nd_{90}Tb_{10}$ exhibits very small extra coherent scattering at positions corresponding to (001) and (003) but with slightly higher $\frac{\sin\theta}{\lambda}$ values. A similar pattern is observed for polycrystalline Nd, implying that the ordering in $Nd_{90}Tb_{10}$ is one with a modulated antiferromagnetic structure. The extra scattering is absent at 20K. The extra coherent scattering in $Nd_{90}Dy_{10}$ occurred at reciprocal lattice sites implying a ferrimagnetic alignment of the Nd and Dy moments. On the basis of the intensity of the neutron diffraction peaks at 4.2K the magnetic structure of $Nd_{90}Dy_{10}$ was deduced to be one in which the magnetic moment on the ion lies at an angle to the basal plane - the ferromagnetic cone structure.

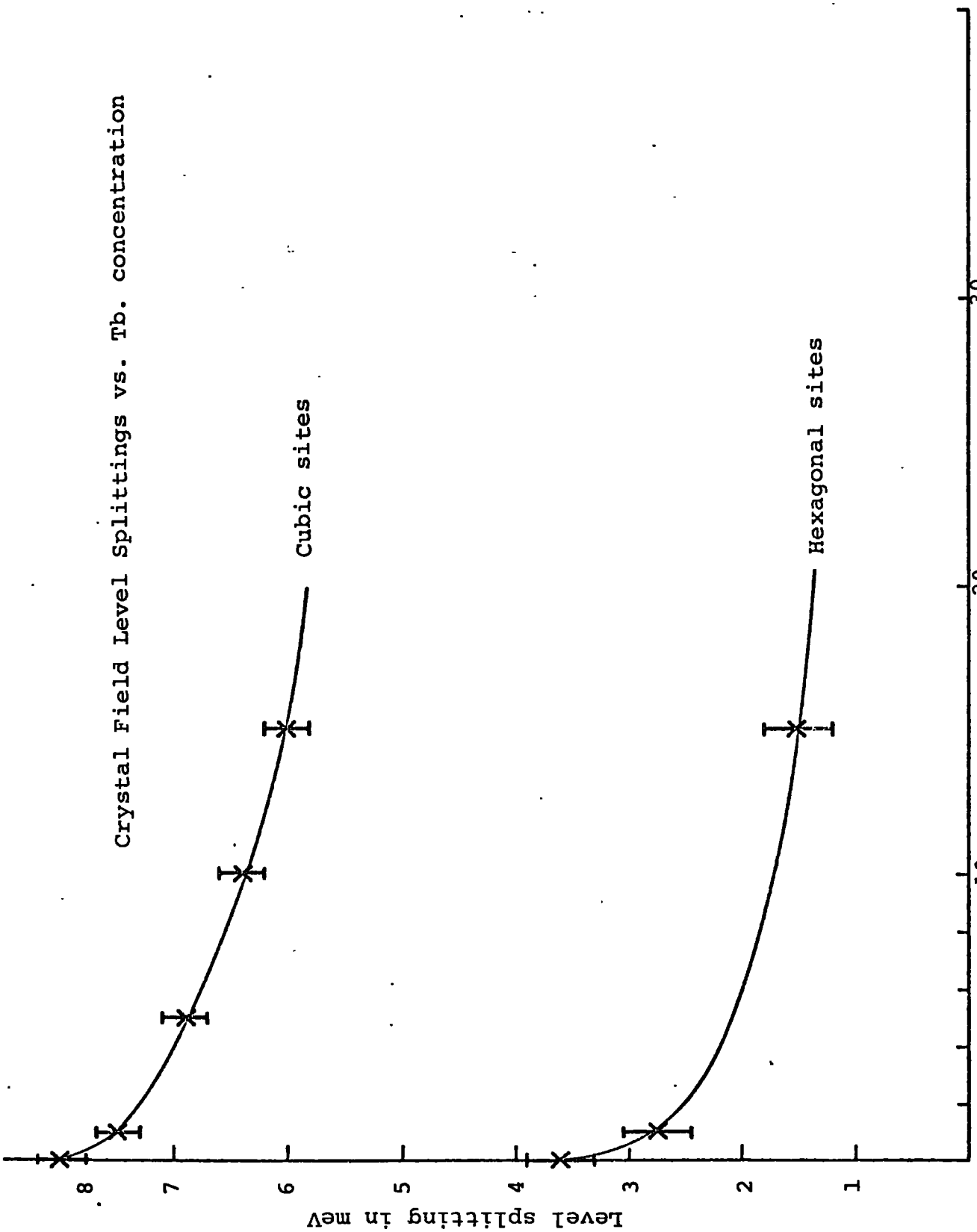
Crystal Field Level Splittings vs. Tb. concentration
Cubic sites
Hexagonal sites
Level splitting in meV
% Tb in Pr.
1
2
3
4
5
6
7
8
10
20
30

FIG. 5.17

The moment in the basal plane was determined to be $1.98\mu_B$ and the c-axis component to be $0.26\mu_B$, giving a total moment of $2.0\mu_B$ at an angle of approximately 10^o to the basal plane direction. The total moment evaluated from the neutron diffraction data is 5% greater than the theoretical moment, derived assuming that both Dy and Nd take their full ionic moments and the moments are aligned antiparallel.

Extra coherent scattering is observed in $Nd_{90}Ho_{10}$ at reciprocal lattice points except (00ℓ) and close to the origin. Assuming that this weak peak close to the origin is the satellite $(000)^{\pm}$, then the position of the extra scattering implies a ferromagnetic spiral structure (like $Pr_{20}Ho_{80}$ and $Nd_{20}Ho_{80}$; see Sections 5.2 and 6.1). The turn angle evaluated from the position of the satellite of the origin is 68^o and the moment in the c-direction as $2.2\mu_B$. No reliable estimate of the moment in the basal plane could be made from the intensity of the weak $(000)^{\pm}$ satellite. The derived value of the axial moment, $2.2\mu_B$, is 15% higher than that calculated on the basis of an antiparallel alignment of the Nd and Ho moments, assuming that they take their free ion values. Furthermore, the appearance of a weak satellite of the origin implies that a small component of the total moment lies in the basal plane. The c-axis component of the total moment evaluated from the neutron diffraction data is therefore in error, due to the difficulty in obtaining an accurate estimate of the scattering from the weak magnetic

structure and having to compare this with the equally small scattering from the dhcp structure. The magnetic structure of $Nd_{90}Ho_{10}$ at 4.2K may still be inferred, however, to be a ferromagnetic cone structure with the moments lying close to the c-axis.

The susceptibility vs. temperature plots for the Nd-Ho alloy system in the dhcp phase exhibited two magnetic transitions with decreasing temperature, corresponding to ordering on the hexagonal and cubic sites. The ordering temperatures did not change with increasing Ho concentration, as in the Pr-Ho alloys (see Table 5.8 and Fig. 5.8) but stayed constant becoming sharper as the Ho concentration increased. The behaviour of the Dy-Nd alloy system is also different from that of the Pr-Dy alloy system. The susceptibility vs. temperature plots of Nd and some Nd-Dy alloys are shown in Fig. 5.18. The susceptibility of pure Nd exhibits two distinct peaks which may be associated with ordering on the hexagonal sites (30K) and the cubic sites (8K). As the Dy concentration is increased the height of the peak associated with ordering on the hexagonal site decreases until at 5at.% Dy it is absent. However, for greater than 2 at.% Dy a third peak appears in the susceptibility at 21K. This peak does not disappear at 5at.% Dy but remains clearly visible in all but the 30at.% Dy alloy, when there is no distinction between hexagonal and cubic sites and the alloy orders at 26K. The appearance of this extra peak in the susceptibility

Susceptibility vs. temperature for some Nd-Dy alloys and elemental Nd.

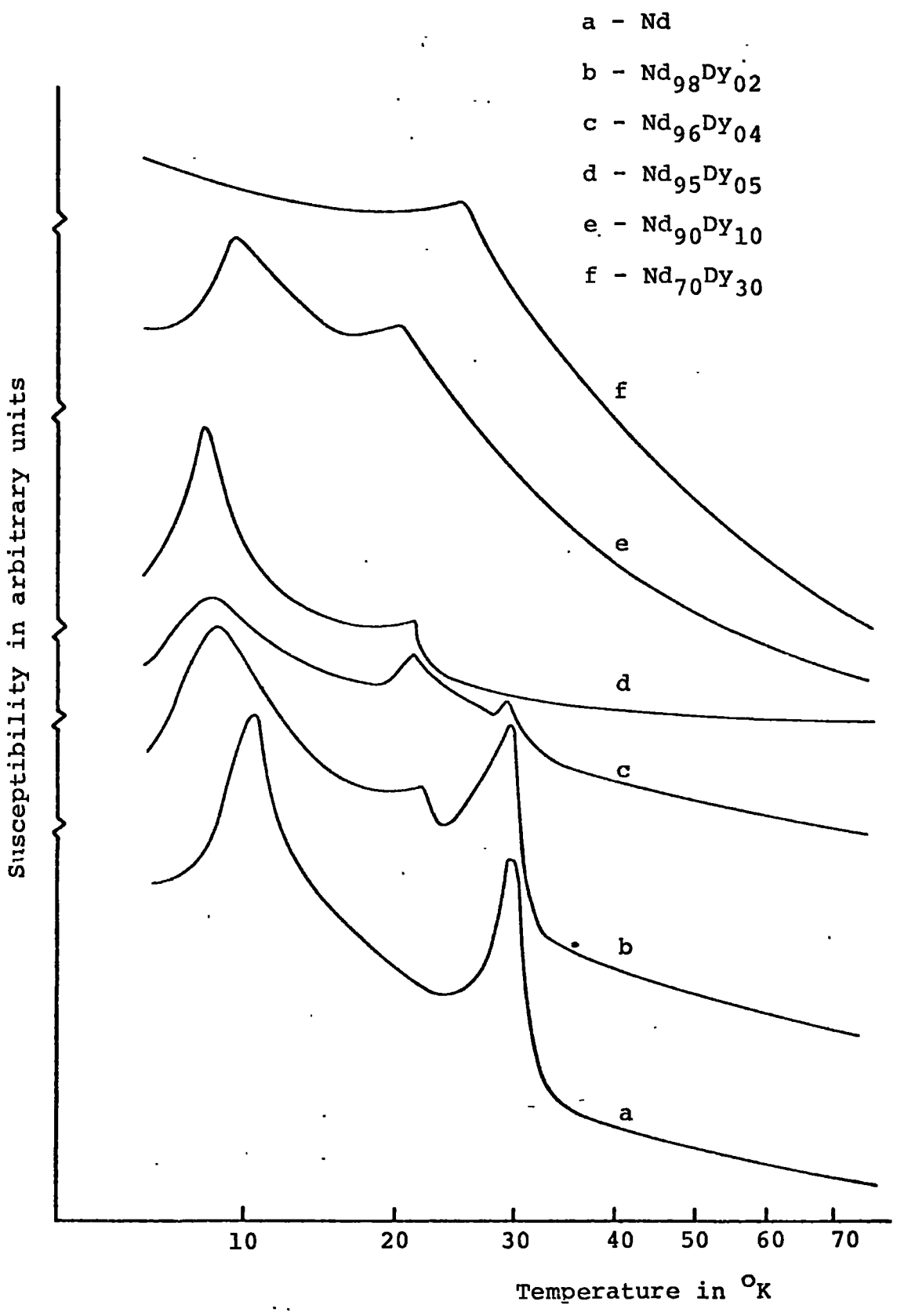

FIG. 5.18

and the disappearance of the original peak is probably associated with a change in the magnetic ordering on the hexagonal site, since the peak associated with the cubic site ordering remains at almost the same temperature for all the alloys. The neutron diffraction results presented earlier in this section for the alloy $Nd_{90}Dy_{10}$ do indeed suggest a magnetic structure at 4.2K which is different from that found in pure Nd.

The inverse susceptibility of Pr, Nd and some Pr-Dy, Pr-Tb and Nd-Dy alloys is shown plotted against temperature in Figs. 5.19 to 5.21. From eqn. 2.5 it can be seen that the slope of the inverse susceptibility vs. temperature plot is proportional to the moment on the alloy and from a knowledge of the moments on Pr and Nd (see Table 1.1) the moments on the other alloys may be evaluated. The paramagnetic moments calculated in this way along with the theoretical paramagnetic moments derived from the formula

$$\mu = \sqrt{\mu_a x + \mu_b (1-x)}$$

where μ_a and μ_b are the moments on the constituent ions and x is the fractional concentration of the 'a' ions, are given in Table 5.9. With increasing heavy rare earth content the observed paramagnetic moment increases to well above the theoretical value, almost reaching the free ion value of the heavy rare earth metal. Such large increases in paramagnetic moment have been observed

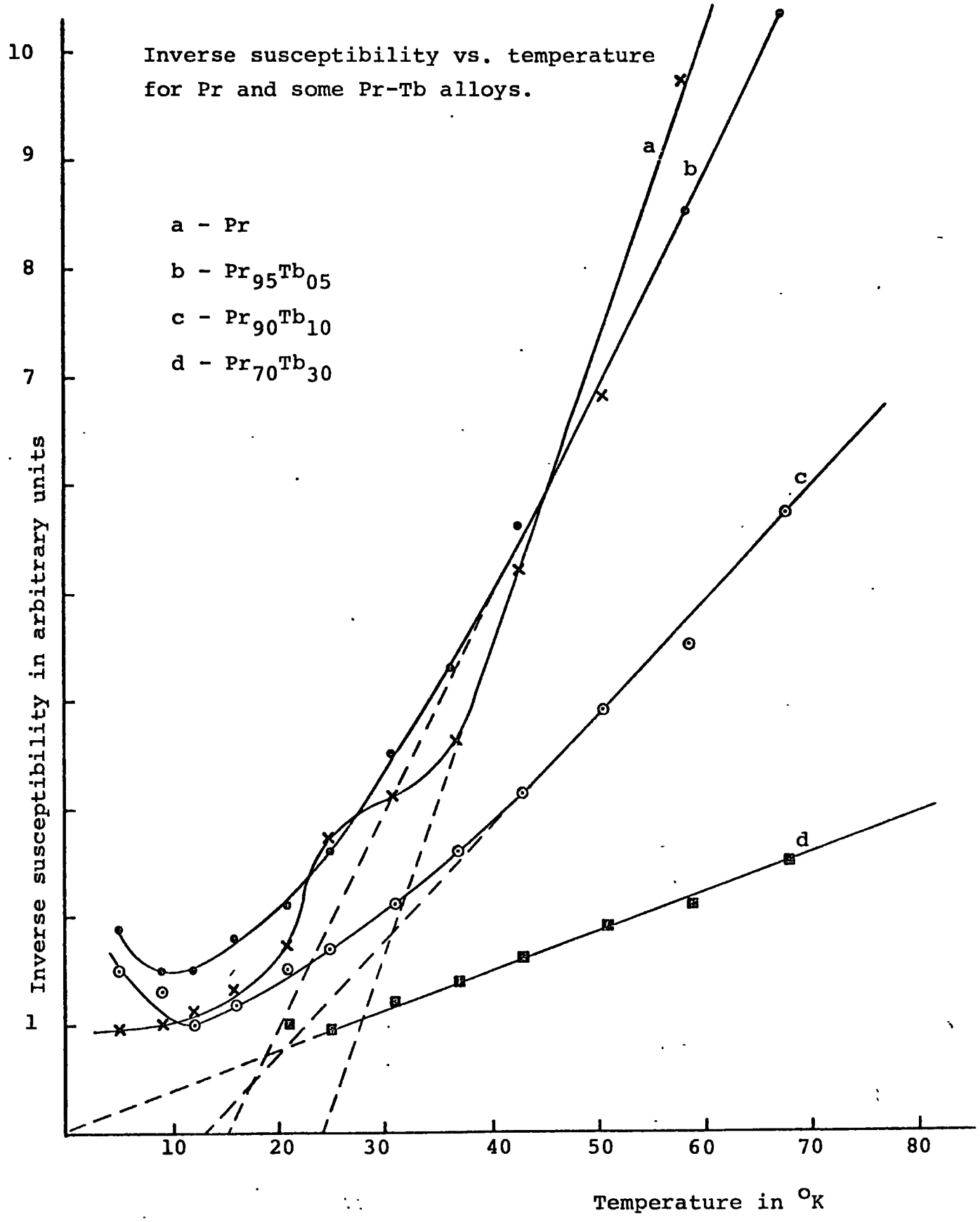
Inverse susceptibility vs. temperature
for Pr and some Pr-Tb alloys.
a - Pr
b - $Pr_{95}Tb_{05}$
c - $Pr_{90}Tb_{10}$
d - $Pr_{70}Tb_{30}$
Inverse susceptibility in arbitrary units
Temperature in °K
10
9
8
7
1
10
20
30
40
50
60
70
80
a
b
c
d

FIG. 5.19

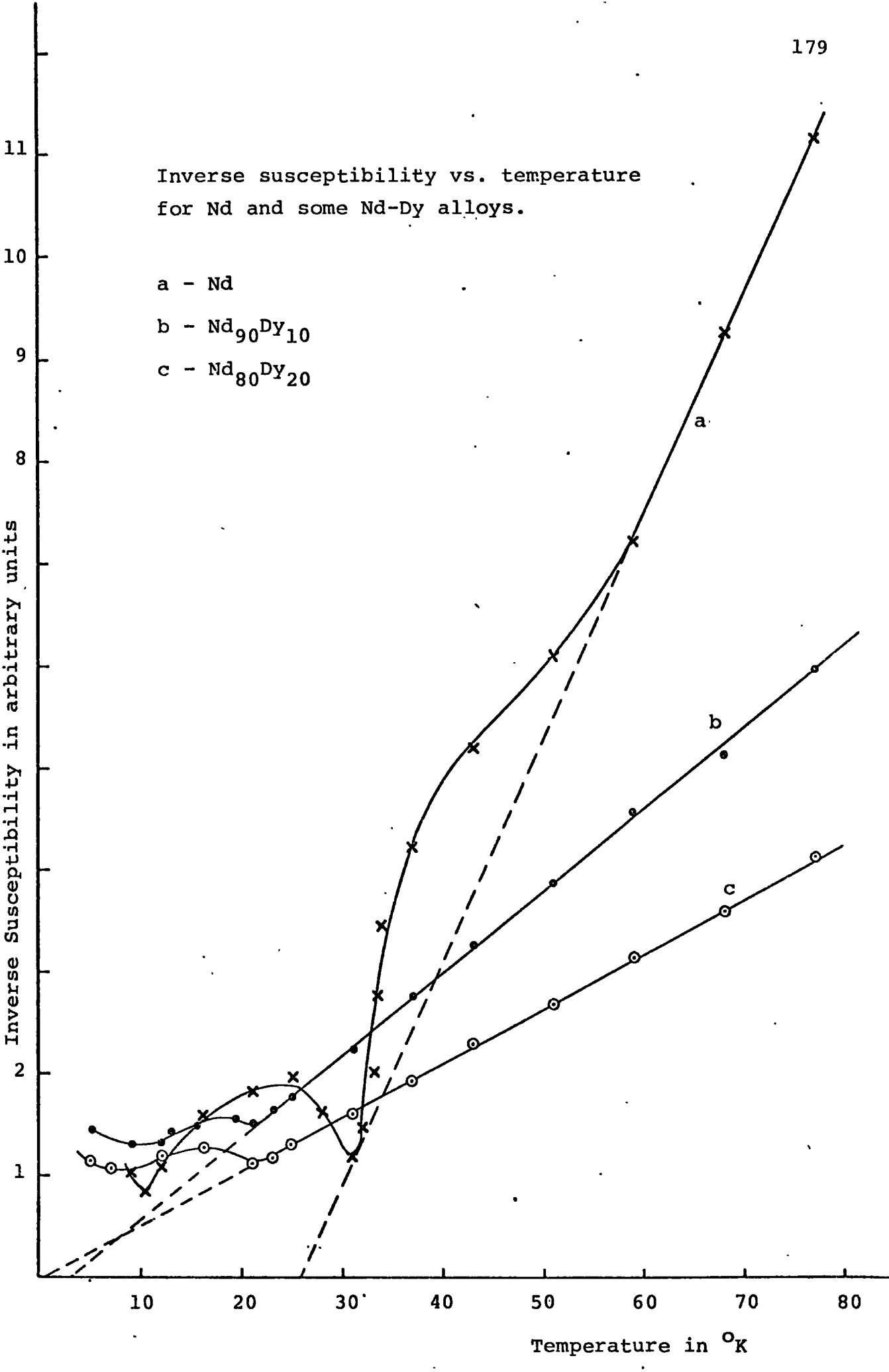
Inverse susceptibility vs. temperature
for Nd and some Nd-Dy alloys.
a - Nd
b - $Nd_{90}Dy_{10}$
c - $Nd_{80}Dy_{20}$
a
b
c
Inverse Susceptibility in arbitrary units
1
2
8
9
10
11
10
20
30
40
50
60
70
80
Temperature in ^{o}K

FIG. 5.20.

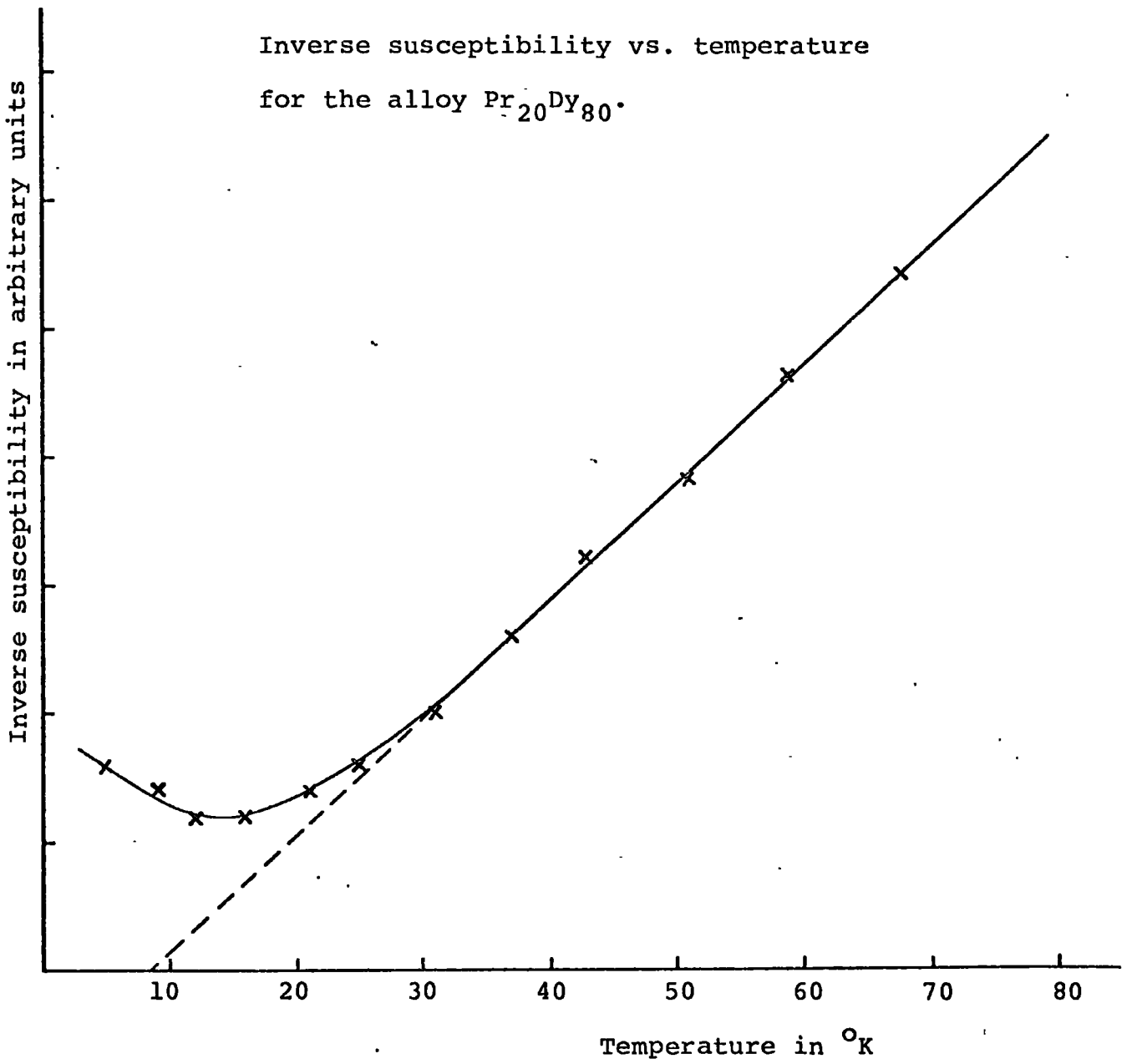
Inverse susceptibility vs. temperature
for the alloy $Pr_{20}Dy_{80}$.
Inverse susceptibility in arbitrary units
10
20
30
40
50
60
70
80
Temperature in °K

FIG. 5.21

TABLE 5.9

OBSERVED AND THEORETICAL PARAMAGNETIC MOMENTS AND TEMPERATURE AXIS INTERCEPTS T' FOR SOME LIGHT-HEAVY RARE EARTH ALLOYS

Alloy	μ(obs.)$\pm$ 0.3μ_B	μ (theo.)	T' $\pm$ 0.5^{o}
$Pr_{99}Tb_{01}$	3.7	3.6	21.5
$Pr_{95}Tb_{05}$	4.1	4.0	15.5
$Pr_{90}Tb_{10}$	5.7	4.5	13.0
$Pr_{70}Tb_{30}$	9.6	6.0	-1.0
$Nd_{90}Dy_{10}$	5.9	4.7	3.0
$Nd_{80}Dy_{20}$	6.8	5.6	0.5
$Pr_{80}Dy_{20}$	6.1	5.6	8.5

previously by Thoburn et al (1958) and Finnemore et al (1968) (in La-Gd alloys) and Fradin et al (1968) (in Sc-Gd alloys). Also shown are the temperature axis intercepts for each of the alloys from the inverse susceptibility vs. temperature plots.

The temperature axis intercept T', may be identified with the paramagnetic Curie point, θ'. For a ferrimagnetic alloy an expression was derived in Section 2.1 relating the paramagnetic Curie point to the Curie constants and exchange constants of the ions on the two sublattices (eqn. 2.17) giving

$$\theta' = - \frac{C_a C_b}{C_a + C_b} \left[x\lambda_{aa} + (1-x)\lambda_{bb} - 2\lambda_{ab} \right]$$

where a and b denote the two constituents of the alloy and x is the fractional concentration of constituent a. λ_{aa}, λ_{bb} and λ_{ab} are the exchange constants between ions on the same sublattice and ions on the different sublattices.

From the paramagnetic Curie points θ', given in Table 5.9, the exchange constants λ for the three interactions involved in the Pr-Tb system and the Nd-Dy system were calculated. The exchange constants are shown in Table 5.10. A complete set of data on the Pr-Dy alloy system was not available, but from a knowledge of λ(Pr-Pr) and λ(Dy-Dy) obtained for the Pr-Tb and Nd-Dy alloy systems the value of λ(Pr-Dy) was calculated from the paramagnetic Curie point of the inverse susceptibility vs. temperature plot for the alloy $Pr_{20}Dy_{80}$.

TABLE 5.10

OBSERVED AND CALCULATED EXCHANGE INTEGRALS

Element		I (obs.) in eV	I (calc.) in eV
Pr-Pr	$(0.69 \pm 0.02) \times 10^{3}$	$(5.7 \pm 0.2) \times 10^{-5}$	2.3×10^{-5}
Nd-Nd	$(0.75 \pm 0.02) \times 10^{3}$	$(5.2 \pm 0.2) \times 10^{-5}$	1.7×10^{-5}
Tb-Tb	$(1.47 \pm 0.02) \times 10^{3}$	$(4.6 \pm 0.3) \times 10^{-4}$	4.0×10^{-4}
Dy-Dy	$(1.13 \pm 0.02) \times 10^{3}$	$(2.9 \pm 0.3) \times 10^{-4}$	4.4×10^{-4}
Pr-Tb	$(0.49 \pm 0.02) \times 10^{3}$	$(8.8 \pm 0.2) \times 10^{-5}$	5.7×10^{-5}
Pr-Dy	$(0.45 \pm 0.02) \times 10^{3}$	$(3.5 \pm 0.2) \times 10^{-5}$	0.9×10^{-5}
Nd-Dy	$(0.42 \pm 0.02) \times 10^{3}$	$(9.8 \pm 0.2) \times 10^{-5}$	3.6×10^{-5}

Using eqn. 2.21 the macroscopic exchange constants λ were converted into exchange integrals between neighbouring ions. These derived exchange integrals for the pure metals are also shown in Table 5.10, compared with the exchange integrals evaluated for the pure metals from eqn. 2.4 using the known Curie temperatures of the pure metals. The tabulated inter-ionic exchange integrals are derived for a 50% alloy composition and they are compared with the theoretical exchange integral evaluated using the observed Néel point of that alloy. For the light-heavy rare earth series the 50% alloy falls in the Sm. phase, (see Sections 5.2(ii)& 6.2). From the table it can be seen that the exchange integrals derived from the dhcp alloys are in good agreement with those obtained from eqn. 2.4.

Finally, the derived exchange constants were substituted into the expression for the ferrimagnetic Néel point derived for the alloy systems (eqn. 2.18). The Néel termperatures predicted by this expression increase with increasing heavy rare earth content, but their absolute value is not the same as is observed experimentally.

CHAPTER 6

DISCUSSION OF RESULTS

In this chapter the experimental results on the light-heavy rare earth alloys given in Chapter 5 will be discussed in terms of the theory of magnetic ordering in the rare earth metals presented in Chapter 2. Following the same format as in Chapter 5, the discussion will be presented with reference to the three crystallographic phases of the light-heavy rare earth alloys.

6.1 H.C.P. PHASE

6.1(i) Variation of the Néel temperature on alloying

The R.K.K.Y. interaction which is responsible for the long range periodic spin structures in the rare earths and their alloys may be written as,

$$I(r_{ij}) = \frac{9Z\pi}{2\Omega} A^2 N(\varepsilon_f) \phi (2k_f R_{ij}) \qquad \ldots(6.1)$$

where $N(\varepsilon_f)$ is the density of states at the Fermi surface and the other symbols are as defined in Section 2.4. On alloying i.e. changing the interionic distances, the terms A^2, $N(\varepsilon_f)$ and $\phi(2k_f R_{ij})$ can be expected to change.

Assuming that the ground state energy of the antiferromagnetic phase is given by

$$E = \Omega I(r_{ij}) \langle J \rangle$$

where $\langle J \rangle$ is the average spin variable operating in the

alloy at that temperature, then for a two component magnetic system

$$E = 3kT_N = \frac{9\pi Z}{2}\left[xA_1^2 + (1-x)A_2^2\right]N(\varepsilon_f)\sum_{ij}\phi(2k_fR_{ij}).\bar{G} \quad \ldots(6.2)$$

where $\bar{G} = \sum_{\alpha=1}^{2} c_\alpha(g_\alpha-1)^2 J_\alpha(J_\alpha+1)$

The suffices $_1$ and $_2$ refer to the two components and $N(\varepsilon_f)$ and k_f are the density of states and Fermi wavevector of the alloy respectively.

A plot of T_N vs. $\bar{G}$ is a straight line (see Fig. 5.12) for the heavy rare earths, the heavy-heavy alloys and the light-heavy alloys. This implies that the dominant feature in the variation of the ordering temperature on alloying is the change in the de Gennes function or average de Gennes function for the alloys. Closer examination of Fig. 5.12 reveals small deviations of the light-heavy rare earth alloys from ideality becoming more pronounced with increasing light rare earth addition. These small effects may be ascribed to changes in A^2_{ave}, $N(\varepsilon_f)$ and $\sum_{ij}\phi(2k_f R_{ij})$ with increasing c/a ratio. The heavy-heavy rare earth alloys would not be expected to show any deviation as the change in c/a ratio across the entire composition range is negligible.

To examine the dependence of the exchange interaction on alloying it is necessary to remove the dominating effect of the de Gennes function. A quantity which is independent

of the value of the effective spin variable operating in the material is the turn angle and any changes in the exchange due to alloying would be reflected in this term.

6.1(ii) Variation of the initial turn angle on alloying

The variation of the initial turn angle, ω_i, with the c/a ratio of some light-heavy rare earth alloys, the heavy rare earth metals and some heavy rare earth -Y alloys is shown in Fig. 5.13 (see Section 5.2(i)). Observation of a turn angle ω implies that a stable helical spin structure exists in the material. The stabilisation of a helical spin structure in the anti-ferromagnetic region of the rare earth metals is due to the occurrence of a maximum in the generalised susceptibility function $\chi(\bar{q})$, for some vector $\bar{q} > 0$ and directed along the c-axis of the hcp structure (see Section 2.5). The value of the vector $\bar{q}$ maximising $\chi(\bar{q})$ has been identified with the vector calipering the webbing feature in the Fermi surface. The feature of the magnetic structure stabilised by the maximum in $\chi(\bar{q})$ at $\bar{q}_0$ is the wave vector of the helical structure, for which the observable turn angle is given in terms of the lattice parameter c, by

$$\omega_i = \bar{q}_0 c \qquad \ldots(6.3)$$

On alloying, this webbing feature is clearly retained, but the width of the webbing, as measured by the magnitude of the turn angle, is reduced. Equivalently the effect of

alloying may be visualised as stabilising a new helical spin structure in the heavy rare earth alloys which occurs at a maximum in $\chi(\bar{q})$ for a value of $\bar{q}_o$ smaller than the value of $\bar{q}_o$ in the pure metal.

Fleming and Liu (1970) have used the dependence of the details of the band structure (and hence $\chi(\bar{q})$) on the axial ratio, c/a, of the hexagonal close packed lattice to determine the variation of the turn angle with pressure for the rare earth metals. The high pressure values of the lattice parameters were derived using experimental data for the elastic constants. On the basis of these calculations the theoretical value of $\frac{d\omega}{dp}$ for Tb was shown to be in close agreement with the experimental neutron diffraction data of Umebayashi et al (1968).

It is unclear from the original data of Umebayashi et al how this close agreement between the experimental value of $\frac{d\omega}{dp}$ and the theoretical value of $\frac{d\omega}{dp}$ due to Fleming and Liu is obtained, as the sign of $\frac{d\omega}{dp}$ determined by each author is different. The work of Fleming and Liu implies a decrease in the initial turn angle with pressure, whilst the data of Umebayashi shows an increase in the initial turn angle. The difference almost certainly arises from the evaluation of the high pressure lattice parameters in the antiferromagnetic region. Tb undergoes very rapid changes in both c/a and directional compressibility on ordering due to the large magnetoelastic constants. It is clear from eqn. 6.3 that the wrong choice of axial

lattice parameter for that temperature and pressure will give the incorrect value for the initial turn angle. In spite of this shortcoming however, the model calculation itself appears to be capable of predicting the dependence of some of the magnetic properties of the metal on pressure, or more directly on the c/a ratio of the metallic system, through the dependence of position and height of the peak in $\chi(\bar{q})$ on the c/a ratio of the metal. Further, of course, since p and c/a are directly related, the model is applicable to alloy systems in which both c/a and ω change as a result of alloying.

In the Pr-Tb and Nd-Tb alloy systems the magnetoelastic interactions are likely to decrease as the addition of a light rare earth serves to dilute the magnetic properties of the heavy rare earth. It should be possible to use the results of Fleming and Liu to compare the predictions of their model with the observed variation of the turn angle on alloy composition, since the values of $\frac{d\omega}{dp}$ can be taken to be correct for the c/a values used in the derivation.

The observations of the Tb-Pr and Tb-Nd systems show that the antiferromagnetic state becomes unstable with addition of the light rare earth component. At sufficiently high concentrations only ferromagnetic ordering is observed indicating that the turn angle has decreased to zero. Assuming that ω_i decreases linearly with increasing c/a i.e. with increasing pressure, and

that there is a direct equivalence between increasing pressure and increasing c/a ,then using the theoretical value of $\frac{d\omega}{dp} = -0.23$ deg.kbar^{-1} derived by Fleming and Liu, it is readily shown that the limiting value of c/a at which the turn angle is reduced to zero is c/a = 1.586.

Measurements of the axial ratio and ordering temperatures for the two series of alloys are shown in Fig. 6.1 (The 20% Nd-Tb sample was prepared from a different batch of elemental Tb than the other specimens in this series. This Tb consistently gave anomalous lattice parameters from the Tb used for the other specimens across the entire composition range. We believe this may be associated with the source material as supplied by various distributors. This is consistent with the findings of other laboratories (Harris 1970). In consequence greater weighting is given to the low Nd concentrations in drawing the experimental curve). From the figure it is clear that in the Tb-Pr system, extremely good agreement is obtained between the predicted and observed values of the critical c/a ratio for which ω becomes zero and the antiferromagnetic state disappears. The results for the Tb-Nd system show some divergence however, the limiting composition observed experimentally being 16%Nd, whereas the predicted composition deduced from the critical c/a value is close to 20% Nd.

It would have been interesting to compare the observed variation of the turn angle in comparable Dy alloys with

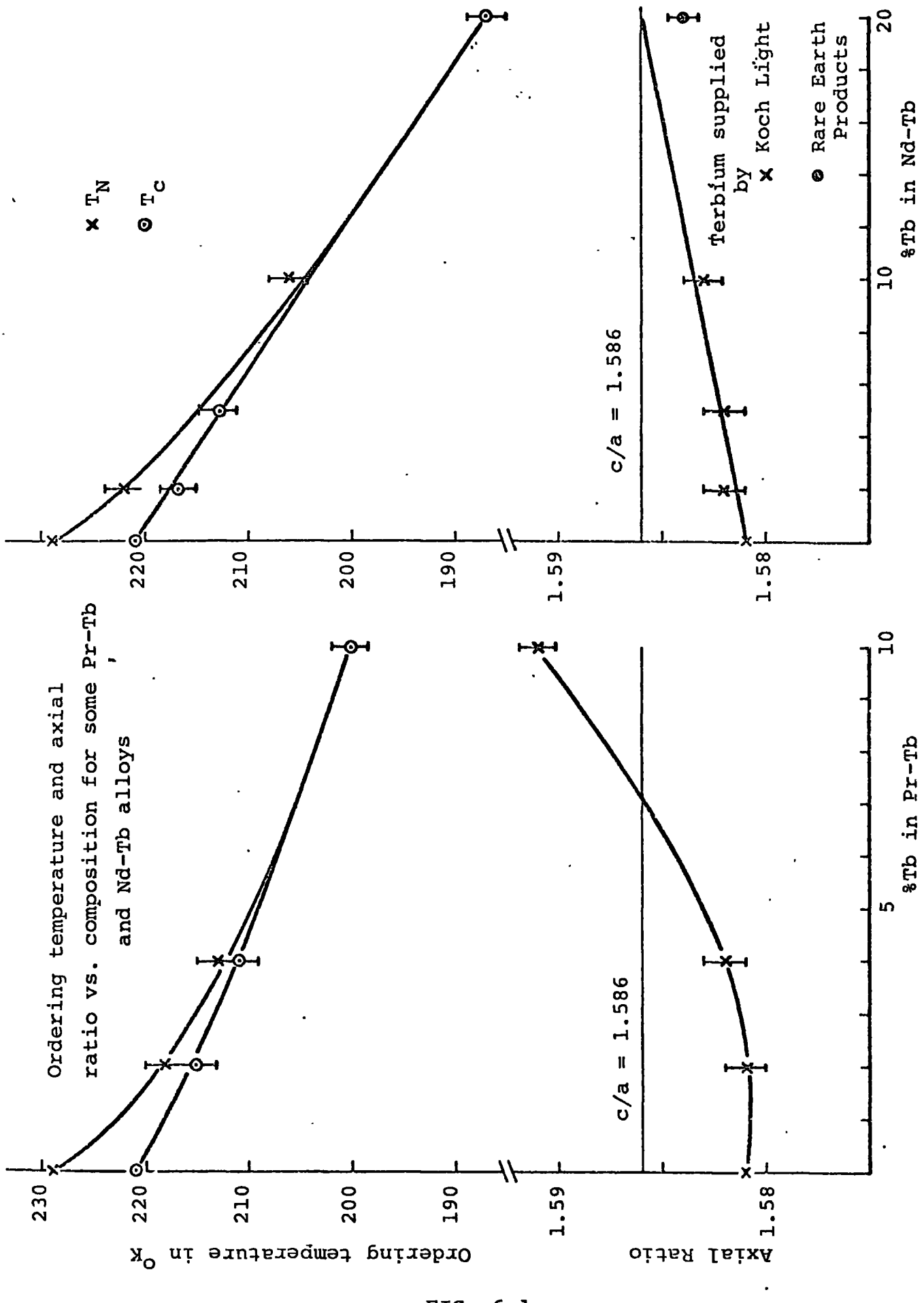
Ordering temperature and axial ratio vs. composition for some Pr-Tb and Nd-Tb alloys
Ordering temperature in °K
Axial Ratio
× T_N
⊙ T_c
c/a = 1.586
Terbium supplied by
× Koch Light
● Rare Earth Products
%Tb in Nd-Tb
%Tb in Pr-Tb
230
220
210
200
190
1.59
1.58
5
10
20

FIG. 6.1

the value of $\frac{d\omega}{dp}$ $\left[\equiv \frac{d\omega}{d(c/a)}\right]$ predicted by Fleming and Liu, however, the range of c/a values used in the theoretical work is too small to allow reliable extrapolation over the range observed in the neutron diffraction studies. Crude estimates can be made by converting the observed lattice parameters to a volume change and therefore to an effective applied pressure, using the compressibility date of Gschneidner (1961). This leads to experimental values of $\frac{d\omega}{dp}$ = - 0.57°/kbar (Dy-Pr) and - 1.8°/kbar (Dy-Nd) which are to be compared with the predicted figure of $\frac{d\omega}{dp}$ = - 0.38°/kbar. The form of the agreement here is probably all that can be expected in view of the rather large approximations made.

The expression for the interlayer turn angle is given by (see Section 2.2)

$$\cos \omega_i = - \frac{I(1)}{4I(2)} \qquad \ldots(6.4)$$

Using the free electron model for the exchange interaction given by eqn (6.1) the variation of the exchange with pressure may be written as

$$\frac{dI(r_{ij})}{dp} = \frac{dA^2}{dp} + \frac{dN(\varepsilon_f)}{dp} + \frac{d\Sigma\phi}{dp}\ (2k_f\ R_{ij}) \qquad \ldots(6.5)$$

In the model proposed by Fleming and Liu no account is taken of the variation of the first term, the s-f interaction potential, with pressure. Various authors have considered it and either assumed it was constant or

very small (Liu 1962, Bloch and Pauthenet 1964, Darby and Taylor 1966). More recently Lindgard et al (1975) have shown that A is in fact dependent on the scattering vector $\bar{q}$ and may not be treated as a constant. Evaluation of A in the light heavy rare earth alloys is further complicated since the 4f shell of the light rare earths is far more extended than in the heavy rare earths and this fact may make the interaction potential A, concentration dependent.

It appears then, that there are two main processes affecting the magnetic ordering on alloying. The first, and by far the major contribution, is the reduction in de Gennes function in the alloy. Secondly, there is the effect of the change in the axial ratio on the exchange interaction via the modification of the electronic energy bands in the alloy.

In the following subsections we go on to discuss some of the other observed magnetic properties of the hcp light-heavy rare earth alloys.

6.1 (iii) Variation of the helical turn angle with temperature.

The heavy rare earth metals, their alloys with Y and with each other all exhibit a decrease in the interlayer turn angle with decreasing temperature. This behaviour has been attributed to the appearance of super zone boundaries which cut the Fermi surface and thus modify the exchange (see Section 2.5(i).)

Neutron diffraction experiments on the Ho and Dy based alloys in the hcp phase indicate that the turn angle

does not vary from its initial value by more than 5 degrees throughout the entire antiferromagnetic region (see Tables 5.3 and 5.5). Since a helical spin structure is observed in the alloys,it must be assumed that the webbing feature of the Fermi surface is retained on alloying and further if the super zone boundaries still exist they must cut the webbing (see Fig 6.2). The width of the webbing is proportional to the length of the vector $\bar{q}_o$ and the webbing feature occurs symmetrically placed about AH in the middle of the Fermi surface in the double zone scheme. For a turn angle of 30^o, say, $\bar{q}_o = 0.33(\pi/c)$ and the super zone boundaries occur at distances along ΓAΓ proportional to the length of the vector $k = \pm n \frac{2\pi q}{12c}$. Thus there must be six super zone boundaries between Γ and A. Since the width of the webbing is $\bar{q}_o$ then there are two super zone boundaries which cut the Fermi surface. On this basis the turn angle should vary with temperature, even though the magnetisation, and thus the width of the super zone boundaries, is small in the antiferromagnetic region of the light-heavy rare earth alloys.

It can be seen from Fig. 6.2 that whereas the super zone boundaries lie close to the webbing feature in Dy they are actually coincident with the flat region of the webbing surface in Nd_{30} Dy_{70}. In Dy the energy discontinuities associated with the super zone boundaries perturb the Fermi surface and alter the value of the s-f interaction via a redistribution of the conduction electrons

Fermi surface of Dy (after Keeton and Loucks) simply extended to a Dy alloy.

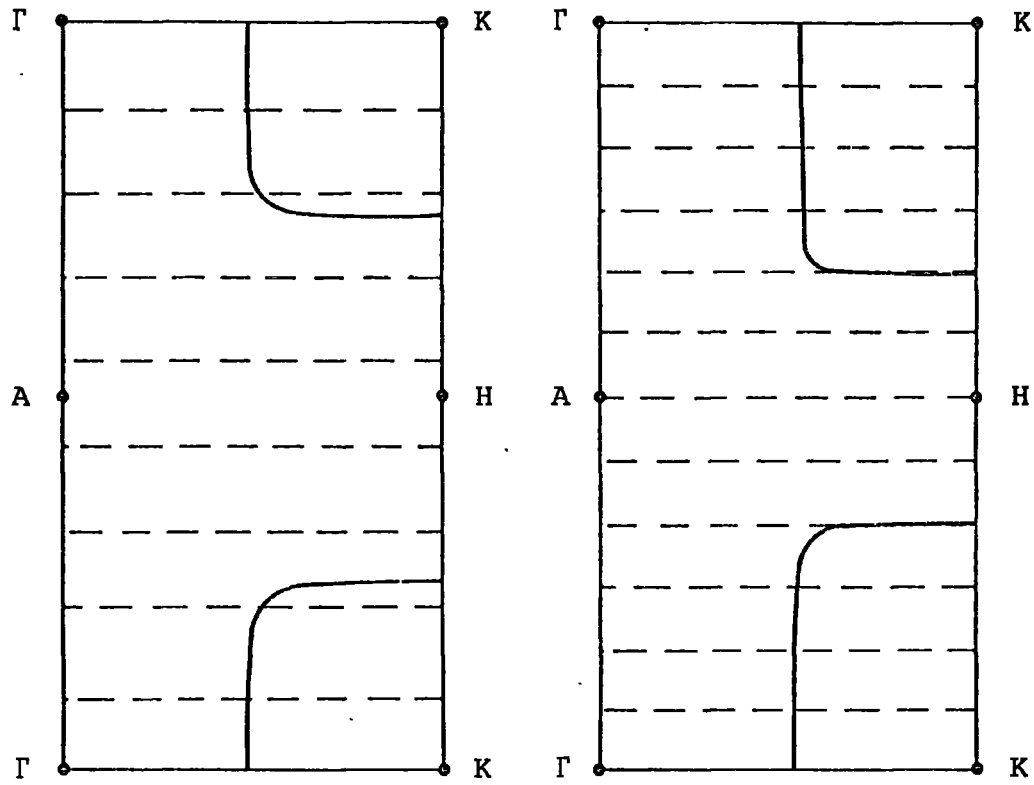

Dy

$q_o = 0.47\ (\frac{\pi}{c})$

$k_z = \pm\ n\frac{2}{9}\ (\frac{\pi}{c})$

$Nd_{30}Dy_{70}$

$q_o = 0.33\ (\frac{\pi}{c})$

$k_z = \pm\ n\frac{2}{12}\ (\frac{\pi}{c})$

FIG. 6.2

across the energy gap. In the alloy Nd_{30} Dy_{70} the super zone boundaries do not actually cut the Fermi surface but lie parallel to it. In this case there is no significant perturbation of the Fermi surface and the magnitude of the s-f interaction is unchanged.

It is unlikely that the super zone boundaries would have no effect at all as the webbing feature is not ideally flat as shown in the figure. The effect, however, would be small and could account for the slight changes in the turn angle with temperature.

6.1 (iv) Variation of the critical field with temperature

The theory of Nagamiya et al (1962) and Kitano and Nagamiya (1964) which explains the observed temperature dependence of the critical field of the heavy rare earths, is based on the assumptions that there is a large axial anisotropy confining the spins to the basal plane and that the spiral is composed of identical atoms (see Section 2.3). The critical field is then given by

$$H_c = - 7.76\mu_s I(2)\sin^4\omega/2 \qquad \ldots(6.6)$$

where μ_s is the spontaneous magnetic moment per ion. If the addition of a light rare earth serves merely to dilute the exchange, and as a consequence change the turn angle, then the critical field will rise rapidly with increasing temperature from the Curie point as in pure Dy. The Pr_{10} Dy_{90} and Nd_{10} Dy_{90} alloys show this behaviour. (see Fig. 5.10a). Neutron diffraction

experiments on the alloys Pr_{30} Dy_{70} and Nd_{30} Dy_{70} indicate that the turn angle is almost constant with temperature over the entire helical spin region. This implies that the exchange, $I(r_{ij})$ is constant and that the critical field, H_c, for the alloys should increase with decreasing temperature in the same way that the spontaneous magnetisation increases with decreasing temperature. This is not observed to be the case and the critical field shows a peculiar dependence upon temperature (see Fig. 5.10b).

For the two alloys Pr_{30} Dy_{70} and Nd_{30} Dy_{70} the assumptions on which the theory of Kitano and Nagamiya are based may be invalidated. Firstly, the axial anisotropy may be relaxed on alloying a light rare earth with a heavy rare earth. The c/a ratio of the two alloys is much closer to the theoretical value of c/a for the ideal hcp structure than the c/a ratio of the parent heavy rare earth and, in the notation of Kasuya (1966) (see Section 2.7.), the value of v_2^0 decreases by 30% which implies that the leading term in the axial anisotropy, B_2^0, changes by a similar amount, whereas the in-plane anisotropy increases slightly through the term v_6^6. For a sufficiently large applied field at high enough temperature the moments may be pulled out of the basal plane to achieve a ferromagnetic alignment. Secondly, the spiral is not uniform, but contains a significant number of light rare earth ions. In the rare earth metals the spin, $\underline{S}$, and the

total angular momentum, $\underline{J}$, are not always parallel to one another. Because of the strong Russell-Sanders coupling, it is necessary to project $\underline{S}$ onto $\underline{J}$ through the relationship (see Section 1.4)

$$\underline{S} = (g_J - 1)\ \underline{J}$$

For the light rare earths the factor $(g_J - 1)$ is negative and for the heavy rare earths it is positive. Thus, the spin is aligned parallel to the total angular momentum in the heavy rare earths and antiparallel to the total angular momentum in the light rare earths. In an applied magnetic field the moments on the Pr and Dy ions are forced to align parallel to one another, thus causing the spins on the different ions to lie anti-parallel, since the applied field cannot break the Russell-Saunders coupling. This would have the effect of distorting the fan structure.

Below 100K both $Pr_{30}\ Dy_{70}$ and $Nd_{30}\ Dy_{70}$ have critical field values which decrease rapidly with decreasing temperature, showing a behaviour similar to that observed in pure Dy. It may be assumed that below this temperature the axial anisotropy is large enough to restrain the spins to the basal plane and in this temperature region the effect of the slight change in turn angle with temperature is observed.

The variation of the exchange parameters I(1) and I(2) with temperature for the alloys $Dy_{70}\ Pr_{30}$ and

Nd_{30} Dy_{70} is shown in Fig 5.11. These exchange parameters have been calculated from eqn. 6.5 and 6.4 using the observed values of the turn angle and critical field. Since the turn angle is almost constant then the variation of I(1) and I(2) probably reflects the behaviour of the critical field, H_c,in these alloys.

6.1(v) Low temperature ordering

The Curie temperatures of the Tb and Dy alloys, and the spin re-orientation temperature of the Ho alloys, decrease with increasing light rare earth content i.e. with increasing c/a ratio, except in the case of Nd-Dy alloys with low Nd content in which the Curie temperature rises initially and then falls, (see Figs. 5.3 to 5.8). The Curie temperature of Dy under pressure (Robinson et al 1966) and of some Dy rich Dy-Gd alloys under pressure (Milstein and Robinson 1967), increases for small increases in hydrostatic pressure (<5kbar) and then decreases with further increases in pressure. The behaviour of the Dy rich Nd-Dy alloys can be seen to be consistent with this, bearing in mind that the application of hydrostatic pressure to a heavy rare earth is equivalent to alloying it with a light rare earth.

When plotted against the reduced de Gennes function the Curie temperatures show no general behaviour like the Néel temperatures, rather each alloy system separately shows a linear relationship with the reduced de Gennes function for that alloy system. This implies

that the dominant feature in the reduction of the Curie point on alloying a heavy rare earth with a light rare earth, is the reduction in the de Gennes function as it is in the reduction of the Néel point on alloying. A plot of $T_c/\overline{G}$ vs. c/a for the light-heavy rare earth alloys does not reveal any general behaviour either. This suggests that the exchange is determined by a further term in eqn. 6.1. This term is probably a contribution due to the crystal field and would be different for each alloy system.

At 4.2K the ordered spin structures of the alloys examined by neutron diffraction were found to be identical to that observed in the parent heavy rare earths. Since both components of any of the alloys studied have anisotropy energies which favour the spins remaining in the basal plane this result is not surprising, though the values determined for the axial component of the moment in the ferromagnetic cone structure of Pr_{20} Ho_{80} and Nd_{20} Ho_{80} (see Table 5.5) suggest that there is a slight relaxation of the axial anisotropy due to light rare earth addition (see also Section 6.1(iv)).

The net moments evaluated for all the ferromagnetic spin structures are consistent only with an antiparallel alignment of the light rare earth moment and the heavy rare earth moment, assuming that each component has its full ionic moment. Since the spins are aligned ferromagnetically then the moments will be aligned antiparallel

(see Section 6.1(iv)) and the net moment in the alloy will be the difference between the full ionic moments of each species multiplied by their appropriate compositions in the alloy.

6.2 SM PHASE

The magnetic properties of the light-heavy rare earth alloys in the Sm phase are a direct result of the unique crystal structure of that phase. At the hcp-Sm phase boundary the ferromagnetic structure of the alloys (ferromagnetic cone structure in the case of the Ho based alloys) disappears and is replaced by an antiferromagnetic structure which is retained to 4.2K. The turn angle of the structure is approximately 60^{o} for all the alloys regardless of constituents and varies only slightly between the ordering temperature and 4.2K. The magnetic structure of the alloys in the Sm phase at 4.2K is one in which the net moments on each layer lie in the basal plane, but are amplitude modulated along the c-axis. The value of the turn angle of the modulation is 60^{o} which implies that the net ordered moment on every third layer is zero (see Fig. 5.15). This layer can be identified with a cubic site layer in the Sm structure, (see Appendix A2).

The complexity of the Sm phase magnetic structures is due in part to the existence of two structural domains in any material adopting the Sm structure. The two domains are equally populated over the crystal and differ only

by a rotation of 180° about the normal to the layers, i.e. the c-axis. Thus if the first domain has a stacking sequence ABABCBCAC... then the second domain will have the stacking sequence ACACBCBAB... A basal plane spiral magnetic structure with a turn angle of 60° propagating in each of the two domains will appear to rotate in opposite directions around the c-axis. The resultant will be a structure with zero net moment on every third site (see Fig. 6.3). The molecular field at this site will also be zero since the moments on two adjacent hexagonal sites are parallel to one another, and antiparallel to the moments on the next two adjacent hexagonal sites.

The derived magnetic structure for the Sm phase alloys is similar to that of pure Sm itself; except that in pure Sm the ferromagnetically aligned moments are perpendicular to the hexagonal layers. The structure is thus uniaxial and does not give rise to $(00\ell)^{\pm}$ satellites, whereas these satellites are observed in the light-heavy rare earth alloys in the Sm phase. Since the two constituents of the light-heavy rare earth alloys both favour moments lying in the basal plane, it could be expected that the moments in the Sm phase alloys would adopt this structure too.

The moments on the Sm phase alloys at 4.2K are all larger than those predicted theoretically by a magnetic structure in which the moments on the two species are antiparallel and which assumes that each rare earth

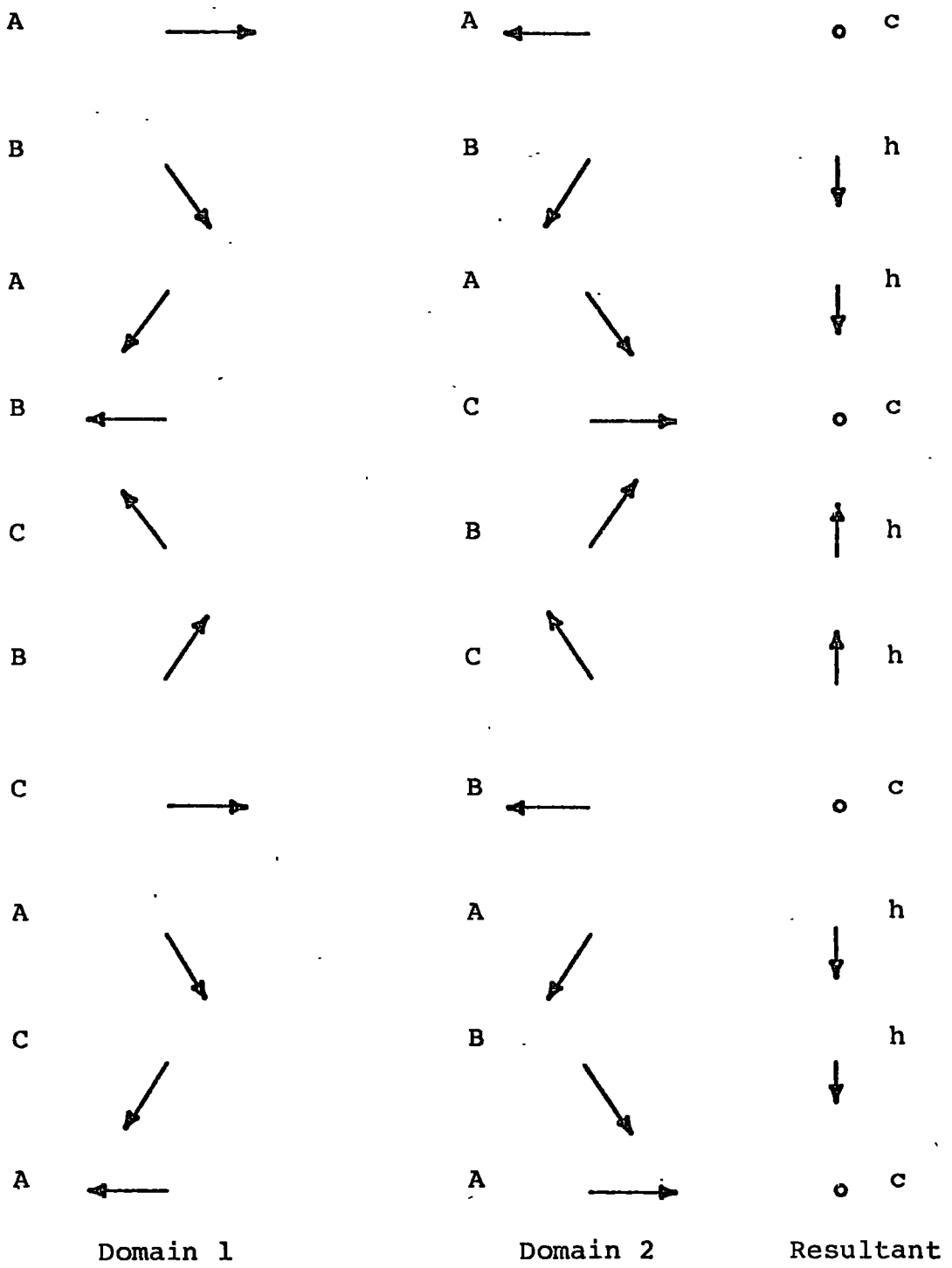

FIG. 6.3 Spin structure of Sm. phase alloys

moment adopts its full ionic value. On the simple Weiss molecular field model of magnetism (see Section 2.1) the exchange field responsible for the ordering in the Sm phase alloys is given by

$$H_{ex} = \frac{3kT_N}{g(J + 1)\mu_B} \qquad \ldots(6.7)$$

where k is Boltzman's constant, T_N, g and J are the Néel temperature, Landé g factor and total angular momentum of the alloy respectively.

For $Pr_{45}Tb_{55}$ H_{ex} = 72T which is in excess of the magnetic field responsible for crystal field level crossing and hence spontaneous magnetic ordering in Pr, (see Section 2.8). Thus it may be assumed that the moment on the Pr ion adopts its full ionic value in $Pr_{45}Tb_{55}$. Assuming that Tb adopts its full ionic moment value then the magnetic moment of the alloy determined from neutron diffraction is consistent only with a non-collinear alignment of the Tb and Pr moments and the angle between the moment directions is deduced to be 150^{o}. The observed easy directions of magnetisation in pure Tb and pure Pr are the b and a directions respectively which lie at an angle of 30^{o} to each other in the basal plane. The observed value of the moment in the alloy implies that the Pr and Tb ions retain their own identity at 4.2K despite being alloyed together.

The exchange field operative in the Dy and Ho-light rare earth alloys is much less than in the Tb alloys

and is probably insufficient to saturate the ionic moment on the light rare earth component. Good agreement between the observed value of the moment and the theoretically predicted value,on a collinear antiparallel moment structure, is obtained if it is assumed that the heavy rare earth adopts its full ionic moment value and the light rare earth a moment value 2/3 of its ionic value. From the moment values, then, it is not possible, except in the case of $Pr_{45}Tb_{55}$, to state whether the light rare earth and the heavy rare earth moments are collinear or at some angle to one another. It was not possible to evaluate the moment on the alloy $Nd_{60}Tb_{40}$ because of the extra scattering which obscured the satellite peaks below 70K. The fact that both the Pr and Nd ions do not take their full moment values in the Dy and Ho alloys at 4.2K may be associated with crystal field quenching of the light rare earth moments in these alloys.

The anomalous scattering in the alloys $Pr_{45}Tb_{55}$ and $Nd_{60}Tb_{40}$ can be discussed in terms of scattering from some extra ordering which appears in the structure at low temperature. We assume that $Nd_{60}Tb_{40}$ has the same magnetic structure as the other Sm phase light-heavy rare earth alloys.

Although there is no net moment on the cubic site layers, within the layers there is an ordered magnetic structure. Following Koehler and Moon (1972) we assume that the moments in the layers become coupled to the

moments in the adjacent cubic layers forming an ordered magnetic structure throughout the crystal on a hexagonal lattice,with 3 atoms per unit cell and a stacking sequence ABCABC... along the c-axis. The coupling between layers is quite weak in comparison with the in-plane exchange as adjacent cubic site layers are over 8.5A^{O} apart. The extra scattering in the Tb-light rare earth alloys may be associated with scattering from this new ordered structure.

On the basis of the crystal field term V_6^6 which has the same sign for Nd and Tb it is assumed that the moments on the Nd and Tb ions are aligned antiparallel. Then the net zero moment on a cubic site layer may be assumed to be composed of adjacent rows of antiferromagnetically aligned ions as in Fig. 6.4(a). The ions then couple together ferromagnetically,parallel to the 101 plane as shown in Fig. 6.4(b). The observed diffraction pattern of $Nd_{60}Tb_{40}$ shows two large peaks at angles corresponding to the (200) and (209) reflections in a magnetic unit cell which is double the size of the chemical unit cell in the c-direction and along one of the basal plane axes. This structure also predicts peaks corresponding to an antiferromagnetic structure along the c-axis. Since these cubic site layers are 26A^{O} apart,the scattered intensity can be expected to be weak which may account for the fact that it is not observed in the diffraction pattern of $Nd_{60}Tb_{40}$.

The moments on the Pr ions and the Tb ions in $Pr_{45}Tb_{55}$

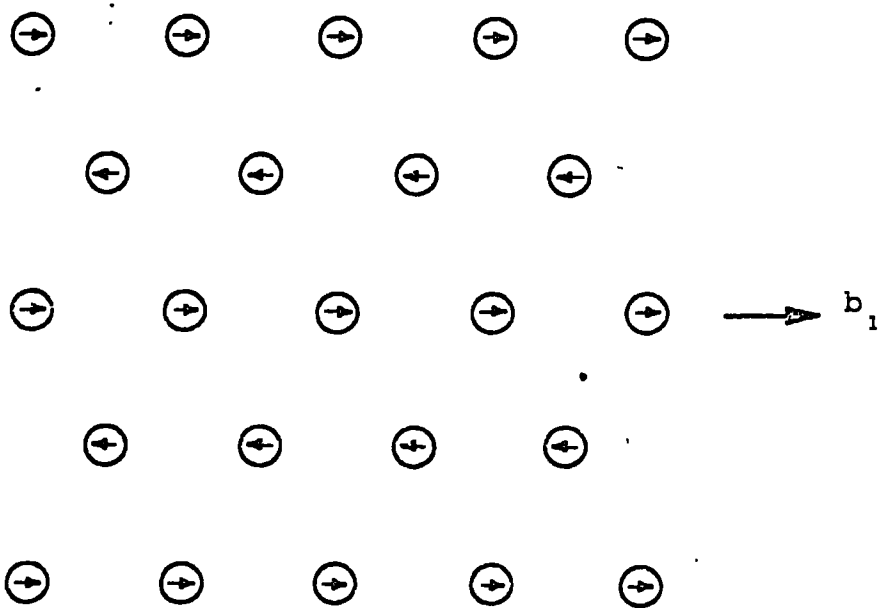

FIG. 6.4a
Spin structure on a cubic site layer

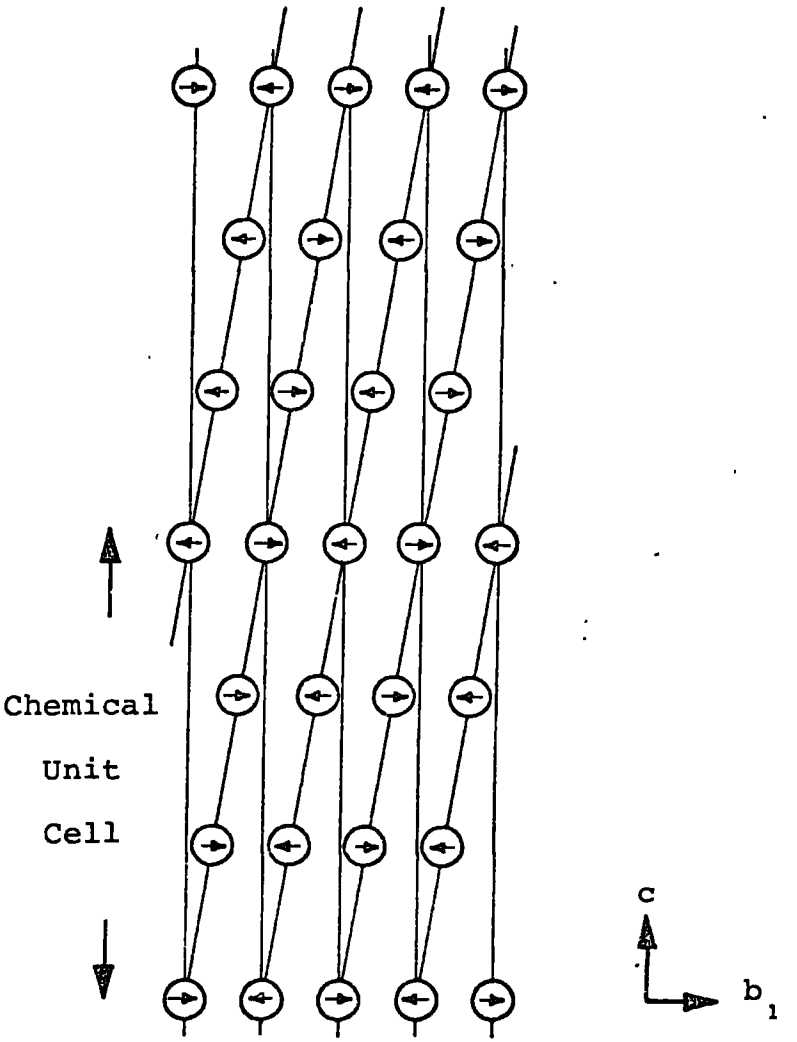

FIG. 6.4b
Coupling between cubic layers along the c-axis

are not collinear, which is consistent with the change in sign of V_6^6 between Pr and Tb, but lie at an angle of 150^o to one another. This implies that the spin structure on a cubic site layer so as to achieve a configuration with zero net moment will not be as simple as in Fig. 6.4(a). In turn,this may destroy the possibility of any long range order propagating on the cubic sites since the moment directions on adjacent cubic layers may not be the same. Regions of short range magnetic order may exist and the observation of a broad, diffuse peak in the diffraction pattern of $Pr_{45}Tb_{55}$ at an angular position corresponding to an (003) reflection in the nine layer Sm structure serves to confirm this. The temperature dependence of the broad peak intensity may be associated with the random distribution of ionic species on each layer resulting from alloying. Since the ordering on the cubic site layers is relatively unaffected by the hexagonal site ordering,at the Néel point there may still be the remnants of an ordered structure on the cubic sites. The much stronger Tb-Tb exchange as compared with the Pr-Tb or Pr-Pr coupling might serve to preserve the short range order to a temperature of approximately $2T_N$. Extra scattering above T_N which could be ascribed to short range order was not observed in the diffraction pattern of $Nd_{60}Tb_{40}$.

The modulated basal plane ferromagnetic structure has also been reported by Achiwa and Kawano (1973) for some Sm phase Tb-light rare earth alloys. Their results

are similar to those obtained in this investigation except that they do not observe any extra coherent neutron scattering in the diffraction pattern of the alloys down to 4.2K and conclude that the cubic site moments are disordered.

6.3 D.H.C.P. PHASE

It is clear from susceptibility vs. temperature results on the dhcp light-heavy rare earth alloys (see Figs. 5.3 to 5.8) that the addition of a small quantity of a heavy rare earth metal to either of the light rare earth metals Pr or Nd does not produce an immediate increase in the magnetic transition temperature. In fact,in the Pr based alloys initially the addition of a heavy rare earth metal suppresses the transition at 21K in pure Pr. In the Pr-Tb and Pr-Dy alloys however, for higher concentrations of heavy rare earth (> 5at.%) the magnetic transition temperature reappears and increases as the concentration of heavy rare earth increases. The ordering is weak as evidenced by the very small neutron diffraction peaks associated with the magnetic ordering at 4.2K, and it is not until a fairly high concentration of heavy rare earth is present (particularly $Pr_{70}Tb_{30}$) that the ordering is substantial.

The magnetic ordering in polycrystalline Pr is a result of the exchange coupling the ionic spins together via the conduction electron cloud (see Section 2.4). The Hamiltonian of the exchange interaction may be written

$$\mathcal{H}_{ex} = - (g-1)^2 \, I(r_{ij}) \, \underline{J}_i . \underline{J}_j$$

where the spin angular momenta $\underline{S}$ have been replaced by the total angular momenta $\underline{J}$. Similarly, the exchange between a light rare earth ion and a heavy rare earth ion may be written

$$\mathcal{H}'_{ex} = - (g_\ell - 1)(g_h - 1) \, I'(r_{ij}) \, \underline{J}_{i\ell} . \underline{J}_{jh}$$

where ℓ and h stand for light and heavy rare earth respectively. The factor (g-1) is negative for the light rare earths and positive for the heavy series, thus $\mathcal{H}'_{ex}$ has the opposite sign to $\mathcal{H}_{ex}$. Physically, this is because the charge cloud polarisation at a Pr ion due to another Pr ion is of opposite sign to that due to a Tb ion. Since $\mathcal{H}'_{ex}$ can be expected to be larger than $\mathcal{H}_{ex}$, then for small concentrations of heavy rare earth in a light rare earth the total exchange actually decreases, until the exchange field at a light rare earth ion site due to the magnetisation of the light rare earth sublattice is equal and opposite to the exchange field acting at that ionic site due to the magnetisation of the heavy rare earth sublattice i.e.

$$x \left| \mathcal{H}_{ex} \right| = (1-x) \left| \mathcal{H}'_{ex} \right| \qquad \ldots(6.8)$$

In the Weiss molecular field theory the exchange field at an ion site may be replaced by λM. Thus eqn. 6.8 may be re-written as

$$x \lambda_{aa} M_a = (1-x) \, \lambda_{ab} M_b$$

If two light rare earth metals are alloyed then the magnetic transition temperatures increase for all concentrations of one light rare earth in another as the exchange interactions both have the same sign and the total exchange is never identically zero. The measurements of McEwen et al (1973) on Pr-Nd alloys show that a single crystal alloy of 5.6% Nd in Pr has a transition temperature of 7K, which is consistent with the theory outlined above.

Since the sample of polycrystalline Pr used in this investigation has an ordering temperature of 21K it may be assumed to have a molecular field of 30.5T,as this is the value of the applied magnetic field which will cause crystal field splitting and hence magnetic ordering (see Section 2.8). The addition of Tb causes the effective molecular field to decrease from 30.5T to zero and then to increase in a negative sense. At 30at.% Tb long range antiferromagnetic order is observed by neutron diffraction and thus it may be assumed that this concentration of Tb is equivalent to a field at the Pr ion sites in the opposite direction to the Pr-Pr exchange field and magnitude 61.0T. (31.5T to reduce the Pr-Pr exchange to zero and a further 31.5T to cause crystal field level crossing). Using the Pr-Tb exchange constant determined in Section 5.4 (see Table 5.10) the exchange field at a Pr ion site due to the Tb sublattice may be evaluated from the expression

$$H_{ex} = 0.3\lambda\ (\text{Pr-Tb})\ M_{Tb}$$

and is of value 36.5T. To within a factor of 2 it appears

that the Tb sublattice does provide a strong enough exchange field to cause long range ordering in the alloy. The inelastic neutron scattering results shown in Fig. 5.17 are further evidence that the first excited crystal field levels on both the cubic and hexagonal sites are approaching the ground state and that some long range ordering will be established. The discrepancy between the experimental and theoretical molecular fields may be due in part to the fact that for a 30at.% Tb alloy the crystal field levels may have changed considerably,due to the contraction of the unit cell and crystal field level crossing may occur for fields less than 30.5T. Nevertheless, the agreement to within a factor of 2 between the observed and theoretical molecular fields is remarkable,in view of the assumptions made in deriving the exchange constants using a Weiss molecular field model of magnetism.

Using the exchange constants determined for the Nd-Dy alloys the molecular field at a Nd ion site due to the magnetisation of the Nd sublattice is 66T and the molecular field at that site due to the magnetisation of the Dy sublattice is 115T. From the preceding arguments the introduction of Dy will decrease the molecular field at a Nd site becoming zero for

$$xH_{ex}(Nd\text{-}Dy) = (1-x)\ H_{ex}(Nd\text{-}Nd)$$

which gives $x = 0.36$

The ordering in alloys with greater than 36at.% Dy

should show a single magnetic ordering temperature as the exchange is now dominated by the Nd-Dy interaction. Experimentally this behaviour is observed in the alloy $Nd_{70}Dy_{30}$ which displays only one ordering temperature and it is assumed that in this alloy the Nd-Dy exchange interaction is already dominating the Nd-Nd exchange interaction.

However, long range ordering is observed in the Nd based alloys before the critical concentration of heavy rare earth is reached. $Nd_{90}Dy_{10}$ orders ferrimagnetically with moments pointing 10^{o} out of the basal plane at 4.2K. This ordered structure can be associated with the total ordered structure due to ordering on the cubic and hexagonal sites. It is not possible from the powder neutron diffraction data to state unambiguously that all the moments i.e. on both cubic and hexagonal sites, point out of the basal plane at the same angle, due to the overlapping of the magnetic reflections. However, crystal field calculations (Fig. 6.5) show that there is a change in the direction of the easy axis of magnetisation away from the basal plane for a Nd ion on a hexagonal site. It is assumed that at the lower (cubic site) ordering temperature the cubic site moments align parallel with the hexagonal site moments. At the critical concentration the exchange is dominated by the heavy rare earth component and there is no longer any distinction between cubic and hexagonal sites.

As yet it is unclear why the susceptibility of the

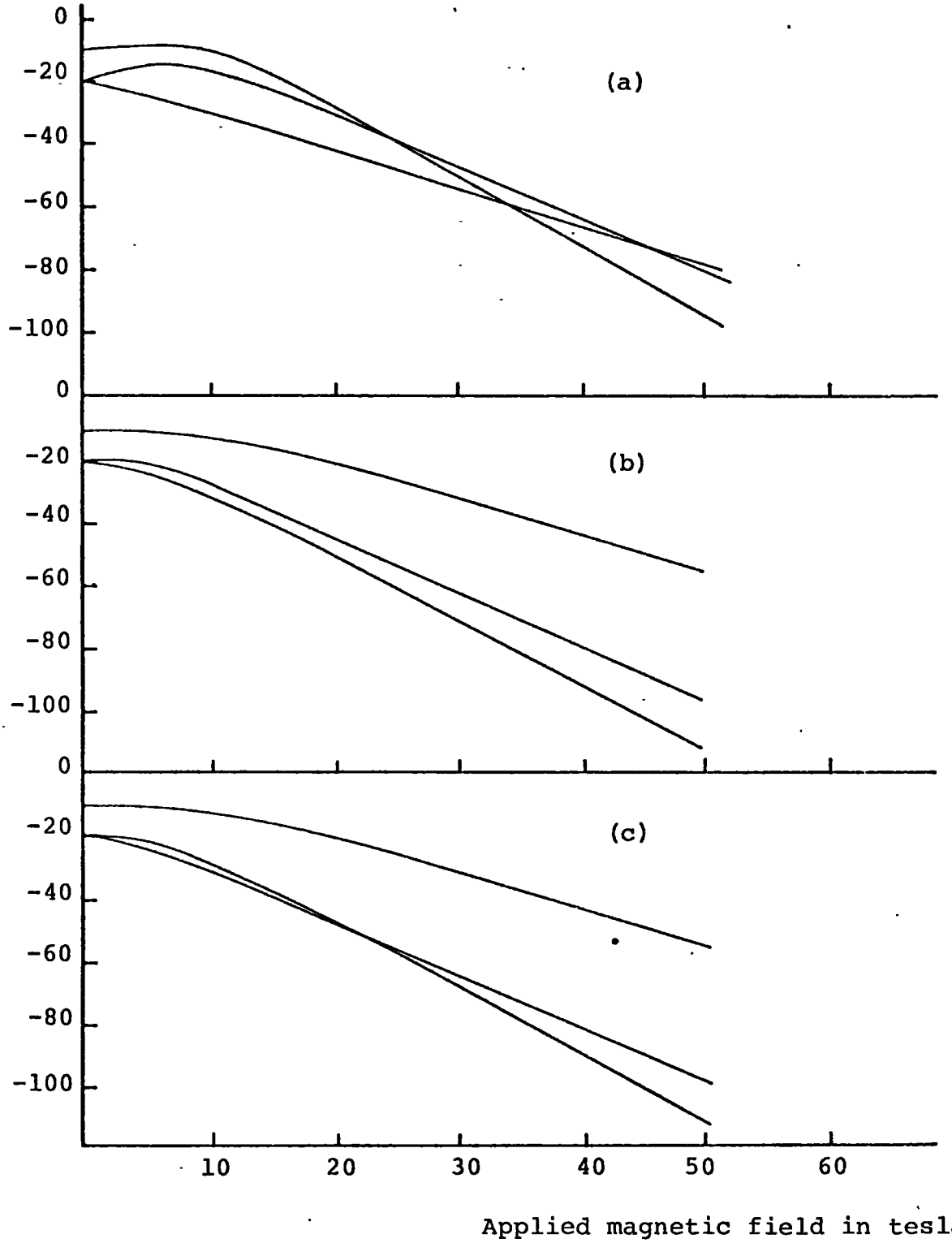

FIG. 6.5 Lowest crystal field split levels of Nd^{3+} ion in a hexagonal environment. External field applied (a) along c-axis (b) at 80^{o} to c-axis and (c) in the basal plane.

hexagonal site moments in pure Nd diminishes rapidly with low concentrations of Dy, disappearing completely for 5at.% Dy whilst another peak appears at a slightly lower temperature for alloys containing more than 2at.% Dy. (see Table 5.7). The change in the exchange, due to the change in the average number of Nd or Dy ions surrounding a Nd ion, accompanied by the change in anisotropy favouring a new direction of magnetisation may account for the decrease in one, and the appearance of the other signal from the hexagonal site moments.

6.4 SUMMARY OF RESULTS

The results obtained in this investigation show that alloys between the light and heavy rare earth metals form three distinct crystallographic and magnetic phases dependent upon the alloy composition.

In the heavy rare earth rich hcp alloys the light rare earth metal acts essentially as a simple magnetic diluent; the bulk magnetic properties of the alloys being an extension of the heavy rare earth metals through the dominating effect of the change in the de Gennes factor. The addition of a light rare earth metal does, however, cause a change in the axial ratio of the heavy rare earth metal which, in turn, shifts the energy bands in the material. The effect of alloying has been successfully correlated with the change in the generalised electron susceptibility $\chi(q)$ through observation of the change in the initial turn angle of the helical structure, ω_i, a quantity both independent

of the de Gennes factor and uniquely determined in neutron diffraction experiments. Using this model the stability of the helical phase in the Tb-light rare earth alloys has been explained.

The complex magnetic structure found for the alloys in the Sm phase (approximately equal proportions of heavy and light rare earth) which bears little resemblance to the magnetic properties of either constituent is determined by the unique crystallographic structure of the Sm phase. In all but the Tb-light rare earth alloys no indication was found of ordering on the cubic sites, but just on the hexagonal sites. By analogy with the magnetic structure of Sm metal itself a model for the cubic site ordering in Pr-Tb and Nd-Tb alloys is proposed.

The addition of a small quantity of a heavy rare earth metal to a light rare earth metal (such that the alloy remains in the dhcp crystallographic phase) does not produce an instantaneous increase in the magnetic ordering temperature of the dhcp light rare earth metal. The results have been successfully analysed on a two sublattice Weiss model of magnetism derived for a ferrimagnetic alloy. In this model the effective exchange field actually decreases with increasing heavy rare earth content due to the opposing directions of the charge cloud polarisation at a Pr ion site due to a Pr ion or a Tb ion.

The values of the exchange integrals in the alloys predicted by the model are in good agreement with those

derived from the magnetic transition temperatures of the pure metals. Further the model predicts the alloy composition for which there is a single ordering temperature in the Nd rich Nd-Dy alloys and spontaneous long range ordering in the Pr rich Pr-Tb alloys.

CHAPTER 7

CONCLUSION AND SUGGESTIONS FOR FURTHER WORK

A prominent feature apparent from the results on the light-heavy rare earth alloy systems obtained in both neutron diffraction and susceptibility vs. temperature measurements is that the magnetic properties of all the alloy systems may be most conveniently treated within the framework of the three crystallographic phases that they form dependent upon composition, rather than as six separate alloy systems, although there are naturally similarities between the individual alloy systems.

On the addition of less than 30at.% light rare earth to a heavy rare earth the crystallographic structure remains the same as that of the parent heavy rare earth metal i.e. hcp, and the magnetic properties of the alloy are essentially those of a magnetic dilution system. The Néel temperatures of the alloys follow a $^{2}/_{3}$ power law with reduced de Gennes factor, implying that the dominant feature in determining the magnetic ordering is the value of the spin variable operating in the alloy. The moments determined from neutron diffraction experiments are consistent only with an antiparallel alignment of the moments on the light and heavy rare earth ions, assuming that the moments on the ions take their full ionic values. Alloying a light rare earth with a heavy rare earth causes an increase in the axial ratio of the heavy rare earth and the effect of the change in lattice parameter on the

magnetic ordering can be seen in the change between the initial turn angle in the alloy and in the heavy rare earth metals. Following a model initially proposed to account for the change in the turn angle in the heavy rare earth metals with applied hydrostatic pressure via the shift in the electronic energy bands, the change in the initial turn angle between the alloy and the parent heavy rare earth has been correlated with the change in the c/a ratio observed in alloying. This model predicts almost exactly the c/a ratio for which the Pr-Tb alloy system orders ferromagnetically direct from the paramagnetic phase i.e. for which $\omega_i = 0$.

The complex magnetic structure of the alloys in the Sm phase is determined by the complicated crystal structure of this phase, in which there are two equally populated coexisting structural domains in the sample. The resultant magnetic structure may be described by a modulation wave propagating along the c-axis which goes to zero at every cubic site layer. Thus the ordering in the alloys is associated with an antiferromagnetic structure on the hexagonal sites. The moments on the alloys are all bigger than that expected theoretically for an antiparallel alignment of the light and heavy rare earth moments, assuming that the moment on each ion takes its full ionic value. If it is assumed that the moment on the light rare earths is quenched by the crystal field to $^2/_3$ its ionic value then much better agreement is obtained with

the observed net moments, except in the case of $Pr_{45}Tb_{55}$. In this alloy if the moments on the ions take their full ionic value then the observed net moment in the alloy is consistent with a structure in which the moments lie at 150^{o} to each other. Such an orientation is consistent with the moments lying along their own easy direction of magnetisation instead of strictly antiparallel. Since the easy directions of Nd and Tb coincide, it is assumed that the moments lie antiparallel in this alloy, although this could not be verified experimentally.

In Sm and the Tb based Sm phase alloys there is also evidence from neutron diffraction and susceptibility vs. temperature plots that the cubic site moments form an ordered structure separately from the hexagonal sites. The model proposed originally to explain the magnetic structure of the cubic sites in Sm metal has been extended to predict a magnetic structure which describes the ordering of the cubic site layers in alloys between a light and a heavy rare earth metal.

In the dhcp phase (light rare earth rich alloys) the presence of a few atomic % of a heavy rare earth metal does not produce an instantaneous increase in the ordering temperature of the light rare earth, but rather the ordering temperature decreases (in Pr based alloys) or remains almost constant (in Nd based alloys). It is shown that this is because the charge cloud polarisation due to a light rare earth acting at a light rare earth ion

site is opposite to that for a heavy rare earth acting at a light rare earth ion site and thus the effective exchange actually decreases with increasing heavy rare earth content. At a critical concentration of heavy rare earth, the exchange field at a light rare earth ion site, due to the magnetisation of the heavy rare earth sublattice, dominates the exchange field at the light rare earth ion site due to the magnetisation of the light rare earth sublattice and the alloy orders magnetically. This is indeed the case for the Pr-Tb alloy system but not for the Nd-Dy alloy system which is already ordered below the critical concentration. However, the Nd-Dy alloy system does show a change in the form of the susceptibility vs. temperature plot at this concentration - there no longer being any distinction between hexagonal and cubic sites in the material.

A two sublattice model of magnetism, derived using the Weiss formalism, is proposed which describes the magnetic properties of the ferrimagnetic light heavy rare earth alloys. Exchange constants between ions on the two sublattices have been determined and these are compared with exchange constants evaluated from the transition temperatures of the pure metals. The two are in good agreement and further the Pr-Tb exchange constant, evaluated from the results in the dhcp alloys, predicts the correct value of the exchange field which must be applied to a Pr ion on the basis of the opposing exchange field of the light-light and the light-

heavy interactions to cause crystal field level crossing and hence spontaneous magnetic ordering.

Of necessity in such a broad based investigation as this, it is not possible to cover every aspect in detail. Nevertheless, it is still clearly possible to draw general conclusions about the magnetic properties of some light-heavy rare earth alloy systems which can be used as a basis for more detailed work in the future.

Obviously neutron diffraction experiments on single crystals rather than powders would yield significantly more information on the magnetic structure of the alloys, especially in the dhcp and Sm phases where there are two site symmetries and the magnetic scattering from a powder is weak. Neutron diffraction experiments coupled with more susceptibility vs. temperature measurements on the low percentage Dy in Nd alloys would yield a complete understanding of magnetic ordering in that system and likewise in any other Nd-heavy rare earth alloy system.

Of importance in the magnetic ordering of Pr and the Pr-heavy rare earth alloys are the crystal field level splittings, particularly from the groundstate to the first excited states on both the hexagonal and cubic sites. With a single crystal these could be measured using a triple axis spectrometer. This would be the first direct measurement of crystal field levels in an alloy and would serve to remove much of the guesswork from crystal field calculations.

From the hcp phase results it is clear that the exact nature of the band structure is obviously important in determining the details of the helical magnetic ordering in the heavy rare earth metals and alloys. The direct observable related to the band structure (and independent of the spin variable operating in the alloy) is the turn angle of the magnetic structure, which is uniquely measurable in neutron diffraction experiments. Much more work, both experimental and theoretical, could be initiated in this area to quantify the relationship between the band structure and the magnetic ordering.

APPENDIX 1

Derivation of the theoretical scattered intensity for some magnetic structures.

The complete expression for the neutron-magnetic scattering is (eqn. 3.22)

$$I_{hk\ell} = B \sum_{\mu\nu} \left[\delta_{\mu\nu} - \frac{\kappa_\nu \kappa_\mu}{\kappa^2}\right] \sum_{ij} \exp\left[i\,\underline{\kappa}.(\underline{r}_i - \underline{r}_j)\right] J_i^{\mu} J_j^{\nu} \qquad \ldots(A1.1)$$

where $B = \frac{Am}{L} \exp(-2W) \left[\frac{e^2\gamma}{2mc^2}\right]^2 g^2 f^2(\kappa)$

The sum over i and j in the magnetic structure factor may be restricted to a single unit cell by writing

$$\sum_{ij} \rightarrow N_c \sum_{\substack{i \text{ all crystal} \\ j \text{ unit cell}}} \rightarrow N_c^2 \sum_{ij}$$

all crystal unit cell

where N_c is the number of unit cells in the crystal. The magnetic structure factor may be further simplified by writing

$$\underline{r}_i = \underline{\ell} \quad \text{and} \quad \underline{r}_i - \underline{r}_j = \underline{r}$$

Thus, $\sum_{ij} \exp\left[i\underline{\kappa}.(\underline{r}_i - \underline{r}_j)\right] J_i^{\mu} J_j^{\nu} = \sum_{\ell,r} \exp(i\underline{\kappa}\underline{r}) J_\ell^{\nu} J_r^{\mu}$

The unit cell must be chosen to be commensurate with both the chemical and magnetic structures.
The symbols μ and ν in eqn A1.1 run over all x, y and z and the three cartesian components of the scattering vector must be resolved before eqn A1.1 can be evaluated.

Let the scattering vector κ have a component κ_z in the Oz direction and a component κ_b in the basal plane, and let Oz lie along the c-axis. Then the components of κ in the x, y and z directions are

$$\kappa_x = \kappa \sin\theta \cos\psi$$
$$\kappa_y = \kappa \sin\theta \sin\psi$$
$$\kappa_z = \kappa \cos\theta$$

where θ and ψ are shown in Fig. A1.1

Finally, eqn A1.1 may be evaluated for a specific spin structure if the moment on an ion site is specified in its three cartesian components.

1. UNIFORM BASAL PLANE SPIRAL WITH TURN ANGLE ϕ

$$J_\ell^x = J_o \cos \underline{k}_o.\underline{\ell} = J_o \cos \phi_\ell$$
$$J_\ell^y = J_o \sin \underline{k}_o.\underline{\ell} = J_o \sin \phi_\ell$$
$$J_\ell^z = 0$$

where J_o is the thermally averaged value of the total spin on that site. Substituting into eqn (A1.1)

$$I_{hk\ell} = B J_o^2 \sum_{\ell,r} \exp(i\underline{\kappa}.\underline{r}) \left[\left(1 - \frac{\kappa_x^2}{\kappa^2}\right) \cos\phi_\ell \cos\phi_{\ell+r} - \frac{\kappa_x \kappa_y}{\kappa^2} \left(\cos\phi_\ell \sin\phi_{\ell+r} + \sin\phi_\ell \cos\phi_{\ell+r} \right) + \left(1 - \frac{\kappa_y^2}{\kappa^2}\right) \sin\phi_\ell \sin\phi_{\ell+r} \right]$$

Before summing over ℓ and r the components of κ must be averaged over the crystallographic domains. There are 6 basal plane domains each differing by a rotation

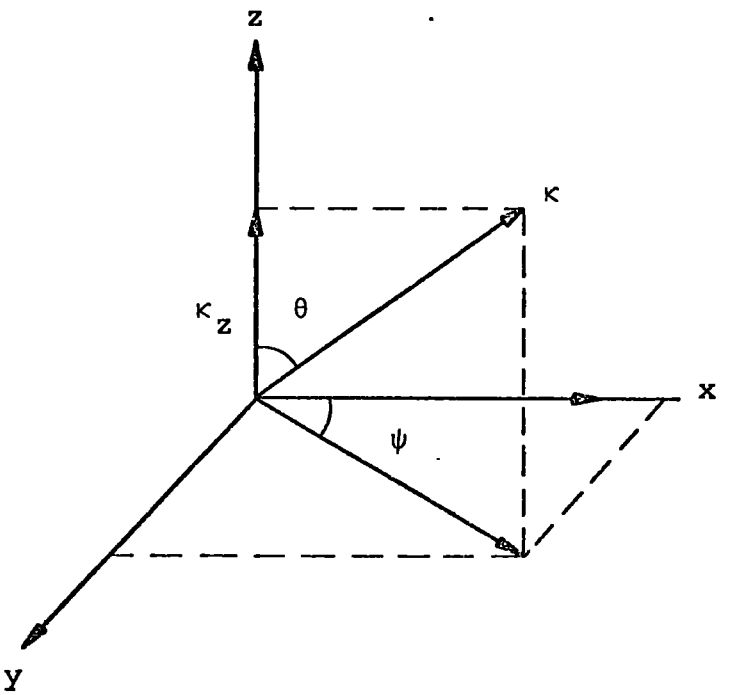

FIG. A1.1 Construction defining the cartesian co-ordinates of the scattering vector.

of 60^{o}. Let $\{\kappa_i^2\}$ be the average of κ_i^2 over all domains.

Thus, $\{\kappa_x^2\} = \frac{\kappa^2}{6} \sum_{m=o}^{5} \sin^2\theta \cos^2(\psi + \frac{m\pi}{3})$

$$= \frac{\kappa^2}{12} \sin^2\theta \sum_{m=o}^{5} \left[1 + \cos 2(\psi + \frac{m\pi}{3})\right]$$

$$= \frac{\kappa^2 \sin^2\theta}{2}$$

Similarly, $\{\kappa_y^2\} = \frac{\kappa^2 \sin^2\theta}{2}$

Also, $\{\kappa_x\kappa_y\} = \frac{\kappa^2}{6} \sum_{m=o}^{5} \sin^2\theta \sin(\psi + \frac{m\pi}{3}) \cos(\psi + \frac{m\pi}{3})$

$$\{\kappa_x\kappa_y\} = \frac{\kappa^2 \sin^2\theta}{12} \sum_{m=o}^{5} \sin 2(\psi + \frac{m\pi}{3})$$

Then, $\{\kappa_x\kappa_y\} = 0.$

Hence, $\left[1 - \frac{\{\kappa_x^2\}}{\kappa^2}\right] = \left[1 - \frac{\{\kappa_y^2\}}{\kappa^2}\right] = \left[1 - \frac{\kappa^2 \sin^2\theta}{2\kappa^2}\right]$

$$= \frac{1}{2}\left[1 + \frac{\kappa_z^2}{\kappa^2}\right]$$

Therefore, $I_{hk\ell} = \frac{BJ_o^2}{2}\left[1 + \frac{\kappa_z^2}{\kappa^2}\right] \sum_{\ell,r} \exp(i\underline{\kappa}.\underline{r})$

$$x\ (\cos\phi_\ell \cos\phi_{\ell+r} + \sin\phi_\ell \sin\phi_{\ell+r})$$

$$= \frac{BJ_o^2}{2}\left[1 + \frac{\kappa_z^2}{\kappa^2}\right] \sum_{\ell,r} \exp(i\underline{\kappa}.\underline{r}) \cos(\phi_\ell - \phi_{\ell+r})$$

Now for a uniform spiral $\phi_{\ell+r} - \phi_\ell = \phi_r$

Then, $I_{hk\ell} = \frac{BJ_o^2}{2}\left[1 + \frac{\kappa_z^2}{\kappa^2}\right] \sum_{\ell,r} \exp(i\underline{\kappa}.\underline{r}) \cos\phi_r$ ...(A1.2)

From eqn. A1.2 since the magnetic structure factor is not identical to the nuclear structure factor the scattered magnetic intensity will appear at positions

symmetrically disposed around the nuclear peak. There will be satellites associated with every allowed nuclear peak as $I_{hk\ell}$ is always greater than zero since κ_z and κ are always positive (see Section 4.6)

2. FERROMAGNETIC ALONG Ox BUT AMPLITUDE MODULATED ALONG C-AXIS

$$J_\ell^x = J_o \cos \underline{k}_o . \underline{\ell} . = J_o \cos\phi_\ell$$

$$J_\ell^y = J_\ell^z = 0$$

$$I_{hk\ell} = BJ_o^2 \sum_{\ell,r} \exp(i\underline{\kappa}.\underline{r}) \left[\left(1 - \frac{\kappa_x^2}{\kappa^2}\right) \cos\phi_\ell \cos\phi_{\ell+r} \right]$$

$$= \frac{BJ_o^2}{2} \left[1 + \frac{\kappa_z^2}{\kappa^2}\right] \sum_{\ell,r} \exp(i\underline{\kappa}.\underline{r}) \cos\phi_\ell \cos\phi_{\ell+r} \quad \ldots(A1.3)$$

The satellites observed for this structure are the same as for the uniform basal plane spiral except that the intensity is modulated by extra factor $\cos\phi_{\ell+r}$. The magnetic structure factor is evaluated in Appendix 2.

3. FERROMAGNETIC SPIRAL, TURN ANGLE ϕ

$$J_\ell^x = J_o \cos\phi_\ell \sin\beta$$

$$J_\ell^y = J_o \sin\phi_\ell \sin\beta$$

$$J_\ell^z = J_o \cos\beta$$

where β is the semi apex angle of the cone on which the moments lie.

$$I_{hk\ell} = BJ_o^2 \sum_{\ell,r} \exp(i\underline{\kappa}.\underline{r}) \left[\left[(1 - \frac{\kappa_z^2}{\kappa^2})\cos^2\beta\right]\right.$$

$$+ \left[(1 - \frac{\kappa_x^2}{\kappa^2})\cos\phi_\ell\cos\phi_{\ell+r} + (1 - \frac{\kappa_y^2}{\kappa^2})\sin\phi_\ell\sin\phi_{\ell+r}\right]\sin^2\beta$$

$$- \frac{\kappa_x\kappa_y}{\kappa^2}(\cos\phi_\ell\sin\phi_{\ell+r} + \sin\phi_\ell\cos\phi_{\ell+r})\sin^2\beta$$

$$\left. - 2\frac{\kappa_x\kappa_z}{\kappa^2}(\cos\phi_\ell\sin\beta\cos\beta) - 2\frac{\kappa_y\kappa_z}{\kappa^2}(\cos\phi_\ell\sin\beta\cos\beta)\right]$$

In this structure there are 12 domains, 6 in the basal plane differing by a rotation of 60^o and 2 in the c-direction separated by a rotation of 180^o.

Averaging over domains,

$$\{\kappa_x^2\} = \frac{\kappa^2}{12}\sum_{n=o}^{1}\sin^2(\theta + n\pi)\sum_{m=o}^{5}\cos^2(\psi + \frac{m\pi}{3})$$

$$= \frac{\kappa^2}{4}\sum_{n=o}^{1}\sin^2(\theta + n\pi) \quad \text{by previous result}$$

$$= \frac{\kappa^2}{8}\sum_{n=o}^{1}(1 - \cos 2(\theta + n\pi))$$

$$= \frac{\kappa^2\sin^2\theta}{2}$$

$$\{\kappa_y^2\} = \frac{\kappa^2}{12}\sum_{n=o}^{1}\sin^2(\theta + n\pi)\sum_{m=o}^{5}\sin^2(\psi + \frac{m\pi}{3})$$

$$= \frac{\kappa^2\sin^2\theta}{2} \quad \text{by analogy}$$

$$\{\kappa_z^2\} = \frac{\kappa^2}{2}\sum_{n=o}^{1}\cos^2(\theta + n\pi)$$

$$= \frac{\kappa^2}{2} \frac{1}{2} \sum_{n=o}^{1} (1 + \cos 2(\theta + n\pi))$$

$$= \frac{\kappa^2}{4} 4\cos^2\theta = \kappa_z^2$$

Therefore $\left[1 - \frac{\{\kappa_x^2\}}{\kappa^2}\right] = \left[1 - \frac{\{\kappa_y^2\}}{\kappa^2}\right] = \left[1 - \frac{\kappa^2 \sin^2\theta}{2\kappa^2}\right]$

$$= \frac{1}{2}\left[1 + \frac{\kappa_z^2}{\kappa^2}\right]$$

and $\left[1 - \frac{\{\kappa_z^2\}}{\kappa^2}\right] = \left[1 - \frac{\kappa_z^2}{\kappa^2}\right]$

Consider the cross terms:

$\{\kappa_x\kappa_y\} = \kappa^2 \sin^2\theta\cos\psi\sin\psi = \frac{\kappa^2}{2}\sin^2\theta\sin 2\psi$

i.e. $\{\kappa_x\kappa_y\} = \frac{1}{12} \frac{\kappa^2}{2} \sum_{m=o}^{5} \sin 2(\psi + \frac{m\pi}{3}) \sum_{n=o}^{1} \sin^2(\theta + n\pi)$

Thus, $\{\kappa_x\kappa_y\} = 0$ since the average value of

$$\sum_{m=o}^{5} \sin 2(\psi + \frac{m\pi}{3}) \quad \text{is zero}$$

$\kappa_x\kappa_z = \kappa^2 \sin\theta\cos\theta\cos\psi = \frac{\kappa^2}{2}\sin 2\theta\cos\psi$

i.e. $\{\kappa_x\kappa_z\} = \frac{1}{12} \frac{\kappa^2}{2} \sum_{n=o}^{1} \sin 2(\theta + n\pi) \sum_{m=o}^{5} \cos(\psi + \frac{m\pi}{3})$

Thus, $\{\kappa_x\kappa_z\} = 0$ since $\sum_{m=o}^{5} \cos(\psi + \frac{m\pi}{3})$ has an average value of zero

$\kappa_y\kappa_z = \kappa^2 \sin\theta\cos\theta\sin\psi = \frac{\kappa^2}{2}\sin 2\theta\sin\psi$

$\{\kappa_y\kappa_z\} = 0$ by analogy with $\{\kappa_x\kappa_z\}$

$$\text{Therefore } I_{hk\ell} = BJ_o^2 \sum_{\ell,r} \exp(i\underline{\kappa}.\underline{r}) \left[\cos^2\beta \left(1 - \frac{\kappa_z^2}{\kappa^2}\right) \right.$$

$$+ (\cos\phi_\ell \cos\phi_{\ell+r} + \sin\phi_\ell \sin\phi_{\ell+r}) \times$$

$$\left. \times \sin^2\beta \, \frac{1}{2} \left(1 + \frac{\kappa_z^2}{\kappa^2}\right) \right]$$

For a uniform basal plane spiral $\phi_{\ell+r} - \phi_\ell = \phi_r$

$$I_{hk\ell} = BJ_o^2 \cos^2\beta \; G^2_{hk\ell} \left(1 - \frac{\kappa_z^2}{\kappa^2}\right) \qquad \ldots(A1.4)$$

$$I_{hk\ell} = BJ_o^2 \, \frac{1}{2} \sin^2\beta \left[\sum_{\ell,r} \exp(i\kappa.r)\cos\phi_r \right] \left(1 + \frac{\kappa_z^2}{\kappa^2}\right) \quad ..(A1.5)$$

The magnetic scattering from the ferromagnetic spiral structure may be resolved into two components. The first,(eqn A1.4) has a magnetic structure factor identical to the nuclear structure factor and thus the scattered magnetic intensity occurs at reciprocal lattice points along with the nuclear scattering unless $\frac{\kappa_z}{\kappa} = 1$ in which case the intensity is zero. Such instances occur for magnetic diffraction lines with the indices (00ℓ),and the scattering may be associated with the ferromagnetically aligned spins in the structure which lie along the c-axis. The second component of the scattering (eqn. A1.5) may be associated with the basal plane spiral. Since the magnetic structure factor is not identical to the nuclear structure factor the diffraction lines occur at positions

symmetrically disposed around the reciprocal lattice points. There are satellites of all allowed nuclear peaks since $I_{hk\ell}$ is never zero. The magnetic structure factor is evaluated in Appendix 2.

4. MODULATED MOMENT - CAM

$$J_\ell^x = J_\ell^y = 0 \qquad J_\ell^z = J_o \cos\phi_\ell$$

$$I_{hk\ell} = BJ_o^2 \sum_{\ell,r} \exp(i\underline{\kappa}.\underline{r}) \left[(1 - \frac{\kappa_z^2}{\kappa^2}) \cos\phi_\ell \cos_{\ell+r} \right]$$

$$\{\kappa_z^2\} = \frac{\kappa^2}{2} \sum_{n=o} \cos^2(\theta + n\pi) \text{ on averaging over domains}$$

$$= \kappa_z^2$$

$$\text{Therefore } \left[1 - \frac{\{\kappa_z^2\}}{\kappa^2} \right] = \left[1 - \frac{\kappa_z^2}{\kappa^2} \right]$$

$$I_{hk\ell} = BJ_o^2 \left[1 - \frac{\kappa_z^2}{\kappa^2} \right] \sum_{\ell,r} \exp(i\underline{\kappa}.\underline{r}) \cos\phi_\ell \cos\phi_{\ell+r} \qquad \ldots(A1.6)$$

The intensity of the magnetic satellites in the CAM structure is identical to that of the Ox ferromagnet with c-axis modulation (eqn. A1.3) except that (00ℓ) magnetic satellites are absent.

5. FERROMAGNETIC ALONG Ox

$$J_\ell^x = J_o \quad J_\ell^y = J_\ell^z = 0.$$

$$I_{hk\ell} = BJ_o^2 \sum_{\ell,r} \exp(i\underline{\kappa}.\underline{r}) \left[1 - \frac{\kappa_x^2}{\kappa^2} \right]$$

$$I_{hk\ell} = \frac{BJ_o^2}{2} \sum_{r} \exp(i\underline{\kappa}.\underline{r}) \left[1 + \frac{\kappa_z^2}{\kappa^2} \right] = \frac{BJ_o^2}{2} \left[G_{hk\ell} \right]^2 \left[1 + \frac{\kappa_z^2}{\kappa^2} \right] \qquad \ldots(A1.7)$$

The basal plane ferromagnetic structure gives rise to magnetic scattering at all allowed reciprocal lattice points.

6. FERROMAGNETIC ALONG Oz

$$J_\ell^x = J_\ell^y = 0 \qquad J_\ell^z = J_0$$

$$I_{hk\ell} = BJ_0^2 \sum_{\ell,r} \exp(i\underline{\kappa}.\underline{r}) \left[1 - \frac{\kappa_z^2}{\kappa^2}\right]$$

$$I_{hk\ell} = BJ_0^2 \left[G_{hk\ell}\right]^2 \left[1 - \frac{\kappa_z^2}{\kappa^2}\right] \qquad \ldots(A1.8)$$

The scattered magnetic intensity from an Oz ferromagnet appears at the reciprocal lattice points in the chemical unit cell unless $\frac{\kappa_z}{\kappa} = 1$ i.e. for an (00ℓ) diffraction peak.

The observed diffraction patterns for all the magnetic structures are summarised in Table 3.1.

APPENDIX 2

EVALUATION OF MAGNETIC STRUCTURE FACTORS

A2.1 UNIFORM BASAL PLANE SPIRAL IN THE H.C.P. PHASE

The 4.2K magnetic structure of $Ho_{20}Pr_{80}$ and $Ho_{80}Nd_{20}$ is the ferromagnetic spiral. The magnetic diffraction pattern associated with this structure may be conveniently resolved into two components; the diffraction pattern from a c-axis ferromagnet plus the diffraction pattern from a uniform basal plane spiral (see Appendix 1). The structure factor for the ferromagnetic spin arrangement is identical to the nuclear structure factor whereas the structure factor for the spiral spin arrangement takes the form

$$\left[G_{hk\ell}\right]^2 = \sum_{\ell,r} \exp(i\underline{\kappa}.\underline{r})\cos\phi_r \qquad \ldots(A2.1)$$

where ϕ is the turn angle of the structure and has the value 36^o in both alloys at 4.2K.

To evaluate the magnetic structure factor we must construct the magnetic unit cell and the chemical unit cell in such a way that they are identical. Consider the following sequence of ten layers:

layer, n	0	1	2	3	4	5	6	7	8	9	10
ϕ	0	36	72	108	144	180	216	252	288	324	360
stacking	A	B	A	B	A	B	A	B	A	B	A

The stacking refers to the position of the atoms on the hexagonal layer with respect to the zeroth layer (see

Section 1.2).

If the position vector of the atom in the layer n=0 corresponds to the first value of $\underline{\ell}$ in the summation, this atom will be the origin of $\underline{r}$ for this value of ℓ.

For the (hkℓ) reflection:

$$\kappa.r = 2\pi\frac{n\ell}{10} \qquad \text{A type layer}$$

$$= 2\pi\left[\frac{\Delta}{3} + \frac{n\ell}{10}\right] \qquad \text{B type layer}$$

The summation over $\underline{r}$ for a particular value of $\underline{\ell}$ gives:

$$\sum_{\ell,r=o}^{9} \exp(i\underline{\kappa}.\underline{r})\cos\phi_r = 1 + 2\cos 2\pi\left[\frac{\Delta}{3} + \frac{\ell}{2}\right]$$

$$\times\left[0.809\cos\frac{8\pi\ell}{10} - 0.309\cos\frac{4\pi\ell}{10} - \frac{1}{2}\right]$$

$$+ 2\cos\pi\ell\left[0.309\cos\frac{6\pi\ell}{10} - 0.809\cos\frac{2\pi\ell}{10}\right] \qquad \ldots(A2.2)$$

To evaluate the sum over all $\underline{\ell}$ in the particular cell it is necessary to re-label the layer n=1 with n=0 and express the stacking with respect to this layer as an A layer. This gives the sequence

layer, n	0	1	2	3	4	5	6	7	8	9	10
ϕ	0	36	72	108	144	180	216	252	288	324	360
stacking	A	B	A	B	A	B	A	B	A	B	A

This sequence is identical to the previous one

and repetition of this process will merely produce ten identical sequences. Thus, the sum over all $\underline{\ell}$ and $\underline{r}$ is simply ten times the sum over $\underline{r}$ for a particular value of $\underline{\ell}$ i.e.

$$\sum_{\ell,r} \exp(i\underline{\kappa}.\underline{r})\cos\phi_r = \frac{1}{10} \sum_{\ell,r=0}^{9} \exp(i\underline{\kappa}.\underline{r})\cos\phi_r$$

Further, the sequence may start with the spin on the zeroth site pointing in any one of ten directions which corresponds to starting the spiral at an arbitrary point with respect to the lattice. Thus

$$\left[G_{hk\ell}\right]^2 = 10 \sum_{\ell,r} \exp(i\underline{\kappa}.\underline{r})\cos\phi_r$$

The evaluation of the magnetic structure factor for various diffraction lines must be carried out with respect to the ten layer cell. For example the $(002)^+$ satellite has the indices (00,2.2) in the two layer cell and in the ten layer cell this becomes (00,11).

The magnetic structure factors evaluated for the satellite lines are

00ℓ $\quad G^2 = 500$

$h0\ell$ (ℓ odd) $\quad G^2 = 125$

$h0\ell$ (ℓ even) $\quad G^2 = 350$

A2.2 UNIFORM BASAL PLANE SPIRAL IN THE SM PHASE

The magnetic form factor has the same expression as before

$$\left[G_{hk\ell}\right]^2 = \sum_{\ell,r} \exp(i\underline{\kappa}.\underline{r})\cos\phi_r$$

where ϕ is the turn angle. In the Sm phase alloys the satellites are observed at angular separations from the nuclear peaks which correspond to a turn angle of 60^o. To evaluate the magnetic structure factor the calculation proceeds exactly as before by first constructing a magnetic unit cell and a chemical unit cell which are identical. Consider the following sequence of 18 layers,

layer, n	0	1	2	3	4	5	6	7	8	9	10	11	12	13	14	15	16	17	18
cos ϕ	1	½	-½	-1	-½	½	1	½	-½	-1	-½	½	1	½	-½	-1	-½	½	1
stacking	A	B	C	B	C	A	C	A	B	A	B	C	B	C	A	C	A	B	A

For the (hkℓ) reflection $\underline{\kappa}.\underline{r} = 2\pi\frac{n\ell}{18}$ A layer

$$\underline{\kappa}.\underline{r} = 2\pi\left[\frac{\Delta}{3} + \frac{n\ell}{18}\right] \quad \text{B layer}$$

$$\underline{\kappa}.\underline{r} = 2\pi\left[\frac{2\Delta}{3} + \frac{n\ell}{18}\right] \quad \text{C layer}$$

The summation over $\underline{r}$ for a particular value of ℓ gives

$$\sum_{\ell,r=o}^{17} \exp(i\kappa.r)\cos\phi_r = \left[1 + \exp\left(\frac{2\pi i\ell}{3}\right)\cos\frac{2\pi\ell}{18}\right]G_{\Delta,\ell}$$

$$\text{where } G_{\Delta,\ell} = \left[1 - \exp(i\pi\ell)\right]\left[1 + 2\cos 2\pi\left(\frac{\ell}{3} - \frac{\Delta}{3}\right)\right]$$

...(A2.3)

Re-labelling the layer n=1 with n=0 and expressing the stacking sequence with respect to this layer as an A layer gives

layer, n	0	1	2	3	4	5	6	7	8	9	10	11	12	13	14	15	16	17	18
cosϕ	1	½	-½	-1	-½	½	1	½	-½	-1	-½	½	1	½	-½	-1	-½	½	1
stacking	A	B	A	B	C	B	C	A	C	A	B	A	B	C	B	C	A	C	A

where the stacking sequences have been obtained from the previous one by the replacements

$$B \rightarrow A$$

$$C \rightarrow B$$

$$A \rightarrow C$$

The sum over $\underline{r}$ for this particular value of $\underline{\ell}$ is

$$\sum_{\ell,r=0}^{17} \exp(i\underline{\kappa}.\underline{r})\cos\phi_r = \left[1 + \exp(\frac{2\pi i\ell}{2})\cos\frac{2\pi\ell}{9}\right]G_{\Delta,\ell} \quad \ldots(A2.4)$$

Returning to the original sequence, the original layer with n=2 must be re-labelled n=0 and the summation repeated

layer,n	0	1	2	3	4	5	6	7	8	9	10	11	12	13	14	15	16	17	18
cosϕ	1	½	-½	-1	-½	½	1	½	-½	-1	-½	½	1	½	-½	-1	-½	½	1
stacking	A	C	A	B	A	B	C	B	C	A	C	A	B	A	B	C	B	C	A

where the replacements are C→A, B→C, and A→B.

The sum over $\underline{r}$ for this particular value of $\underline{\ell}$ is

$$\sum_{\ell,r=0}^{17} \exp(i\underline{\kappa}.\underline{r})\cos\phi_r = \left[1 + \exp(\frac{2\pi i2\ell}{3})\cos\frac{2\pi\ell}{18}\right]G_{\Delta,\ell} \quad \ldots(A2.5)$$

Further repetition of this process gives rise to sums corresponding to eqns. (A2.3), (A2.4) and (A2.5)

for each set of three successive layers. Hence, the complete sum over $\underline{\ell}$ and $\underline{r}$ is

$$\sum_{\ell,r} \exp(i\underline{\kappa}.\underline{r})\cos\phi_r = 6G_{\Delta,\ell}\left[3 + \cos\frac{2\pi\ell}{18}\left[\exp(\frac{2\pi i\ell}{3}) + \exp(\frac{2\pi i 2\ell}{3})\right]\cos\frac{2\pi\ell}{9}\exp(i\pi\ell)\right] \quad \ldots(A2.6)$$

The satellite lines must be indexed with respect to the 18 layer unit cell before eqn. (A2.6) can be evaluated.

A2.3 BASAL PLANE FERROMAGNET IN SM PHASE WITH MODULATION IN THE C-DIRECTION

The magnetic structure factor for this structure is given by the expression (see Appendix 1)

$$\left[G_{hk\ell}\right]^2 = \sum_{\ell,r} \exp(i\underline{\kappa}.\underline{r})\cos\phi_\ell\cos\phi_{\ell+r}$$

The expression contains the weighting factor $\cos\phi_\ell\cos\phi_{\ell+r}$ rather than $\cos\phi_r$ as the sum now depends upon the phase of the modulation relative to the lattice. A modulated basal plane ferromagnetic structure is shown in Fig. 5.15. In this structure the modulation reduces the amplitude of the resultant moment on the cubic sites to zero and on the hexagonal sites to a value $\frac{\sqrt{3}}{2}$ of their full value. Thus for this structure $\left[\cos\phi_\ell\right] = \frac{\sqrt{3}}{2}$ or 0, the value zero corresponding to a cubic site.

For the first stacking sequence examined in Section A2.2

layer, n	0	1	2	3	4	5	6	7	8	9	10	11	12	13	14	15	16	17	18
$\cos\phi_{\ell+r}$	+1	0	-1	-1	0	+1	+1	0	-1	-1	0	+1	+1	0	-1	-1	0	+1	+1
stacking	A	B	C	B	C	A	C	A	B	A	B	C	B	C	A	C	A	B	A

where we have used $\left[\cos\phi_{\ell}\right] = \pm 1, 0$ for convenience instead of $\pm\frac{\sqrt{3}}{2}, 0$.

For a given $\underline{\ell}$, the sum over $\underline{r}$ for this sequence is

$$\sum_{\ell,r=0}^{17} \exp(i\underline{\kappa}.\underline{r})\cos\phi_{\ell}\cos\phi_{\ell+r} = \left[1 + \exp(\frac{2\pi i 5\ell}{18})\right] G_{\Delta,\ell} \quad \ldots(A2.7)$$

where $G_{\Delta,\ell}$ is defined in eqn. A2.3.

The second sequence is obtained by treating the layer denoted by n=1 in the above sequence as the origin of the new sequence, keeping the modulation $\cos\phi_{\ell+r}$ with the same layer as above and re-labelling the stacking with respect to this layer as an A layer. For this sequence the sum vanishes because $\cos\phi_{\ell} = 0$. The next sequence, obtained by repeating the process is

layer, n	0	1	2	3	4	5	6	7	8	9	10	11	12	13	14	15	16	17	18
$\cos\phi_{\ell+r}$	-1	-1	0	+1	+1	0	-1	-1	0	+1	+1	0	-1	-1	0	+1	+1	0	-1
stacking	A	C	A	B	A	B	C	B	C	A	C	A	B	A	B	C	B	C	A

For a particular value of $\underline{\ell}$ the sum over $\underline{r}$ for this sequence is

$$\sum_{\ell,r=0}^{17} \exp(i\underline{\kappa}.\underline{r}) = \exp(\frac{-2\pi i 5\ell}{18})\left[1 + \exp(\frac{2\pi i 5\ell}{18})\right] G_{\Delta,\ell} \quad \ldots(A2.8)$$

Hence the sum of the first three stacking sequences is

$$\left[1 + \exp\frac{-2\pi i 5\ell}{18}\right]\left[1 + \exp\left(\frac{2\pi i 5\ell}{18}\right)\right]G_{\Delta,\ell}$$

$$= 2\left[1 + \cos\frac{2\pi 5\ell}{18}\right]G_{\Delta,\ell} \qquad \ldots(A2.9)$$

Further repetition gives sums equal to (A2.9) for each set of three successive layers. Then the summation for the whole unit cell, allowing for the factor $\frac{\sqrt{3}}{2}$, is

$$\sum_{\ell,r} \exp(i\underline{\kappa}.\underline{r})\cos\phi_{\ell}\cos\phi_{\ell+r} = 9\left[1 + \cos\frac{2\pi 5\ell}{18}\right]G_{\Delta,\ell} \qquad \ldots(A2.10)$$

The magnetic structure factor for a basal plane ferromagnetic structure with no scattering from the cubic sites can be evaluated from eqn. (A2.10) if the satellite lines are indexed in the 18 layer cell.

Making the assumption that the scattering is zero from one of the hexagonal sites not from a cubic site, leads to a magnetic structure factor

$$\left[G_{hk\ell}\right]^2 = 9\left(1 + \cos\frac{2\pi 7\ell}{18}\right)G_{\Delta,\ell} \qquad \ldots(A2.11)$$

and the structure factor for no scattering from the other hexagonal site

$$\left[G_{hk\ell}\right]^2 = 9\left(1 + \cos\frac{2\pi 11\ell}{18}\right)G_{\Delta,\ell} \qquad \ldots(A2.12)$$

The two structure factors (A2.11) and (A2.12) give identical values of $\left[G_{hk\ell}\right]^2$ for the satellites observed

in the Sm structure. Table A2.1 shows the calculated structure factors for the magnetic satellites due to a 60^{o} basal plane spiral (eqn. A2.6) and an Ox ferromagnetic structure with no scattering from either (i) half the hexagonal sites or (ii) the cubic sites. $G_{\Delta,\ell}$ has the value 6 for ℓ odd and 0 for ℓ even.

From Table A2.1 it can be seen that on the basis of the observed scattering it is possible to distinguish between the three models.

A useful property of the sum $\sum_{\ell,r} \exp(i\underline{\kappa}.\underline{r})\cos\phi_{\ell}\cos\phi_{\ell+r}$ may be obtained by summing it over a complete set of reflections. In the hexagonal structure

$$\underline{\kappa}.\underline{r} = 2\pi\left(\frac{m\Delta}{3} + \frac{n\ell}{18}\right)$$

where m and n describe the position of a given spin in the basal plane and along the c-axis respectively with reference to the position of the spin at the origin of $\underline{r}$.

Consider a set of reflections of the type (hk0), (hk1), (hk2)...(hk17) then their sum will be

$$\sum_{\ell=0}^{17} \exp(i\underline{\kappa}.\underline{r}) = \sum_{\ell=0}^{17} \exp 2\pi i\left(\frac{m\Delta}{3} + \frac{n\ell}{18}\right)$$

where ℓ is used here as a Miller index. The above sum will be zero unless n = 18p where p is an integer or zero, and in this case

$$\sum_{\ell=0}^{17} \exp(i\underline{\kappa}.\underline{r}) = 18\exp\left(\frac{2\pi i m\Delta}{3}\right)$$

TABLE A2.1

COMPARISON OF MAGNETIC STRUCTURE FACTORS FOR 60^{o} SPIRAL AND Ox FERROMAGNET IN SM PHASE

ℓ	ℓ' †	G(spiral)	$G(S_c=0)$	$G(S_h=0)$
1	$\bar{1}^+,2^-$	46.6	44.6	12.6
3	0^+	162.0	81.0	81.0
5	$1^+,4^-$	148.1	12.6	104.8
7	$2^+,5^-$	129.1	104.8	44.6
11	$4^+,7^-$	129.1	104.8	44.6
13	$5^+,8^-$	148.1	12.6	104.8
15	9^-	162.0	81.0	81.0
17	$7^+,10^-$	46.6	44.6	12.6

† ℓ' are indices corresponding to satellites indexed in the Sm unit cell.

Now consider the sum over Δ ($\equiv k-h$), which corresponds to the sum over a total of 3 x 18 reflections of the type

(000), (001), (002),..... ....(00,17)

(100), (101), (102),..... ....(10,17)

($\bar{1}$00), ($\bar{1}$01), ($\bar{1}$02),..... ....($\bar{1}$0,17)

Then $\sum_{\Delta=0,1,2} \exp(\frac{2\pi i m\Delta}{3}) = 3$ if $m = 3p$ where p is an integer or zero

$= 0$ if $m = 3p$

Hence $\sum_{\ell,\Delta} \sum_{\underline{\ell},\underline{r}} \exp(i\underline{\kappa}.\underline{r})\cos\phi_{\ell}\cos\phi_{\ell+r} = \sum_{\underline{\ell},\underline{r}} 54\cos\phi_{\ell}\cos\phi_{\ell+r}$

($\ell=18p$, $m=18p'$)

$= 0$ if $\ell=18p$ and $m=18p'$

Now if $\underline{r}$ runs over the unit cell, the only value of $\underline{r}$ satisfying $\ell=18p$ and $m=18p'$ is $\underline{r} = 0$.

Therefore $\sum_{\ell,\Delta} \sum_{\underline{\ell},\underline{r}} \exp(i\underline{\kappa}.\underline{r})\cos\phi_{\ell}\cos\phi_{\ell+r} = \sum_{\underline{\ell}} 54\cos^2\phi_{\ell}$

$= 54\sum_{\underline{\ell}} \frac{1}{2}(1 + \cos 2\phi_{\ell})$

Now for the modulated basal plane ferromagnetic structure

$$\phi_{\ell} = \frac{2\pi n}{6} + \phi_0$$

where ϕ_0 is the phase of the modulation with respect to the lattice.

If $\underline{\ell}$ runs over the unit cell, i.e. n runs from 0 to 17,

then,

$$\sum_{n=0}^{17} \frac{1}{2}\left[1 + \cos\frac{2\pi n}{6} + \phi_0)\right] = \sum_{n=0}^{17} \frac{1}{2} = 9$$

Therefore, $\sum_{\ell,\Delta} \sum_{\underline{\ell},\underline{r}} \exp(i\underline{\kappa}.\underline{r})\cos\phi_{\ell}\cos\phi_{\ell+r} = 486$

and is independent of the phase angle, ϕ_0.

Now most of the reflections in the set above vanish; the only non-zero ones are

(003), (00,15)

(101), (107), (10,13)

($\bar{1}$05), ($\bar{1}$0,11), ($\bar{1}$0,17)

Ignoring the distinction between (10ℓ) and ($\bar{1}$0ℓ) and using the fact that I(101) = I(10,17); I(105) = I(10,13); I(107) = I(10,11); I(003) = I(00,15); where I(hkℓ) denotes the intensity of the (hkℓ) magnetic diffraction line then the sum of the structure factors for (003), (101), (105) and (107) will be 243.

This result is used in the calculation of the absolute value of the ordered moment.

APPENDIX 3

BAND STRUCTURE CALCULATIONS FOR THE HEAVY RARE EARTHS

An electron in a metal moves in a periodic electrostatic potential due to the regular spacing of the ions. The form of the potential is

$$V(r) = V(r-R)$$

where R is any direct lattice vector, and as a result the wave function of the electron is of the form

$$\psi_k(r) = u_k(r) \exp(i\underline{k}.\underline{r}) \qquad \ldots(A3.1)$$

i.e. a Bloch wave, where $u_k(r) = u_k(r-R)$, reflecting the periodicity of the lattice. The wave vector $\underline{k}$, which specifies the state of the electron is not unique since the addition of any reciprocal lattice vector $\underline{K}$ to it gives a wave number which may equally be used to specify the same state. In order to label the states uniquely it is necessary to restrict $\underline{k}$ to a unit cell of the reciprocal lattice i.e. to within the Brillouin zone. Within the zone the number of the allowed values of $\underline{k}$ is equal to the number of unit cells in the crystal lattice. For each value of $\underline{k}$ there are many energy levels, or energy bands $E_n(\underline{k})$, which can accommodate at most two electrons of opposite spin per unit cell of the crystal lattice. The integer n labels the band. This representation of E(k) is known as the reduced zone scheme. In reciprocal space the energy bands are continuous functions of $\underline{k}$, are

periodic such that $E_n(\underline{k}) = E_n(\underline{k}+\underline{K}_n)$ and have the same symmetry as the crystal lattice. This latter fact greatly simplifies energy band calculations since it is only necessary to calculate $E(\underline{k})$ for $\underline{k}$ values within a small portion of the Brillouin zone, the energy in the other parts being obtained by symmetry.

The reciprocal lattice of the hcp heavy rare earth metals is hexagonal and the Brillouin zone is the prism, (see Fig. A3.1)., formed by the planes which bisect the lines joining the origin $\underline{K}=0$ to the nearest reciprocal lattice points. Fig. A3.1 shows the Fermi surface (see later) of Tm in the double zone scheme. The wedge bounded by the symmetry points ΓMKHLA where A is on the same axis as Γ and lies in the plane LM, has a volume of $^1/_{24}$th of the Brillouin zone and calculation of the energy bands inside this volume is sufficient to specify the energy bands in the complete Brillouin zone.

The simplest wave functions which have the Bloch form (eqn.A3.1) are those with $u_k(r)$ = constant i.e. plane waves, and these correspond to the case $V(r) = 0$. The energy of an electron with wave number $\underline{k}$ is just $E(\underline{k}) = \frac{\hbar^2 k^2}{2m}$. If $|\underline{k}|$ is unrestricted in value the energy band in any given direction in reciprocal space is parabolic in form. This is the well known result for free electrons. The effect of a weak crystalline potential $V(r)$ is to introduce energy gaps and planes of energy discontinuity into the parabola at certain positions in the Brillouin

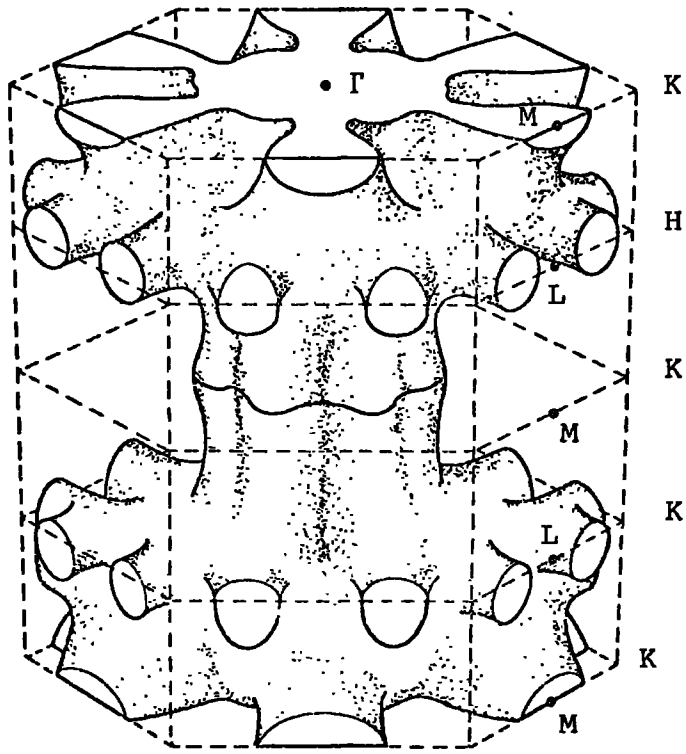

FIG. A3.1 The Fermi Surface for Tm in the double zone scheme

zone.

The conduction electrons fill the lowest energy bands up to some maximum energy, the Fermi energy E_f, and for the heavy rare earth metals E_f intersects the third and fourth bands. The surface bounding the occupied region of k-space is known as the Fermi surface. For free electrons, assuming $V(r) = 0$, the occupied region is a sphere of radius k_f where $\frac{\hbar^2 k_f^2}{2m} = E_f$. A small crystalline potential distorts the spherical surface, particular near the planes of energy discontinuity, and the effective area of the Fermi surface is reduced.

To construct the Fermi surface of real materials it is necessary to derive a crystalline potential which adequately describes the effect of each electron and nuclei on each other electron in the crystal. The potential used in all the energy band calculations for the rare earth metals is the muffin-tin potential originally introduced by Matthiess (1964). In this method the potential is approximated by a spherically symmetric region within a sphere about each atomic site and constant in the region outside these spheres. The wave functions for the electrons are assumed to retain the Bloch form, being simply linear conbinations of wave functions like eqn. A3.1. The energy bands in the material may now be calculated by solving Schroedinger's eqn. with this potential. This procedure produces an extremely complicated band structure and a Fermi surface which looks like Fig. A3.1.

The trunk is composed of the s and f electron bands and the arms perpendicular to the c-axis of the d-bands.

The generalised electron susceptibility $\chi(\underline{q})$ may be calculated from a knowledge of the energy bands and the Fermi distribution function for each band, $f_{\underline{k}}$. Such a calculation was first performed by Evenson and Liu (1969) along the line Γ to A in the Brillouin zone, using an expression of the form

$$\chi(\underline{q}) = \frac{1}{N} \sum_{k} \frac{f_{\underline{k}} - f_{\underline{k}+\underline{q}}}{E_{\underline{k}+\underline{q}} - E_{\underline{k}}} \qquad \ldots(A3.2)$$

The calculations were confined to $\underline{q}$ along the line ΓA in the Brillouin zone because all the ordered magnetic structures observed in the heavy rare earth metals can be described by a wave vector in that direction (see Section 2.2).

From eqn. A3.2 it can be seen that a large contribution to $\chi(\underline{q})$ results when the energy of an occupied state, $E_{\underline{k}}$ is approximately equal to that of an unoccupied state $E_{\underline{k}+\underline{q}}$. Because of the Fermi distribution function, essentially all the states below E_f are occupied at low temperature and all above E_f are empty. This requires $E_{\underline{k}}$ to be slightly less than E_f and $E_{\underline{k}+\underline{q}}$ slightly greater; hence $\underline{k}$ must lie just inside the Fermi surface. Similarly, $\underline{k}+\underline{q}$ must be slightly outside the Fermi surface. Whilst there are many pairs of points $E_{\underline{k}}$ and $E_{\underline{k}+\underline{q}}$ which satisfy the above requirements for the Fermi surface, there must be a large

number of such pairs of points separated by the same $\underline{q}$ in order to obtain a large $\chi(\underline{q})$. Lomer (1962) first pointed out that the existence of large nearly flat parallel areas separated by $\underline{q}$ were the Fermi surface feature required to produce a maximum in $\chi(\underline{q})$.

The details of the calculation of $\chi(\underline{q})$ are included in the original paper of Evenson and Liu (1969) and a review of band structure calculations in the rare earth metals is given by Freeman (1972).

APPENDIX 4

DERIVATION OF THE SUSCEPTIBILITY, χ , AND ORDERING TEMPERATURE, T_{FN}, FOR A FERRIMAGNETIC ALLOY

The magnetisation on the two sublattices A and B is given by eqn. 2.15

$$M_a = \frac{C_a}{T}\left[H - x\lambda_{aa}M_a - (1-x)\,\lambda_{ab}M_b\right]$$

$$M_b = \frac{C_b}{T}\left[H - (1-x)\,\lambda_{bb}M_b - x\lambda_{ab}M_a\right] \qquad \ldots(A4.1)$$

Solving these two equations simultaneously gives

$$M_a = \frac{C_a\left[T+C_b\lambda_{bb}(1-x)\right] - C_aC_b(1-x)\lambda_{ab}}{\left[T+C_ax\lambda_{aa}\right]\left[T+C_b(1-x)\lambda_{bb}\right] - C_aC_bx(1-x)\lambda_{ab}^2}\,H$$

$$M_b = \frac{C_b\left[T+C_ax\lambda_{aa}\right] - C_aC_bx\lambda_{ab}}{\left[T+C_ax\lambda_{aa}\right]\left[T+C_b(1-x)\lambda_{bb}\right] - C_aC_bx(1-x)\lambda_{ab}^2}\,H \qquad \ldots(A4.2)$$

The inverse susceptibility $1/\chi = \dfrac{H}{M_a+M_b}$

$$\text{i.e. } \frac{1}{\chi} = \frac{T^2+T\left[C_ax\lambda_{aa}+C_b(1-x)\lambda_{bb}\right] - C_aC_bx(1-x)(\lambda_{ab}^2-\lambda_{aa}\lambda_{bb}}{T(C_a+C_b) + C_aC_b\left[x\lambda_{aa}+(1-x)\lambda_{bb}-2\lambda_{ab}\right]}$$

Multiplying numerator and denominator by C ($\equiv C_a+C_b$) gives

$$= \frac{T^2C+TC\left[C_ax\lambda_{aa}+C_b(1-x)\lambda_{bb}\right] - C_aC_bx(1-x)\,(\lambda_{ab}^2-\lambda_{aa}\lambda_{bb})}{C\cdot\left[TC + C_aC_b\left[x\lambda_{aa} + (1-x)\,\lambda_{bb} - 2\lambda_{ab}\right]\right]}$$

Let $TC + C_a C_b (x\lambda_{aa} + (1-x)\lambda_{bb} - 2\lambda_{ab}) = D$. Then the numerator may be factorised in terms of D

$$\text{Numerator} = TD - TC_aC_b\left[x\lambda_{aa} + (1-x)\lambda_{bb} - 2\lambda_{ab}\right] + TC\left[C_a x\lambda_{aa} + C_b(1-x)\lambda_{bb}\right]$$

$$- C\,C_aC_b x(1-x)\,(\lambda_{ab}^2 - \lambda_{aa}\lambda_{bb})$$

$$\text{Therefore, } \frac{1}{\chi} = \frac{T}{C} - \frac{TC_aC_b\left[x\lambda_{aa} + (1-x)\lambda_{bb} - 2\lambda_{ab}\right] + TC\left[C_a x\lambda_{aa} + C_b(1-x)\lambda_{bb}\right] - C\,C_aC_b x(1-x)\,(\lambda_{ab}^2 - \lambda_{aa}\lambda_{bb})}{CD}$$

Multiplying numerator and denominator by C and factorising the numerator,

$$\text{Numerator} = \left[TC + C_aC_b\left[x\lambda_{aa} + (1-x)\lambda_{bb} - 2\lambda_{ab}\right]\right]\left[\lambda_{aa}C_a^2 x + \lambda_{bb}(1-x)C_b^2 + 2\lambda_{ab}x(1-x)C_aC_b\right]$$

$$- \left[TC + C_aC_b\left[x\lambda_{aa} + (1-x)\lambda_{bb} - 2\lambda_{ab}\right]\right]\left[\lambda_{aa}C_a^2 x + \lambda_{bb}(1-x)C_b + 2\lambda_{ab}x(1-x)C_aC_b\right]$$

$$- TCC_aC_b\left[x\lambda_{aa} + (1-x)\lambda_{bb} - 2\lambda_{ab}\right] + TC^2\left[C_a x\lambda_{aa} + C_b(1-x)\lambda_{bb}\right]$$

$$- C^2C_aC_b\,(\lambda_{ab}^2 - \lambda_{aa}\lambda_{bb})\,x(1-x)$$

$$\text{Therefore, } \frac{1}{\chi} = \frac{T}{C} + \frac{1}{\chi_o} + \frac{A}{C^2D}$$

$$\text{where } \frac{1}{\chi_o} = \frac{1}{C^2}\left[\lambda_{aa}C_a^2 x + \lambda_{bb}(1-x)C_b^2 + 2\lambda_{ab}x(1-x)C_aC_b\right]$$

$$\text{and } A = -TC\lambda_{aa}xC_a^2 - TC\lambda_{bb}(1-x)C_b^2 - 2TC\lambda_{ab}x(1-x)C_aC_b$$

$$- C_a^3C_bx\lambda_{aa}\left[x\lambda_{aa} + (1-x)\lambda_{bb} - 2\lambda_{ab}\right]$$

$$- C_aC_b^3(1-x)\lambda_{bb}\left[x\lambda_{aa} + (1-x)\lambda_{bb} - 2\lambda_{ab}\right]$$

$$- 2C_a^2C_b^2x(1-x)\lambda_{ab}\left[x\lambda_{aa} + (1-x)\lambda_{bb} - 2\lambda_{ab}\right]$$

$$- TCC_aC_b\left[x\lambda_{aa} + (1-x)\lambda_{bb} - 2\lambda_{ab}\right]$$

$$+ TC^2\left[C_ax\lambda_{aa} + C_b(1-x)\lambda_{bb}\right]$$

$$- C^2C_aC_bx(1-x)\ (\lambda_{ab}^2 - \lambda_{aa}\lambda_{bb})$$

The expression for A may be simplified to

$$A = TC\left[2C_aC_b\lambda_{ab}\left[1 - (1-x)\right]\right]$$

$$- C_aC_b\left[\left[x\lambda_{aa} + (1-x)\lambda_{bb} - 2\lambda_{ab}\right]\left[C_a^2x\lambda_{aa} + C_b^2(1-x)\lambda_{bb} + 2x(1-x)\lambda_{ab}\right]\right]$$

$$- C^2C_aC_bx(1-x)\ (\lambda_{ab}^2 - \lambda_{aa}\lambda_{bb})$$

and then further rewritten in terms of D as

$$A = D\left[C_aC_b2\lambda_{ab}(1-x+x^2)\right]$$

$$- C_a^2C_b^2\left[\left[x\lambda_{aa} + (1-x)\lambda_{bb} - 2\lambda_{ab}\right]\left[2\lambda_{ab}(1-x+x^2)\right]\right]$$

$$- C_aC_b\left[\left[x\lambda_{aa} + (1-x)\lambda_{bb} - 2\lambda_{ab}\right]\left[C_ax\lambda_{aa} + C_b(1-x)\lambda_{bb} + 2x(1-x)\lambda_{ab}\right]\right]$$

$$- C^2C_aC_bx(1-x)C_aC_b(\lambda_{ab} - \lambda_{aa}\lambda_{bb})$$

Therefore, $$\frac{A}{C^2D} = \frac{2C_aC_b\lambda_{ab}(1-x+x^2)}{C^2} - \frac{B}{C^2D}$$

where $$B = C_aC_b\left[C_aC_b\left[x\lambda_{aa}+(1-x)\lambda_{bb}-2\lambda_{ab}\right]\left[2\lambda_{ab}(1-x+x^2)\right]\right.$$
$$+ \left[x\lambda_{aa}+(1-x)\lambda_{bb}-2\lambda_{ab}\right]\left[C_a^2x\lambda_{aa}+C_b(1-x)\lambda_{bb}+2x(1-x)\lambda_{ab}\right]$$
$$\left.+ C^2C_aC_b(\lambda_{ab}^2 - \lambda_{aa}\lambda_{bb})\right]$$

The result of the above long division may be incorporated in $\frac{1}{\chi_o}$ to give

$$\frac{1}{\chi_o'} = \frac{1}{C^2}\left[\lambda_{aa}C_a^2x + \lambda_{bb}(1-x)C_b^2 + 4\lambda_{ab}x(1-x)C_aC_b\right]$$

The expression for B may be simplified giving

$$B = C_a^2x\left[\lambda_{aa}(x\lambda_{aa}-2\lambda_{ab}) + \lambda_{ab}^2(1-x)\right]$$
$$+ C_b^2(1-x)\left[\lambda_{bb}\left[(1-x)\lambda_{bb}-2\lambda_{ab}\right] + \lambda_{ab}^2(1-x)\right]$$
$$+ 2C_aC_bx(1-x)\left[\lambda_{ab}\left[x\lambda_{aa}+(1-x)\lambda_{bb}-\lambda_{ab}\right]-\lambda_{aa}\lambda_{bb}\right]$$
$$+ 2x(1-x)\lambda_{ab}\left[x\lambda_{aa}+(1-x)\lambda_{bb}-2\lambda_{ab}\right]$$

The complete expression for the inverse susceptibility is

$$\frac{1}{\chi} = \frac{T}{C} + \frac{1}{\chi_o'} + \frac{K'}{T-\theta'}$$

where $$\theta' = \frac{C_aC_b}{C}\left[x\lambda_{aa} + (1-x)\lambda_{bb}-2\lambda_{ab}\right]$$

and $$K' = \frac{B}{C^3}$$

The ferrimagnetic Néel temperature may be found simply by setting either of the denominators of eqn. A4.2 to zero

$$\text{i.e. } \left[T + C_a x\lambda_{aa}\right]\left[T + C_b(1-x)\lambda_{bb}\right] - C_a C_b x(1-x)\lambda_{ab}^2 = 0$$

Taking the positive square root this yields

$$T_{NF} = -\frac{1}{2}\left[C_a x\lambda_{aa} + C_b(1-x)\lambda_{bb}\right] + \frac{1}{2}\left[\left[C_a x\lambda_{aa} - C_b(1-x)\lambda_{bb}\right]^2 + 4x(1-x)C_a C_b \lambda_{ab}^2\right]^{\frac{1}{2}}$$

CHAPTER 1 - REFERENCES

ACHIWA, N., KAWANO, S. 1973
J. Phys. Soc. Japan 35 303

BEHRENDT, D.K., LEGVOLD, S., SPEDDING, F.H., 1958
Phys. Rev. 109 1544

BLY, P.H., CORNER, W.D., TAYLOR, K.N.R., 1969
J.A.P. 40 4787

BOWDEN, G.J. 1975
Private Communication

BOZORTH, R.M., GABINO, R.J. 1966
Phys. Rev. 147 487

BUCHER, E., SCHMIDT, P.H., JAYARAMAN, A., ANDRES, K.
MAITA, J.P., DERNIER, P.D. 1970
Phys. Rev. 132 3911

CABLE, J.W., WOLLAN, E.O., KOEHLER, W.C., WILKINSON, M.K.
1961
J.A.P. 32 495

CABLE, J.W., MOON, R.M., KOEHLER, W.C., WOLLAN, E.O., 1964
Phys. Rev. Letts. 12 553

CHATTERJEE, D., TAYLOR, K.N.R. 1972
J. Phys. F. 2 151

CHILD, H.R. 1964
Doctoral dissertation, University of Tennessee

CHILD, H.R., KOEHLER, W.C., WOLLAN, E.O., CABLE, J.W., 1965
Phys. Rev. 138 A1655

CHILD, H.R., KOEHLER, W.C., 1968
Phys. Rev. 174 562

CORNER, W.D., ROE, W.E., TAYLOR, K.N.R., 1962
Proc. Phys. Soc. (London) 80 927

DAANE, A.H., RUNDLE, R.E., SMITH, H.S., SPEDDING, F.H. 1954
Acta. Cryst. 7 532

DARNELL, F.J., MOORE, E.P., 1963
J.A.P. 34 1337

DIETRICH, O.W., ALS-NIELSEN, J. 1967
Phys. Rev. 162 315

FINEMORE, D.K., WILLIAMS, L.J., SPEDDING, F.H.
HOPKINS, D.C. 1969
Phys. Rev. 176 712

FLIPPEN, R.B. 1964
J.A.P. 35 1047

FUJIMORI, H., GOTO, K., WILLIAMS, D.E.G., 1974
J. Phys. F. 4 2152

GRAHAM, C.D., 1962
J. Phys. Soc. Japan 16 1310

GREEN, R.W., LEGVOLD, S., SPEDDING, F.H., 1961
Phys. Rev. 122 827

GSCHNEIDNER, K.A., 1961
"Rare Earth Alloys", D. Van Nostrand. P.13. P.69

HARRIS, I.R., RAYNER, G.V., 1969
J.L.C.M. 17 336

HEGLAND, D.E., LEGVOLD, S., SPEDDING, F.H. 1963
Phys. Rev. 131 158

HUME-ROTHERY, W., 1939
"Structure of Metals and Alloys". Inst. Metals, London.

JOHANSSON, B., ROSENGREN, A., 1975
Phys. Rev. 11 2836

JOHANSSON, K., LEBECH, B., NIELSEN, M., BJERRUM-MOLLER, H.,
MACKINTOSH, A.R. 1970
Phys. Rev. Letts. 25 524

JOHANSSON, T., MCEWEN, K.A., TOUBORG, P. 1971
J. de Phys. 32 C1 372

KAWANO, S., ACHIWA, N., 1975
J. Phys. Soc. Japan 38 285

KOEHLER, W.C., CABLE, J.W., WOLLAN, E.O., WILKINSON, M.K.
1962(a)
Phys. Soc. Japan Suppl. 17 B-III 32

KOEHLER, W.C., CABLE, J.W., WOLLAN, E.O., WILKINSON, M.K.
1962(b)
Phys. Rev. 126 1672

KOEHLER, W.C., CHILD, H.R., WOLLAN, E.O., CABLE, J.W., 1963
J.A.P. 34 1335

KOEHLER, W.C., 1965
J.A.P. 36 1078

KOEHLER, W.C., CABLE, J.W., CHILD, H.R., WILKINSON, M.K.,
WOLLAN, E.O., 1967
Phys. Rev. 158 450

KOEHLER, W.C., 1972
"Magnetic Properties of Rare Earth Metals" ed. Elliot R.J.
P.81., Pub. Plenum

KOEHLER, W.C., MOON, R.M. 1972
Phys. Rev. Letts. 29 1468

KUCHIN, V.M., SEMENKOV, V.A., SHIL'STEIN, S.Sh., Yu, B., 1969
Sov. Phys. J.E.T.P. 28 649

MCEWEN, K.A., COCK, G.J., ROELAND, L.W., MACKINTOSH, A.R.
1973
Phys. Rev. Letts. 30 287

MOON, R.M., CABLE, J.W., KOEHLER, W.C. 1964
J.A.P. Suppl. 35 1041

NACHMAN, J.F., LUNDIN, C.E., RAUSCHER, G.P. 1963
Tech. Rep. No. 1 Contract No. Nonr 3661 (02)
Denver Research Inst.

NERESON, N.G., OLSEN, C.E., ALPERIN, H.A. 1964
J.A.P. 35 1045

NIGH, H.E., LEGVOLD, S.E., SPEDDING, F.H., BEANDRY, B.V. 1964
J. Chem. Phys. 41 3799

PALMER, P.J., CHIKALLE, T.D., 1971
J.L.C.M. 24 233

RICHARDS, D.B., LEGVOLD, S., 1969
Phys. Rev. 186 508

SCHIEBER, M., FONER, S., DOCLO, R., MCNIFF, E.J., 1968
J.A.P. 39 885

SHABITA, T., NAGAMIYA, T., 1975
J. Phys. Soc. Japan 38 1286

SMART, J.S., 1966
"Effective field theories of Magnetism", W.B. Saunders Company. P. 23

SPEDDING, F.H., VALLETTA, R.H., DAANE, A.H. 1962
Trans Am. Soc. Metals 55 483

SPEIGHT, J.D., HARRIS, I.R., RAYNOR, G.V. 1968
J.L.C.M. 15 317

STRANDBERG, D.L., LEGVOLD, S., SPEDDING, F.H., 1962
Phys. Rev. 27 2046

TAYLOR, K.N.R., 1970
Contemp. Phys. 11 423

TAYLOR, K.N.R., DARBY, M.I. 1972
"Physics of Rare Earth Solids", Chapman and Hall. P. 4

THOBURN, W.C., LEGVOLD, S., SPEDDING, F.H. 1958
Phys. Rev. 110 1298

TISSOT, L., BLAISE, A. 1970
J.A.P. 41 1180

VAN VLECK, J.H. 1932
"The theory of electric and magnetic susceptibilities", O.U.P. P. 249

WILKINSON, M.K., KOEHLER, W.C., WOLLAN, E.O., CABLE, J.W.
1961(a)
J.A.P. 32 485

WILKINSON, M.K., CHILD, H.R., MCHARQUE, C.J., KOEHLER, W.C., WOLLAN, E.O., 1961(b)
Phys. Rev. 122 1409

WILL, G., NATHANS, R., ALPERIN, H.A. 1964
J.A.P. 35 1045

WOLLAN, E.O. 1967
J.A.P. 38 1371

CHAPTER 2 - REFERENCES

BELOV, K.P., LEVITIN, R.E., NIKITIN, S.A., 1964
Sov. Phys. Uspekhi 7 179

BLEANEY, B., 1963
Proc. Roy. Soc. (London) A276 39

BJERRUM MOLLER, H., HOUMANN, J.G., MACKINTOSH, A.R., 1967
Phys. Rev. Letts. 19 312

BOWDEN, G.J., BUNBURY, D. St. P., MCCAUSLAND, M.A.H., 1971
Phys. C. 4 1840

CABLE, J.W., WOLLAN, E.O. 1968
Phys. Rev. 165 733

COOPER, B.R., 1968
Phys. Rev. 169 281

COOPER, B.R., WANG, Y.L., 1968
Phys. Rev. 172 539

COOPER, B.R., WANG, Y.L., 1969
Phys. Rev. 185 696

ELLIOT, R.J., 1961
Phys. Rev. 124 346

ELLIOT, R.J., WEDGEWOOD, F.A. 1964
Proc. Phys. Soc. 84 63

ELLIOT, R.J., 1965
"Magnetism" Vol. IIA ed. Rado, G.T. and Suhl, H., P.385
Pub. Academic Press.

ENZ, U. 1961
J.A.P. 32 225

HERPIN, A., MERIEL, P. 1961
J. de Physique 22 337

HUTCHINGS, M.T., 1964
Solid State Phys. 16 227

JENSEN, J., HOUMANN, J.G., BJERRUM MOLLER, H. 1975
Phys. Rev. B. 12 303

JOHANSSON, T., LEBECH, B., NIELSEN, M.,
BJERRUM MOLLER, H., MACKINTOSH, A.R., 1970
Phys. Rev. Letts. 25 524

KASUYA, T. 1956
Prog. Theoret. Phys. 16 45

KASUYA, T. 1966
"Magnetism" Vol. IIB ed. Rado, G.T., and Suhl, H., P.27
Pub. Academic Press.

KEETON, S.C., LOUCKS, T.L., 1968
Phys. Rev. 168 672

KITANO, Y., NAGAMIYA, T. 1964
Prog. Theoret. Phys. 31 1

KITTEL, C. 1971
"Introduction to Solid State Physics" pub. Wiley P.529

LAX, B., BUTTON, K.J., 1962
"Microwave Ferrites and Ferrimagnetics" pub. Magraw Hill
P. 104

LINDGARD, P.A., HARMAN, B.N., FREEMAN, A.J. 1975
Phys. Rev. Letts. 35 383

LIU, S.H. 1961
Phya. Rev. 123 470

MACKINTOSH, A.R., BJERRUM MOLLER, H. 1972
"Magnetic Properties of Rare Earth Metals" ed. Elliot,
R.J. Plenum. P. 187

MIWA, H., YOSIDA, K. 1961
Prog. Theoret. Phys. 26 693

MORRISH, A.H., 1965
"Physical Principles of Magnetism" ed. Wiley P.282

NÉEL, L. 1932
Ann. Phys. 18 5

RAINFORD, B.D. 1971
A.I.P. Conference "Magnetism and Magnetic Materials"
ed. Graham, C.D. and Rhyne, J.J.

RUDERMANN, M.A., KITTEL, C. 1954
Phys. Rev. 96 99

STEVENS, K.W.H., 1952
Proc. Phys. Soc. A65 209

TRAMMELL, G.T. 1963
Phys. Rev. 131 932

YOSIDA, K. 1957
Phys. Rev. 106 893

CHAPTER 3 - REFERENCES

BACON, G.E., 1962
Neutron Diffraction, O.U.P., P. 183

BLUME, M., FREEMAN, A.J., WATSON, R.E., 1962
J. Chem. Phys. 37 1245

BROWN & FORSYTH 1973
"The Crystal Structure of Solids", Arnold, P.47

HALPERN, O., JOHNSON, J.H., 1939
Phys. Rev. 55 898

HERPIN, A., MERIEL, P., VILLAIN, J. 1959
C.R. Acad. Sci. Paris 249 1334

INTERNATIONAL TABLES FOR X-RAY CRYSTALLOGRAPHY Vol. III
ed. Lonsdale K. P. 233

KOEHLER, W.C., 1961a
Acta. Cryst. 14 535

KOEHLER, W.C., 1961b
J. Appl. Phys. 32 205

KOEHLER, W.C., 1971
"Magnetic Properties of Rare Earth Metals" ed. Elliot
R.J. Plenum P. 81

LANDER, G.H., BRUN, T.O., 1970
J. Chem. Phys. 53 1387

LOVESEY, S.W., RIMMER, D.E. 1969
Rept. Prog. Phys. 32 333

MACKINTOSH, A.R., BJERRUM MOLLER, H. 1971
"Magnetic Properties of Rare Earth Metals" ed. Elliot R.J.
Plenum. P. 187

MARSHALL, W., LOVESEY, S.W. 1971
Theory of Thermal Neutron Scattering ,O.U.P., P.173

TRAMMELL, G.T. 1953
Phys. Rev. 92 1387

VAN VLECK, J.H. 1939
Phys. Rev. 55 924

VILLAIN, J. 1959
J. Phys. Chem. Solids 11 303

YOSHIMORI, A., 1959
J. Phys. Soc. Japan 14 807

CHAPTER 4 - REFERENCES

BACON, G.E., 1962
O.U.P. "Neutron Diffraction". P. 32

BASTON, A.H. 1972
A.E.R.E. Report M2570

BEHRENDT, D.R., LEGVOLD, S., SPEDDING, F.H. 1963
Phys. Rev. 109 1544

BRUGGER, R.M. 1965
"Thermal Neutron Scattering" ed. Egelstaff P.A.
Academic Press. P.54

CHATTERJEE, D., TAYLOR, K.N.R., 1972
J. Phys. F. 2 151

DYER, R.F., LOW, G.G.E.,
A.E.R.E. Report R3494

FONER, S., 1956
Rev. Sci. Inst. 27 548

FONER, S., 1959
Rev. Sci. Inst. 30 548

SALMANS, L.R., STRNAT, K., HOFFER, G.I. 1968
U.S.A.F. Technical Report AFML - TR - 68159

TURCHIN, V.F. 1965
"Slow Neutrons" Silvan Press (Jerusalem) P.68

REFERENCES - CHAPTER 5

BEHRENDT, D.R., LEGVOLD, S., SPEDDING, F.H. 1958
Phys. Rev. 109 1544

CHATTERJEE, D., TAYLOR, K.N.R. 1972
J. Phys. F. 2 151

CHILD, H.R., KOEHLER, W.C., WOLLAN, E.O., CABLE, J.W. 1965
Phys. Rev. 138 A1655

DARNELL, F.J., MOORE, E.P. 1963
J.A.P. 34 1337

FINNEMORE, D.K., WILLIAMS, L.J., SPEDDING, F.H.,
HOPKINS, D.C. 1968
Phys. Rev. 176 712

FRADIN, F.Y., ROSS, J.W., ISACCS, L.L., LAM, D.J. 1968
Phys. Letts. 28A 276

KAWANO, S., ACHIWA, N., 1974
J. Phys. Soc. Japan 375 569

TAYLOR, K.N.R., DARBY, M.I., 1972
"Physics of Rare Earth Solids" P. 69 pub. Chapman & Hall.

THOBURN, W.C., LEGVOLD, S., SPEDDING, F.H. 1958
Phys. Rev. 128 1297

REFERENCES - CHAPTER 6

ACHIWA, N., KAWANO, S. 1973
J. Phys. Soc. Japan 35 303

BLOCH, D., PAUTHANET, R. 1964
Proceedings of the International Conference on Magnetism
P. 225 pub. Inst. of Phys.

DARBY, M.I., TAYLOR, K.N.R. 1966
J.A.P. 37 1442

FLEMING, G.S., LIU, S.H. 1970
Phys. Rev. B. 2 164

GSCHNEIDNER, K.A. 1961
"Rare Earth Alloys" p. 55 pub. Van Nostrand.

HARRIS, I.R., 1970
Private Communication

KASUYA, T. 1966
"Magnetism Vol. IIB" P. 27 ed. Rado, G.T. and Suhl, H.
pub. Academic Press.

KITANO, Y., NAGAMIYA, T. 1964
Prog. Theo. Phys. 31 1

KOEHLER, W.C., MOON, R.M. 1972
Phys. Rev. Letts. 29 1468

LINDGARD, P.A., HARMAN, B.N., FREEMAN, A.J., 1975
Phys. Rev. Letts. 35 383

LIU, S.H., 1962
Phys. Rev. 127 1889

MCEWEN, K.A., COCK, G.J., ROELAND, L.W., MACKINTOSH, A.R. 1973
Phys. Rev. Letts. 30 287

MILSTEIN F., ROBINSON, L.B. 1967
Phys. Rev. 159 466

NAGAMIYA, T., NAGATA, K., KITANO, Y. 1962
Prog. Theo. Phys. 27 1253

ROBINSON, L.B., TAN, S.I., STERRETT, F.F., 1966
Phys. Rev. 141 548

UMEBAYASHI, H., SHIRANE, G., FRAZER, B.C., DANIELS, W.B.
1968
Phys. Rev. 165 688

REFERENCES - APPENDIX 3

EVENSON, W.E., LIU, S.H. 1969
Phys. Rev. 178 783

FREEMAN, A.J. 1972
"Magnetic Properties of Rare Earth Metals" ed. Elliot, R.J.
pub. Plenum. P. 245

LOMER, W.M. 1962
Proc. Phys. Soc. (London) 80 489

MATTIESS, L.F. 1964
Phys. Rev. 133 A1399